

The University of Nottingham

School of Mechanical, Materials, and Manufacturing Engineering

MACRO-SCALE MODELLING OF THE IMPACT RESPONSE OF 3D WOVEN COMPOSITES FOR AEROSPACE APPLICATIONS

by

Weiyi Kong

MSc, BEng (Hons)

Thesis submitted to the University of Nottingham for the degree of Doctor of Philosophy

August 2016

Abstract

The objective of this work is to develop a reliable simulation methodology that can be applied to predict the impact response of the components made with 3D textile composites in aero engine applications. Textile composites are excellent candidate materials for the design of aero engine fan containment casings, which are required to sustain the high velocity impact during a fan blade out (FBO) event. This work is focused on a particular form of 3D woven textile composites, in which reinforcement through the thickness is provided by the interlocking weft or warp yarns.

An extensive experimental characterisation was conducted for the composites with four different types of reinforcement. The in-plane mechanical properties under the quasi-static tensile, compressive and shear loadings were obtained. The compressive properties at high strain rate were determined in split Hopkinson pressure bar tests. In additional to that, ballistic impact tests were conducted with these composite materials to study their response to high velocity impact loads.

The properties determined in the mechanical tests were employed to specify the input data for a commercially available material model in the finite element (FE) software, LS-DYNA. The model was validated by simulating the ballistic impact tests. Good agreement between the predictions and the experimental results was ensured. Once validated, the material model was applied in a range of parametric studies. Since the plate impact tests cannot fully represent the complexity of the FBO event, effects of the projectile shape, the impact obliquity, the target size and the target curvature on the impact performance were investigated by means of parametric studies.

To ease the simulation cost encountered during the modelling of a large casing structure, mixed element type analysis (META) was employed for its FE models, where the computationally costly solid elements were coupled with simpler shell elements. The predictive capability of the META models was assessed by comparing their predictions with those of the corresponding solid-element-only models. The study has shown that this method can substantially reduce the simulation time without compromising the accuracy of predictions.

Acknowledgements

I would like to express my sincere gratitude to the main supervisor of this work, Dr. Richard Brooks, for his patience, continuous encouragement, outstanding support and insightful guidance, and to Dr. Elena Sitnikova for her excellent help in this project and in revising this thesis, and also to the other members of the supervision team: Prof. Shuguang Li and Prof. Andrew Long.

The financial support to this project was provided by AVIC Commercial Aircraft Engine (ACAE) CO., Ltd, China and this support is gratefully acknowledged. Thanks to Dr. Shoufeng Hu, Dr. Zhiqiang Wang and colleagues of ACAE for their advices to this project.

The help from the fellow PhD students of this joint research program, Qing Pan, Tianhong Yu and Xiantao Zhao, is sincerely acknowledged.

Thanks to the members of Polymer Composite Research Group, especially to Stanley Chacko Salem and Paul Turner for their help in high strain rate testing.

I also would like to thank the School of Mechanical, Materials and Manufacturing Engineering for the use of the school facilities, especially to the technical staff: Paul Johns and Ben Jennison for the help in manufacturing composite materials, Thomas Buss and Jason Greaves for mechanical tests, John Hinchliffe and Andrew Plummer for manufacturing the testing rigs. Special thanks for the access to the University of Nottingham High Performance Computing Facility.

Finally, I am grateful to my family for the constant encouragement and unconditional support in every aspect of my work, as always. Without you guys, I would not be the person I am today.

Contents

Abstract I
Acknowledgements II
Contents III
Abbreviations and Notations VII
Chapter 1 Introduction 1
1.1 Background 1
1.2 Aims and objectives 4
1.3 Thesis layout 5
Chapter 2 Literature review 7
2.1 Introduction 7
2.2 Composite materials 7
2.2.1 Constituents 7
2.2.2 2D laminated composites 8
2.2.3 3D textile composites 9
2.2.4 3D woven composites 10
2.3 Modelling/analysis of 3D textile composites 12
2.3.1 Multi-scale modelling 12
2.3.2 Macro scale modelling 14
2.3.3 Failure criteria 15
2.3.4 Damage mechanics 17
2.3.5 Modelling strain rate effects 18
2.3.6 Selection of material models for this study 20
2.4 The characterisation testing of 3D woven composites 21
2.4.1 Experimental methods 21
2.4.2 Experimental characterisation of 3D woven composites under QS loading 24
2.4.3 Dynamic characterisation testing of 3D woven composites 25

2.5 Impact testing 27
2.5.1 Tests and simulations related to FBO 27
2.5.2 Impact testing of 3D textile composites 29
2.6 Summary 34
Chapter 3 The mechanical testing of 3D woven composites 35
3.1 Introduction 35
3.2 Manufacturing 35
3.3 Tested materials 38
3.4 Quasi-static tests 43
3.4.1 Methodology 43
3.4.2 Results 48
3.5 Split Hopkinson Pressure bar 66
3.5.1 Methodology 66
3.5.2 Results 69
3.6 Conclusions 76
Chapter 4 Ballistic impact tests on the 3D woven composites 78
4.1 Introduction 78
4.2 Set-up of ballistic impact tests 78
4.3 Data acquisition and processing 82
4.4 Experimental data and analysis 83
4.4.1 Impact velocity data analysis 83
4.4.2 Statistical analysis of ballistic impact test data 84
4.4.3 Comparison of ballistic resistances of the four composites 87
4.5 Damage and failure after the ballistic impact 88
4.5.1 Visual inspection 88
4.5.2 X-ray computed tomography (XCT) 92
4.6 Conclusions 99

Chapter 5 Phenomenological macro scale modelling for impact behaviour of 3D woven composites 100
5.1 Introduction 100
5.2 The input data for MAT162 101
5.2.1 Elastic and strength properties 102
5.2.2 Parameter calibration by single element modelling 104
5.2.3 Strain rate scaling 112
5.2.4 Assessment of the input sets under high rate loadings 115
5.2.5 Discussions 118
5.2.6 Inputs for CF-IM7 120
5.3 Simulation of the ballistic impact tests 121
5.3.1 Methodology 121
5.3.2 Velocity prediction 123
5.3.3 Prediction of damage and failure 125
5.4 Conclusions 129
Chapter 6 Parametric study for plate impact tests 130
6.1 Introduction 130
6.2 Literature review 130
6.2.1 Projectile Shape 130
6.2.2 Obliquity 132
6.2.3 Curvature of the target 132
6.2.4 Conclusions 133
6.3 Methodology 133
6.4 Results and discussion 136
6.4.1 Shape of projectile 136
6.4.2 The span to thickness ratio 143
6.4.3 Oblique impact 146
6.4.4 Curvature of the target plate 149

6.5 Conclusions 152

Chapter 7 Mixed element type analysis (META) and simulation of casings under impact loadings 153

7.1 Introduction 153

7.2 META analysis for plate impact 154

7.2.1 General Methodology 154

7.2.2 Differences between MAT58 and MAT162 156

7.2.3 The relation between the prediction and the definition of the regions 160

7.2.4 META for thick plates 162

7.2.5 Deformation response of the plate 164

7.2.6 Damage prediction 167

7.2.7 Using the ANN model with META 170

7.3 META analysis for casing impact 170

7.3.1 Methodology 171

7.3.2 Accuracy 172

7.3.3 Saving 175

7.4 Casing impact study 175

7.4.1 Methodology 176

7.4.2 Results 177

7.5 Conclusions 183

Chapter 8 Conclusions and Recommendations 185

8.1 Conclusions 185

8.2 Recommendations for future work 189

References 191

Appendix 1. Macro scale artificial neural network (ANN) material model from multi-scale modelling 209

Appendix 2. The properties of titanium 215

Abbreviations and Notations

Abbreviations

2D	Two-dimensional
3D	Three-dimensional
FBO	Fan blade out
FE	Finite element
UD	Unidirectional
QI	Quasi-isotropic
PMC	Polymeric matrix composite
CMC	Ceramic matrix composite
MMC	Metal matrix composite
VARTM	Vacuum-assisted resin transfer moulding
CDM	Continuum damage mechanics
QS	Quasi-static
SHPB	Split Hopkinson pressure bar
FSP	Fragment simulating projectile
GF-1	3D woven composite with glass fibres: Type 1
GF-2	3D woven composite with glass fibres: Type 2
CF-T300	3D woven composite with T300 carbon fibre
CF-IM7	3D woven composite with IM7 carbon fibre
QI-IM7	IM7 carbon fibre laminates with a quasi-isotrpic layup
XCT	X-ray computed tomography
T1M1	MAT162 input set based on modelling the bilinear tensile behaviour (Method 1) of the weft direction (Direction 1)
T2M1	MAT162 input set based on modelling the bilinear tensile behaviour (Method 1) of the weft direction (Direction 2)
TM3	MAT162 input set which based on tensile behaviour without considering bilinearity (Method 3)

C	MAT162 input set based on compressive behaviour
ANN	Artificial Neural Network
META	Mixed element type analysis
SEO	Solid-element-only models
BR	Ballistic impact model with rigid titanium projectile
BD	Ballistic impact model with deformable titanium projectile
BC	Ballistic impact model with composite projectile
RD	Rotational impact model with deformable titanium projectile

Notations

ρ	Density
E	Young's modulus
G	Shear modulus
ν	Poisson's ratio
σ	Normal stress
τ	Shear stress
ε	Normal strain
γ	Shear strain
$\dot{\varepsilon}$	Strain rate
S	Strength
S_{T}	Tensile strength
A_{fabric}	Area of dry fabric
m_{fabric}	Weight of dry fabric
t_{f}	Thickness of the fabric
V_{f}	Fibre volume fraction
A	Cross-sectional area of specimens
F_{L}	Force in the longitudial direction of the specimens
σ_{L}	Stress in the longitudial direction of the specimens
σ_{T}	Stress in the transverse direction of the specimens
ε_{L}	Strain in the longitudial direction of the specimens
ε_{T}	Strain in the transverse direction of the specimens

ε_{+45}	Strain in the 45° direction to the loading direction
ε_{-45}	Strain in the -45° direction to the loading direction
C_{bar}	Velocity of sound in the steel bars in SHPB apparatus
E_{bar}	Young's modulus of the steel bars in SHPB apparatus
ρ_{bar}	Density of the steel bars in SHPB apparatus
ε_{i}	Incident strain signal
ε_{r}	Reflected strain signal
ε_{t}	Transmitted strain signal
Δ	Pulse duration
α	Transmission ratio
L	Length of the specimen in the SHPB tests
$\dot{\varepsilon_0}$	Reference strain rate
S_0	Strength at the reference strain rate
C_{rate}	Strain rate scaling coefficient
a	Deceleration of the projectile due to air drag
D	Air drag
m	Projectile mass
V	Projectile velocity
C_{d}	Drag coefficient
Re	Reynolds number
ν_k	Kinematic viscosity
d	Characteristic length of the projectile
V_{i}	Impact velocity
V_{r}	Residual velocity
V_{50}	Ballistic limit
β	Parameter in Jonas-Lambert equation
p	Parameter in Jonas-Lambert equation
f_{i}	Failure indicator in the failure criteria of MAT162
S_{RT}	Dynamic strength
E_{RT}	Rate-dependent elastic modulus
F_{ij}	Strength coefficient tensor in Tsai-Wu failure criterion
R/S	Radius to span ratio for curved plates

Chapter 1 Introduction

1.1 Background

Polymer matrix composites (PMC), which possess low weight and high static and fatigue strength, have been used to replace metals in aircraft engines since the early 1970s. Temperature requirements limit the use of PMCs to low temperature components such as fan containment casings and fan blades etc., as shown in Figure 1-1. The fan containment casing, the diameter of which can be as large as 3000 mm (GE90 [1]), is the largest component in aero engines. When the fan casing is made from low density PMC rather than mature alloys, the weight can be reduced considerably.

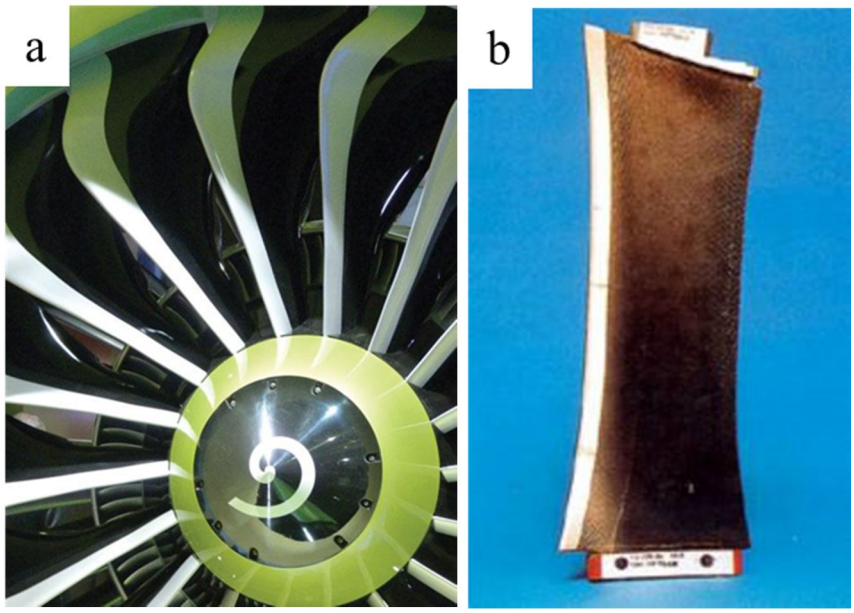


Figure 1-1 (a) Composite fan blades and fan casings of CFM Leap engines [2]; (b) A carbon fibre reinforced epoxy Trent fan outlet guide vane [3].

However, safety is clearly a key issue when developing a PMC fan casing. Bird strike and fan blade-out are two of the most severe scenarios of engine damage, in which objects with large velocities impact on the fan casing, causing significant damage. In a poorly designed fan casing, a so-called uncontained failure occurs, where the blade may penetrate the fan casing and hit the cabin, leading to serious consequences to the overall aircraft structural integrity.

Generally speaking, two types of fan casing designs have been developed,

namely softwall and hardwall as shown in Figure 1-2. As stated in a report from NASA [4]: *"Nearly all current commercial engines that have titanium fan blades use either hardwall cases made with metal alloys or softwall containment systems made with a metal alloy case overwrapped by aramid fibres in either a woven or braided form."* The earliest approach for fan blade containment was the hardwall design, where a metallic fan casing wall was made sufficiently thick to avoid blade fragment penetration. In this approach, a large amount of metallic material is used for containment, thus engine efficiency is largely sacrificed to achieve safety. During the 1970s and 1980s, softwall design was developed and first employed by General Electric in the commercial engine CF-34. This design involved wrapping fabrics around the metallic casing to contain the blade impact. The failed blade is therefore allowed to penetrate the metallic casing as long as the outside fabric catches the blade fragments and ensures containment. Hence, the thickness and the weight of the metallic fan casing could be reduced as compared to the hardwall design.

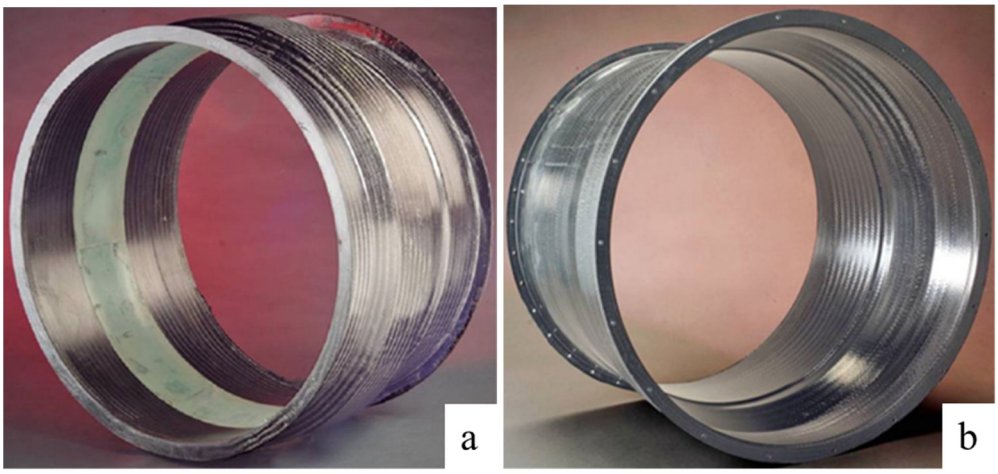


Figure 1-2 Composite softwall (a) and hardwall (b) fan casing prototype [4].

In spite of the two mature fan casing designs being available, the aero engine industry is still seeking to reduce the weight of the fan casing. Currently, significant effort is being made on developing integrated composite fan casings. Even though many composites have been considered to be valid alternatives to alloys, the GEnx [5] series developed by GE Aviation and the LEAP series [6] developed by CFM International are the only two series of engines that employ integrated composite fan casings at the moment.

The main issue impeding the wide application of composites for fan casing

components are the high costs in design and testing. For example, in the work by NASA Glenn Research Centre [4], a multi-scale testing approach was proposed for both hardwall design and softwall design. Major complexities in these tests make the development of a fan casing extremely expensive, even for metallic materials, let alone composite materials whose properties can be tailored by designing their lay-up orientation or architectures. In addition, it is compulsory to conduct a blade-out test on a real engine where the engine will be destroyed [7]. It is obviously not feasible to carry out this test on each material variation. On the other hand, there is a lack of standard material tests and analysis approaches which can reliably guide how the composite materials could be designed to perform best in a fan casing application. It is very likely that the design procedures could be much less dependent on testing and less expensive, if predictive methodologies and design tools for simulating the behaviour of composites under impacts loading were developed.

PMCs have been used in the aerospace industry for decades. The majority of PMC components involve stacking plies of lamina of various orientations into the desired structure. Numerical tools and analytical models for these laminated composites are well developed. However, for the application in fan blade containment casing design, which needs to account for the impact performance, the laminated composites are not the best choice due to their well-known vulnerability to delamination failure. Even a tool drop could lead to delamination which would consequently degrade the performance of the structure. To resolve the issue of weak delamination resistance of laminated composites, 3D textile composites have been developed. Their main difference to the laminated composites is the reinforcement in the thickness direction, which makes the material resistant to delamination. The architectures of 3D textile composites are much more complicated than those of 2D laminates, as are the failure and damage mechanisms. The well-developed methods for laminates are therefore not applicable for 3D textile composites.

However, the majority of current research is still focused on laminated composites which have shown to deliver a good mechanical performance in numerous industrial applications, while being relatively cheap to manufacture and easy to analyse. By contrast, for 3D textile composites, major complications are involved. The performance of 3D textile composites as structures or parts,

or the so-called macro scale performance, is strongly dependent on the architecture of the reinforcement, which is defined at the meso scale. The properties of yarns further rely on a smaller scale, the micro scale, where yarns are decomposed as fibres and matrix. A small change at the micro or meso scale may make a significant difference to the structural performance at the macro scale. Furthermore, composites with the same constituents and the same type of the weave can have very different properties because of different geometric properties of the reinforcement, such as size of the yarn cross-section and space between the yarns. Such complications bring great challenges to the analysis and design of the components made from 3D textile composites. Currently, there is a lack of well-established predictive methods for the analysis of 3D textile composites. Furthermore, due to the limited research on 3D textile composites, there is a shortage of material property data for extensive validation of numerical analysis methods developed. Finally, the manufacturing of 3D textile composites often involves impregnating the closely-packed 3D reinforcements with resins. If it is carried out inappropriately, instability and uncertainty could be brought into the 3D textile composites and very likely make the analysis approaches inapplicable.

To facilitate the design and development of 3D textile PMCs for the application of fan containment casing in civil aircraft engines, AVIC Commercial Aero Engine Co., Ltd (ACAE), which is a Chinese civil aero engine designer and manufacturer, established a joint program with the University of Nottingham. This thesis is the result of one of the four collaborative doctoral projects of this program. The topics of the four projects are:

1) Micro and meso scale modelling and characterisation [8];
2) Continuum damage mechanics [9];
3) Macro scale modelling (this thesis);
4) Manufacturing process modelling [10].

1.2 Aims and objectives

This doctoral project is aimed at developing predictive macro scale modelling approaches for analysing the response of 3D textile composite components under high velocity impact loadings, towards the development of integrated composite fan casings. The main objectives, listed as the following

items, are however not limited to numerical simulations:

1) To identify appropriate types of 3D textile composite materials which are suitable for the development of fan containment casings;

2) To establish experimental techniques for the systematic characterisation of 3D textile composites under quasi-static and dynamic loadings, and to determine the necessary input parameters required by the simulations;

3) To establish impact testing techniques for assessing the impact resistance of 3D textile composites and obtain comprehensive experimental data, including failure and damage modes, against which the simulations can be validated;

4) To develop simulation methodologies of macro scale finite element (FE) simulation for components of 3D textile composites, particularly fan containment casing, under critical impact loading conditions with good accuracy of predicting impact resistance, damage and failure;

5) To conduct a systematic parametric study of the key factors affecting the impact performance of integrated 3D textile composite containment casings;

6) To develop simulation methodologies for the FE analysis of large composite structures, such as fan containment casings, with high computational efficiency and good accuracy.

1.3 Thesis layout

This thesis is composed of eight chapters. The background and motivation for the current research are outlined in Chapter 1. In Chapter 2, a literature review is presented, where 3D woven PMCs are screened out as appropriate candidates for the development of integrated fan casings. Research works on material characterisation tests, impact tests and simulations of 3D woven PMCs are covered to understand the state of the art and to highlight the novelty and importance of this project.

In Chapter 3, the experimental characterisation of 3D woven composite materials is reported. Two carbon fibre composites and two glass fibre composites have been considered. The weave type of the reinforcing fabric was the same in all the composites, yet geometric properties of the weave were different. Their mechanical properties were determined at quasi-static loading, as well at high strain rates. The detailed account of the testing procedures,

equipment used and data processing techniques applied was given.

Impact testing of the 3D woven composites is described in Chapter 4. Ballistic impact tests were carried out on flat plates of all four materials. The resistance to penetration was assessed by determining a ballistic limit in each case. The failure and damage modes of the tested composite plates are presented and discussed.

In Chapter 5, a phenomenological macro scale simulation methodology by employing the commercially available composite material model MAT162 in LS-DYNA is presented. By using the properties obtained from the characterisation tests and proper calibration of the inputs, this method is able to achieve good accuracy when simulating the above ballistic impact tests. Meanwhile, the limitations of MAT162 are also discussed.

Chapter 6 addresses the differences between plate impact and FBO impact. Four factors, namely the shape of projectile, target size, impact obliquity and target curvature have been considered and their effects on the impact performance of the composites were investigated by using the calibrated inputs determined as part of ballistic impact modelling in Chapter 5.

The efficiency of finite element modelling for large composite structures by using expensive solid elements is addressed in Chapter 7. A mixed finite element type analysis was employed, where computationally cheaper element formulation (in this study thin shell elements) are used for the regions far away from the impact site. The accuracy and efficiency of this method was assessed. Then, it was employed to simulate several casing impacts, which more closely resemble the FBO impact than the plate impact tests.

In the final chapter, the main conclusions of this project are summarised. Recommendations for future research are made.

Chapter 2 Literature review

2.1 Introduction

In this chapter, a brief review of types of composite materials is given first, from which 3D woven composites are identified as more appropriate candidates for the design of fan containment casings. Then, the approaches for modelling the impact behaviour of 3D woven composites are reviewed, with emphasis on macro scale modelling methods. Improvements to these methods lie in the failure criteria, damage mechanics and strain rate effects involved. These are reviewed to understand the state of art and to select those that can be applied for defining the impact response of the textile composite in the present study. Finally, the experimental characterisation of 3D woven composites, under both quasi-static loading and high-strain-rate loadings, is reviewed.

2.2 Composite materials

2.2.1 Constituents

Composite materials are comprised of two or more separate phases, or constituents, where the strong and stiff constituent is known as the reinforcement, while the softer constituent is referred to as the matrix. Based on the material of the matrix, composites are usually categorised into three groups: polymeric matrix composites (PMC), metal matrix composites (MMC) and ceramic matrix composites (CMC) [11]. Two types of polymers, thermosets or thermoplastics, are commonly employed when manufacturing the PMCs. In thermoset polymers, the liquid resin of low viscosity is cured into a solid state by chemical cross-linking. Thermoset matrices remain solid when subsequently heated, as the cross-links are not broken at high temperatures. While the molecular chains in thermoplastics will disentangle, transferring the solid thermoplastic into a viscous liquid at high temperatures. One of the major disadvantages of thermoplastics is the high viscosity in a liquid state, which makes composite manufacturing by impregnating the continuous aligned fibres with thermoplastic matrices rather difficult.

The most common types of reinforcements in PMCs are the carbon, glass and aramid fibres. Carbon fibres possess excellent tensile strength, compressive

strength, strength to weight ratio, stiffness and high temperature resistance as compared to glass and aramid fibres. However, they are the most expensive. Glass fibres have fairly good mechanical properties and the lowest production cost. However, their densities are much larger than those of the other two fibres. Aramid fibres are excellent in terms of tensile strength, fatigue resistance and abrasion resistance, and fairly good in terms of cost and stiffness. They are also ductile to fracture whilst the other two are very brittle. Yet, their compressive strength is several times lower than their tensile strength.

Fibres are broadly categorised as continuous fibres and short fibres. In the aerospace applications, the continuous fibre composites are usually employed. The structure of the reinforcement can vary greatly, ranging from the unidirectional alignment of the fibres, other forms of continuous fibres can be produced by using technology originally developed for manufacturing textiles, e.g. weaving, braiding, knitting and etc..

This study focuses on thermoset composites reinforced with glass and carbon fibres, which are the most relevant to aero engine applications.

2.2.2 2D laminated composites

Most of the common types of high performance composites fall into the category of 2D laminated composites, where a number of thin laminae are stacked to the designated thickness and shape. A lamina can be unidirectional, if the continuous fibres are aligned in a single direction, or have textile reinforcements. Some of the common types of textile reinforcements are shown in Figure 2-1.

Unidirectional lamina and some types of the fabric laminae are usually available in form of a pre-preg, which is a tape or sheet of fibrous reinforcements impregnated with resin and then partially cured. To manufacture a desired component, multiple layers of pre-pregs of various orientations are stacked and then fully cured by heating under pressure in vacuum moulding or autoclave moulding.

For the textile reinforcements provided as dry fabrics, liquid resin impregnation is usually employed, such as the resin transfer moulding (RTM). The reinforcing fibres/fabric are placed in a mould and injected with pre-catalysed resin, which usually has low viscosity, until the reinforcements are

fully wetted. Cure takes place inside the mould, often assisted by heating.

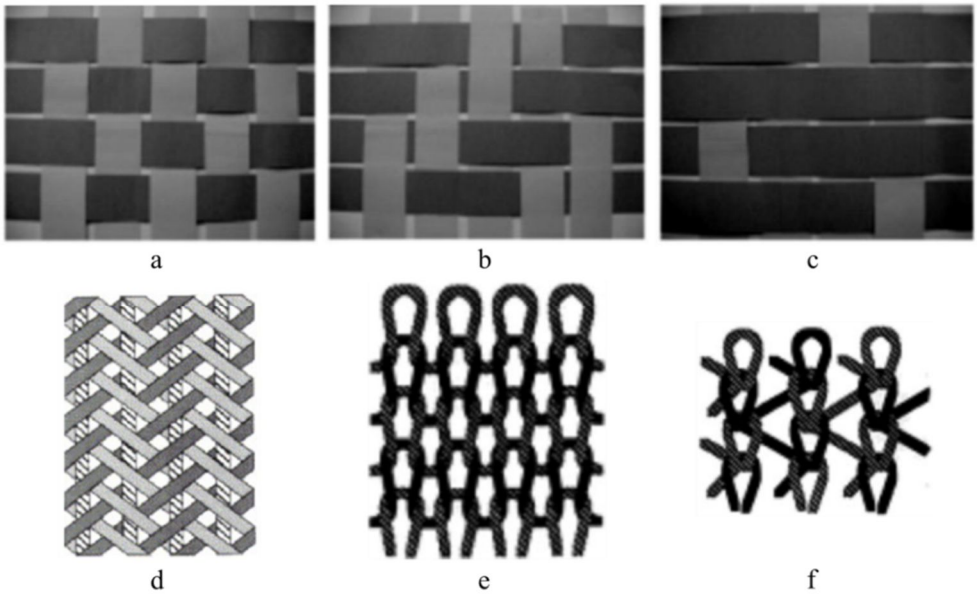


Figure 2-1 Schematics of common textile reinforcements in laminated composites: (a) plain weave, (b) twill weave, (c) 8-harness satin weave, (d) triaxial braid, (e) weft knitting and (f) warp knitting[12, 13].

Although the laminated composites are known for their high specific modulus and strength in the in-plane directions, as well as the possibility of being tailored for a specific application, all of them suffer from the lack of reinforcement binding different layers of laminae. Consequently, the composite laminates are vulnerable to inter-ply delamination, which undermines their impact resistance [14]. The low impact resistance restricts the use of laminated composite materials for the design of fan casing components. In addition, the delamination damage usually results in a significant degradation of mechanical properties, especially the compressive strength and fatigue performance [15].

2.2.3 3D textile composites

With reinforcing fibres in all three directions, 3D textile composites are much more resistant to penetration and delamination. A number of methods, such as embroidery [16] and z-pins [17], have been employed to introduce the through-thickness reinforcement to laminated composites. At the same time, integrated 3D textile reinforcements are also being developed, where 3D fabrics are produced by techniques of textile weaving, braiding, stitching and knitting [18, 19].

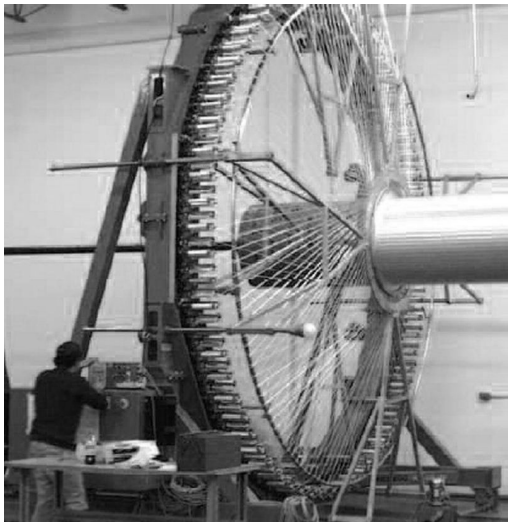


Figure 2-2 A braiding machine by Fibre Innovations available from [20].

Although 3D composites have better resistance to impact damage than the laminates, not all of the 3D textile manufacturing techniques are applicable for producing ring-shaped components of a large size, as required for the fan containment casings. In the review by Mouritz et al. [15], it was noted that 3D braiding, stitching and knitting have manufacturing restrictions in producing large and thick parts. Specifically, a braiding machine is usually significantly larger than the product itself, as shown in Figure 2-2. To manufacture a casing of 2000 mm diameter, very large braiding machines would have to be devised, which would be rather costly.

On the other hand, the manufacturing constraints are substantially less significant for the 3D weaving process. Complex near-net-shape 3D woven preforms can be produced on standard industrial weaving looms used for 2D woven fabrics at a faster rate by introducing minor changes to the weaving loom. In addition, 3D woven composites have been reported to have high resistance to low-velocity impact damage [21]. The degradation of mechanical properties is also much less severe than that of 2D counterpart laminates [22].

It can be concluded that 3D woven composites are the feasible candidates for the application in the fan containment casings. Therefore, in the following review, the primary focus will be on 3D woven composites.

2.2.4 3D woven composites

There are various forms of 3D woven textiles produced by either the conventional machines or specially designed devices. Also, different

classification terminology is employed by different groups of researchers [23-25]. The most common woven composite types fall into the category of 3D woven interlock composites, in which the layers of fabrics are interlocked through the thickness by another set of yarns. These can be roughly categorised by the path of the interlocking yarns, with four examples being shown in Figure 2-3. Higher fibre volume fraction in the through-thickness direction can be achieved by orthogonal interlocking but angle-interlock preforms are more suitable for producing complex shaped structures because of their better distortion capability [26].

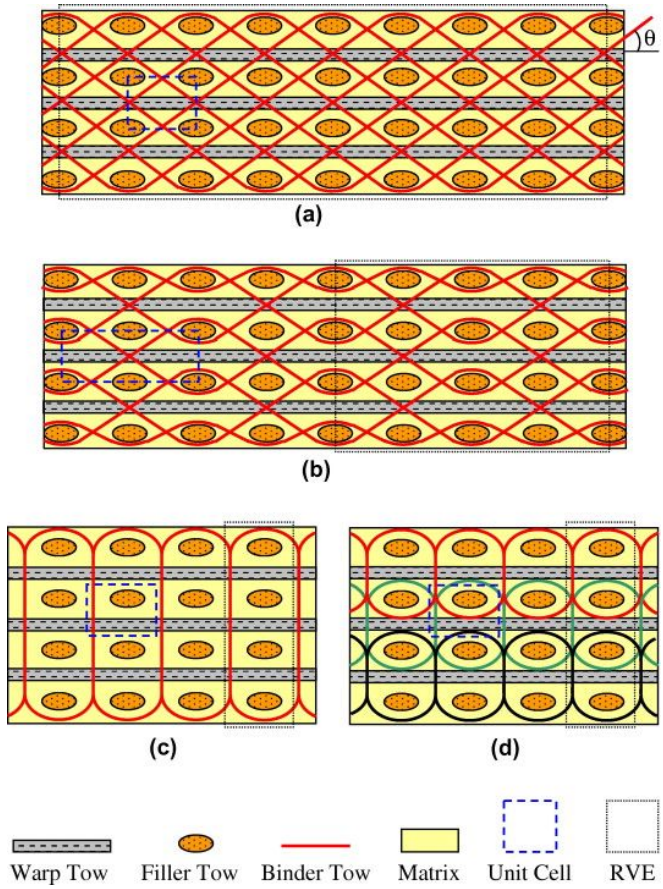


Figure 2-3 Architectures of 3D woven composites: (a) through-thickness angle-interlock, (b) layer-to-layer angle-interlock, (c) through-thickness orthogonal-interlock and (d) layer to layer orthogonal-interlock [26].

In the late 1990s, new types of 3D woven composites, called 2.5 D woven composites, were developed [27-29]. These were the ceramic matrix composites (CMC) that were employed for manufacturing the components of aero engines. Instead of using the third set of yarns (binder), as in conventional 3D woven composites, the reinforcement through the thickness was provided by the interlocking weft or warp yarns. Different types of 2.5D woven composites can

be distinguished based on the path of through-thickness reinforcements. Specifically, schematic drawings of through-thickness angle interlock and layer-to-layer angle interlock are shown in Figure 2-4 (a) and (b), respectively.

Based on the review of the open literature, very limited research has been conducted for 2.5D CMC woven composites up to date [30-33]. Research on 2.5D PMC woven composites is even more limited [34-36]. It mainly focuses on developing the numerical tools and methodologies for analysing general 3D textile composites by taking advantage of the simpler architectures of 2.5D woven textiles. No information regarding the impact performance of 2.5D woven composites could be found, both in terms of the modelling work, as well as the experimental investigations.

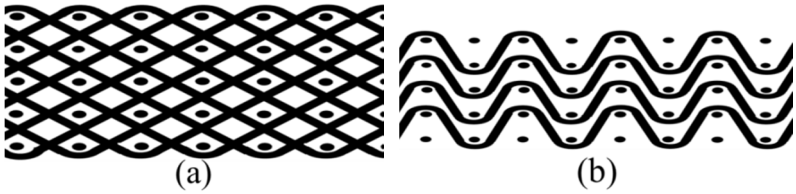


Figure 2-4 Types of 2.5D weave: (a) through-thickness angle interlock; (b) layer-to-layer angle interlock.

2.3 Modelling/analysis of 3D textile composites

2.3.1 Multi-scale modelling

Various types of the reinforcement architectures in 3D woven composites have been described in Section 2.2.4. Each of the weave types can also vary in terms of geometrical parameters, such as the size and the spacing of the yarns. Variation in geometric parameters of the weave affects the mechanical properties of the composite, hence to ensure that the material delivers its best performance in real-life applications, optimal configuration of the composite should be determined. Due to a very large number of parameters involved, it is not feasible to determine the optimal weave architecture experimentally with due consideration to both design requirements and ease of manufacturing. Therefore, development of the reliable and robust virtual characterisation tools would undoubtedly facilitate the design of these textile composites [37].

However, characterisation of 3D woven composites is far from being straightforward. While the mechanical behaviour of the unidirectional composites is understood reasonably well, and a large variety of the models have

been proposed to define the damage and failure in those materials, question of modelling the constitutive behaviour of 3D textile composites still remains open. The performance of components made from textile composites is dependent on entities of very small length scales, such as a representative volume or unit cell, representing the composite at a mesoscale and the fibre yarns at a microscale. Therefore, the constitutive models of textile composites should account for the multi scale nature of these materials [38]. One of the most common approaches is known as hierarchical or sequential multiscale modelling [39]. It involves a bottom up information transfer and homogenisation as graphically represented in Figure 2-5, where the modelling of the upper scale is dependent on the modelling of constituents and their spatial arrangements. Eventually, at a macroscale, the heterogeneous composite materials are regarded as monolithic materials, with their constitutive behaviour being defined based on the homogenised mesoscale material response.

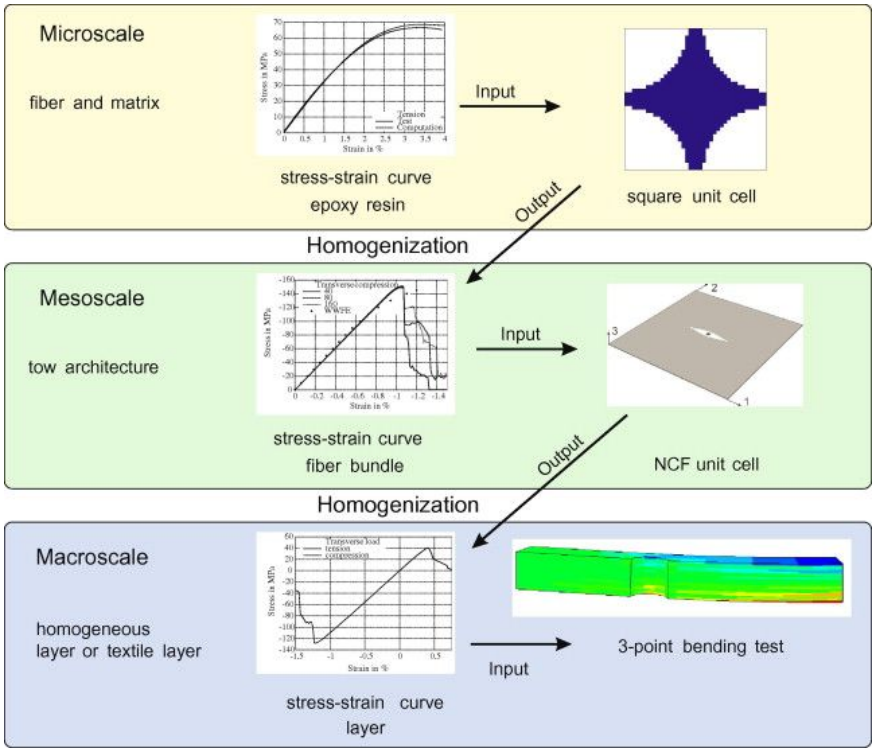


Figure 2-5 Multi-scale modelling and information transfer by Ernst et al. [40].

The multiscale modelling allows predicting material response at a component scale, hence it can be employed in particular for modelling the impact behaviour of 3D woven composites. Numerous examples [41-50] of multi-scale modelling being applied to predict the macro scale impact response

of 3D composites are presented in a review on this aspect [26]. Therefore, the multi-scale modelling provides a capability of defining the constitutive behaviour of the textile composites when simulating the FBO event.

However, there is a lack of systematic methodology that could be implemented as material models in finite element codes and used directly by engineers for the design of the textile composites. To offer a solution to this issue, such simulation methodology was developed by a different researcher in the same team [8]. The model developed has been validated based on the experimental data obtained as part of the present project. However, being a research development, at present the model is not a standard part of any commercial software, hence it cannot be commonly employed in the engineering design. In the present project, alternative approach to modelling the response of textile composites has been explored. It should involve definition of macro scale constitutive behaviour of textile composite which is independent of the multi-scale modelling methodology.

2.3.2 Macro scale modelling

A number of studies [51-54] have been reported in the open literature, where the impact response of 3D woven composites was analysed at macro scale by using a homogenised material model and properties, without taking into account the complex architecture or the analysis at the lower scales.

Naik and Meduri [53] developed an analytical method for evaluating the impact response of PMCs based on wave propagation and energy balance. A similar method was employed in [54] to analyse the ballistic impact of 3D orthogonal woven E-glass/epoxy composites by determining the energies dissipated via eight mechanisms. However, these analytical approaches are not applicable for the analysis of fan casings, because they involve numerous assumptions. Specifically, they only consider impacts normal to the target and a cylindrical projectile with a flat end. Furthermore, in order to quantify the energy dissipation through each mechanism, numerous experiments would be required. Accurate predictions in terms of critical velocities have been reported, but no prediction of the material damage of the target has been made.

Schwer [51] suggested a method for modelling the impact response of 3D woven composites by using shell elements. The elastic behaviour was defined

by an orthotropic elastic constitutive relation. Material failure was predicted by the Tsai-Wu failure criterion [55] and the post failure behaviour was defined by an isotropic scaling damage formulation. The modelling results were compared with experiments where the strain histories during the impact were measured, and good agreement was found.

Pankow et al. [52] employed a homogenised material model to simulate the shock tube tests of 3D woven S-glass fibre / SC-15 epoxy composites. The composites were composed of six layers of weft fibres, five layers of warp fibres and orthogonal Z-fibre reinforcements, which accounted for 6% of total fibre volume fraction. Each layer of fibres was modelled by a layer of shell elements with orthotropic elastic behaviour and Hill's anisotropic theory of plasticity, where the author assumed the yield stress ratios were the same as the elastic moduli ratios. The onset of matrix cracking under transverse loading was predicted by the maximum strain criterion. After the onset, the matrix dominated properties E_2 and G_{12} were degraded to 1%. The dynamic properties of the matrix at various strain rates were obtained via split Hopkinson pressure bar (SHPB) experiments. However, no due consideration was given to modelling the through-thickness reinforcement, which should strongly affect the mechanical behaviour of 3D textile composites as compared to conventional 2D laminated composites. Good correlation between the measured and the predicted deflection of the plate was obtained, and reasonably accurate predictions of the matrix damage were reported.

These studies suggest that the macro scale modelling which does not involve multi-scale homogenisation has potentials in capturing important aspects of the impact response of 3D woven composites, in spite of the simplifications involved. At the same time, in terms of accurate definition of the constitutive behaviour, the existing modelling methods still require substantial improvements. This includes due consideration to strain rate effects, appropriate criteria for the damage onset and the damage evolution.

2.3.3 Failure criteria

Most 3D woven composites are orthotropic materials. Nine constitutive constants need to be determined to fully describe the elastic response of the materials, namely axial stiffness, shear stiffness and Poisson's ratio in the three

directions.

The material model also needs to describe the termination of elastic behaviour, i.e. the onset of damage. This is usually achieved by defining appropriate failure criteria, which are the mathematical expressions used to describe the stress or the strain state at the damage initiation. So far the vast majority of the efforts in developing failure criteria were made for unidirectional composites, which are the simplest configuration of composite materials. There are many ways to categorise these failure criteria, such as whether they focus on in-plane or inter-laminar failure [56], or whether they are failure mode dependent or independent as in Table 2-1. Mode-dependent failure criteria usually contain a group of equations and each failure mode is represented in one equation, whilst mode-independent failure criteria predict the occurrence of damage without identifying the failure mode. In addition to that, the failure criteria can be further categorised as interactive or non-interactive [57]. The interactive failure criterion implies that the failure in one mode can also influence the other failure modes, whereas this kind of interaction is not accounted for by non-interactive failure criteria.

Table 2-1 Mode independent and mode dependent failure criteria

Mode independent criteria	Mode dependent criteria
Tsai-Wu [55]	Hashin-Rotem [58]
Hill [59]	Hashin [60]
Tsai-Hill [61]	Lee [62]
Hoffman [63]	Christensen [64]
Chamis [65]	Chang-Chang [66]

The maximum stress/strain criteria are the non-interactive failure criteria which suggest that the failure occurs when the stress or strain acting in any of the material directions reaches a critical value. These types of criteria are commonly applied to define the fibre failure in tension, as follows:

$$\sigma_1 \geq X_{\mathrm{T}} \tag{2-1}$$

$$\varepsilon_1 \geq \varepsilon_{1\mathrm{T}} \tag{2-2}$$

The values of material limits, maximum tensile stress X_{T} and maximum tensile strain $\varepsilon_{1\mathrm{T}}$ are obtained from experimental testing. In a similar way, the maximum criteria for other loading conditions can be obtained.

One of the first failure criteria devised for predicting failure of UD composites is the polynomial stress tensor criterion proposed by Tsai and Wu [55]. Its generalised form is expressed as:

$$F_i\sigma_i + F_{ij}\sigma_i\sigma_j + F_{ijk}\sigma_i\sigma_j\sigma_k \geq 1, \quad i,j,k = 1,2,\dots,6 \tag{2-3}$$

where F is the strength coefficient tensor. The interaction term F_{12} needs to be determined in biaxial loading tests. When biaxial test data are not available, F_{12} is sometimes determined by assuming a lamina, under an equal biaxial stress state in tension fail at the same stress level as it does under uniaxial transverse tension.

To date, numerous failure criteria have been proposed by various researchers for composite materials. Those include strain invariant failure theory [67], the multi-continuum theory [68] and micro-mechanics based failure theory [69]. There is also an increasing interest in predicting the initiation of failure according to fracture energy-based failure criteria [70]. More information about failure theories can be found from World-Wide Failure Exercise (WWFE-I and WWFE-II) [71, 72]. Continuous efforts are still being made towards a complete and validated methodology for predicting the failure of UD composites.

2.3.4 Damage mechanics

Once the damage is initiated, damage evolution takes place and leads to the degradation of mechanical properties. Numerically, the damage evolution is often reflected as either sudden reduction or gradual degradation of the material properties. Sudden degradation suggests that the material properties are reduced instantaneously to a fraction of their original values. The latter approach, as pointed out in [73], does not reflect the true physical response of the material, because it does not take into account the constraints, which are imposed on the failed region by the adjacent undamaged material.

Numerically, gradual degradation can be represented by strain softening. Strain-softening response in composites is usually described based on the concept of continuum damage mechanics (CDM). The basic idea of CDM is to treat the composite as a homogenous material, and to account for degradation of its material properties at a macro-scale by defining them as functions of the quantities called damage variables. These can take values from zero to unity, where zero corresponds to a virgin material, while unity indicates complete damage. Similar to failure modelling, a large variety of damage models have been developed, the best known of which include those proposed by Talreja [74, 75], Ladeveze et al. [76], Pickett et al. [77], Frantziskonis and Joshi [78], Randles and Nemes [79], Engblom and Yang [80], Yazdchi [81], Matzenmiller et al. [82]. However, as concluded in a recent review on this aspect [56], a complete and rational methodology for describing the damage of composite has yet to be developed.

2.3.5 Modelling strain rate effects

Polymers, which form the matrix constituent in PMC, are generally regarded as viscoelastic materials. For a viscous material, the shape change under loading is related to the duration of the loading. The macroscopic shape change of polymers is due to bending, stretch and straightening of molecule chains before yielding or slippage of molecule chains during the yielding. These microscopic mechanisms need time to take place, hence the material properties are presented differently when the testing speed is changed.

Some of the materials that form the reinforcement of PMC can also be strain rate dependent. Studies found in the open literature suggest that the carbon fibres are strain rate insensitive in terms of stiffness, ultimate strength and failure strain [83, 84]. On the other hand, the rate sensitivity have been reported for glass fibres, e.g. S2 glass fibres [85], and aramid fibres, e.g. Kevlar^{TM} fibres [85, 86]. It should be noted that the behaviour of the fibre/matrix interface can be also strain rate sensitive [87, 88]. Therefore, being comprised of polymeric matrices, fibres and interfacial layers, PMCs can have very obvious strain rate sensitivity, as summarised by the reviews in this aspect [89, 90]. It was even demonstrated that there can be a change in the failure mechanisms as the strain rate increased [91].

To define the rate sensitive response of PMC at a macro-scale, two types of modelling methods have been reported in the literature, namely, viscoplastic models [92-98] and rate-dependent failure criteria [99-104].

The viscoplastic models were inspired by the well-established plastic and viscoplastic equations for the nonlinear behaviour of metals. It was originally proposed as an one-parameter plasticity model [92] to describe the nonlinear behaviour of composite materials. It was based on the Hill-type yield function [59], assuming that the material was in a plane stress state and no plasticity in the fibre direction. Later, the model was further developed to account for the strain rate effects [93, 94]. The parameters were determined by fitting the models to experimental data. This method was found to be reasonably accurate for both UD and woven composites and was therefore used in later research [95, 96]. Similar models [97, 98] have also been developed in recent years.

As an alternative, the failure criteria incorporating rate-dependent properties can be used to define the response of the composite materials at high strain rate loading [103]. In this approach, the failure criteria involve material properties which are scaled with respect to the strain rate. The most commonly used strain rate scaling functions for metals are the Cowper-Symonds power law [105], and the Johnson-Cook's constitutive model [106] where the logarithmic strain rate dependency is assumed for the yield stress. Those approaches were adapted for modelling strain rate dependency in composite materials, by assigning the rate sensitivity to damage initiation strengths and the elastic moduli.

Daniel et al. [103] tested a UD AS4 carbon fibre / 3501-6 epoxy laminate in off-axis and longitudinal directions at strain rates up to 400 /s. The rate-dependent elastic moduli and strengths were defined by the logarithmic functions similar to the one in Johnson-Cook's constitutive model as follows:

$$E(\dot{\varepsilon}) = E(\dot{\varepsilon}_0)(1 + C_E \log_{10} \frac{\dot{\varepsilon}}{\dot{\varepsilon}_0}) \tag{2-4}$$

$$S(\dot{\varepsilon}) = S(\dot{\varepsilon}_0)(1 + C_S \log_{10} \frac{\dot{\varepsilon}}{\dot{\varepsilon}_0}) \tag{2-5}$$

where C_E and C_S are the scaling parameters. The scaled properties were employed in various failure criteria, including the mode-dependent non-interactive criteria such as maximum stress/strain criteria, the mode-independent interactive criteria (Tsai-Hill [61] and Tsai-Wu [55]), and the mode-dependent and partially interactive ones by Hashin-Rotem [58], Sun [107] and Daniel [108]. The failure envelopes were compared with a limited number of experimental data points. It was concluded that, although the scaling is based on the assumption of linear behaviour before failure, it is an effective and useful engineering tool when combined with the appropriate failure criteria.

Recently, a phenomenological strain rate dependent failure theory is proposed for modelling UD carbon fibre composites [102]. Four criteria were employed to account for the tensile and compressive failure of fibres, as well as the matrix. A key postulate of this theory was that matrix shear deformation was the only mode affected by strain rate effects. The strain rate dependency of the other modes occurred because the maximum shear stress was inclined to the principal planes of material symmetry. Therefore, the quasi-static mechanical properties were scaled to become the dynamic properties in the failure criteria by a second order polynomial function, which was calibrated by fitting the in-plane shear strength versus shear strain rate. The model was implemented in ABAQUS/Explicit for solid elements with reduced integration and then validated by comparing predictions of a single element under the longitudinal and off-axis compression against the published experimental data in [109, 110].

It can be concluded that the strain rate modelling at macro scale is still mostly limited to the laminated composites. Neither the viscoplastic models nor the strain rate dependent failure criteria models have investigated 3D woven composites.

2.3.6 Selection of material models for this study

The above review shows that the three important elements for impact simulation, namely failure criteria, damage mechanics and strain rate dependency, remain nearly unexplored for 3D woven composites. Among the available macro-scale material model for composite materials, MAT162 [111] in LS-DYNA [112] is the only one which has these three crucial features implemented.

MAT162 is designated for the macro-scale analysis of composites with plain weave lamina, which bear much similarity to 3D woven composites, especially the one with layer-to-layer interlocks in Figure 2-4. A generalised form of the Hashin criteria [104] is employed to define the damage onset. The merits of the Hashin criteria are therefore inherited.

In addition, the damage model developed by Matzenmiller et al. [82] is implemented in MAT 162. It is capable of characterising the growth of damage and strain softening following the damage onset and simulating matrix damage, fibre fracture, fibre crush and delamination. The study by Williams and Vaziri [113] has shown that Matzenmiller's progressive post-failure models based on CDM improve the prediction of impact damage of composite structures significantly.

Furthermore, the logarithmic scaling functions, Eq.(2-4) and (2-5), are incorporated with Hashin failure criteria in MAT162. Studies have been carried out by several research groups [99, 100, 114], confirming that FE modelling with MAT162 is capable of accurately predicting the strain rate dependent behaviour of laminated composite materials.

Based on these, MAT162 has been selected to carry out macro-scale modelling in this study.

2.4 The characterisation testing of 3D woven composites

2.4.1 Experimental methods

In FE modelling of impact response of composites, the constitutive behaviour of the material is defined by appropriate material models, in which material properties should be specified as inputs. Under impact loading, the material properties can vary with the strain rate, and an appropriate representation of this variation is crucial for accurate prediction of the impact response of composites. This dependency can be established experimentally, by conducting material characterisation tests. The experimental characterisation of composites as presented here is divided into three groups, each corresponding to different ranges of strain rates. Quasi-static testing is usually carried out at strain rates from 10^{-4} to 10^{-3}/s, intermediate strain rates range from 10^{-1} to 10^{2}/s and high strain rates are in the order of 10^{3}/s or above. In view of the different ranges

of strain rates and loading modes, various experimental techniques, as summarised in Table 2-2, have been developed. The experimental techniques that are particularly relevant to the present work are introduced first, followed by a review of the literature reporting the testing of 3D woven composites. More information about these experimental techniques can be found in [115, 116].

Table 2-2 Experimental techniques for different loading modes and strain rates reproduced from [115].

Mode	Strain rate (s^{-1})	Testing
Compression	<0.1	Conventional testing machine
	0.1-100	Servo-hydraulic machine
	0.1-500	Drop weight test
	200-10^4	Hopkinson pressure bar
	10^4-10^5	Air gun apparatus
Tension	<0.1	Conventional testing machine
	0.1-100	Servo-hydraulic machine
	10^4	Expanding ring
	$>10^5$	Flyer plate
Shear	<0.1	Conventional testing machine
	0.1-100	Servo-hydraulic machine
	10-10^3	Torsional impact
	100-10^4	Hopkinson pressure bar in torsion
	10^3-10^4	Double-notch punch
	10^4-10^7	Pressure-shear plate impact

In terms of QS testing of composite materials, a wide range of methods have been established and standardised by the American Society for Testing and Materials (ASTM), e.g. in-plane tension [117] and shear [118].

The characterisation with strain rates up to 10^2 /s generally employs servo hydraulic testing machines or drop weight tests. The drop weight tests are usually performed on a drop tower, in which a falling, weighted striker is lifted to a predefined height and then released, impact onto the specimen.

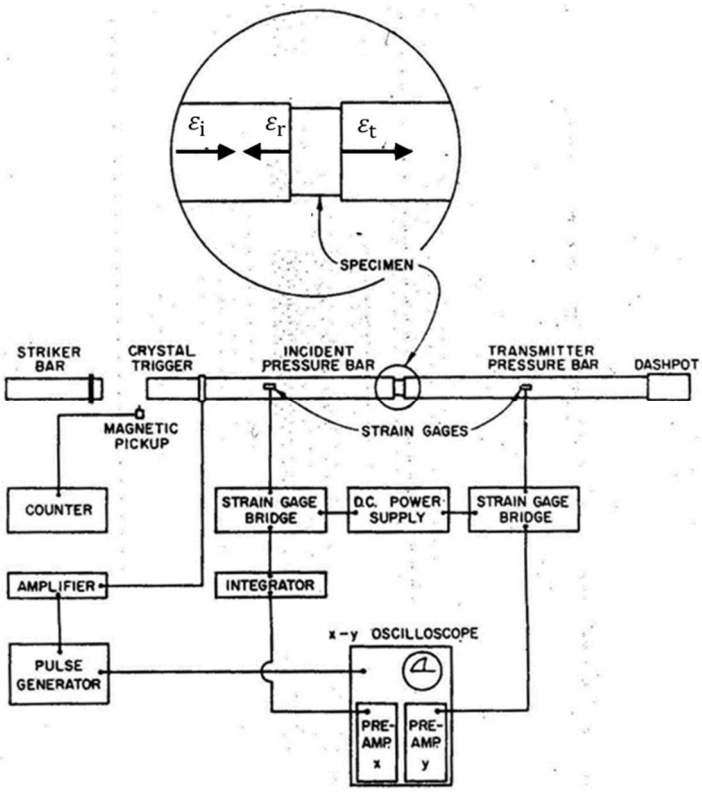


Figure 2-6 A schematic diagram of Split Hopkinson pressure bar apparatus [119].

The split Hopkinson pressure bar (SHPB) is widely used to test materials at strain rate from 10^2 to 10^4 /s. A typical SHPB apparatus is sketched in Figure 2-6. The histories of the stress, strain and strain rate in the specimen could be obtained in SHPB tests. This technique was initially designed for compression testing. Later, it was modified and applied for dynamic tension, shear and torsion tests [120].

The strain rates achieved in SHPB test are similar to the average strain rates in the material during an FBO event, although the strain rate can vary across the fan casing due to the complexity of the FBO. The rate dependency measured in SHPB tests can be therefore used when defining the rate-dependent constitutive relations in finite element simulations of the FBO. On the other hand, the values of material properties measured at intermediate rates by using the servo hydraulic testing machines or drop weight tests are of less significance. Because of that, the dynamic characterisation of 3D woven are primarily reviewed with respect to the high strain rate testing by SHPB.

2.4.2 Experimental characterisation of 3D woven composites under QS loading

Regarding the QS characterisation tests for 3D woven composites, only a few studies have been conducted since the 1980s. By mid 1990s, Cox et al. [121-123] had carried out extensive characterisation tests on various types of 3D interlocking woven carbon/epoxy composites under tensile, compressive and bending loadings. At about the same time, Brandt et al. [124] summarised their earlier studies about QS testing of several types of 3D woven glass/epoxy composites and made conclusions about the effects of the Z-fibre proportion on the in-plane tensile, compressive and interlaminar shear strengths. However, one of the conclusions was that the interlaminar shear strength was not improved by the Z-fibres when compared with laminated composites.

However, from mid-1990s to 2015, there had been no characterisation tests which involve several loading modes for 3D woven composites. Characterisation tests were focused on one specific loading mode and its associated damage. For example, several types of 3D woven glass fibre composites with the architectures of orthogonal interlock, normal layered interlock, and offset layered interlock were studied in [125], but only under in-plane tensile loadings. Similarly, the loading is limited to in-plane tension in [126-129] for various types of 3D woven carbon/epoxy composites. While other studies [130, 131] only accounted for in-plane compression.

In 2015, QS characterisation tests which involve several loading modes were reported in [132] for 3D woven composites with IM7 carbon fibre reinforcement. One of the composites was based on the orthogonal weave reinforcement, while the other two had layer-to-layer angle interlock woven reinforcements. Two epoxy systems of ST-15 and PR-520 were used. The experiments conducted were the in-plane tensile tests according to ASTM D3039 [117], combined loading compression according to ASTM D6641 [118] and two-rail shear according to ASTM D7078 [133]. Digital image correlation (DIC) was employed for full field strain measurement. It was found that the debonding of the matrix from fibre tows is the common initial failure mechanism of all three loading types.

A similar publication in the same year [134] also reported several QS characterisation tests for 3D woven carbon/epoxy composites. Four types of

composites with orthogonal woven reinforcements and two types of composites with angle-interlock woven reinforcements were tested in the warp direction under tension according to ASTM D3039 [117], compression according to ASTM D695 [135] and flexure according to ASTM D790 [136]. It was found that one of the two types of angle interlock weave exhibited the highest properties under all loading conditions.

However, in terms of generally applicability for the design and development of 3D woven composite components, these studies are far from sufficient. The material properties of 3D woven composites are directly related to the structure the reinforcement, which can be varied substantially. Therefore, the properties of the composite with a given architecture of reinforcement and constituents should be determined experimentally, unless such data for this specific composite exists. Moreover, as commented in [132] on the publications until 2015, "*The majority present results from limited sample sets no longer represent the latest technology and practices in structural three-dimensional preforming.*"

2.4.3 Dynamic characterisation testing of 3D woven composites

The lack of the experimental data is even more apparent in terms of the dynamic properties of 3D woven composites. Even for 2D laminated composites, whose strain rate dependencies were realised a long time ago, the interest in their high strain rate properties continues in the most recent five years, such as the studies on UD glass/epoxy composites [137, 138], UD carbon/epoxy [103, 109, 110, 139] and 2D textile composites [140, 141]. It is fair to say that SHPB has become the standard technique for the dynamic testing of composite materials, as it was employed in the majority of these studies.

Nearly all the dynamic characterisation tests of 3D woven composites were conducted for those with glass fibres. Since the mid of 2000s, Sun et al. conducted extensive SHPB testing on 3D textile glass fibre composites under various loading conditions at various strain rates up to about 3500/s. These include the in-plane [142] and through-thickness [143] compression of 3D angle-interlock E-glass/vinyl ester woven composites, in-plane compression [144] and tension [145] of composites with 4-step 3D braided E-glass reinforcements, and punch shear [146] of E-glass and Twaron® hybrid 3D

orthogonal woven composites. Later, Pankow et al. [147] introduced high speed digital image correlation (DIC) into the SHPB test on 3D orthogonal woven glass/epoxy composites for full field strain measurement. The composites were tested under in-plane and through-thickness compression at the strain rates up to 1750/s.

The only account on high stain rate testing of 3D woven carbon fibre composites that could be found in the open literature is the work of Gerlach et al. [148], who carried out an extensive experimental study with a composite which had the reinforcement architecture as shown in Figure 2-7.

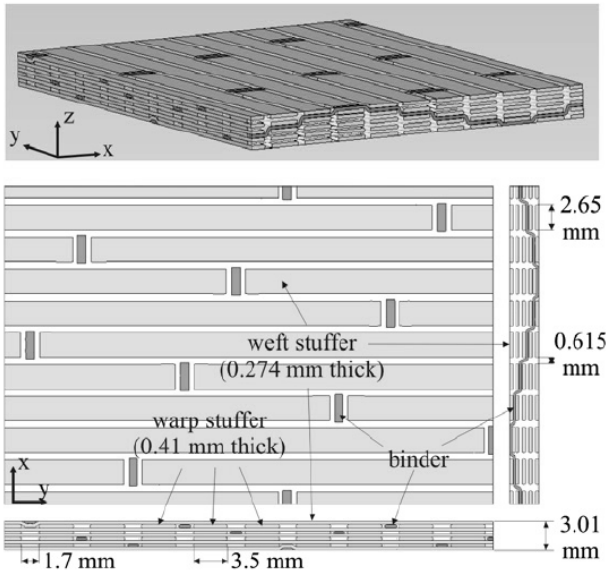


Figure 2-7 The 3D woven carbon fibre composites tested by Gerlach et al. in [148].

The material was tested under the in-plane tension, compression and shear. In addition to that, through-thickness tension, compression and shear were also performed by using cross-like specimens and a specially designed loading device, as shown in Figure 2-8. However, the applicability of this method is questionable, as the results indicated that the through-thickness tensile strength was even lower than the shear strengths at all of the applied strain rates. The volume fractions of the binder yarns were only 3% and 6%. Given the architecture of this type of 3D weave, the through-thickness reinforcement provided by the binders could be very limited. It is very likely that issues will be encountered if this method is used for testing composites with higher through-thickness properties.

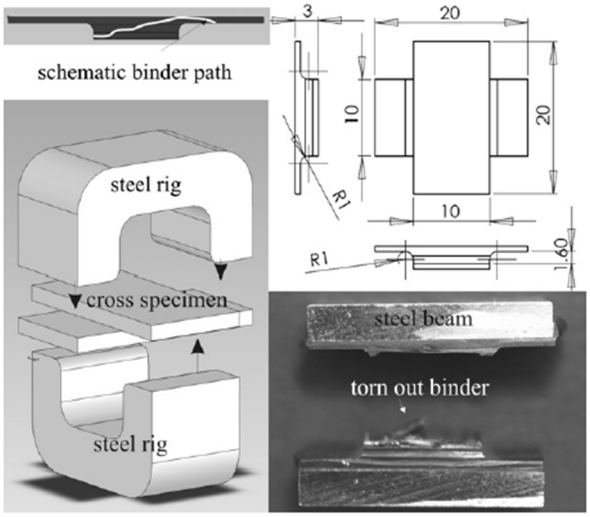


Figure 2-8 Principle of the through-thickness tension tests, specimen dimensions and example of a failed cross specimen in [148].

Similarly, very limited data is available in terms of the dynamic properties of 3D woven composites at intermediate strain rates. It is likely to be related to the fact that 3D textile composites are primarily used in applications where they experience the strain rates which are above the capability range of servo hydraulic testing machines and drop weight tower tests. The only account of intermediate strain rate testing is the work by Hufenbach et al. [149-151], who conducted experiments with glass fibre composites with 3D multi-layered weft knitted reinforcement. A servo hydraulic testing system, along with specially designed specimen fixtures, was applied to test the dynamic properties under in-plane tension, compression and shear, as well as through-thickness shear. Strain rates up to 115 /s were achieved.

It can be concluded that there is severe deficiency of data on the dynamic mechanical properties of 3D woven composites. Specifically, very limited data could be found for carbon fibre 3D woven composites, which are particularly relevant for the aerospace applications because of their superior mechanical properties and the low density.

2.5 Impact testing

2.5.1 Tests and simulations related to FBO

The FBO is a complicated process, as it involves a few stages including the first and the second impact of the released blade, the interaction between the released blade and the trailing blades, and the continuous loading from engine

spool-down and windmilling. To ensure the design of the casing meets the safety requirements, a series of tests are conducted. A multi-scale approach to the design and testing of the composite containment casings was described in a recent report by NASA Glenn Research Centre [4]. It should be noted that the term “multi-scale” here refers to the testing and simulation on composite materials, panels and components, rather than the modelling methodology for textile composite materials as was described in Section 2.3.1. The main testing and modelling procedures as defined in [4] are briefly outlined below to present the readers with an idea about the involved complexity.

Candidate composites were screened at the material level. The composite should be tested in a similar state of strain and at a similar strain rate to the ones of an FBO. In [4], this was achieved by impact tests which employed a soft projectile. This type of projectile generated a high strain energy density in the material before failure, so that the resistance of the material to cracking and delamination could be evaluated.

At the panel level, impact tests were carried out with hard projectiles to evaluate the material resistance to local penetration. The tests on the panels were designed to reproduce the same damage modes as those taking place during the FBO, although the projectile may be different from a real fan blade to achieve this goal. The damage modes were initially not known to the authors. They conducted FBO tests on metallic cases with a real fan blade, and then simulated the panel impact tests to match the damage modes observed in the FBO tests.

At the component level, impact tests, as shown in Figure 2-9, are conducted for a metallic case to match the deformation and damage of the fan case during the blade-out tests. These tests are simulated in LS-DYNA. It was found that the damage modes caused by the fan blades could be obtained experimentally by a specially designed solid cylinder with a hollow tube leading edge, as shown in Figure 2-9. However, a series of tests are required in order to determine the projectile shape. Then it could be used for further testing on casings.

For softwall casings, an additional test, as shown in Figure 2-10, was required to evaluate their post-impact structural integrity during the engine spool down. The test was initially conducted on a metallic case to calibrate the experimental rig so it would produce the loads representing the out-of-balance loads during spool down. Then the test was repeated on composite casings using

the same test conditions.

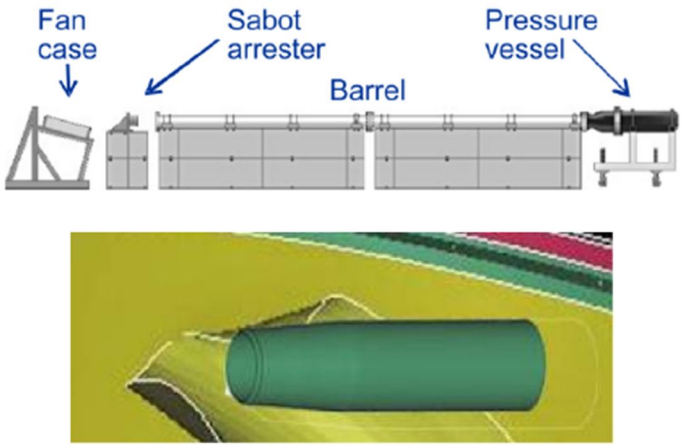


Figure 2-9 The set-up of the gas gun for the impact test at component level, and the shape of the deformed blade and the cylindrical projectile [4]. The length of the barrel is 12.2 m. Other dimensions are not provided in [4].

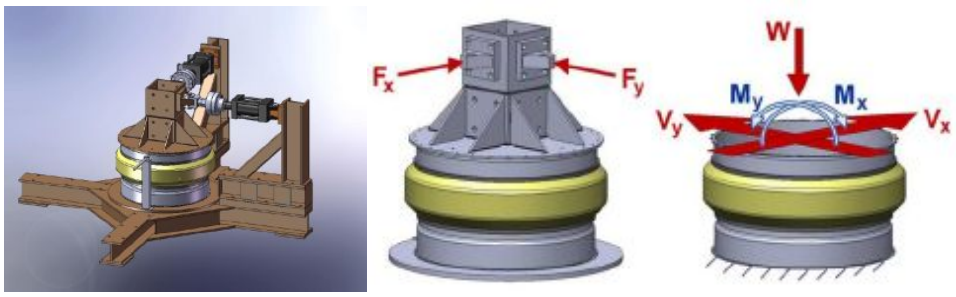


Figure 2-10 The Orbital Loading test rig for softwall design (left); Loading applied by the rig (middle) and resultant loads on the casing (right) [4].

From the involved experiments, it can be seen that a very large financial commitment is needed for such a full scale testing scheme, as it requires not only highly specialised equipment, but also an abundance of materials to produce specimens and components to be tested. So far very limited number of research addressed FBO even for metallic casings numerically [152-155] or experimentally [156-158]. There is no publication related to the FBO of integrated composite fan casings other than this engineering report by NASA [4].

2.5.2 Impact testing of 3D textile composites

In contrast to limited amount of research which directly addressed FBO, numerous studies on testing the composite panels under various impact conditions have been published. The majority of these are related to 2D laminated composites. Systematic account of research on this subject is given in

reviews [159-162]. For 3D textile composites, much fewer publications on their impact testing could be found. These are herein divided into three categories according to impact testing equipment used. These are the drop weight impact tests, modified SHPB impact tests and ballistic impact tests.

A schematic of the drop weight impact tests is shown in Figure 2-11. These tests involve the free drop of impactors of specific shapes onto targets. The maximum impact velocity is constrained by the height of the apparatus and normally less than 10 m/s.

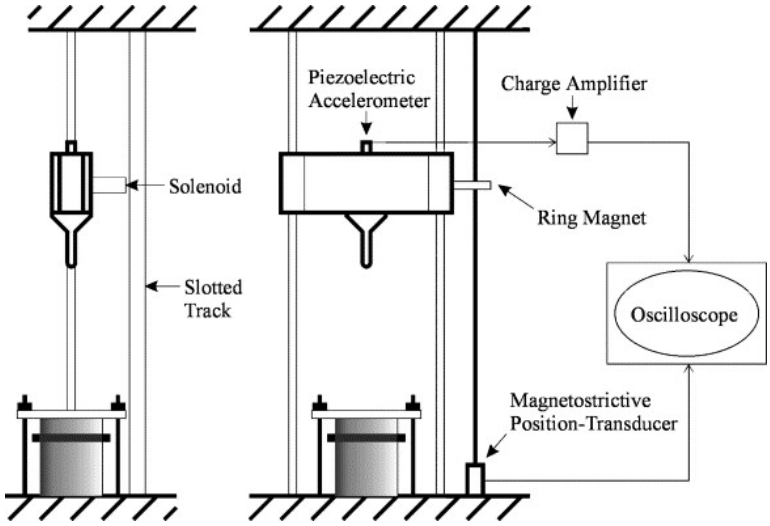


Figure 2-11 A schematic of the drop weight impact test from [163].

A larger impact velocity could be achieved by using a modified SHPB, whose schematic is shown by Figure 2-12. Similar to the conventional SHPB, the striker bar is propelled to impact onto the flat end of the incident bar. Another end of the incident bar has a specific shape, such as a conical indenter in [164]. This end impacts onto the composite targets, which are usually flat panels. The method allows achieving impact velocity of less than 50 m/s. However, this range of velocities is still below the range of velocities during the FBO .Therefore, the modified SHPB impact tests herein are regarded as low velocity impact together with the drop weight impact tests. All the studies employing those two methods for impact testing of 3D woven composites are summarised in Table 2-3.

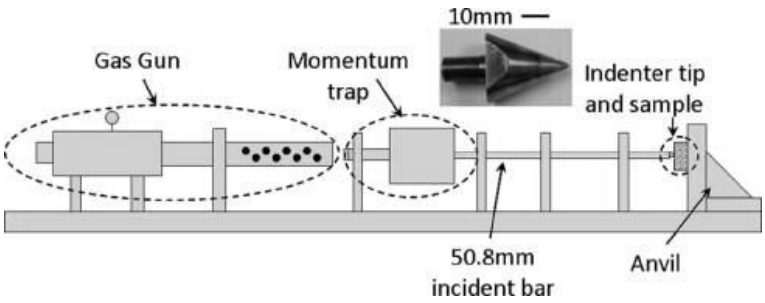


Figure 2-12 A schematic of the SHPB impact test from [164].

Similarly, all the studies related to the ballistic impact tests on 3D woven composites are summarised in Table 2-4. As can be seen, there are rather limited number of publications on this subject. Four of the studies were conducted with composites reinforced in the through-thickness direction by stitching [164-167]. A group of researchers [47, 48, 168, 169] from Donghua University, China carried out ballistic impact tests on 3D woven composites with orthogonal and angle-interlock architectures. However, none of the studies as specified in Table 2-4 were concerned with 3D woven composites of carbon fibres.

Table 2-3 Researches related to the low velocity impact of 3D woven composites.

Author(Year)	Method	Velocity	Energy	Impactor	Target	Thickness	Architecture	Constituents
Hosur et al. (2001) [170]	Drop weight		20,30 and 40 J	12.7 mm diameter hemispherical cylinder	75 mm cicular	8.8 mm	Plain weave with stitching and z-pinning	S2-glass / epoxy vinyl ester
Chiu et al. (2003) [171]	Drop weight		15 J and 20 J	12.7 mm diameter hemispherical cylinder	100×150 mm simply supported by a ring of 50 mm internal diameter	-	3D angle-interlock woven	Carbon / epoxy
Baucom et al. (2005) [163]	Drop weight	≈2 m/s	18 J	19 mm diameter hemispherical cylinder	76 mm circular	≈2.4 mm	3D orthogonal woven	E-glass / vinyl ester
Pearson et al. (2007) [172]	Drop weight	2 m/s	11 J	19 mm diameter hemispherical cylinder	76.2 mm circular	7.2 mm	3D orthogonal woven	E-glass / epoxy vinyl ester
Seltzer et al. (2013) [173]	Drop weight	≈4 m/s	21-316 J	12.7 mm diameter hemispherical cylinder	127×127 mm	6.7 mm 8.3 mm	3D orthogonal woven	S2-glass / epoxy vinyl ester T300 carbon/ epoxy vinyester
Lv et al. (2006) [174]	SHPB	15,25 and 40 m/s		14.5 mm diameter flat end rod	100×15 mm	4 mm	3D orthogonal woven	Hybrid of Aramid and E-glass / polyester
Ji and Kim (2007) [41]	SHPB	18,20 and 22 m/s		14.5 mm diameter hemispherical end	120 mm circular	7 mm	3D orthogonal woven	E-glass / polyester
Walter et al. (2009) [164]	SHPB	5-10 m/s		45° conical indenter	40×40 mm	16.5 mm	Stitched cross-ply laminates	Glass / epoxy

Table 2-4 Researches related to ballistic impact tests of 3D woven composites.

Author(Year)	Velocity	Impactor	Target	Thickness (mm)	Architecture	Constituents
Larsson (1997) [165]	≤700 m/s	6 mm FSP	254×163.5 mm	5	Stitched QI laminates	Carbon/epoxy with Kevlar stitches
Hosur et al. (2004) [166]	≤275 m/s	14 g fsp	125×125 mm	2.8 to 14.3	Stitched plain and satin weave	Carbon/epoxy with Kevlar stitches
Caprino et al. (2007) [167]	65 and 129 m/s	12.7 mm and 29 mm diameter spherical steel projectile	200×200 mm	1.5, 3, 4.5 and 6	Stitched QI laminates	Carbon/epoxy with Kevlar stitches
Sun et al. (2009) [47]	394-749 m/s	7.95 g, 7.62 mm diameter steel cylinder with a conical tip	200×300 mm	15	3D orthogonal woven	E-glass/polyester with aramid binders
Walter et al. (2009) [164]	≈940 m/s	5.56×45 NATO 55 garin and 62 grain projectiles	40×40 mm	16.5	Stitched cross-ply laminates	Glass/epoxy
Li et al. (2010) [48]	210-550 m/s	7.95 g, 7.62 mm diameter steel cylinder with a conical tip	214×192 mm	8.64	3D angle-interlock woven	Aramid/epoxy
Jia et al. (2010) [168]	394-749 m/s	7.95 g, 7.62 mm diameter steel cylinder with a conical tip	200×300 mm	15	3D orthogonal woven	E-glass/polyester with aramid binders
Cui et al. (2010) [169]	210-550 m/s	5.59 g, 7.62 mm diameter cylinder with a hemispherical tip	214×192 mm	10.8	3D angle-interlock woven	Aramid/epoxy
Muñoz et al. (2015) [175]	300-550 m/s	0.706 g, 5.5 mm diameter sphereical steel projectile	100×100 mm	3.02	3D orthogonal woven	Hybrid of glass and carbon fibres with UHMWPE

2.6 Summary

In this chapter, research into 3D woven PMCs and their material characterisation tests, impact tests and modelling techniques have been reviewed. Though 3D woven composites have been shown to deliver improved impact resistance as compared to 2D laminates, only limited experimental data is available in all the reviewed testing aspects. Relatively large number of studies on the numerical modelling of 3D woven composites has been published. The majority of these studies employed multi-scale modelling methodology to define the constitutive behaviour of the composite at a macroscale by homogenising the material response at lower scales, namely micro and meso scales. Some research efforts have also been made where the impact response of 3D woven composites was simulated with good accuracy at the macro scale by using homogenised material models and properties. In these cases, there is no dependence on the complex architecture or on the analysis of the lower scales. To accurately perform such types of modelling, proper consideration of the anisotropic constitutive relations, failure criteria, progressive damage mechanics and strain rate effects are needed. However, as concluded by previous reviewers, failure criteria and damage mechanics are not fully resolved even for 2D laminated composites. Moreover, strain rate effects were not taken into account in the reviewed studies on the impact modelling of 3D woven composites.

Chapter 3 The mechanical testing of 3D woven composites

3.1 Introduction

In this chapter, the mechanical testing of four types of 3D woven composites is described. The manufacturing method is firstly introduced, followed by a section on the architecture of the reinforcement in the cured composites. To obtain input data for the homogenised macro scale modelling, the composites were mechanically characterised by means of quasi-static tests under tension, compression and shear, and also at high strain rates by using split Hopkinson pressure bar (SHPB). Detailed description of data acquisition and processing techniques is provided, and the experimental data are reported and analysed. The major outcomes of the experimental data analysis are summarised and presented in terms of mechanical properties. In addition to that, failure and damage modes are presented and discussed.

3.2 Manufacturing

The characterisation tests were carried out on textile composites reinforced by four types of woven fabrics, details of which are given in Section 3.3. These reinforcements are made from glass-fibre or carbon-fibre, and were manufactured and supplied by SINOMA [176], China. The material was delivered as square panels with dimensions of 1 m × 1 m.

The textile composites were manufactured applying a vacuum-assisted resin transfer moulding (VARTM) process, using the facility available at the University of Nottingham. The schematic of the arrangement of the experimental equipment is shown in Figure 3-1, and the photographs of the equipment are shown in Figure 3-2, where various components of the VARTM assembly are specified.

The photograph of the RTM moulding tool is shown in Figure 3-3. It comprises top and bottom steel plates with a steel picture frame being sandwiched between them. The in-plane mould cavity dimensions are 300 mm × 300 mm. For each type of reinforcement, a picture frame of an appropriate thickness was used to ensure that the composite has a specific fibre volume fraction.

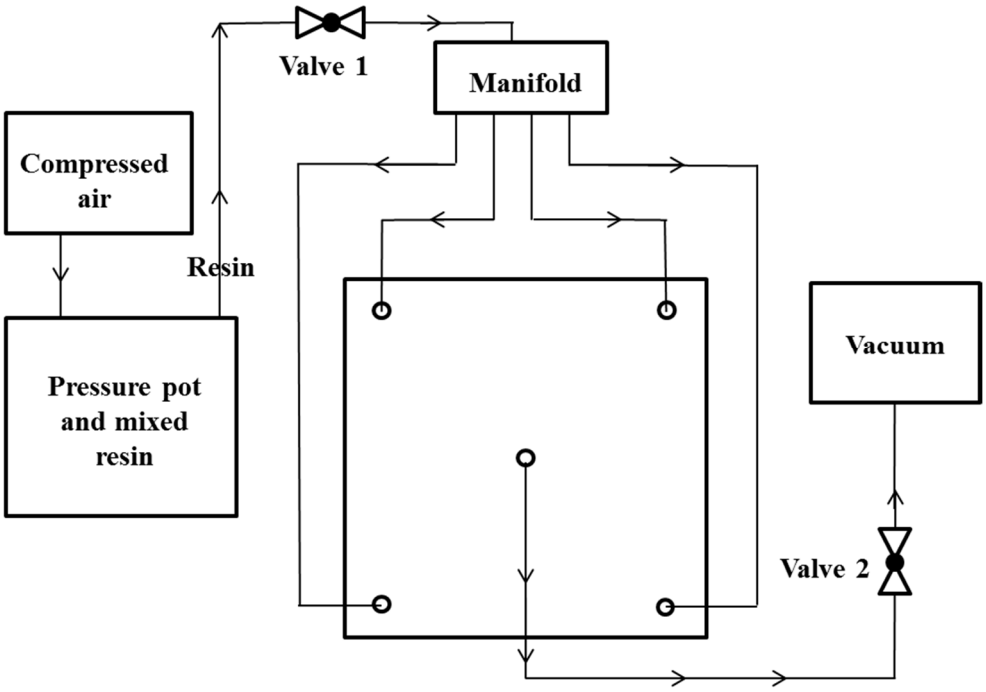


Figure 3-1 A schematic of VARTM.

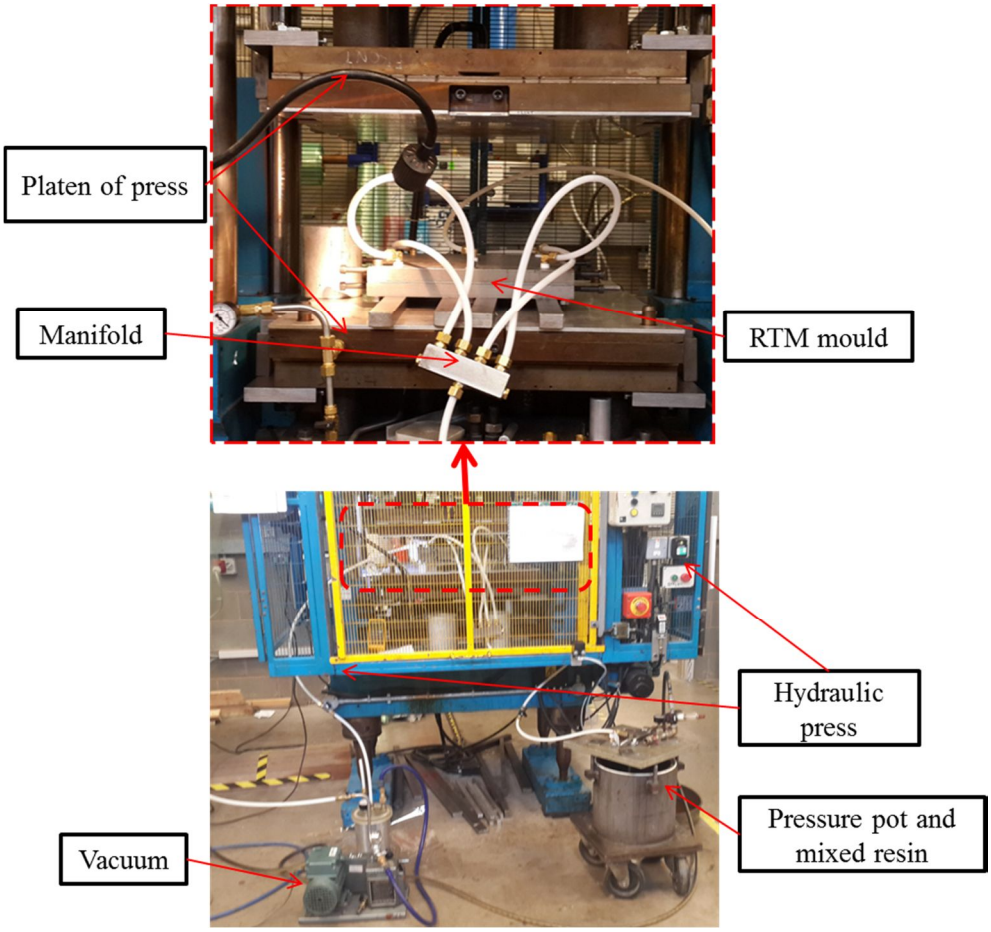


Figure 3-2 Photographs of the equipment used for VARTM.

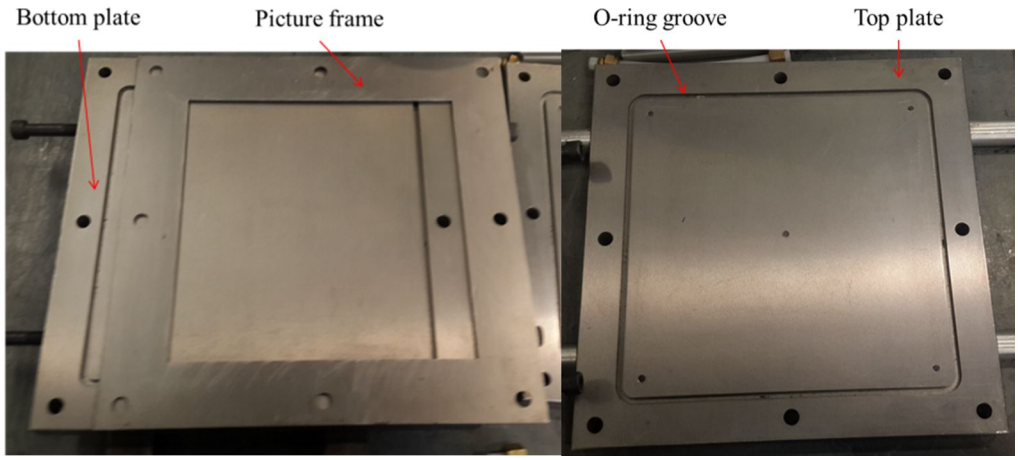


Figure 3-3 Photographs of the mould tool.

The most essential details of the VARTM process are outlined as follows.

a) For resin infusion, a preform was carefully cut into 280 mm × 280 mm panels.

b) The resin system used was Gurit PRIME^{TM} 20LV [177] epoxy infusion resin with a slow hardener, with the weight ratio of 100:26.

c) To ensure uniform thickness in the RTM plates, the tool with dry fabrics inside was compressed by a hydraulic press with 200 kN force.

d) Prior to injection, the tool was heated to 40°C by a heater in the press.

e) During injection, the resin was pressurised by compressed air and injected into the tool through four corner inlets on the top plate. A vacuum pipe was connected to the central outlet to assist resin flow and pump out air and excessive resin.

f) At a constant pressure, the resin flow becomes slower and slower when more resin is injected into the mould. To keep the resin flow speed constant, the pressure was increased to 8 bars in steps as specified in Table 3-1, based on the results of a series of experiments on injection process [10].

g) The injection is finished within 35 minutes from the mixing stage.

h) After the injection, the tool was heated at the rate of 1°C/min up to 100°C and was held at 100°C for two hours to cure the resin.

i) Afterwards, the tool was placed in air to cool to room temperature. The compression was applied to the mould tool throughout the injection, heating and cooling. After cooling, the tool was opened and the cured plate was transferred into an oven to post-cure at 65°C for seven hours.

Table 3-1 The pressure steps during RTM injection.

Vacuum	2bar + Vacuum	4bar + Vacuum	6 bar + Vacuum	8 bar + Vacuum
2 minutes	2.5 minutes	3 minutes	3 minutes	Until the end of injection

The RTM procedures were timed, and the moulding process as described above was followed for every plate to minimise the quality variance. The cured plates were visually examined and plates with large and apparent defects, such as air bubbles and dry regions, were discarded.

3.3 Tested materials

The mechanical tests, as presented in this chapter, were conducted for composites based on four types of preform. Two are made from 75 Tex E-glass fibres and denoted as GF-1 and GF-2. The other two are made from T300 and IM7 carbon fibres and denoted as CF-T300 and CF-IM7 respectively. The properties of these fibres are listed in Table 3-2.

Table 3-2 The properties of fibres used in the four composites.

Fibre	Density (kg/m^3)	E_1 (GPa)	E_2 (GPa)	G_{12} (GPa)	S_T (MPa)
E-glass* [178]	2570	74	-	-	2000
T300 carbon [179]	1780	230	15	15	2500
IM7 carbon [180]	1780	276	19	9.5	5600

* Glass is isotropic.

All of the preforms have the same basic weaving architecture, namely, 2.5D layer-to-layer angle interlock. The geometries were altered following RTM, due to the compaction, which was introduced to achieve a desired fibre volume fraction. In this study, the architecture specified is the one after manufacturing. The RTM manufactured panels were cut into small samples and then observed by using a Nanotom 160NF X-ray computed tomography (XCT) system in one of the parallel project [10]. The XCT images for the four composites are given in Figure 3-4 to Figure 3-7. It should be noted that Figure 3-7 is the result of a trial CF-IM7 panel, which has poor manufacturing quality. Voids and defects

are widely distributed inside this panel. It is only used here to illustrate the reinforcement architecture.

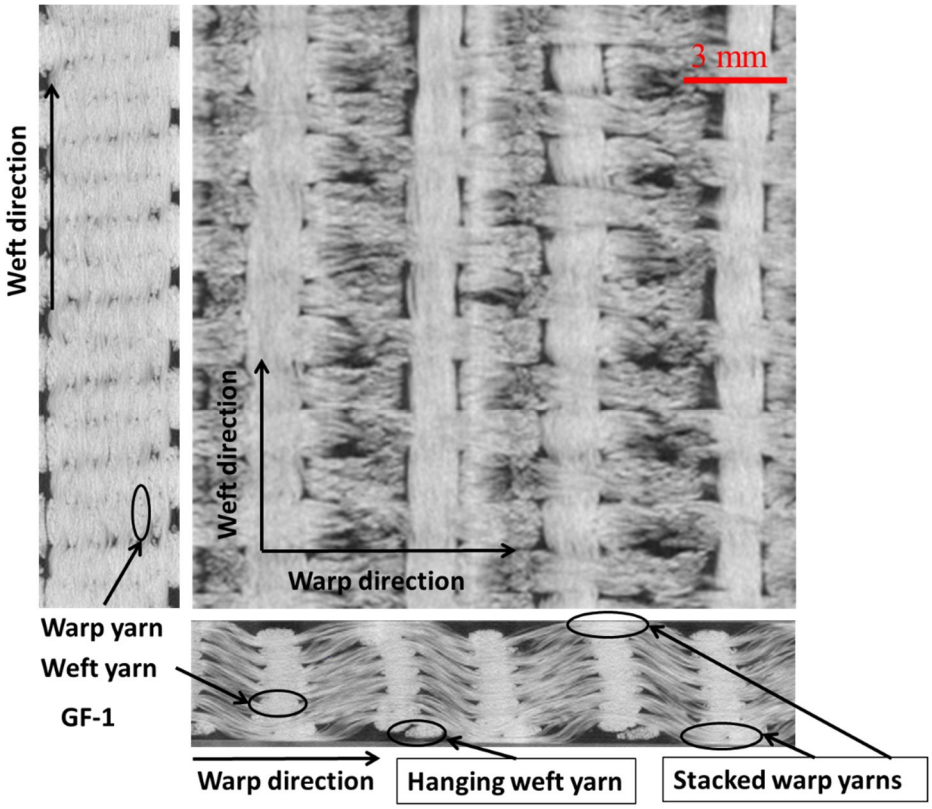


Figure 3-4 XCT images of GF-1 composites from different views [10].

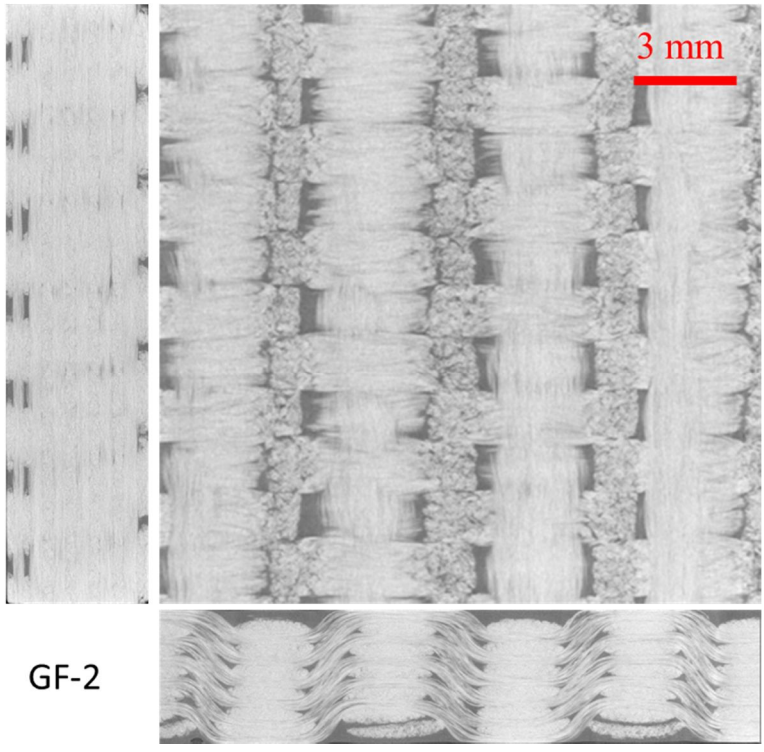


Figure 3-5 XCT images of GF-2 composites from different views [10].

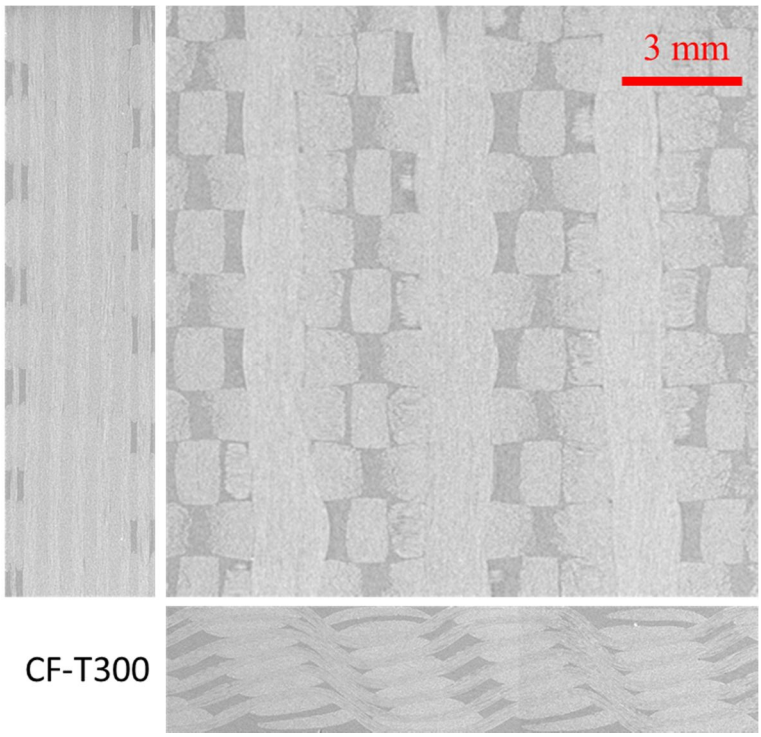


Figure 3-6 XCT images of CF-T300 composites from different views [10].

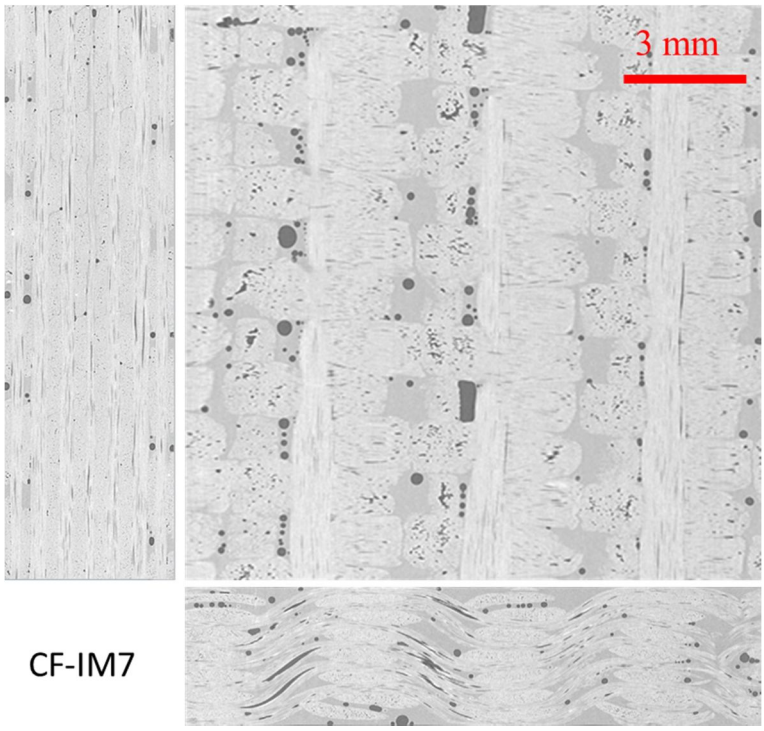


Figure 3-7 XCT images of CF-IM7 composites from different views [10].

There are some differences in the architectures of the four composites, for instance the volume fraction ratio of the warp and weft yarns and the weaving angle of the warp yarns. In addition, the view along the weft yarns in Figure 3-4 shows two stacked warp yarns at the uppermost and lowermost layers. Meanwhile, the lowermost layer of weft yarns is hanging. Such hanging weft

yarns are also found in the carbon composites but there is no stacking of warp yarns.

There is a horizontal offset of weft yarns in all the composites, especially in CF-T300. This could be the result of unnoticed variations during weaving process or handling of dry fabric or the compaction during RTM.

The views along the warp yarns reveal that the weft yarns are fairly straight except for GF-1, whose weft yarns crimp slightly. At the outermost layers, there are resin rich regions amongst the warp yarns. Whereas, inside the composites, the warp yarns are closely packed.

In one of the parallel projects [8], measurements were made on the XCT images to determine the geometric parameters and their variation. There are variations in the real composites, so a minimum of 15 cross-sections were measured and averaged. The differences among the four types of fabrics can be interpreted into six geometric parameters, namely weft space, weft yarn width, weft yarn thickness, warp yarn width, warp yarn thickness and warp yarn weaving angle. The values and standard deviations of these parameters are listed in Table 3-3. Based on this data, unit cells of these composites, e.g. as shown in Figure 3-8 for GF-1 and CF-T300, were built for the development of the artificial neural network (ANN) model described in Appendix 1 and [8].

Each layer of warp yarns in the XCT images contact with the adjacent layer of warp yarns. Therefore, twice the warp yarn width is essentially the unit cell size in the warp direction. In the weft direction, it is twice the weft space. The unit cell sizes of these composites are listed in Table 3-4.

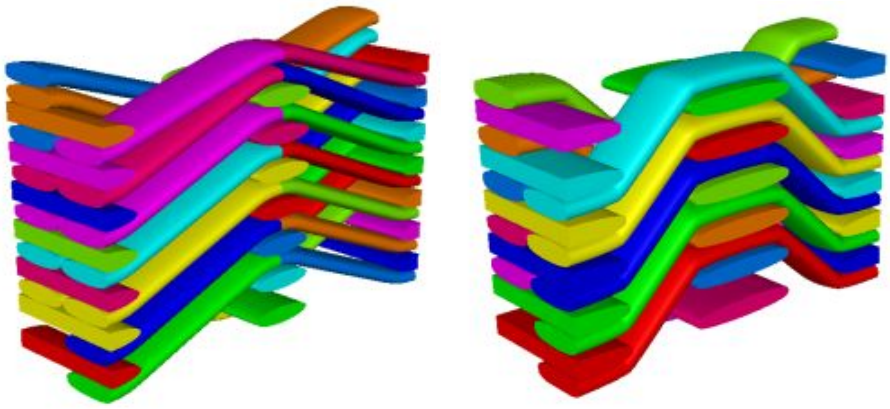


Figure 3-8 The unit cell models of GF-1 (left) and CF-T300 (right) [10].

Table 3-3 The values of the geometric parameters in mm for the four composites [8].

Type	Weft space	Weft yarn width	Weft yarn thickness	Warp yarn width	Warp yarn thickness	Warp yarn weaving angle
GF-1	4.52±0.4	1.45±0.5	0.36±0.05	1.31±0.1	0.38±0.005	23°/27°
GF-2	4.35±0.3	2.48±0.2	0.42±0.06	1.31±0.01	0.37±0.15	38°/43°
CF-T300	3.75±0.5	2.3±0.2	0.36±0.05	1.25±0.14	0.4±0.1	23°/34°
CF-IM7	4.52±0.14	2.26±0.16	0.37±0.03	1.28±0.09	0.37±0.04	25°/36°

Table 3-4 The volume fractions of yarns and fibres of the four composites, and their unit cell sizes.

Type	Yarn volume fraction (warp: weft)	Overall fibre volume fraction	Unit cell size (weft × warp) in mm	Moulded panel thickness in mm
GF-1	48.99%:13.24%	50.95%±0.35%	9.04 × 2.62	4.1
GF-2	42.62%:23.39%	54.00%±0.52%	8.7 × 2.62	4.2
CF-T300	38.02%:28.41%	52.21%±0.63%	7.5 × 2.5	3.7
CF-IM7	41.03%:25.64%	55.46%±0.34%	9.04 × 2.56	4.2

Volume fractions of yarns and fibres are also calculated. The size A_{fabric} and weight m_{fabric} of dry fabrics were measured prior to RTM. Edges where loose yarns are located are excluded. The fibre density ρ_{fibre} is provided by the supplier. The thickness of the picture frame t_{f} is known. Then the overall fibre volume fraction V_{f} is calculated as:

$$V_{\text{f}} = \frac{m_{\text{fabric}}}{\rho_{\text{fibre}} \cdot A_{\text{fabric}} \cdot t_{\text{f}}} \tag{3-1}$$

The geometric properties of the weave, which were measured from the micro-CT images, were used to generate corresponding unit cell models. Based on the unit cell models, the volume of yarns as well as the volume fractions of the weft yarns and the warp yarns were estimated in [8]. The volume fractions of fibres and yarns are listed in Table 3-4. As can be seen, the GF-2 and CF-IM7 composites have very similar overall fibre volume fractions as well as warp to weft yarn volume fraction ratios. Although GF-1 and GF-2 composites are made with the same reinforcement material, their yarn volume fraction ratios are different.

3.4 Quasi-static tests

3.4.1 Methodology

3.4.1.1 QS in-plane tension

The tensile testing generally follows the standard ASTM D3039 [117]. The photograph of the experimental set-up is shown in Figure 3-9. The composite specimens were 250 mm-long and 25 mm-wide. Two types of specimens were cut, with weft and warp yarns aligned in the longitudinal direction, respectively. To improve the specimen clamping and avoid crushing the ends of specimens, aluminium tabs of 50 mm in length, 25 mm in width and 2 mm in thickness were attached at the ends of each specimen with ARALDITE® epoxy adhesive as shown in Figure 3-10 (a). The specimens were clamped by the grips of the Instron testing machine, and tension was applied at a constant displacement rate of 2 mm/min. Given the gauge section of 150 mm in length, the nominal strain rate within the gauge section was 2.22×10^{-4} /s. The force F_{L} was measured by a

200 kN piezoelectric load cell and then converted to stress, σ_L, assuming a constant cross sectional area *A* of the specimen, according to:

$$\sigma_L = \frac{F_L}{A} \tag{3-2}$$

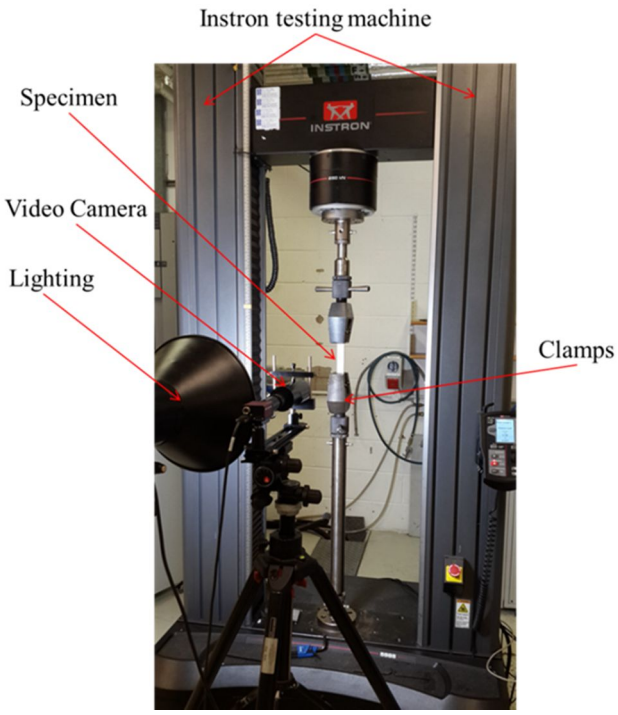


Figure 3-9 The set-up of the QS tensile test.

At least five specimens were tested for each loading direction. Strain was measured by the video gauge method. Random black and white speckles were spray-painted on the specimens as shown in Figure 3-10 (b), and an AVT Stingray F-146B camera was focused on the speckle pattern. A fill-in light was used to increase the contrast. The movements of four target regions as shown in Figure 3-10 (c) were recorded and analysed by Imetrum video gauge software V2.3.1 [181]. Longitudinal strain ε_L was calculated based on the relative displacements of target 1 and target 2, whilst transverse strain ε_T was determined based on target 3 and target 4. Poisson's ratio v_{LT} was also calculated by the software as:

$$v_{LT} = -\frac{\varepsilon_T}{\varepsilon_L} \tag{3-3}$$

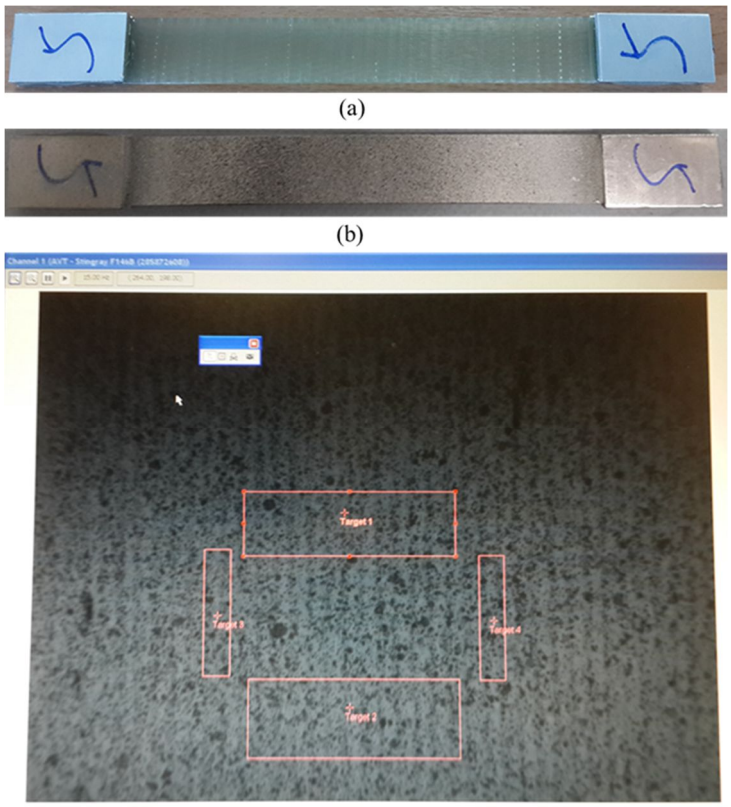


Figure 3-10 (a) Original tensile specimen with aluminium tabs, (b) tensile specimen with speckle patterns and (c) speckle pattern observed by the camera in the software and target regions for calculating strains and Poisson's ratio.

3.4.1.2 QS in-plane compression

The compression tests were also conducted with the Instron testing machine. Rectangular composite specimens of 40 mm in length and 25 mm in width were machined. Two types of specimens were manufactured, with weft and warp yarns being aligned in the longitudinal direction, respectively. To hold the specimen in these tests, a jig used in [182] and [101] was employed. The load was applied in the longitudinal direction. The specimen was clamped at both ends, leaving a 30 mm-long gauge section. The displacement rate was held constant at 1 mm/min, giving a nominal compressive strain rate of 5.56×10^{-4}/s. The stress and strain measurements and the resultant stress-strain curves were obtained using video analysis in a similar manner as those in the tensile tests. The photograph showing the arrangement of the experimental equipment is shown in Figure 3-11.

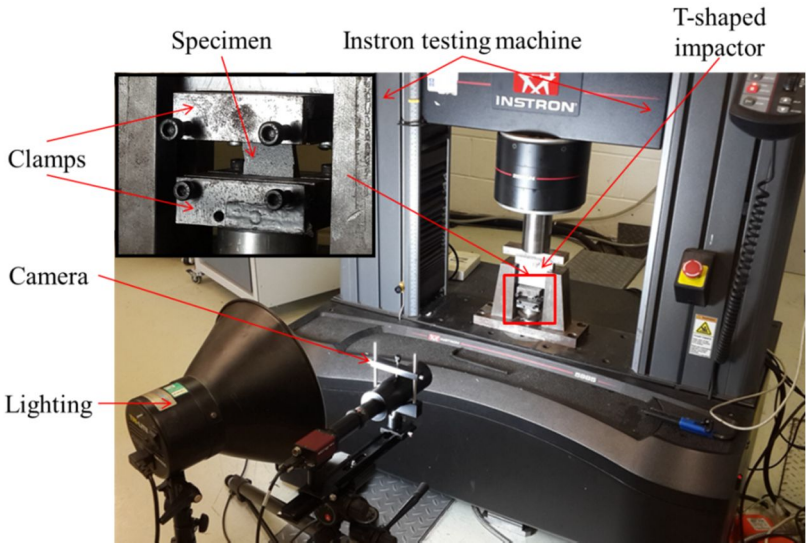


Figure 3-11 The set-up of the QS compression tests with a close-up view of the specimen and the clamp caps

3.4.1.3 QS in-plane Shear

Two types of shear tests were carried out to determine the in-plane shear properties of the composites. The first one, the ±45° off-axis tensile shear test of laminated composites is standardised as ASTM D3518-08 [183]. It was employed to characterise the in-plane shear behaviour due to its simplicity. The specimen size and the attaching of tabs were the same as the normal tension tests. However, the specimen was cut carefully to ensure that both weft and warp yarns were 45° to the longitudinal direction. The force, as well as the longitudinal and transverse strains, ε_{L} and ε_{T} , were measured the same way as in the tensile tests. The shear stress, τ, and the shear strain γ are calculated as follows:

$$\tau = \frac{F_{\mathrm{L}}}{2A} \tag{3-4}$$

$$\gamma = \varepsilon_{\mathrm{L}} - \varepsilon_{\mathrm{T}} \tag{3-5}$$

where A is the cross-sectional area of the specimen.

The second method of measuring the in-plane shear properties employs the ASTM D7078/D7078M standard [184]. The drawing of the specimen, with its dimensions specified, is shown in Figure 3-12. In the figure, the weft yarns are aligned in the 0° direction, while the warp yarns are aligned in the loading direction, at 90°. In addition to that, several specimens were machined and tested,

in which the weft yarns are aligned with the loading direction. This was to check whether the orientation of the yarns in the loading direction affects the measurement of shear properties. To ensure the precise fillet machining at the notches, the specimens were cut by a water jet cutting machine. During the test, the specimen was clamped in the left and right by two L-shape fixture halves as shown in Figure 3-13. The left half of the specimen was pulled upwards at a constant displacement rate of 1 mm/min. The shear strain was obtained based on the strains in ±45° directions, ε_{+45} and ε_{-45}. Shear stress was calculated as the loading force divided by the cross sectional area between the notches.

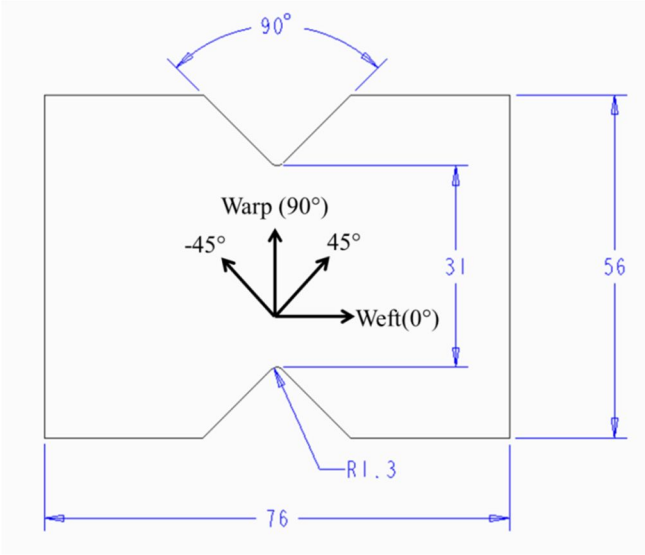


Figure 3-12 The dimensions of the specimen for V-notched rail shear test.

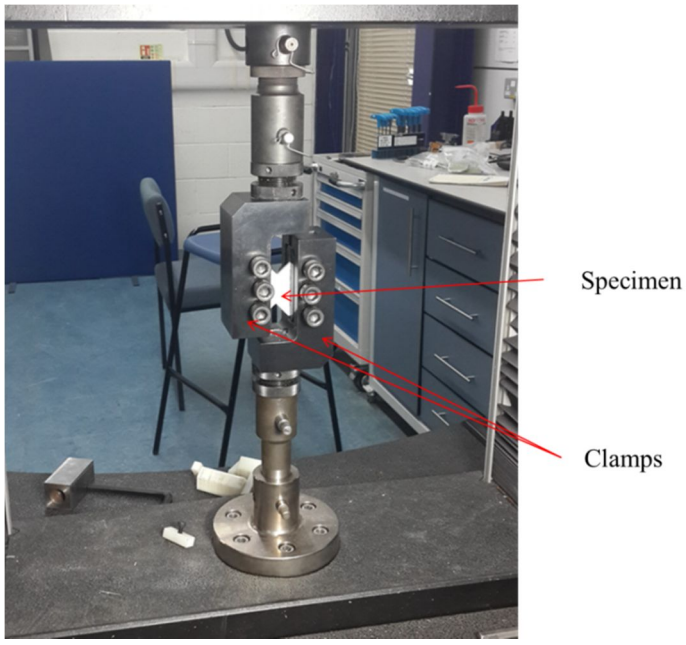


Figure 3-13 The set-up of the V-notch rail shear test including the L-shaped clamps.

$$\gamma = |\varepsilon_{+45}| - |\varepsilon_{-45}| \tag{3-6}$$

$$\tau = \frac{F_L}{A} \tag{3-7}$$

3.4.2 Results

3.4.2.1 Noise of the results

Noise was commonly encountered in the QS tests during the measurement of stress and strain. Figure 3-14 shows a stress-strain curve suffering from severe noise. Although the linear elastic behaviour can be distinguished, the noise brings difficulties in calculating the chord modulus. If any points on the spikes are used in the calculation, the resultant modulus could be far from the real one. The specific cause for the noise could not be identified. The sources of the noise could be the clamping mechanisms, the vibration of the camera and the vibration of the Instron machine.

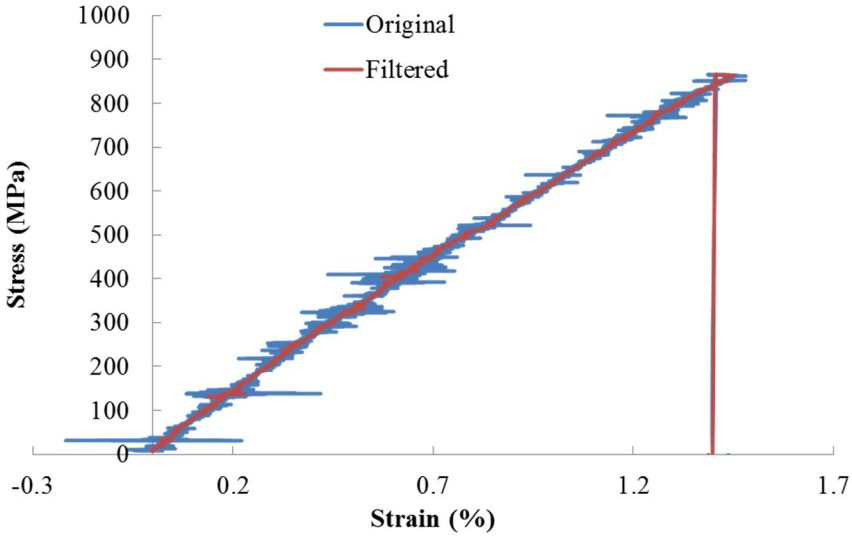


Figure 3-14 A tensile stress-strain curve before and after filtering.

In this study, the noise in the measurements was tackled with a median filter, which is available in the Signal Processing Toolbox of MatLab. The median filter replaces every data point of a signal by the median of this point and a specified number of neighbouring points. Those points that are noticeably different from their surrounding points are discarded. The selection of the number of surrounding points affects the reduction of the number and amplitude

of spikes. Figure 3-15 shows how a series of strain data is changed by choosing different numbers of neighbouring points. Quite a few of spikes of the original data remain when five data points are chosen for the filter, as shown by "New strain-5" in Figure 3-15. Almost all spikes are eliminated when 35 points are used ("New strain-35"). The amplitude of the remaining spikes is also largely reduced. It makes litter difference when the number of points is increased to 45 ("New strain-45"). Therefore, 35 points have been chosen in the filter for this study. The filtered data is also plotted overlapping the original signal in Figure 3-14 and it can be seen that it follows the trend of the original one very well.

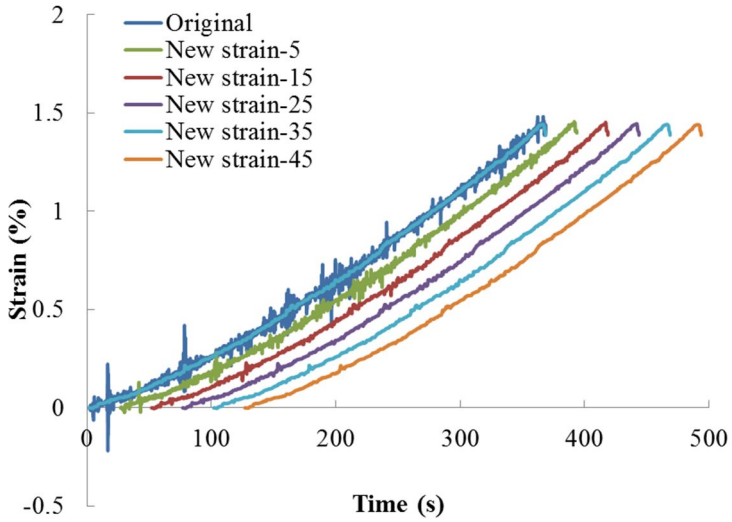


Figure 3-15 The original strain signal and the ones after median filtering.

3.4.2.2 In-plane tension

Typical stress-strain curves obtained from the weft and warp tension tests for the four types of composites are plotted in Figure 3-16 and Figure 3-17, respectively. Values of mechanical properties, measured from the tests, are summarised in Table 3-5.

Weft Results

Under tension in the weft direction, the stress-strain curves of CF-T300 and CF-IM7 are relatively linear, though some stiffness reduction takes place in the later stages of the test. The weft modulus and strength show a positive correlation with the properties of fibres and volume fraction of yarns. The two carbon composites have higher elastic moduli and ultimate tensile stresses, but lower failure strains than those for GF composites. GF-2 has a higher stiffness and strength in the weft direction than those in GF-1 due to the higher yarn

volume fraction of weft yarns in GF-2. In terms of strain energy density to failure, CF-IM7 is higher than the others. This is attributed to the better mechanical properties of IM7 fibres.

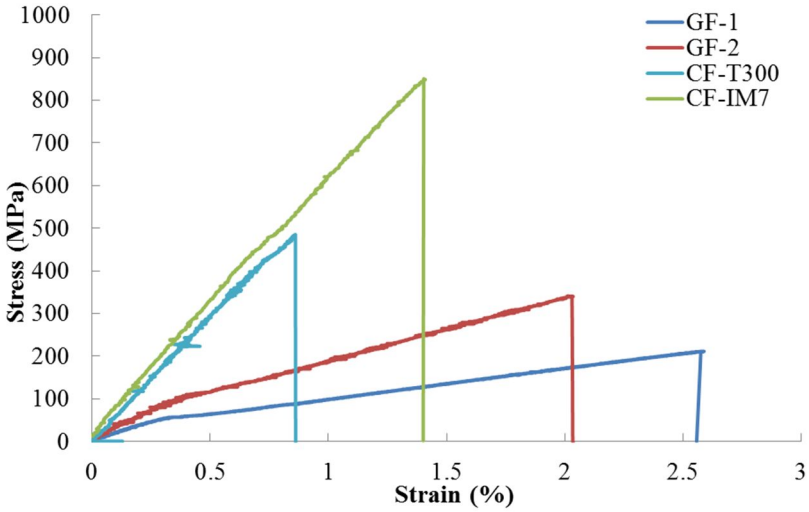


Figure 3-16 Stress-strain curves of weft tension.

Warp Results

The dependency of mechanical properties on fibre/yarn properties is also found for the warp tension curves in Figure 3-17. For instance, the warp yarn volume fraction is higher in GF-1 than that in GF-2 and consequently GF-1 is stiffer and stronger than GF-2 in the warp direction.

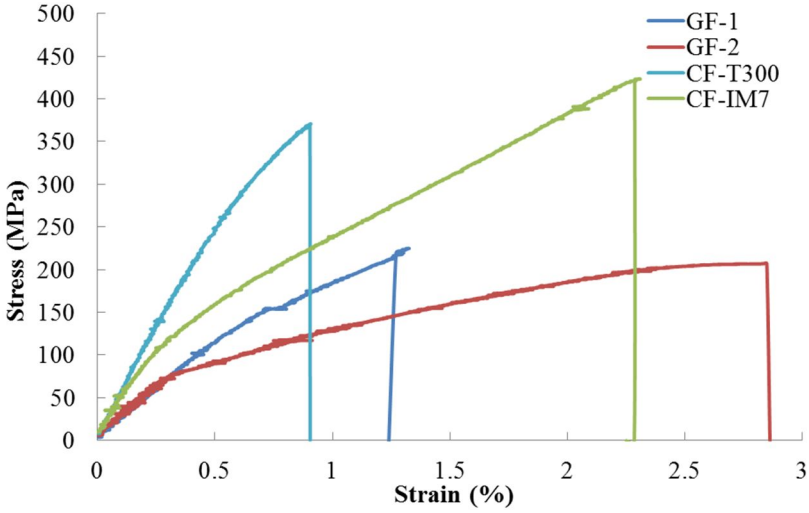


Figure 3-17 Stress-strain curves of warp tension.

Non-linearity can be seen in the warp curves for all four composites. Straightening of the crimped warp yarns is observed in the tested specimens of all four composites, which will be shown in the following section about the

damage and failure modes. This could increase the stiffness, however the combination of cracking and straightening results in a reduction in stiffness and the non-linear behaviour in Figure 3-17.

The numbers of successfully tested specimens are also given in Table 3-5. Because of the limited amount of T300 preform, only a few tensile specimens were machined for this material. Only two specimens were successfully tested for CF-T300, hence no standard deviation is specified in the table.

Table 3-5 The mechanical properties from the in-plane tension tests.

Direction	Property	Material			
		GF-1	GF-2	CF-T300	CF-IM7
Weft	Modulus (GPa)	15.92±0.55	25.67±1.45	55.16	62.71±0.43
	Damage on-setstress (MPa)	57.26±3.39	94.04±8.72	425.02	460.67±56.09
	Maximum stress (MPa)	206.46±13.57	336.79±31.44	485.29	832.11±40.69
	Number of specimens	5	6	1	6
Warp	Modulus (GPa)	24.77±3.12	21.83±0.76	48.68	35.79±3.43
	Damage on-set stress (MPa)	110.08±8.9	80.68±4.07	136.58	161.90±21.59
	Maximum stress(MPa)	223.49±3.35	213.21±6.81	370.53	421.36±25.14
	Number of specimens	5	6	2	6

Damage and Failure Modes

All the stress-strain curves are initially linear. Then a transition, where tangential stiffness begins to degrade, takes place and the curves enter another linear region for the weft tension or become nonlinear for the warp tension. It is of great interest to know what happens during the transition with regard to damage mechanisms. To investigate this, in addition to the five specimens for whole stress-strain curves, some specimens were loaded to a point before the transition

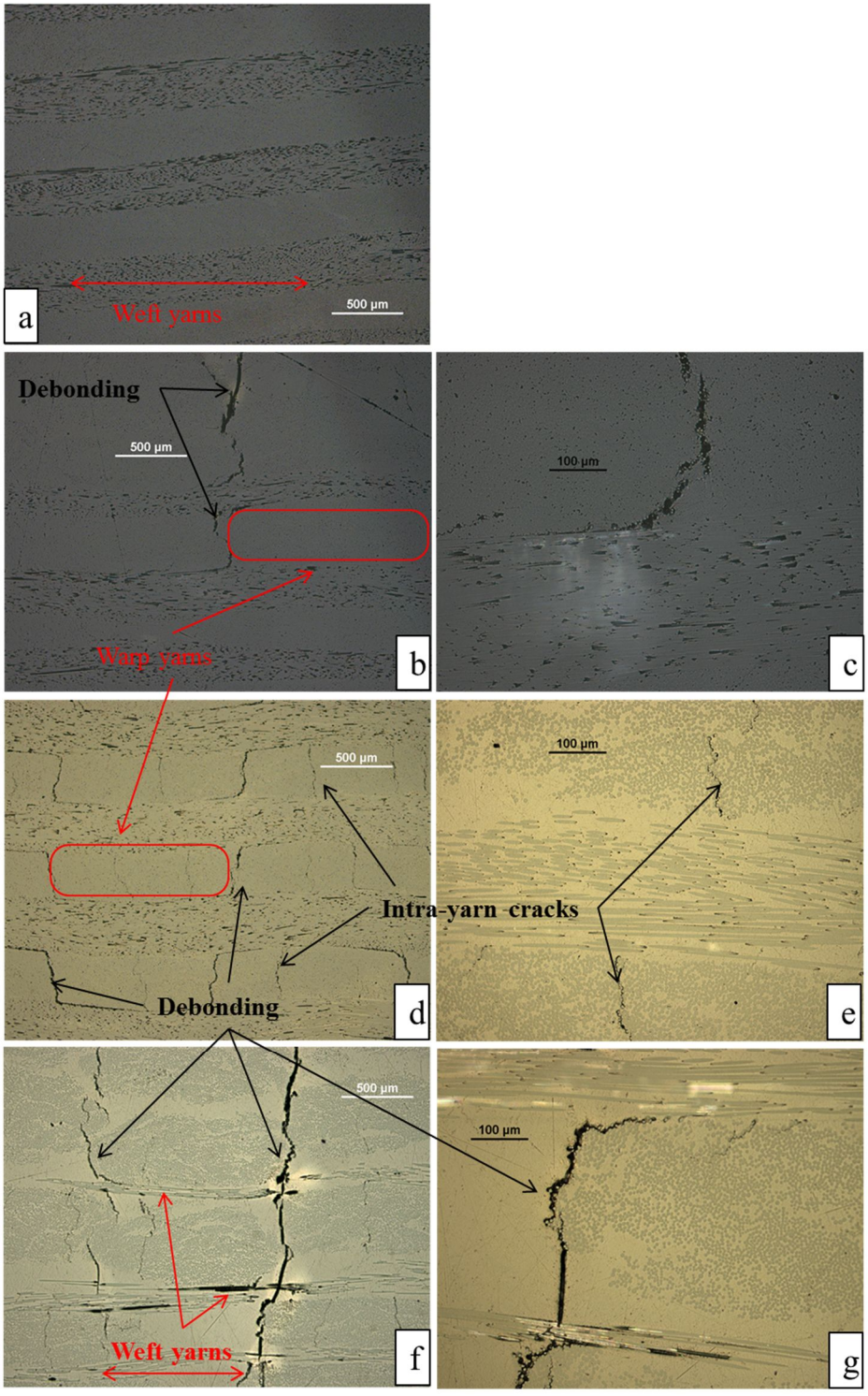


Figure 3-18 Microscopic observation [9] of GF-2 weft tension specimens: (a) loaded to 0.23% of strain; (b) and (c) loaded to 0.43% strain; (d), (e), (f) and (g) loaded to the final failure. (c), (e) and (g) are the zoom-in views of (b), (d) and (f) respectively.

and then unloaded, while some others were loaded to a strain after the transition and then unloaded. Then in one of the parallel projects [9], these tested specimens were cut along the loading direction and made into samples for microscopic observation. The cutting planes are parallel to both the longitudinal

and thickness direction such that the cracks transverse to the loading direction are exposed. Figure 3-18 and Figure 3-19 are the microscopic observations for the tensile specimens of GF-2 in weft and warp respectively.

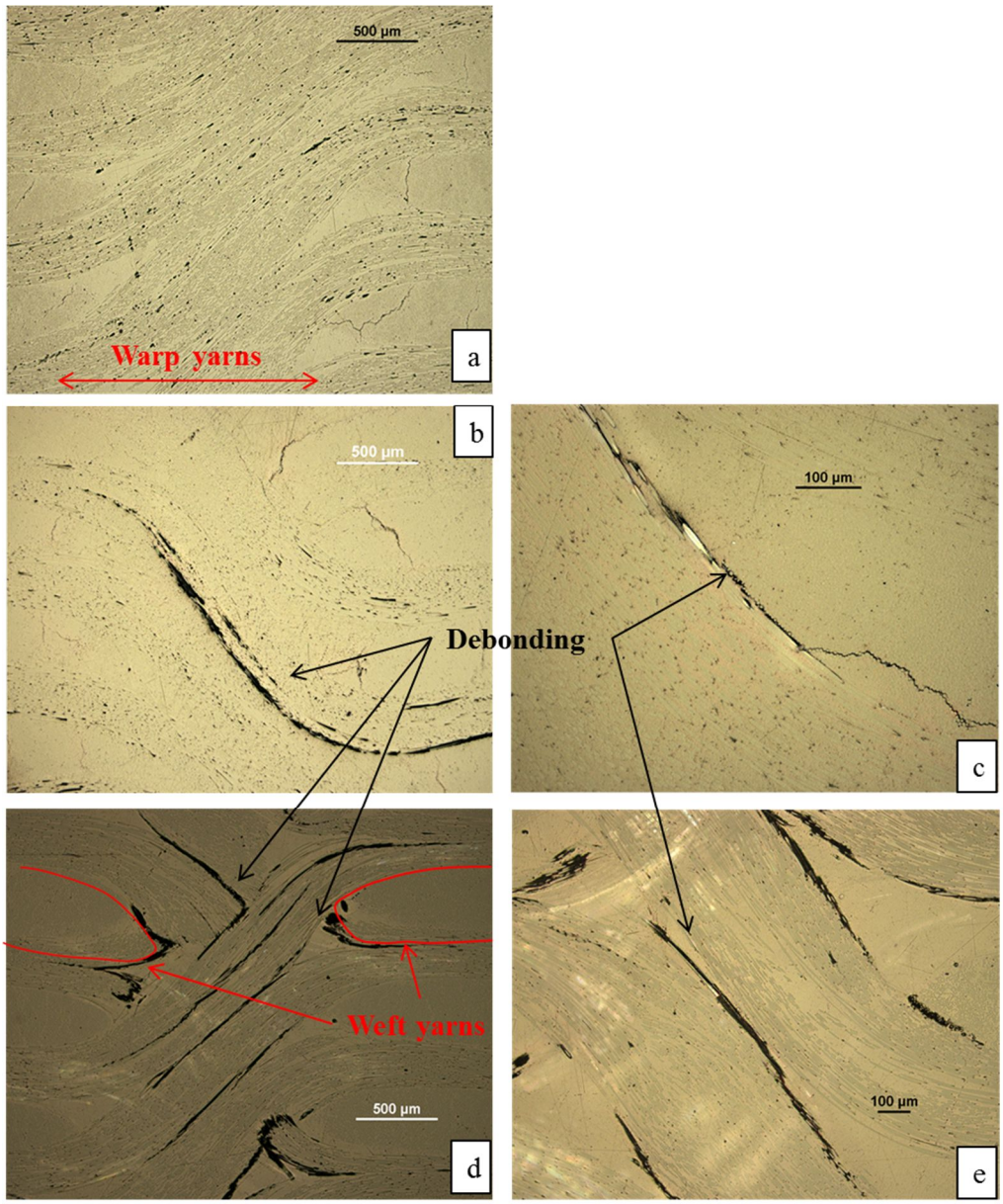


Figure 3-19 Microscopic observation [9] of GF-2 warp tension specimens: (a) loaded to 0.28% of strain; (b) and (c) loaded to 0.47% strain; (d) and (e) loaded to the final failure.

In Figure 3-18 (a), no crack is found when the specimen is loaded to 0.23% strain, which is slightly before the transition. Figure 3-18 (b) and (c) show that yarn debonding took place, transverse to the loading direction, propagating along the boundaries of warp yarns. In this case, the specimen was loaded to 0.43% of strain, slightly after the transition. The transverse debonding reduced the effective area which the loading could act on. This is the most likely reason

for the transition in the weft stress-strain curves. When the specimen was loaded to final failure, as shown by Figure 3-18 (d), the debonding became extensive and widely spread over the specimen. There are also many transverse cracks inside the warp yarns, which are magnified in Figure 3-18 (e). In Figure 3-18 (d) and Figure 3-18 (e), it seems that the debonding and intra yarn cracks do not interact with the weft yarns. However, the cross section of the weft yarn is roughly elliptical and much thinner at the edge of the ellipse, as shown by Figure 3-18 (f). At the final failure, the debonding easily passes the weft yarns and becomes connected with the debonding of the next layer of warp yarns, leading to the long debonding in Figure 3-18 (f).

In Figure 3-19, the transition in warp tension is also likely to be caused by initiation of debonding. At 0.28% of strain, there is no sign of debonding in Figure 3-19 (a). After transition, at 0.47% strain ((b) and (c)), there is a large gap along the path of the crimped warp yarns due to debonding. When the specimen was further strained to the final failure, a significant amount of yarn debonding can be observed in (d) and (e). In addition to along the warp yarn path, the debonding can also be found around the tips of the elliptical weft yarns. The zoom-in views (c) and (e) do not reveal any other failure modes.

Similar observations are found in the carbon fibre specimens, as shown in Figure 3-20 and Figure 3-21, for CF-IM7. The initiation and propagation of debonding is similar to GF-2, however, there is no sign of transverse intra yarn cracking, even when specimens are loaded to failure.

As the above study shows that the transition is due to the initiation and propagation of failure and damage, the stress at which the transition begins is considered in this work as the damage on-set stress. The elastic moduli are calculated from 1000με to 3000 με, which is before the transition, and are representative of the elastic behaviour.

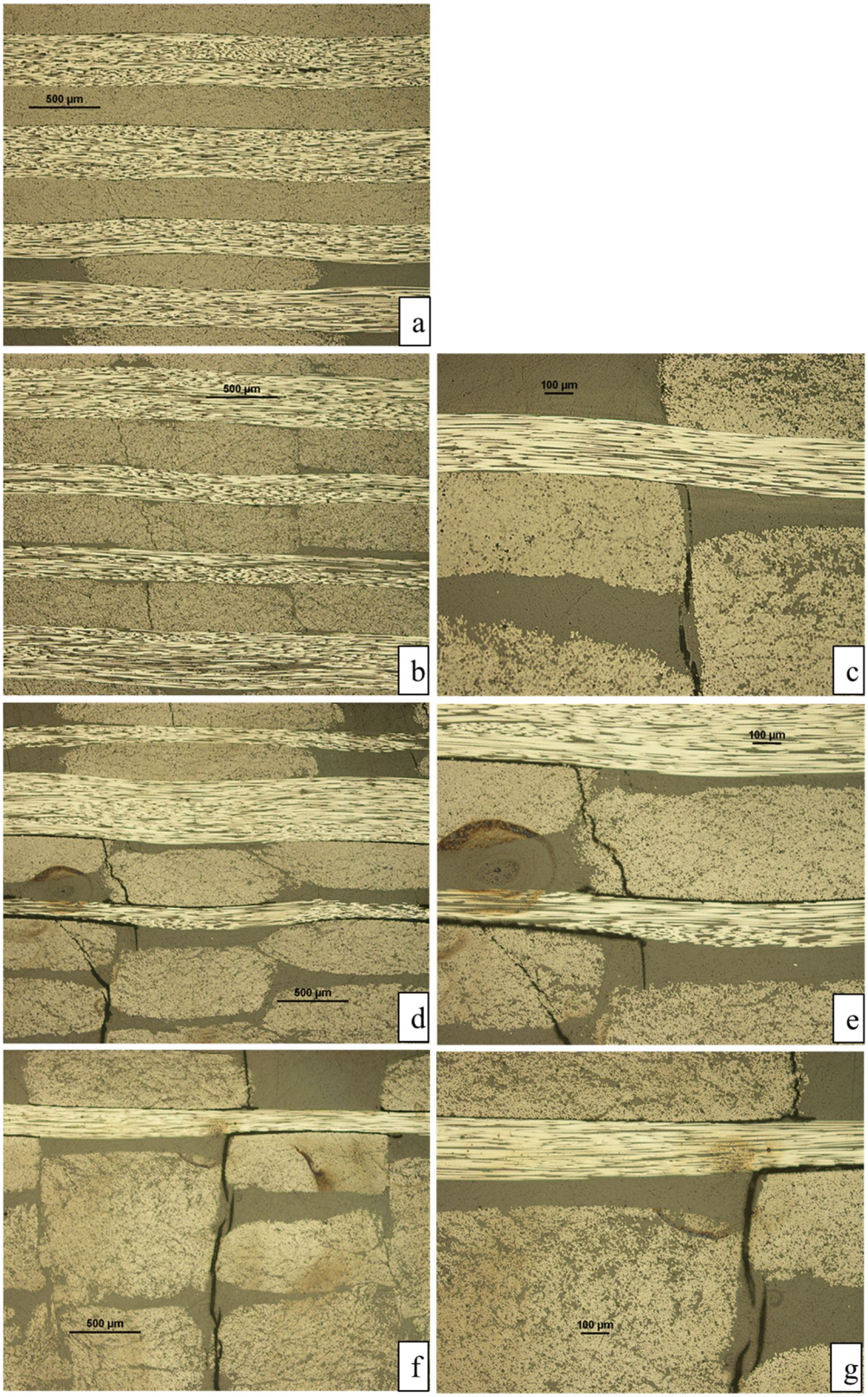


Figure 3-20 Microscopic observation [9] of CF-IM7 weft tension specimens: (a) loaded to 0.4% of strain; (b) and (c) loaded to 0.7% strain; (d) to (g) loaded to the final failure.

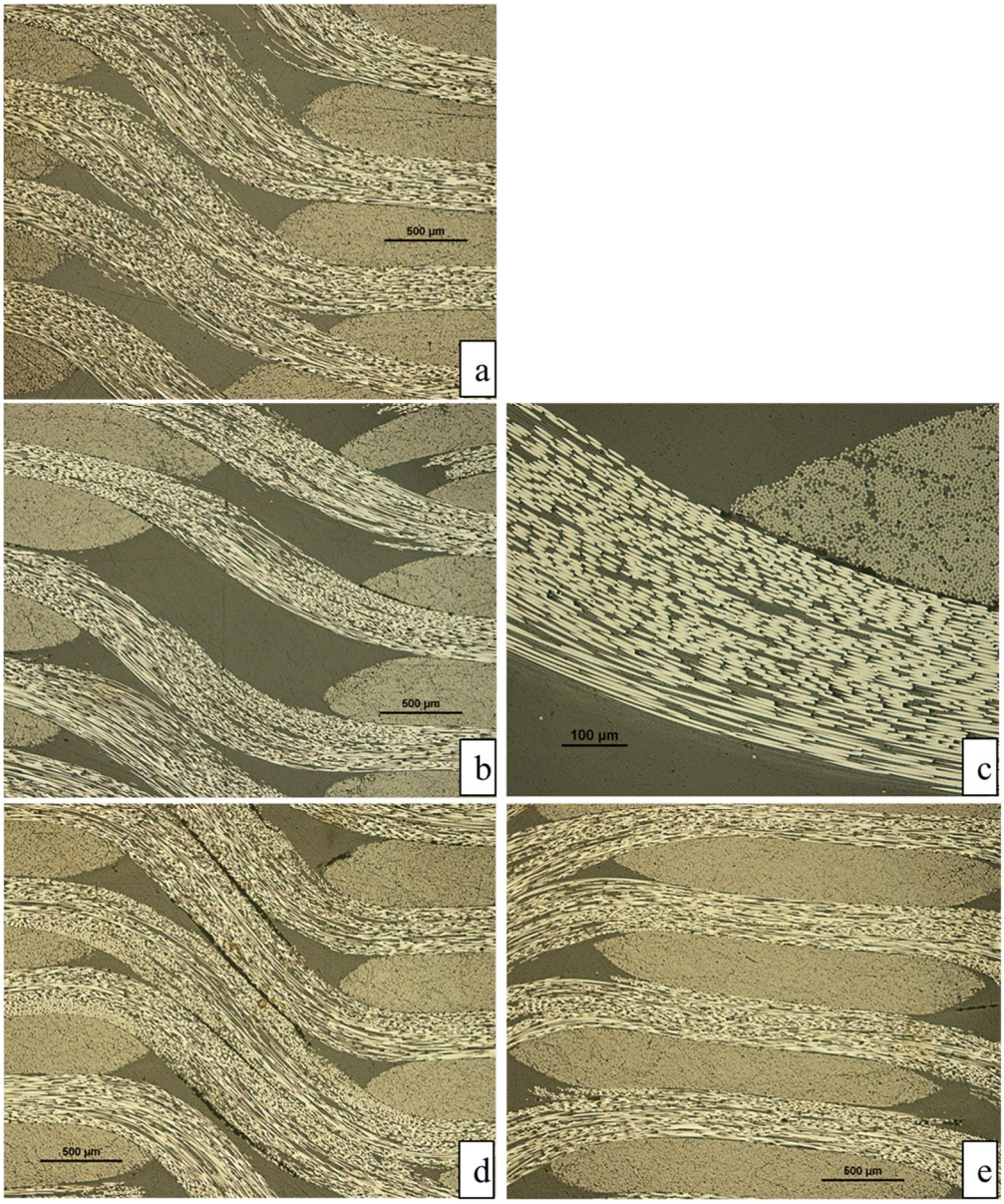


Figure 3-21 Microscopic observation [9] of CF-IM7 warp tension specimens: (a) loaded to 0.2% of strain; (b) and (c) loaded to 0.5% strain; (d) and (e) loaded to the final failure.

In addition to the above mentioned modes of failure and damage for the transition, other modes can be visually observed on the failed specimens. Failure faces of the four materials are shown in Figure 3-22 and Figure 3-23. But, CF composites are difficult to analyse by this method due to their opacity. On the other hand, damage and failure patterns are clearly visible in the semi-transparent GF composite specimens.

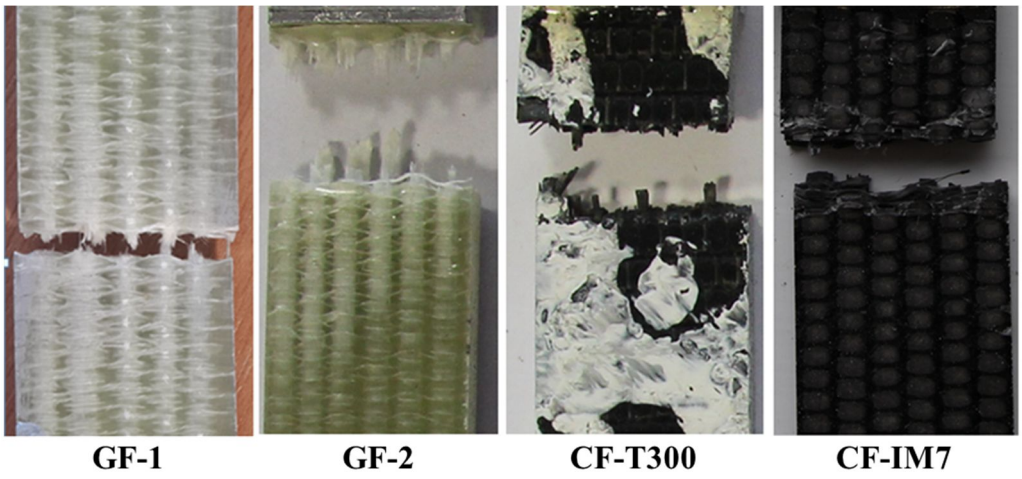


Figure 3-22 Tested weft tension specimens with close-up views of failure surfaces.

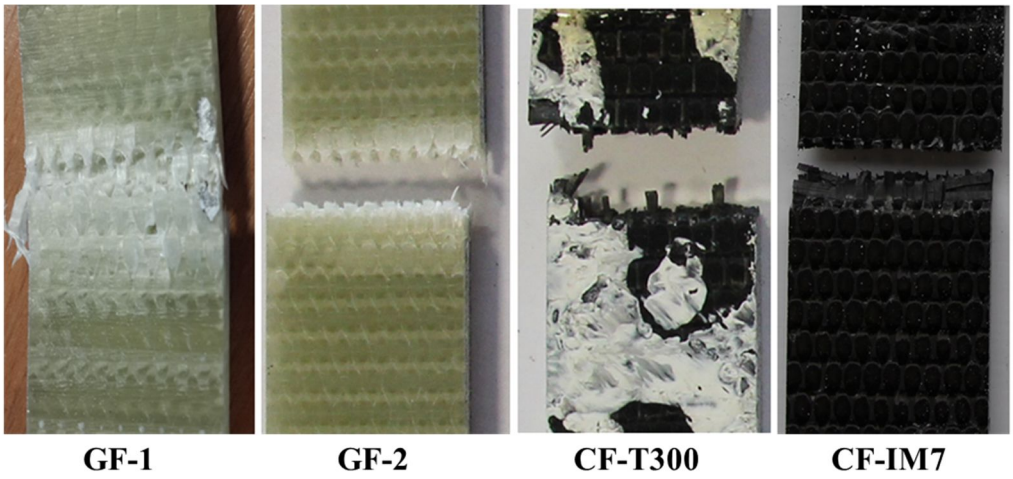


Figure 3-23 Tested warp tension specimens with close-up views of failure surfaces

A photograph of the failed GF-2 specimen is shown in Figure 3-24. For the weft specimen, two major types of crack can be distinguished. One follows the weaving pattern of the warp yarns in the resin rich region. The other is over the weft yarns and almost perfectly transverse to the loading direction. Along with inter-yarn matrix cracking, weft yarns appear to look white even away from the failure surface. Since the weft yarns in the intact specimen are generally transparent, this indicates the debonding of yarns as well as resin cracking within the yarns.

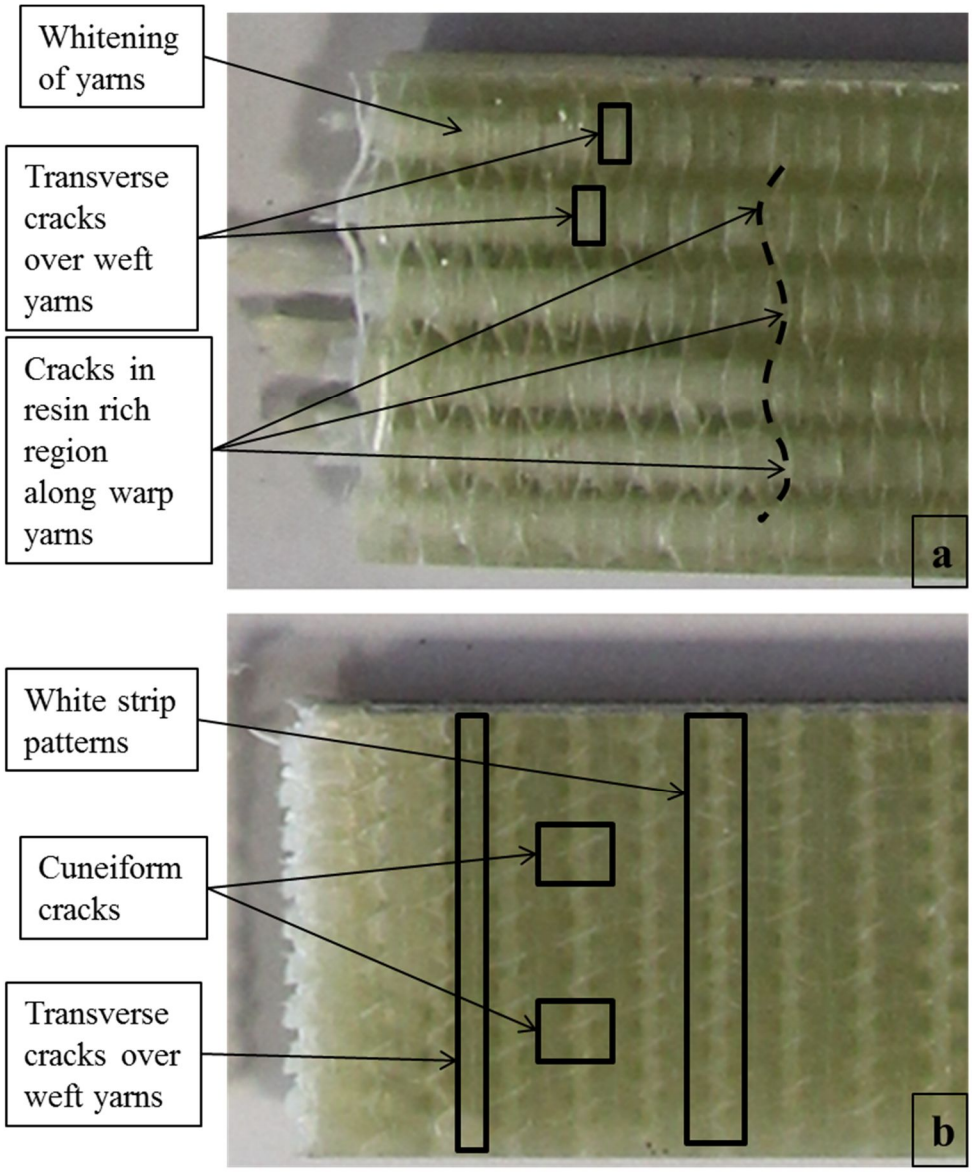


Figure 3-24 Cracks and debonding in the GF-2 (a) weft and (b) warp tension specimens.

The warp specimens also have cracks transverse to the loading direction. They develop over the weft yarns across the entire specimen width. At the same time, there are also cuneiform-like cracks at the superficial resin rich region. It is natural to expect straightening of the warp yarns under tension, and in the end, the specimen breaks when straightened warp yarns fail. Also, due to debonding, wide white striped patterns are found in the resin rich region along the straight weft yarns.

Although the GF-1 specimens appear more damaged due to the lower fraction of weft yarns, the failure and damage modes in them are similar to those in the GF-2 specimens.

3.4.2.3 In-plane compression

The typical stress-strain curves obtained in QS compression experiments for all four composites are plotted in Figure 3-25 and Figure 3-26 for weft and warp compressive tests, respectively. The modulus as well as the compressive strength determined from the tests are summarised in Table 3-6, where the numbers of specimens tested are also provided.

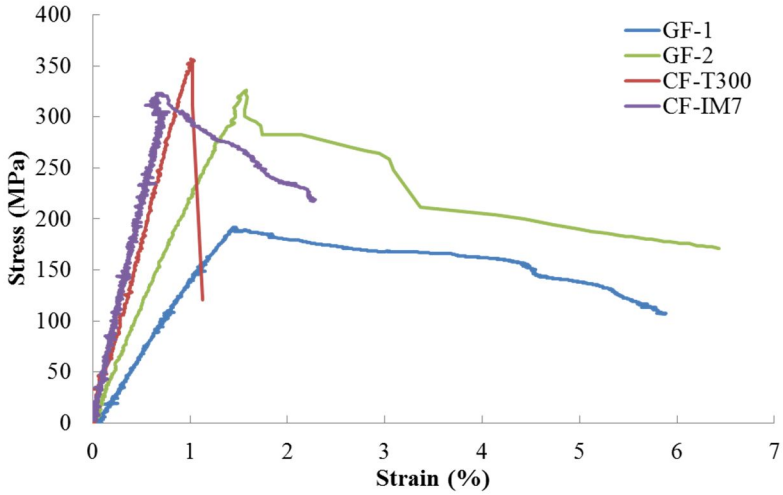


Figure 3-25 Stress-strain curves of weft compression.

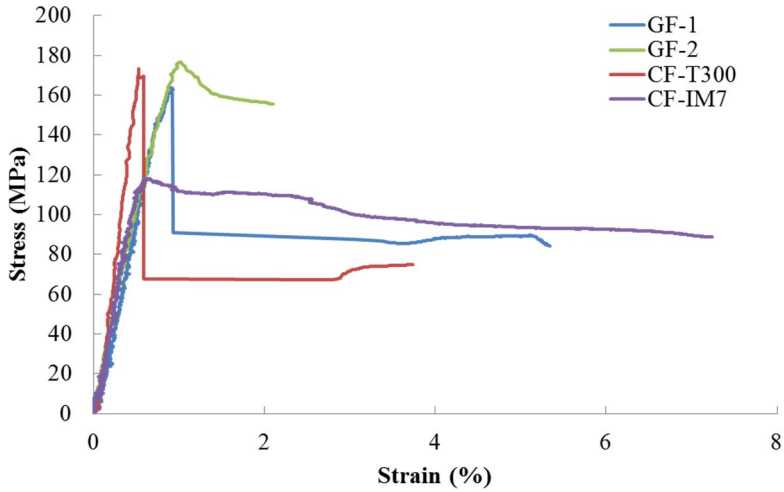


Figure 3-26 Stress-strain curves of warp compression.

In both figures, the curves are generally linear until failure. Similar to the tensile moduli, the moduli of weft compression show correlation with the properties of fibres and the volume fractions of the yarns. The two carbon fibre composites have larger moduli than the two glass composites due to the higher mechanical properties of carbon fibres. The GF-2 modulus is larger than GF-1 because of the higher fraction of weft yarns in GF-2.

However, the rest results of the compression tests show little correlation with the fibre properties and yarn volume fraction. Although the fibres of IM7 outperform T300 significantly with respect to mechanical properties, regarding the manufactured composites of IM7 fibres, i.e. CF-IM7, their weft strength, the warp strength and the warp modulus are less than those of the composites CF-T300. Meanwhile, there is only small difference among the warp moduli of GF-1, GF-2 and CF-IM7.

Table 3-6 The mechanical properties from the in-plane compression tests.

Direction	Property	Material			
		GF-1	GF-2	CF-T300	CF-IM7
Weft	Modulus (GPa)	12.79±1.55	20.15±1.01	39.88±3.21	32.67±8.24
	Strength (MPa)	199.07±5.08	323.18±9.36	386.22±32.81	296.52±17.6
	Number of tests	5	9	7	8
Warp	Modulus (GPa)	19.42±0.44	18.74±0.41	34.92±3.26	23.64±1.72
	Strength (MPa)	173.33±6.92	167.5±15.37	189.45±31.05	113.13±7.06
	Number of tests	5	8	7	8

After the maximum stress in Figure 3-25 and Figure 3-26, load carrying capability remains in all the specimens. This is expected as the failed compression specimens do not fracture into two pieces, in contrast to tensile tests. It can be seen from the front and side views of the failed specimens in Figure 3-27, in spite of the failure, some of the fibres are not disconnected. They are able to provide the residual load carrying capability. Under further loading, more damage is caused and the capability degrades, as reflected by the gradual reduction of stress after failure in Figure 3-25 and Figure 3-26. Exception of stress drop happened for the warp compression of GF-1 and both compressions of CF-T300. However, the drop is not a sign of brittle failure. It is most likely due to the unloading caused by the failure of maintaining stable stroke control after the specimen buckles.

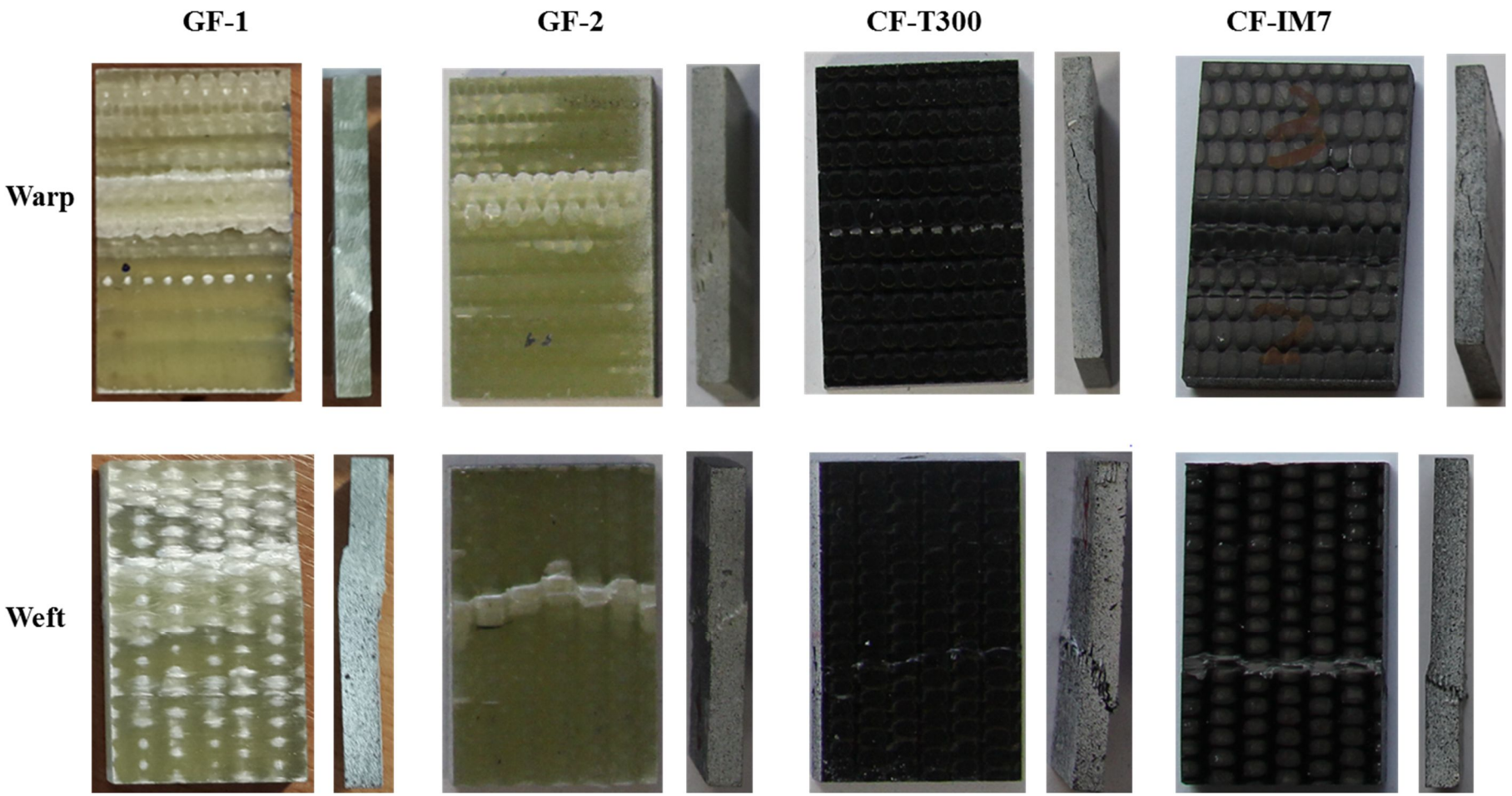


Figure 3-27 The tested compression specimens.

It should be noted that the strain energy density of the post-failure behaviour is comparable to or more than that of the elastic region. This post-failure behaviour needs to be considered in the simulation otherwise the energy dissipation capability would be significantly underestimated.

Regarding failure, similarity can be found in the tested specimens of all four composites. Shear in the through-thickness direction is visible in the photographs of the failed specimens in Figure 3-27. It is easy to see in the side view of the specimens that the failure surfaces in all the specimens are inclined to the loading direction. The mechanisms of failure in the two directions are, however, different. In the warp specimens, the crimping of yarns can easily lead to their debonding. The debonding of different layers of warp yarns eventually merges, forming a failure surface inclined to the loading direction. On the other hand, fibre kinking is clearly the failure mode in the weft specimens which is the expected mode when straight yarns or fibres fail under compression.

3.4.2.4 In-plane shear

The stress-strain curves obtained in tensile shear and V-notch shear tests are shown in Figure 3-28 and Figure 3-29, respectively. It needs to be pointed out that in many cases the tests were stopped before the final failure of specimens has occurred. As can be seen in Figure 3-29, V-notch shear tests were stopped 10% of shear strain, above which pure shear state is unlikely. In the tensile shear tests for GF-2 and CF-T300, the strain measurement failed at relatively low values of strain, as shown Figure 3-28. The cause for this could be paint cracks, which were generated due to matrix cracks on the surface of the specimens. The size of these paint cracks could be similar to the speckles. Consequently, the camera could no longer identify the target regions and the strain measurements failed. Nevertheless, the obtained stress-strain curves are sufficient for understanding their shear behaviour. The GF-1 curves are exceptions in both figures, which eventually drop to zero, indicating specimen breaking into two pieces. The measured mechanical properties are summarised in Table 3-7.

There are similarities in both figures. The curves are generally non-linear except the initial segments. The shear moduli are determined over a strain range from 1500 to 6500 micro strain. For all types of the composites tested, the shear moduli determined were within the range from 3 to 4 GPa. It is well known that

woven fabrics have little resistance to shear loading. The shear of these 3D woven composites is dominated by the behaviour of the matrix. Given they are impregnated with the same matrix system, it is sensible to have similar shear moduli. Beyond the elastic range, the curves become non-linear. This is due to the matrix cracking as well as the rotation of yarns, which tend to align with the loading direction. Stress levels increase but tangential stiffness degrades till the end of test.

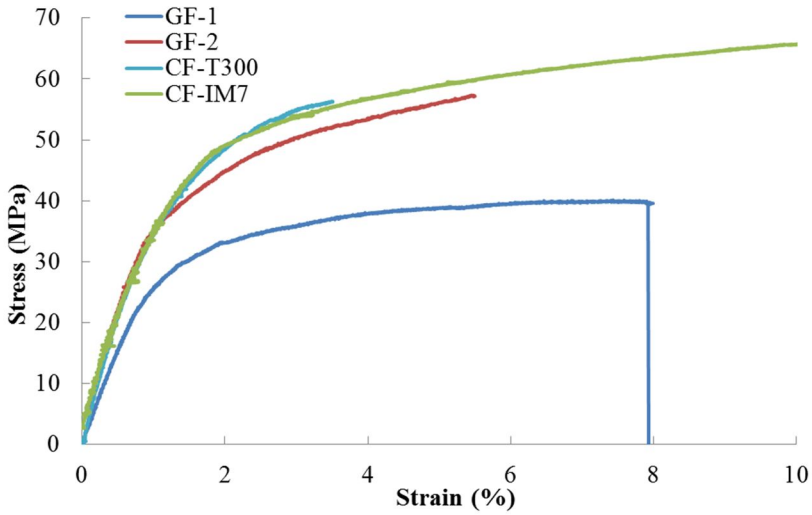


Figure 3-28 Stress-strain curves from 45° off-axis tension for in-plane shear test.

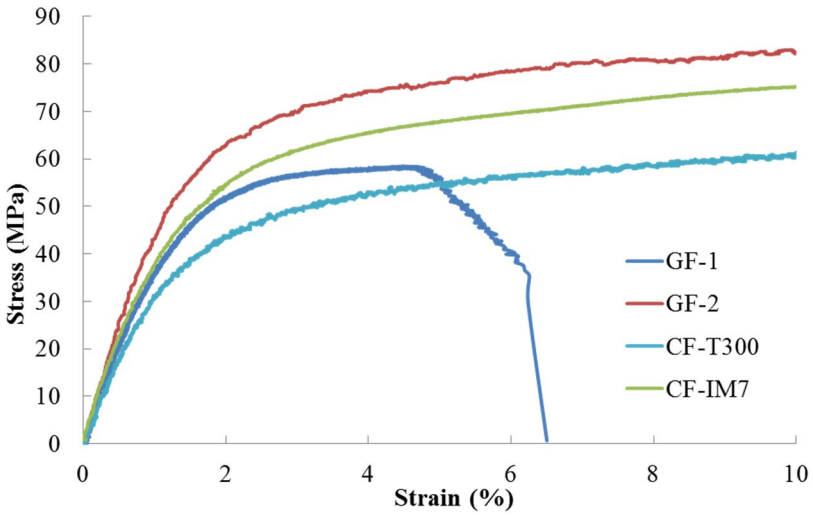


Figure 3-29 Stress-strain curves from V-notch two-rail shear tests.

At the end of the tests, the breakage of specimens occurred only in three cases, namely, in the off-axis tension of GF-1 and GF-2 composites, as well as in the two-rail shear test of GF-1. For the others, the specimens remained in one-piece when they were strained to more than 15% of shear strain. Under large

shear strains, significant fibre rotation took place in the specimen. Further loading the specimen, especially in the off-axis tension tests, would essentially result in testing the yarns under tension. The tests were therefore stopped.

The strength values were determined by offsetting a straight line with shear moduli by 0.2% shear strain as recommended by the rail shear test standard ASTM D7078. The strength values of GF-2, CF-T300 and CF-IM7 obtained in the off-axis tension test are very close to those of the two-rail shear test.

Table 3-7 The in-plane shear properties from two shear tests.

Property	Test type	GF-1	GF-2	CF-T300	CF-IM7
Modulus (GPa)	45°tension	2.99±0.98	3.65±0.32	3.7±0.53	3.38±0.22
	two-rail	4.03±0.14	4.06±0.50	3.41±0.54	3.85±0.42
0.2% offset strength (MPa)	45°tension	28.57±0.83	38.28±1.64	39.41±0.88	42.81±2.62
	two-rail	39.6±1.82	37.04±3.6	37.56±5.86	46.6±3.04
Number of tests	45°tension	6	6	6	6
	two-rail	10	10	10	10

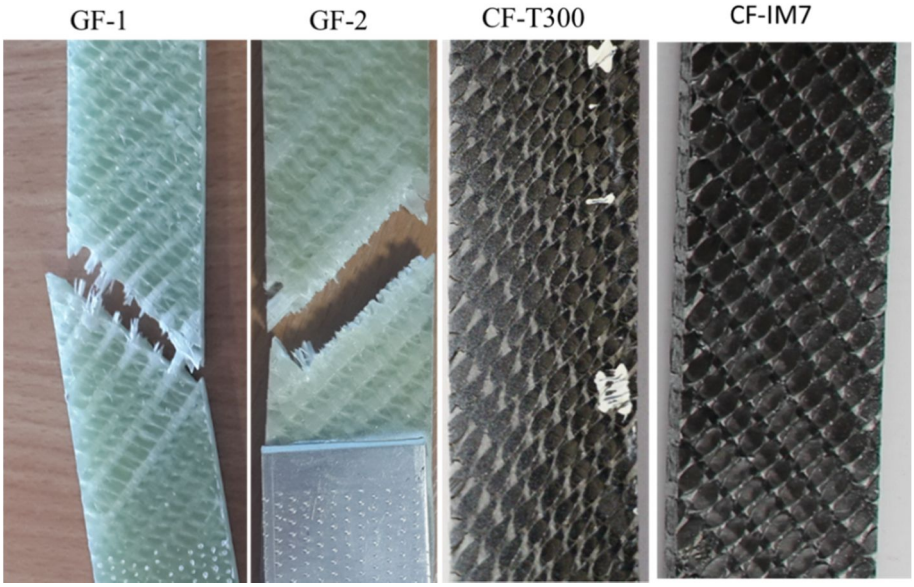


Figure 3-30 The tested specimens of 45° off-axis tension test.

The tested specimens of the off-axis tension test are shown in Figure 3-30. Both GF-1 and GF-2 are broken into two pieces with failure surfaces inclined to the loading direction. During the off-axis tensile loading, both weft and warp yarns are under tension. The weft direction of GF-1 is relatively weaker hence

the failure surface is almost normal to the weft yarns. On the other hand, the warp direction of GF-2 is weaker therefore failure took place normal to the warp yarns. Extensive resin cracking is also observed. Breakage failure does not happen in the CF-T300 and IM7 specimens possibly due to the superior mechanical properties of carbon fibres. Yarn rotation and aligning with the loading direction can be clearly seen in the photographs of the specimens in Figure 3-30. The resin around the yarns was therefore crushed.

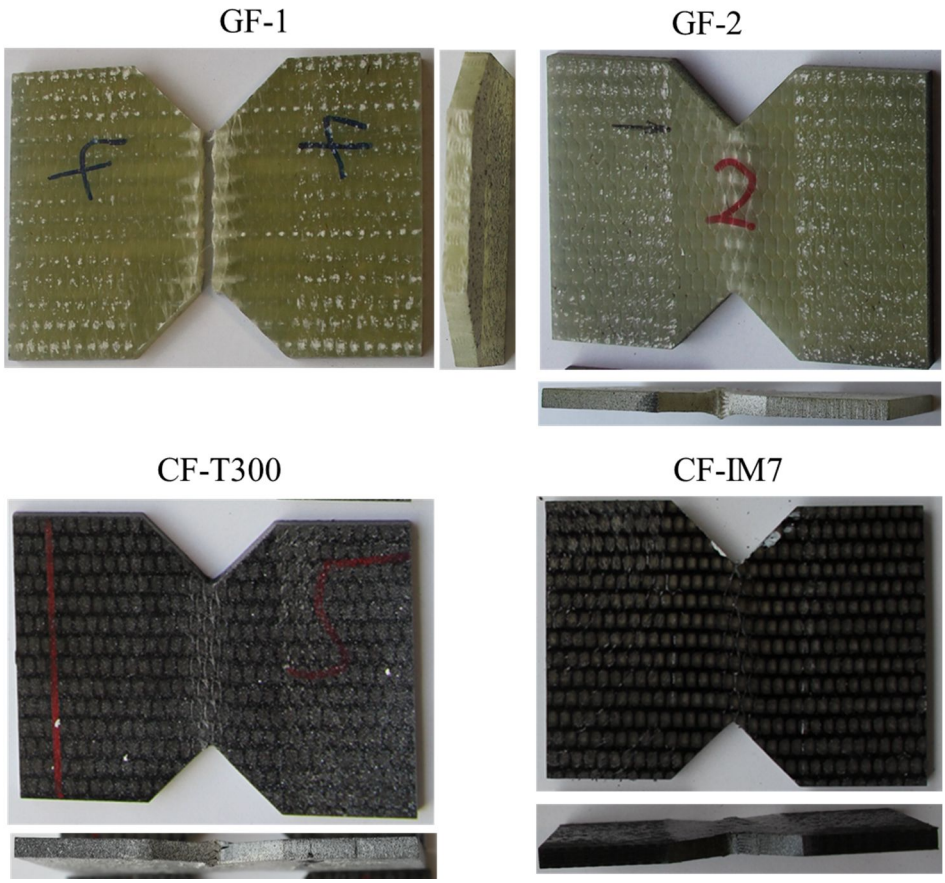


Figure 3-31 Tested specimens of V-notch two-rail shear tests.

Photos of the tested specimens in the two rail shear test are given in Figure 3-31. As was mentioned above, two types of specimens were machined for the two-rail shear test, where either the weft or the warp yarns were normal to the loading direction. Five specimens of each type have been tested. The results in Table 3-7 indicate small standard deviations in the ten specimens, regarding to both the moduli and the strengths. This suggests the irrelevance of yarn direction to this test. In Figure 3-29, GF-1 broke into two pieces at about 6.3% of strain while the others remain in one piece until more than 10% shear strain. A band of damage between the notches could be seen in each specimen along with

kinking of yarns.

3.5 Split Hopkinson Pressure bar

3.5.1 Methodology

To determine the mechanical properties of the composites at high strain rates, a Split Hopkinson Pressure Bar (SHPB) which is available at the University of Nottingham was used. A schematic of its set-up is shown in Figure 3-32. The loading system consists of an incident bar, a transmission bar and a striker bar. A specimen is sandwiched between the incident bar and the transmission bar. The striker bar is propelled by compressed air and accelerated in a barrel. Its velocity is measured by an infrared light gate placed near the muzzle.

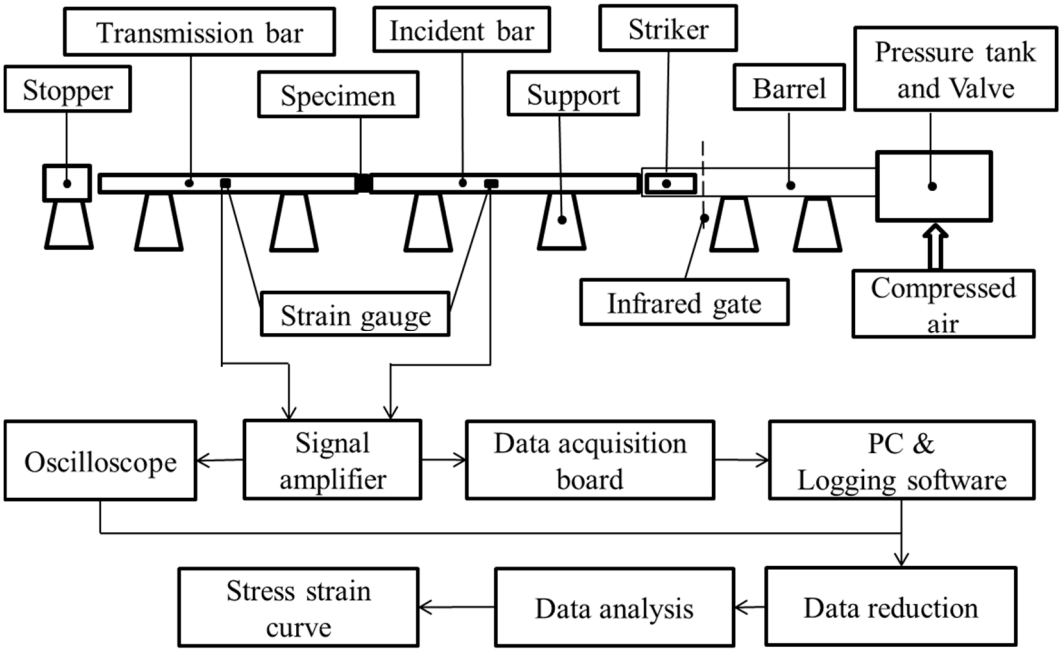


Figure 3-32 A schematic of the compressive SHPB

Basics

The SHPB testing is a well-known material testing technique, which has been documented in numerous sources, hence only the basic principles of this test are covered herein. The detailed description of the SHPB technique can be found for example in [185].

According to the one dimensional stress wave theory, upon the impact between the striker and the incident bar, a compressive stress pulse whose ideal shape is rectangular is generated. Then the stress wave propagates along the

incident bar at a velocity of sound, C_{bar}, defined as:

$$C_{\text{bar}} = \sqrt{E_{\text{bar}}/\rho_{\text{bar}}} \tag{3-8}$$

where E_{bar} and ρ_{bar} are the Young's modulus and density of the bar. The incident strain wave, $\varepsilon_i(t)$, caused by this stress wave is measured and recorded by strain gauges on the bar as a function of time t. The duration of the pulse, Δ, is determined by the length of the striker, L_{striker}, as:

$$\Delta = 2 \times L_{\text{striker}}/C_{\text{bar}} \tag{3-9}$$

The stress wave eventually propagates to the interface between the specimen and the incident bar, where impedance mismatch exist. Only α_1 percent of the incident wave propagates into the specimen while the rest is reflected and propagates backwards in the incident bar. At the interface between the specimen and the transmission bar, again α_2 percent of the wave propagates along the transmission bar. α_1 and α_2 are called transmission ratios. They are numbers ranging from zero to one, zero representing a complete reflection while one represents no reflection and 100% transmission. The can be calculated from the bar and specimen dimensions and properties as follows:

$$\alpha_1 = \frac{2A_{\text{bar}}\,\rho C}{A_{\text{bar}}\,\rho_{\text{bar}}C_{\text{bar}} + A\,\rho C}\%\,,\ \alpha_2 = \frac{2A\,\rho_{\text{bar}}C_{\text{bar}}}{A\rho C\ + A_{\text{bar}}\,\rho_{\text{bar}}C_{\text{bar}}}\% \tag{3-10}$$

where ρ, C, A are the density, sound velocity and cross section area of the specimen.

Theoretically, the product of $\alpha_1 \times \alpha_2$ indicates the amplitude of transmission wave to the incident wave. The strains caused by the reflected stress wave in the incident bar and the stress wave in the transmission bar are denoted as $\varepsilon_r(t)$ and $\varepsilon_t(t)$, respectively.

The general principle of SHPB testing is that the time histories of the strain rate, strain, and stress are determined based on the measured reflected and transmitted strain signals. The strain rate $\dot{\varepsilon}(t)$ and strain $\varepsilon(t)$ of the specimen

are calculated as:

$$\dot{\varepsilon}(t) = 2\frac{C_{\text{bar}}}{L}\varepsilon_r(t) \tag{3-11}$$

$$\varepsilon(t) = 2\frac{C_{\text{bar}}}{L}\int_0^t \varepsilon_r\,(t)dt \tag{3-12}$$

where L is the length of the specimen.

The stress history of the specimen is calculated based on the transmitted strain signal as:

$$\sigma(\text{t}) = \frac{A_{\text{bar}}}{A}E_{\text{bar}} \cdot \varepsilon_t(t) \tag{3-13}$$

Methodology

The photograph of the SHPB apparatus is shown in Figure 3-33. The incident and transmission bars are made of Maraging 300 ultra-high strength steel. Its yield strength is higher than 2000 MPa, the density is 8080 kg/m^3 and elastic modulus is 198 GPa. Both of the bars are 1 metre in length and 25.4 mm in diameter. The steel striker bar is 150 mm in length and 25.4 mm in diameter.

The strain signals were measured by linear strain gauges on the incident bar and the transmission bar. The signals from the strain gauges were magnified by Wheatstone quarter bridges and then recorded by a data acquisition board with 2 MHz of sampling frequency. The magnified strain signals were also displayed and checked on an oscilloscope.

The 3D woven composites were manufactured as flat panels so it is not possible to make disk specimens, which are normally used for testing isotropic materials and sometimes thick laminated composites. The moulded flat panels were cut into samples of 12 mm × 20 mm × composite thickness. Specimens were loaded on the 20-mm-edges and the loading direction was parallel to the 12 mm edges. Two types of samples were made with their weft yarns or warp yarns were aligned to the loading direction respectively. To ensure that the loading surfaces of the specimen are flat and parallel, prismatic specimens were

initially cut by a diamond cutting wheel, and then gradually ground to the final dimensions by using a sample polishing machine and 240 grit sand paper. Prior to testing, RS® High Temperature Grease was applied as lubrication on the specimen/bar interfaces to avoid bulging. The specimens were carefully placed so that their geometric centres were aligned with those of the bars.

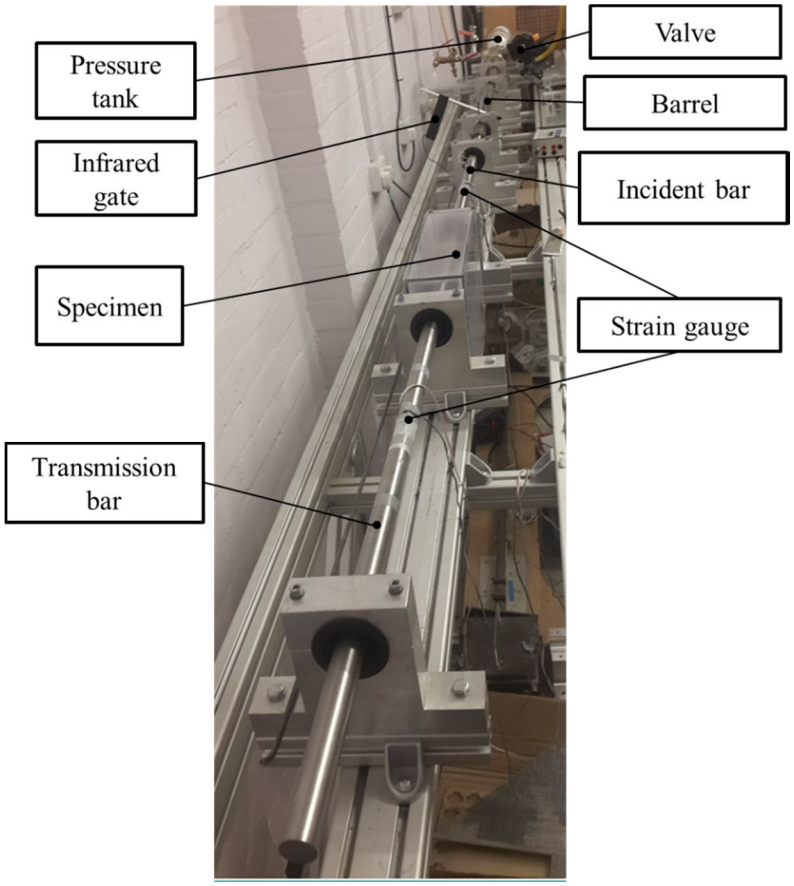


Figure 3-33 A picture of the real compressive SHPB

3.5.2 Results

For different materials and different testing rates, the shapes of the resultant signals share much similarity. Herein, the results of a GF-2 specimen are shown in Figure 3-34 as an example of the typical strain signals captured in the SHPB compression tests. The method of analysing the signals also applies to the other specimens. Given the length and density of the impactor, the duration of the stress wave was approximately 70 μs. As can be seen in Figure 3-34, the incident, reflected and transmission pulses occurred within a 400 μs time span. To capture an event of such short duration, the data acquisition was set to be triggered by the signal of the strain gauge on the incident bar. Because of that, the very beginning of the incident pulse was not recorded. Following the incident pulse,

there were signal fluctuations of ±0.5V. This causes an uncertainty in defining the beginning of the reflected pulse signal. In this study, its zero point on the rising slope is regarded as the beginning. On the other hand, the noise level on the transmission bar was very low before the transmission pulse, hence determining its beginning was relatively straightforward. With the reflected and the transmission pulse measured, the strain rate, strain and stress histories were calculated. These are shown in Figure 3-35 (a), (b) and (c), respectively.

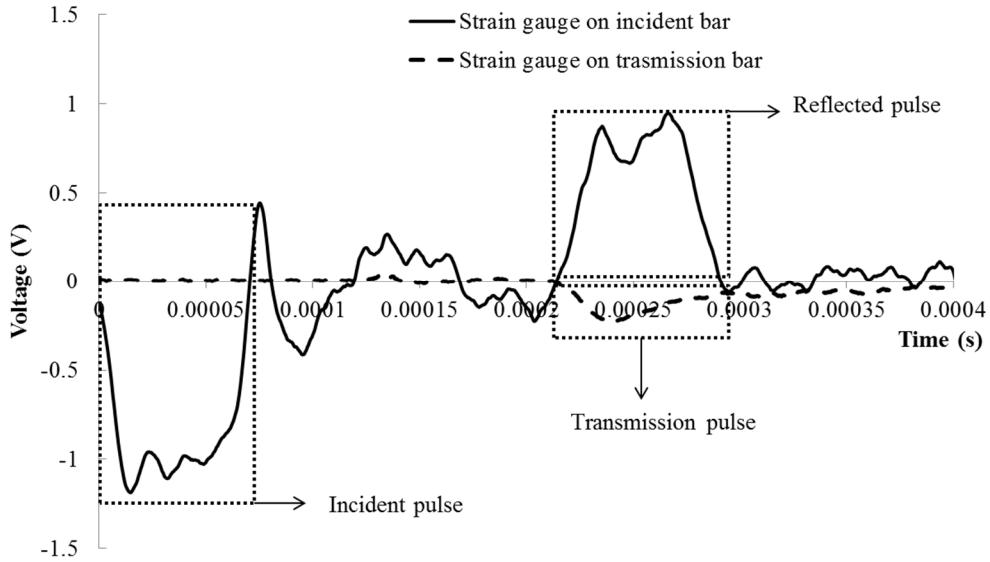


Figure 3-34 Typical shapes of the magnified strain gauge output signals of the SHPB compression test. This figure shown the results of a GF-2 specimen.

As can be seen in Figure 3-35 (a), there are small oscillations in the stain rate history following the initial period of increase. This corresponds to the period from 200 to 650 μs in Figure 3-35 (b), over which the strain increased almost linearly. The average strain rate of 1236 /s over this period is regarded as a nominal constant strain rate in the test considered. Over this time period, the stress also reached its maximum, as can be seen in Figure 3-35 (c), and this is regarded as the compressive strength of the composite at the constant strain rate of 1236 /s.

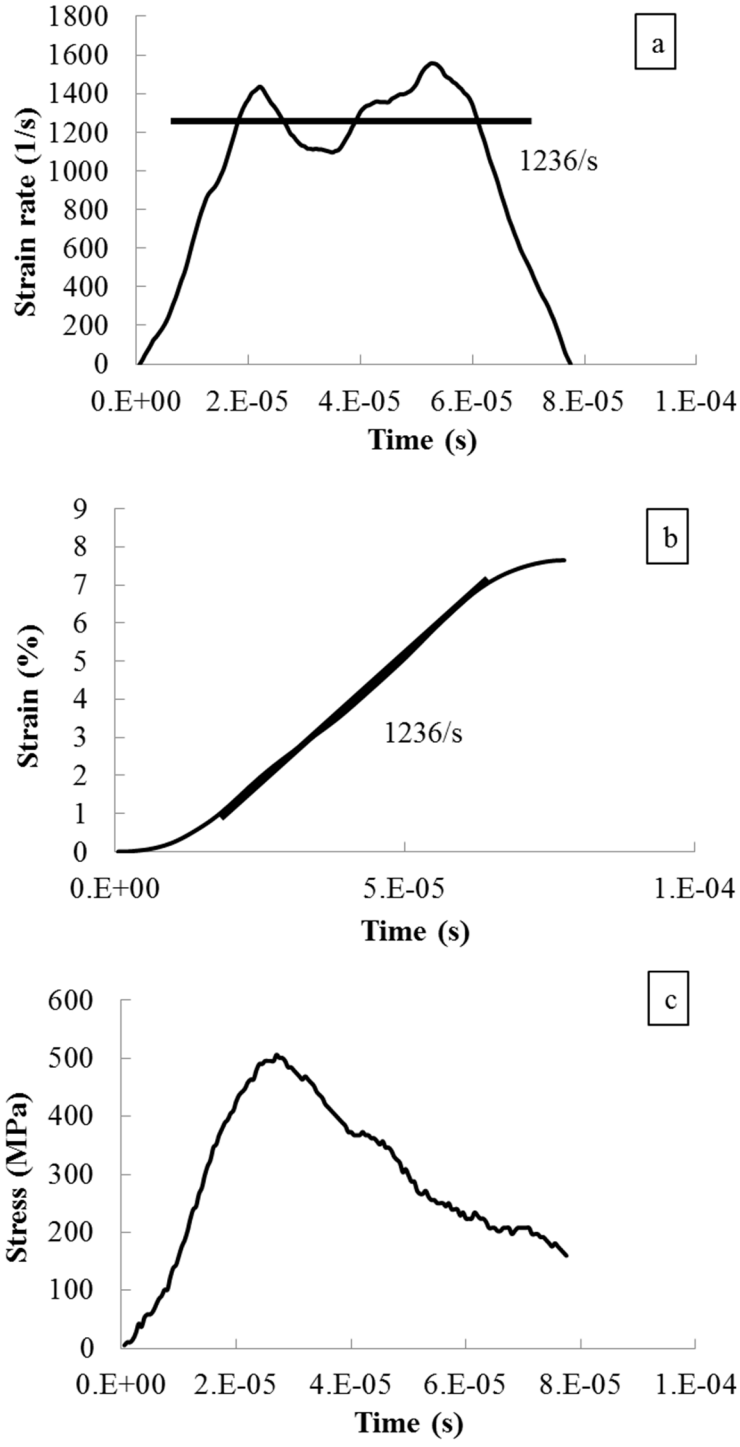


Figure 3-35 (a) Strain rate history, (b) Strain history and (c) Stress history of extracted from Figure 3-34 for the GF-2 specimen. These are the typical shapes of the results of all the tested compression specimens.

There is an issue when plotting a stress-strain curve based on the strain and stress histories as determined in the test. Because of the indirect measurement of stress and strain in the SHPB tests, accurately synchronising these two is not straightforward. In addition to that, uncertainty in determining the exact origin of the reflected pulse, which has been mentioned above, may result in an

additional error when plotting the stress vs the strain. Figure 3-36 is an example of the stress-strain curves for GF-1 obtained by cross plotting of the stress histories and the strain histories. In both cases, at high strain rates, the measurement of the elastic moduli is rather challenging, as the curves are generally non-linear. On the other hand, the increase in the material strength with strain rate is apparent for both warp and weft loading directions. The same conclusions can be made when analysing the experimental data for GF-2 and CF-IM7 composites.

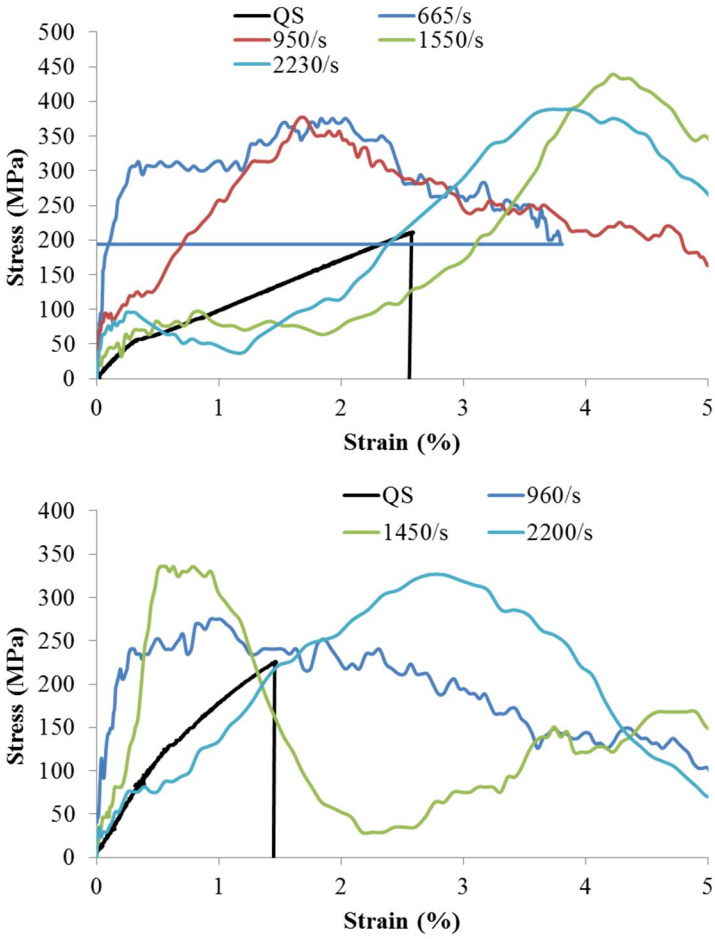


Figure 3-36 The stress-strain curves of compression test on GF-1 in weft (top) and warp (bottom) using SHPB.

To determine the elastic moduli at the various strain rates and subsequently quantify the rate dependence of the composite stiffness, it is crucial that the linear stiffness is measured at a constant strain rate. However, the nominal constant strain rate was achieved at the strain values above 1% of compressive strain, when the response of the material was no longer elastic. In other words, while the material deformed elastically, the strain rate was still increasing hence cannot be considered as a constant.

Due to the difficulties in finding valid dynamic moduli using SHPB, in this study only strain rate dependency of strength is reported. The empirical relation implemented in MAT162 material model [111] of LS-DYNA for strain rate effects is employed, i.e. a natural log relationship. The QS strain rate $\dot{\varepsilon}_0$ =5.56 $\times 10^{-4}$/s and the corresponding strength, S_0, are used as the reference values, together with the SHPB rates, $\dot{\varepsilon}$, and strengths, S_{RT}, to determine the scaling factor C_{rate},.

$$\frac{S_{\mathrm{RT}}}{S_0} = 1 + C_{\mathrm{rate}} \cdot ln\frac{\dot{\varepsilon}}{\dot{\varepsilon}_0} \tag{3-14}$$

The strength ratio in Eq. (3-14) is plotted against the logarithm of strain rate ratio in Figure 3-37. The data points are fitted linearly by least squares method and then the gradient is the strain rate scaling coefficient C_{rate}. The scaling factors for GF-1, GF-2 and CF-IM7 are summarised in Table 3-8. The results of SHPB become closely spaced cluster in this plot, although the actual strain rates vary from several hundred per second up to three thousand per second. For this reason, there is no much statistical value in having several repeats.

Table 3-8 The scaling factors for strength.

Material	Coefficient for weft strength	Coefficient for warp strength
GF-1	0.0686	0.0527
GF-2	0.0387	0.0592
CF-IM7	0.0503	0.121

The goodness of the linear fitting is also indicated in the figures, with respect to the squared regression coefficient. In contrast with the good fitting for GF-1 and GF-2, the CF-IM7 results are scattered. The unit cell sizes of all the three composites are about 9 mm. Given the SPHB specimens are uniformly 20 mm in width, there is still chance that the specimen only covers one unit cell. For CF-IM7, the difference between having one unit cell and two unit cells can be significant due to the superior mechanical properties of carbon fibres, while

the difference can be much less for those with glass fibres.

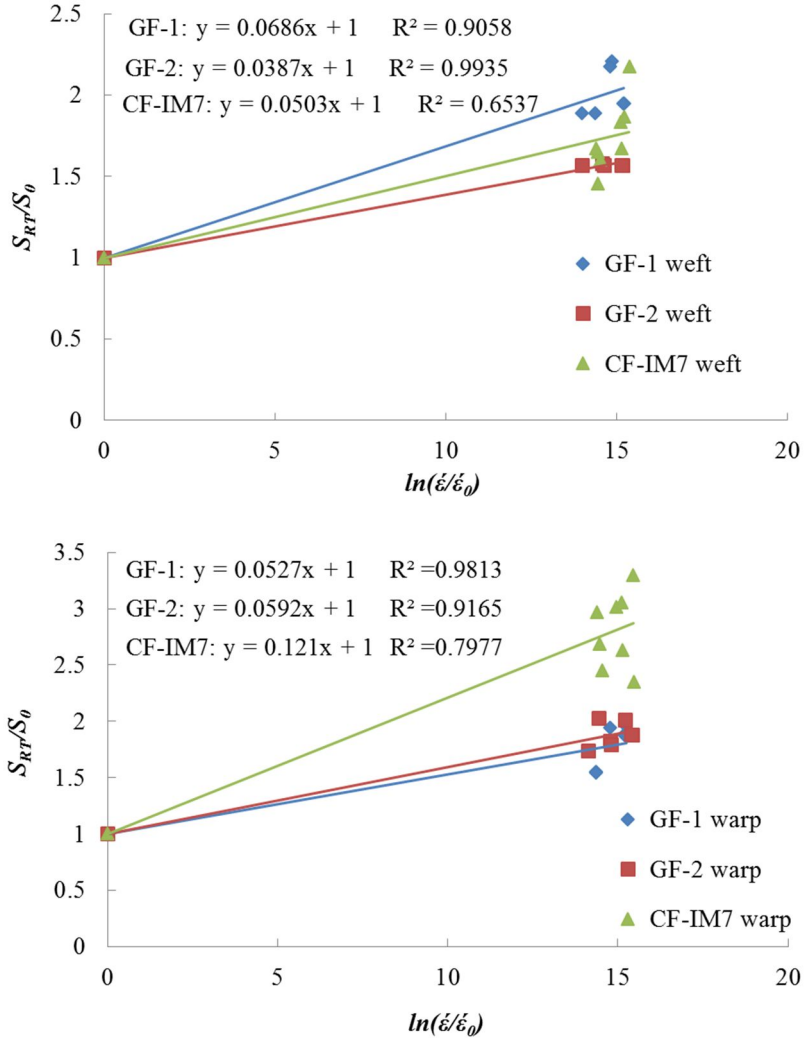


Figure 3-37 The strain rate effect on the weft (top) and the warp (bottom) compression strength for the three composites.

The typical failure modes for the composites in the SHPB test can be seen in the photographs of tested GF-2 specimens in Figure 3-38 (a) and (b). In the weft direction, the failure is due to buckling of the straight yarns around the interface to the bars. At the strain rate of 657 /s, the yarns slightly buckle towards the free surfaces. At high strain rates, the buckling becomes more pronounced. When the rate is 2098 /s, the buckling leads to the brooming pattern at one interface of the specimen.

In the warp specimens, crimped yarns do not take much compressive load but the resin does. After the load exceeds the compressive strength, matrix cracks and debonding develop along the warp path. Warp yarns are also further crimped by the compressive load. These happened at 748 /s, but higher strain

rate made the failure more apparent. At 2777 /s, the separation of yarns from matrix and the increase in the specimen thickness due to further yarn crimping are evident.

These failure modes resemble those under QS compression, namely the fibre kinking of weft specimens and the debonding of warp specimens. They were observed in the GF-1 composite, which has the same reinforcement material as GF-2, and also in the CF-IM7 specimens as shown in Figure 3-38 (c) and (d).

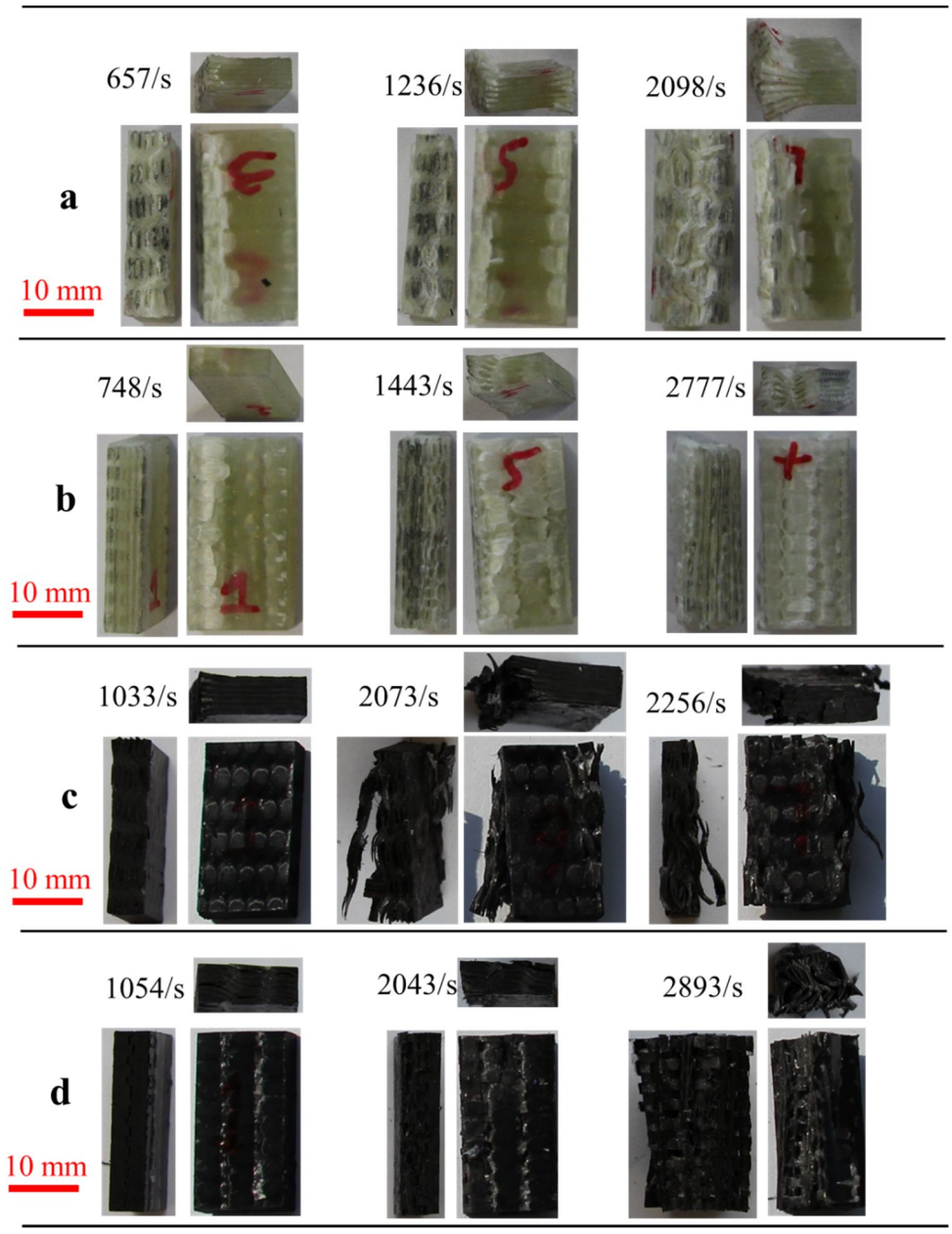


Figure 3-38 Tested SHPB specimens of (a) GF-1 weft, (b) GF-1 warp, (c) CF-IM7 weft and (d) CF-IM7 warp at different strain rates.

3.6 Conclusions

In this chapter, the characterisation of four types of 3D woven composites under quasi-static in-plane tensile, compressive and shear loading conditions is reported.

The tension test reveals that the tensile properties in both the weft and warp direction are positively related to the properties of the fibres and the volume fraction of yarns. Considering strain energy density as an indicator of energy dissipation capability, CF-IM7 outperforms the others. By microscopic observation on specimens loaded to different levels of strain, it was found that, after the initial linear elastic behaviour, debonding and matrix cracks take place, leading to degradation of stiffness.

The compressive properties, however, show little correlation with the fibres and yarn volume fractions, except for the weft compressive strength. The compressive stress-strain curves are generally linear until the maximum strength, where specimens essentially failed as through-thickness shear via fibre kinking for the weft compression or via connection of debondings for the warp compression. Significant load carrying capability remains after the failure and should be taken into account in any simulation.

Two methods, namely 45° off-axis tensile shear and two-rail shear were used for testing the in-plane shear behaviour. No major difference was found between the shear moduli measured by these two methods, or between the measured 0.2% offset strength values. All the curves are initially linear but become non-linear later on. Due to the dominance of matrix in the in-plane shear behaviour, there is little difference among the four types of composites in terms of shear moduli and the offset strengths. Fracture only happened in the glass composites in the directions transverse to the weaker yarns, i.e. the weft of GF-1 and the warp of GF-2. Yarn rotation takes place in the other specimens and makes the tests little representative of a pure shear state at later stages of the tests.

Dynamic compression by using SHPB was carried out to establish the strain rate dependency of GF-1, GF-2 and CF-IM7. The strain rate dependency is established for compressive strength, but not for modulus, which cannot be reliably measured due to the nature of this test. Also, the failure modes of the SHPB specimens resemble those under QS compressive loadings, namely fibre

kinking in the weft compression specimens, and debonding and further crimping in the warp specimens.

Chapter 4 Ballistic impact tests on the 3D woven composites

4.1 Introduction

In this project, the performance of GF-1, GF-2 and CF-IM7 under high velocity impact was studied by ballistic impact tests, relevant to the application in aero engine fan casings for containing high velocity debris during FBO. A gas gun apparatus, which was recently designed and built at the University of Nottingham, was used for this study. In this chapter, the set-up of the ballistic impact tests is described and the results are analysed in terms of ballistic limit. Failure and damage which were examined by using X-ray computed tomography (XCT) and visual inspection are also presented.

4.2 Set-up of ballistic impact tests

The schematic of the ballistic impact test set-up is shown in Figure 4-1. The gas gun consists of a 3.5-metre-long gun barrel of 13 mm inner diameter, a pressure tank where either compressed air or nitrogen can be stored, and a high speed valve which is triggered to release the pressurised gas into the barrel. The projectiles are steel ball bearings of 12.7 mm in diameter. The ability to fire other shapes of projectiles has not been established yet as it requires sabot and sabot-stripping mechanisms. Prior to the test, the projectile was loaded to the bottom of the barrel. The projectile was accelerated by the gas in the barrel, which was pointing to the centre of the target plates, normal to the surface of the target.

The muzzle was approximately 0.2 m away from the target. Given the impact velocities in this study being larger than 100 m/s, the vertical velocity and displacement due to gravity can be considered negligible. A sand bag fixed right behind the target was used as a projectile catcher in cases where the target was penetrated. The impact region was placed inside a polycarbonate box so that the projectile could be contained when it rebounded. The photograph of the gas gun is shown in Figure 4-2.

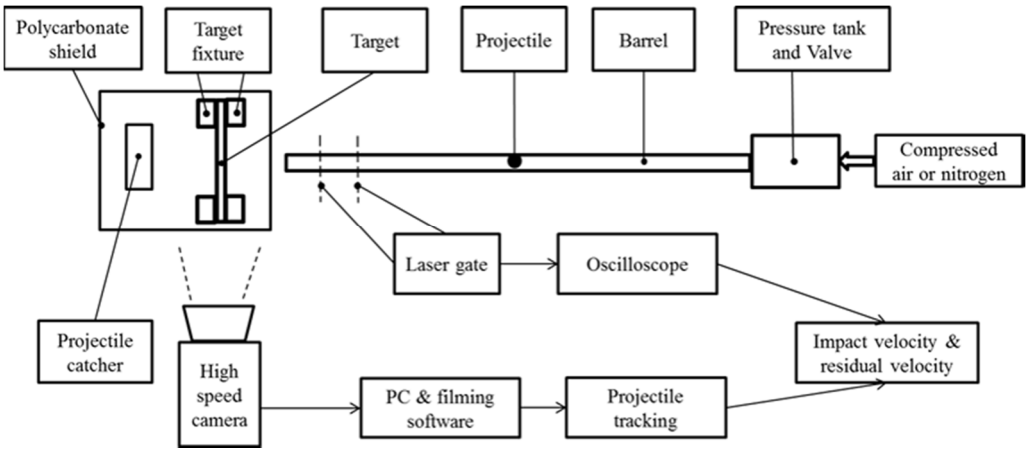


Figure 4-1 A schematic of the set-up of ballistic impact test.

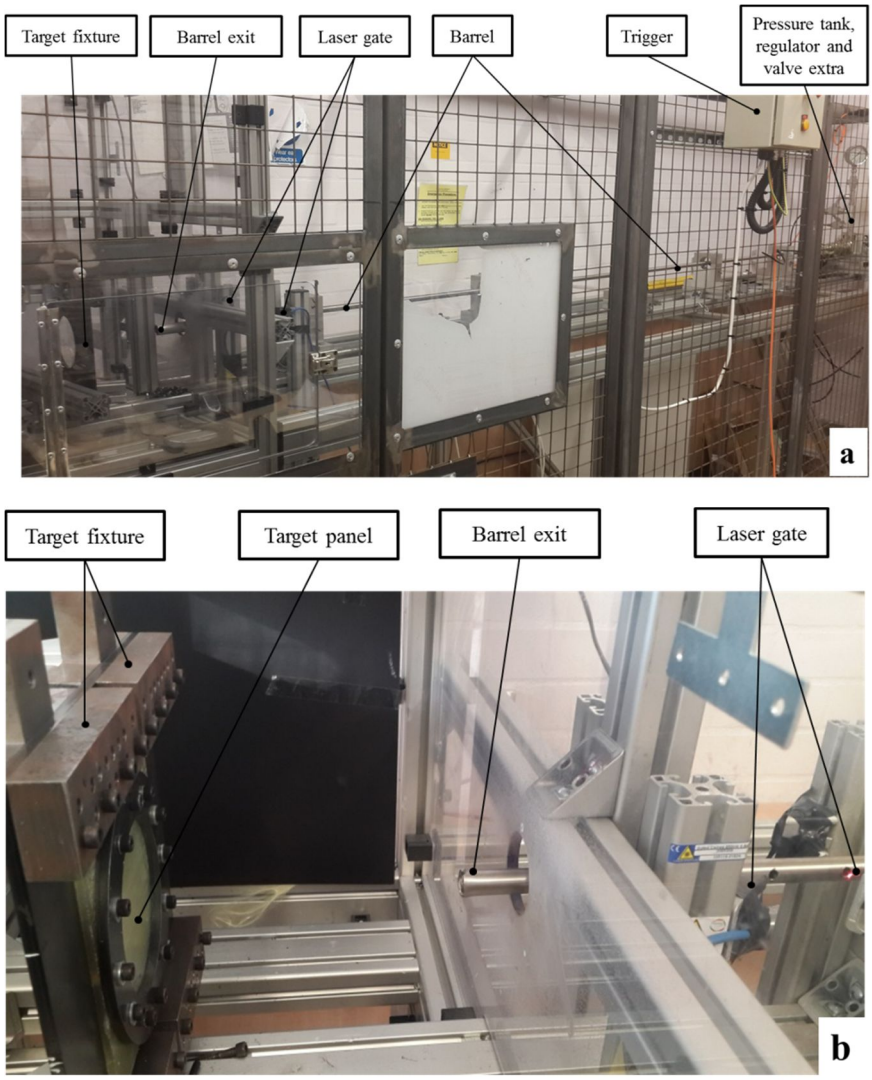


Figure 4-2 Photographs showing (a) the gas gun apparatus and (b) the target with the fixture, the exit of gun barrel and the laser gates.

In the vicinity of the muzzle, two laser gates were placed 10 cm away from each other to provide approximate but instant measurement of the projectile

velocity using an oscilloscope. A Phantom high speed camera along with two Dedocool focused lights was used to film the entire impact process. By this method, the video needs to be processed first to determine the velocity. A discrepancy of about 15% was found between the velocity results of the oscilloscope and the camera. The results from the oscilloscope are considered to be less accurate, as there are two potential sources of error. Firstly, it was found that the fixing mechanism of laser gates failed to firmly secure their positions and the laser gates quivered when the projectile was fired. Repositioning and realignment were sometimes needed. In addition to that, a metal tube was placed at the muzzle to protect it from being damaged by a rebounding projectile. Interaction between the protector and the projectile may alter the velocity, hence there could be a discrepancy between the projectile velocity values in the barrel (measured by the laser gate), and those after exiting the barrel.

Since the projectile travelled over a distance in the air, an assessment was made whether the air drag was a reason for the discrepancy. The deceleration of the projectile, *a*, due to air drag, *D*, is calculated as:

$$a = D/m = \frac{1}{2} C_d V^2 A/m \tag{4-1}$$

where *m* is the projectile mass, *V* is projectile velocity, *A* is the projected frontal area of the projectile, which essentially is a circle, C_d is the drag coefficient and usually determined experimentally. An empirical correlation for a sphere is reported in [186] as:

$$C_d = \frac{24}{Re} + \frac{2.6 \times (\frac{Re}{5})}{1 + (\frac{Re}{5})^{1.52}} + \frac{0.411(\frac{Re}{263000})^{-7.94}}{1 + (\frac{Re}{263000})^{-8}} + (\frac{Re}{461000}) \tag{4-2}$$

Re is the Reynolds number defined by:

$$Re = \frac{Vd}{\nu_k} \tag{4-3}$$

where ν_k is the kinematic viscosity of air, which is related to temperature, e.g. 1.34×10^{-5} m^2/s at 0 C° and 1.53×10^{-5} m^2/s at 20 C° [187], and d is a characteristic length. The velocity changes over 1-metre flying in air at different impact velocities are listed in Table 4-1. These calculations confirmed that air drag has little effect on the velocity of the projectile after it exits the barrel.

Table 4-1 The velocity changes over 1m of flying at different impact velocities.

Impact velocity V (m/s)	ΔV at 0 C°(m/s)	ΔV at 25 C° (m/s)
50	0.183	0.182
100	0.382	0.378
150	0.589	0.584
200	0.765	0.786
250	0.766	0.924

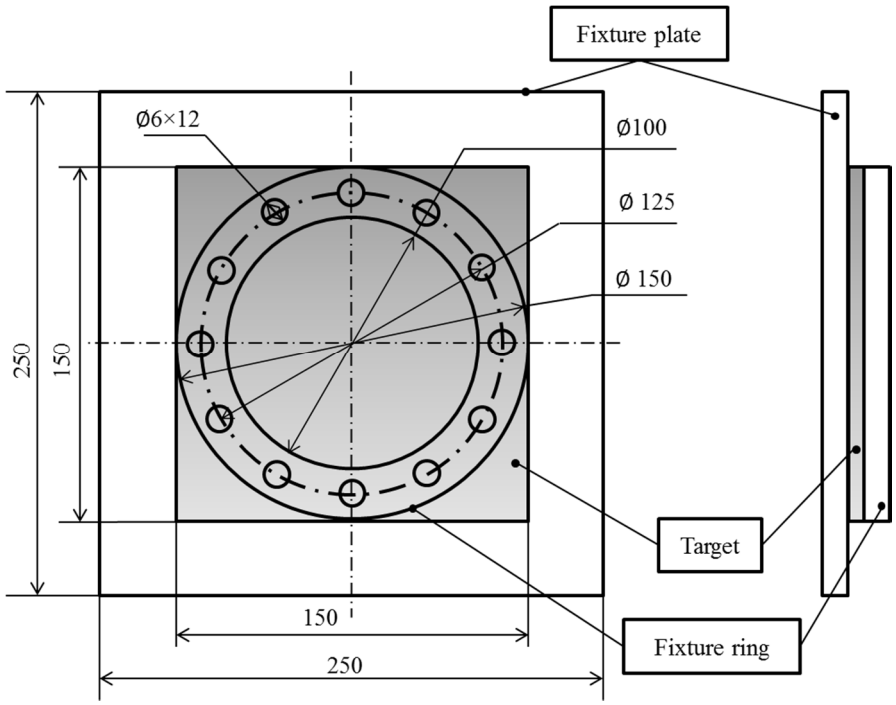


Figure 4-3 A schematic of the target with the fixture and their dimensions.

The target is a 150 mm×150 mm square composite plate, clamped to expose a 100-mm-diameter circular area to the impact. A steel fixture, 250 mm × 250 mm square plate, with a circular cut-out of 100 mm in diameter, was fixed to the testing platform along upper and lower edges as shown in Figure 4-2 (b). The composite plate was placed between the fixture and a steel ring of 100 mm in inner diameter and 150 mm in outer diameter as schematically shown in Figure

4-3. Both the fixture and the ring were 6.35 mm thick. Twelve Ø6 mm holes are drilled through the target, the fixture plate and the ring. And the entire target fixture was tightly bolted together using twelve M6 bolts.

Apart from the three 3D woven composites, a batch of IM7 laminated plates were also tested under the ballistic impact for comparison purpose. The plates are made from unidirectional HexPly® IM7/8552 prepreg provided by Hexcel [188]. 32 plies of the prepreg were laid up in a quasi-isotropic manner $[0/\pm45/90]_{s4}$ and then cured at elevated temperature in an autoclave following the curing schedule recommended by the provider [188]. The thickness of the cured plates is 4 mm, similar to those of the 3D woven composites. The plates were then cut and prepared in the same way as the 3D woven composites.

4.3 Data acquisition and processing



Figure 4-4 One frame of a video showing the impactor before hitting the target.

Each impact test was recorded by the high speed camera as a video file, which also included information as to how many frames were taken per second. The impact and residual velocities of the ball were obtained by processing the video file. The analysis of videos is performed in a tracking software Tracker V4.87 [189]. The analysis of a video file followed these steps:

1) Based on the frame rate as recorded in the video files, the time intervals between the frames were determined. As an example, a single frame of a video file is shown in Figure 4-4. At the bottom of

the image the frame rate of 45016 frames per second is specified.

2) The dimensions are calibrated with respect to the dimensions that are known. The diameter of the projectile of 12.7 mm is chosen, as shown in blue in Figure 4-4.
3) Next, the position of the projectile, as coordinates in each frame, is determined by tracking the point on either the leading or the trailing "edge" of the ball. The horizontal coordinate of the projectile is plotted versus time as shown in Figure 4-5.
4) Finally, the velocity was determined by calculating the gradient of the linear-fitting curve of the plot.

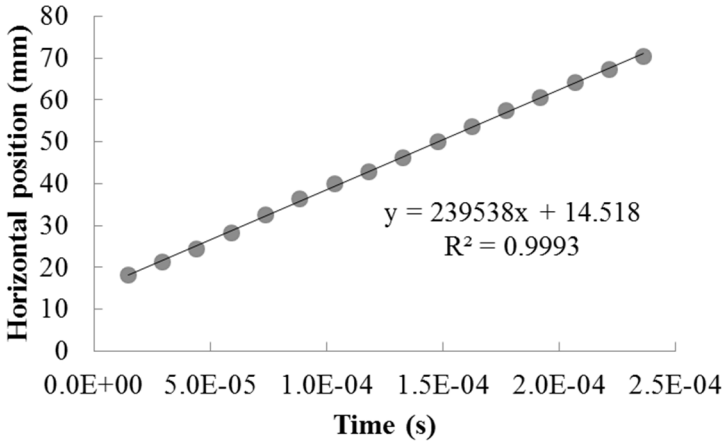


Figure 4-5 A graph showing the projectile position as a function of time as obtained by processing the video file. The determined velocity is 240 m/s and the squared regression coefficient is 0.9993.

As mentioned above, the air drag to the projectile is calculated and found to have negligible effect on the projectile velocity. The data points fit very well with a linear curve, indicating a constant velocity. The regression coefficients of these fitting curves are commonly larger than 0.99.

4.4 Experimental data and analysis

4.4.1 Impact velocity data analysis

The experimental data in terms of impact and residual velocities are summarised in Table 4-2. The negative velocity values indicate those cases where the projectile rebounded. The test at each speed was not repeated due to firstly limited material quantity but more importantly to the lack of mechanism for accurate velocity control. At the moment, the only way is by controlling the pressure with a pressure meter which is only capable of rough regulation. Under

the same pressure, the velocity can vary by 10-20 m/s. Before any accurate velocity control is available, it is impractical to have several repeats at the same velocity.

Table 4-2 The ballistic impact results in terms of impact velocity (V_i) and residual velocity (V_r).

Test	GF-1		GF-2		CF-IM7		QI-IM7	
No	V_i, m/s	V_r, m/s	V_i, m/s	V_r, m/s	V_i, m/s	V_r, m/s	V_i, m/s	V_r, m/s
1	245*	175	256	146	290	221	247	205
2	237	159	232	156	291	254	240	210
3	228	110	236	133	281	265	205	162
4	192	103	234	128	227	165	164	93
5	176	48	222	79	226	181	138	33
6	159	-58	199	77	202	138	88	-31
7	132	-54	183	75	181	112		
8	105	-52	171	37	163	46		
9			166	-68	151	41		
10			149	-66	135	-58		
11					131	-59		
12					125	-56		
13					105	-55		

*The underlined tests are simulated in Chapter 5.

4.4.2 Statistical analysis of ballistic impact test data

A commonly used indicator of impact resistance is the limit velocity V_{50}, at which the projectile penetrates the target at least 50% of the time. Should this value be determined experimentally, a large number of tests at impact velocities close to V_{50} would be required. To save material and effort in determining V_{50}, interpolation or extrapolation is often applied as is the case in this work. Specifically, the Jonas-Lambert equation [190] is commonly used for this purpose. It is expressed as

$$V_r^p = \beta^p (V_i^p - V_{50}^p) \tag{4-4}$$

where V_r and V_i are the residual and initial velocities, β and p are the parameters, and V_{50} is the critical velocity, which is also a parameter of the fitting function.

This expression only defines the dependence between the residual and initial velocities in cases where the penetration takes place, hence it is not applicable for describing the rebounding of the projectile.

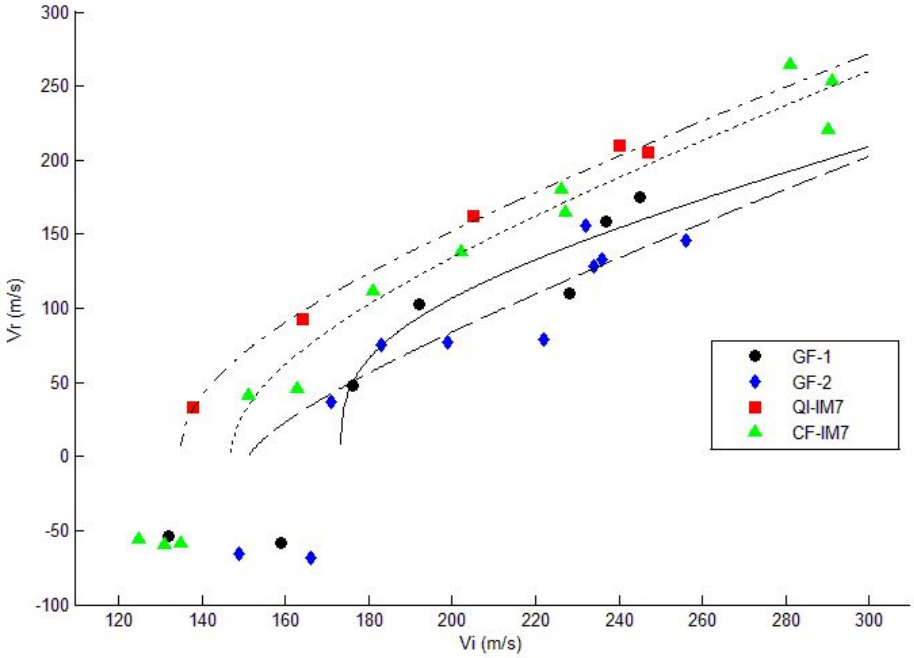


Figure 4-6 Ballistic impact test data fitted with Jonas-Lambert equation for four composites.

Table 4-3 The fitting parameters and their standard error.

	V_{50}		β		p	
	Value	Standard error	Value	Standard error	Value	Standard error
GF-1	173.396	9.326	0.741	0.288	3.139	3.512
GF-2	151.367	60.891	0.971	1.168	1.370	2.073
CF-IM7	160.922	4.013	0.918	0.109	2.840	1.151
QI-IM7	134.036	3.291	1.033	0.101	1.961	0.404

The nonlinear curve fitting was applied to determine V_{50}, β and p in the Curve Fitting Toolbox of MatLab 2013. The values and standard errors of the parameters are summarised in Table 4-3. Fitting curves are shown along with the experimental data from the ballistic impact tests in Figure 4-6.

It is worth noting that the standard error for V_{50} for GF-2 is very large, which indicates that the fit was not reliable. Specifically, as be seen in Table 4-3 and Figure 4-6, the fitted line suggests the perforation of the target in a range of

velocities from 149 m/s to 166 m/s, where projectile rebounding was captured experimentally. For GF-1, one of the parameters, *p*, has a large error, which also suggests that the fit was rather inaccurate. On the other hand, for CF-IM7 and the QI laminate the standard error values are reasonable for all the fitting parameters, hence it is fair to say that the fitting functions for these two materials represent the experimenal data with a sufficient accuracy.

To facilitate the explanation as to how the errors in fitting parameters are related to the quality of the fit, prediction bands were computed as shown in Figure 4-7 as dashed lines. They enclose an area which a new test should be in with 95% probability. The wider are the prediction bands, the larger are the errors in the fitting parameters. As can be seen, for GF-2 and GF-1 composites the prediction bands are wide. This suggests that the fit is generally unreliable, in particular, for GF-1 composite, where the prediction bands are the widest because of the standard error of the exponent *p*, which was largest for GF-1 as compared with all the other composites. The uncertainty in definition of a fitting curve in these two cases arises primarily from the scatter of the experimental data based on which fitting function was calculated. Therefore, the prediction bands also serve as an indication of the scatter of the testing results.

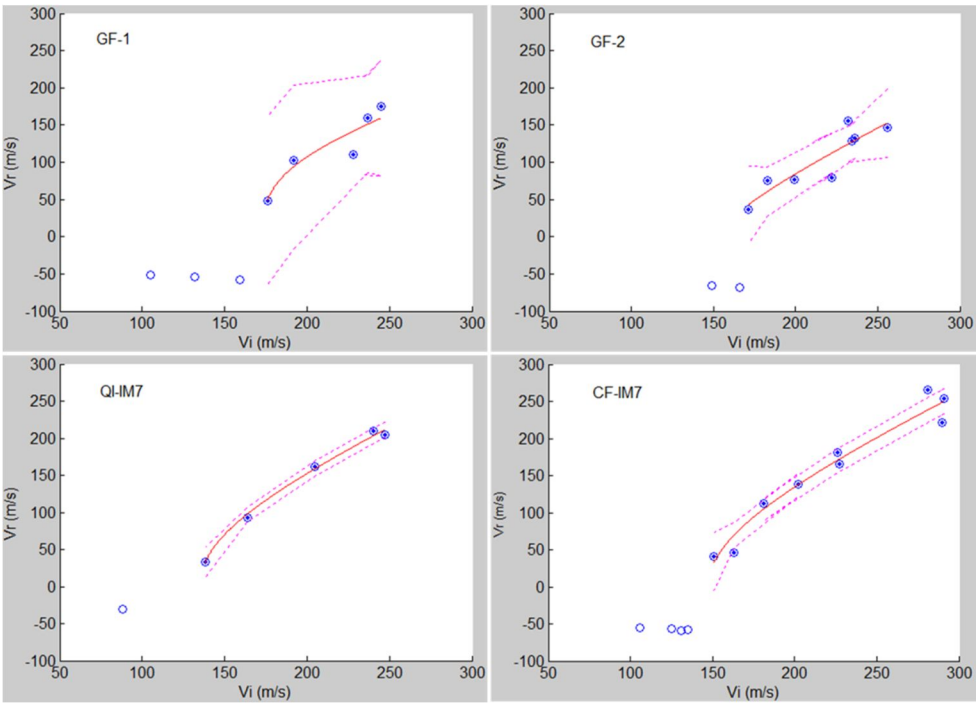


Figure 4-7 Prediction bands of the fitting functions of ballistic impact test data for the four materials.

On the other hand, the fitting curve for the CF-IM7 composite was

constructed based on a similar number of data points as that for GF-2. However, the scatter of the data points is substantially smaller, hence the data fit is much more precise. As can be seen in Figure 4-7, the prediction bands are narrower, and are generally aligned with the fitting curve.

Finally, for QI laminates the fitting curve was calculated based on only five data points, as in the GF-1 analysis, however, there is a substantially lower scatter in the data, and the fit is reasonably precise. The prediction bands are narrow in this case.

It can be concluded that the limit velocity can be estimated reasonably accurately based on the ballistic impact data on CF-IM7 textile composite as well as QI laminates. The ballistic limit estimates for GF-1 and GF-2 are generally unreliable due to a large scatter of the experimental data. A larger number of the tests are required in order to obtain reasonable estimation of limit velocities for these materials.

4.4.3 Comparison of ballistic resistances of the four composites

Despite the poor fitting, it is possible to make a rough assessment on the impact performance of GF-1 and GF-2 based on the experimental data available. Comparing the experimental data in Figure 4-6, it is easy to see that the residual velocities for these two materials are lower than those for CF-IM7 and QI laminate, which indicates that they can dissipate a larger amount of energy during the impact, hence should have a higher impact resistance. As reference values for the critical velocity, the V_{50} = 173 m/s, as was determined by fitting the experimental data, was assumed for GF-1 composite. For GF-2, although the estimated value for V_{50} has a very large standard error, it can be seen in Figure 4-6, most of the GF-2 points are located to the right of the GF-1 ones. This indicates that GF-2 possibly requires a larger impact velocity than GF-1 to achieve the same level of residual velocity. In other words, the ballistic limit of GF-2 is higher than GF-1. Hence in this study, V_{50} = 180 m/s, was chosen as a reference value for GF-2. The ballistic limits for all four composites are summarised in Table 4-4.

The limit velocities, as well as the Lambert extrapolating curves, lead to the same conclusions about the impact resistance. The QI-IM7 laminates has the lowest resistance to impact. If it is used as a baseline, then when the IM7 fibres

are woven into the 3D reinforcements, the limit velocity is increased by about 20% and its corresponding energy is increased by 44%. The weaving process introduces reductions in the in-plane properties, but improvement in the through-thickness properties as well as delamination resistance which lead to an increased impact resistance.

Table 4-4 Ballistic limit V_{50} of the four composites.

	GF-1	GF-2	CF-IM7	QI-IM7
V_{50} (m/s)	173	180*	161	134
Normalised energy[1]	169%	180%	144%	100%
Normalised energy[2]	132%	141%	134%	100%

1. The kinetic energy at the ballistic limit is normalised to the one of QI-IM7.
2. The normalised energy is further normalised to the densities of the plates

The resistance of the glass fibre composites seem to be higher than the carbon fibre composites. For GF-1 and GF-2, the energies derived from the ballistic limits are 69% and 80% higher than the baseline respectively. However, glass fibres are known to have larger density than carbon fibres. The plates in this study have similar thickness, hence the glass plates are heavier. If the above energies are normalised to the densities of the plates, the glass composites GF-1 and GF-2 show almost the same impact resistant as the carbon composite CF-IM7.

4.5 Damage and failure after the ballistic impact

4.5.1 Visual inspection

The internal damage due to impact can be visually observed only for the semi-transparent glass composite plates. As an example, Figure 4-8 shows the back face of a GF-2 plate penetrated at 256 m/s, where four types of failure and damage can be observed, in addition to the obvious modes of crushing and fibre breakage at the impact centre. The red lines were drawn prior to impact to find the centre of the plate. They are irrelevant to the following observation.

The damaged weft yarns, as shown by Figure 4-8 (a), are more opaque than the intact ones. They extend far from the impact point and nearly to the circular periphery in this particular case, due to the stretching by the projectile during

the impact. The warp yarn damage in Figure 4-8 (b) is mainly localised to the impact centre, as crimped warp yarns do not transfer much of the stretching loading.

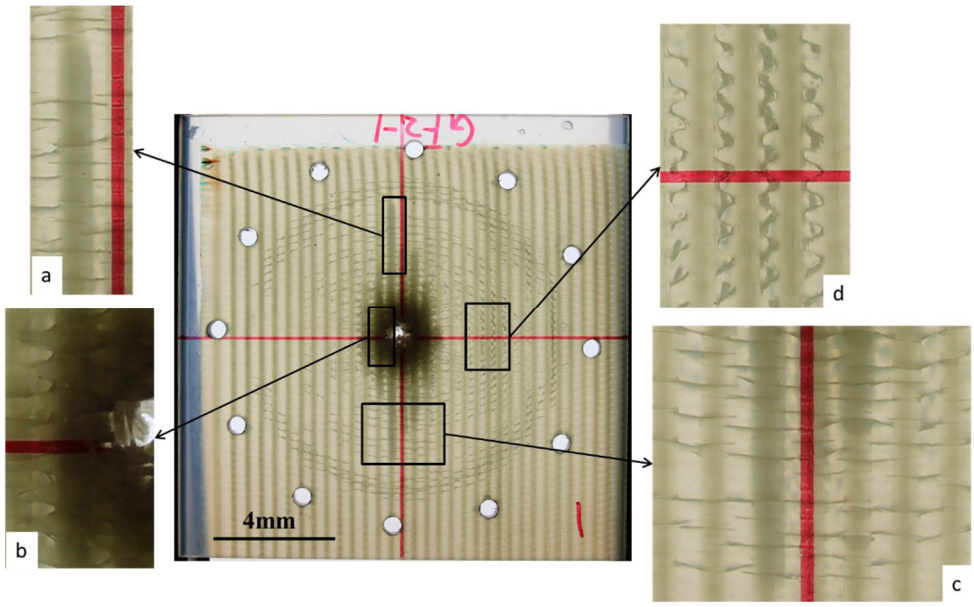


Figure 4-8 A penetrated GF-2 plate with four damage modes: (a) weft yarn debonding from matrix, (b) warp yarn damage in the vicinity of impact, (c) matrix cracks normal to weft yarns and (d) wavy pattern of warp yarn debonding from matrix.

Two types of matrix damage took place at various locations of the plate. The damage in Figure 4-8 (c) resembles matrix cracks found in the quasi-static tensile test in the weft direction, where the cracks are normal to the weft yarns. Wavy patterns of debonding in resin rich regions around the superficial layers of warp yarns, as shown by Figure 4-8 (d), are found as the other matrix damage mode. These two damage modes spread over the target, even for the impact in Figure 4-8, which tends to be a localised event as the impact velocity is well above the ballistic limit. A circular region of cracks of both types is also found around the periphery.

These damage modes are commonly observed in all the tested glass fibre plates, visible from both front and back faces of the impacted plates, although the extents differ. As examples, Figure 4-9 shows three plates of GF-1 tested at 159 m/s, 176 m/s and 237 m/s, along with another three of GF-2 impacted at 149 m/s, 199 m/s and 256 m/s. Note that the limit velocities are 173 m/s and 180 m/s for GF-1 and GF-2, respectively. The damage of weft yarns in the centre of the panel appears to be more extended in GF-2 than in GF-1, indicating the denser weft yarns of GF-2 took more part in resisting penetration than those of GF-1.

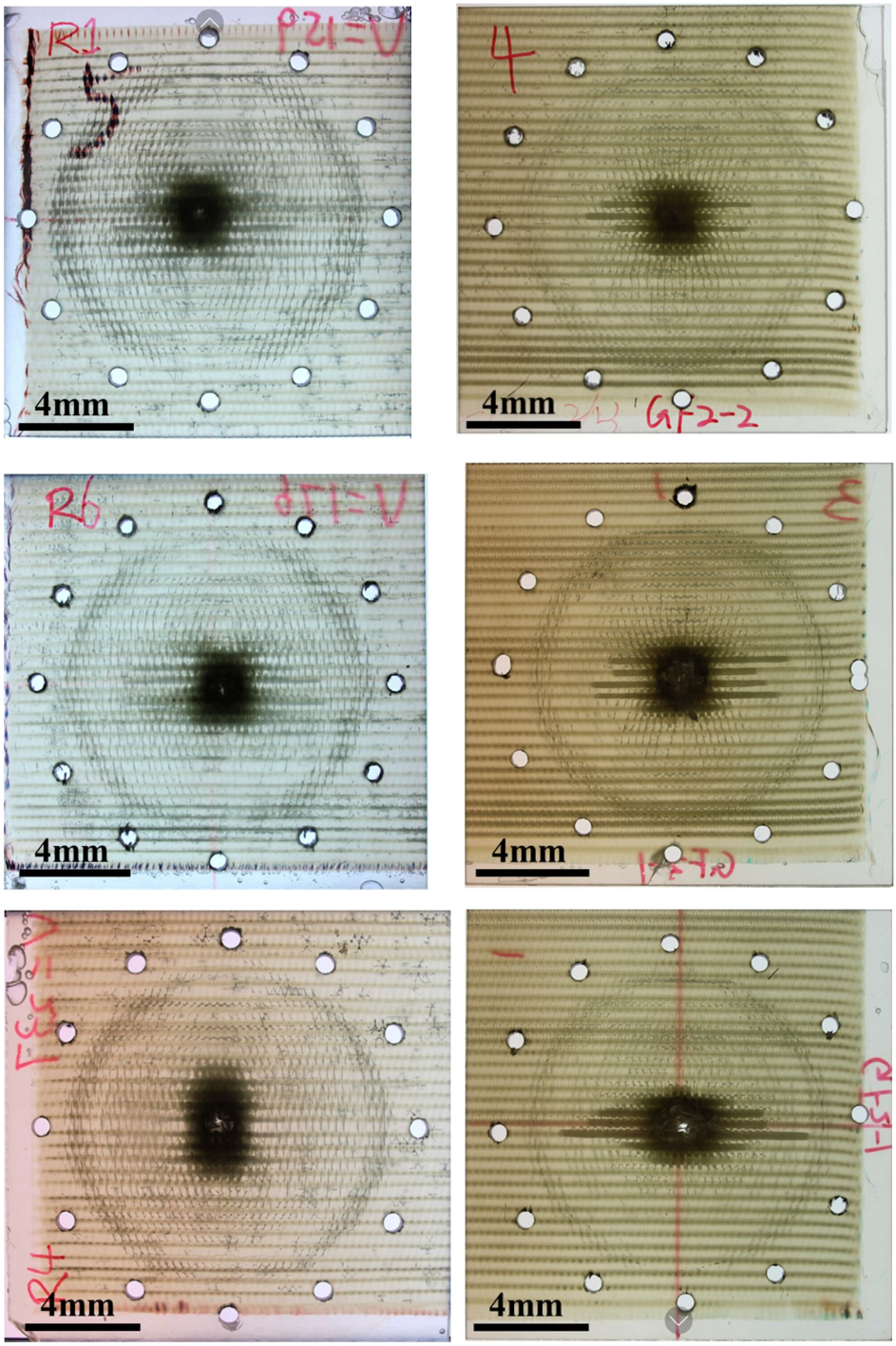


Figure 4-9 The plates of GF-1 impacted at 159 m/s, 176 m/s and 237 m/s on the left column; The plates of GF-2 impacted at 149 m/s, 199 m/s and 256 m/s on the right column. All is viewed from the back face of impact.

Since the extensive damage in the plates occurred in all the impact cases, an effort was made to quantify the extent of damage within the plates. Image processing software ImageJ [191] was used for this purpose. The digitised images of the panels in Figure 4-9 were converted to greyscale images. The damaged regions of the plate are darker than the intact regions, as can be seen in

Figure 4-10 (a). It is worth noting, however, that the internal structure of reinforcement, such as the straight weft yarns, can also be seen as darker lines in the greyscale images. Those darker regions can affect the damage estimation obtained via the image processing, resulting in over-estimation of the damage. Therefore, a segmentation process was performed by setting a threshold for grey value so that the structure of reinforcement would not show in the images.

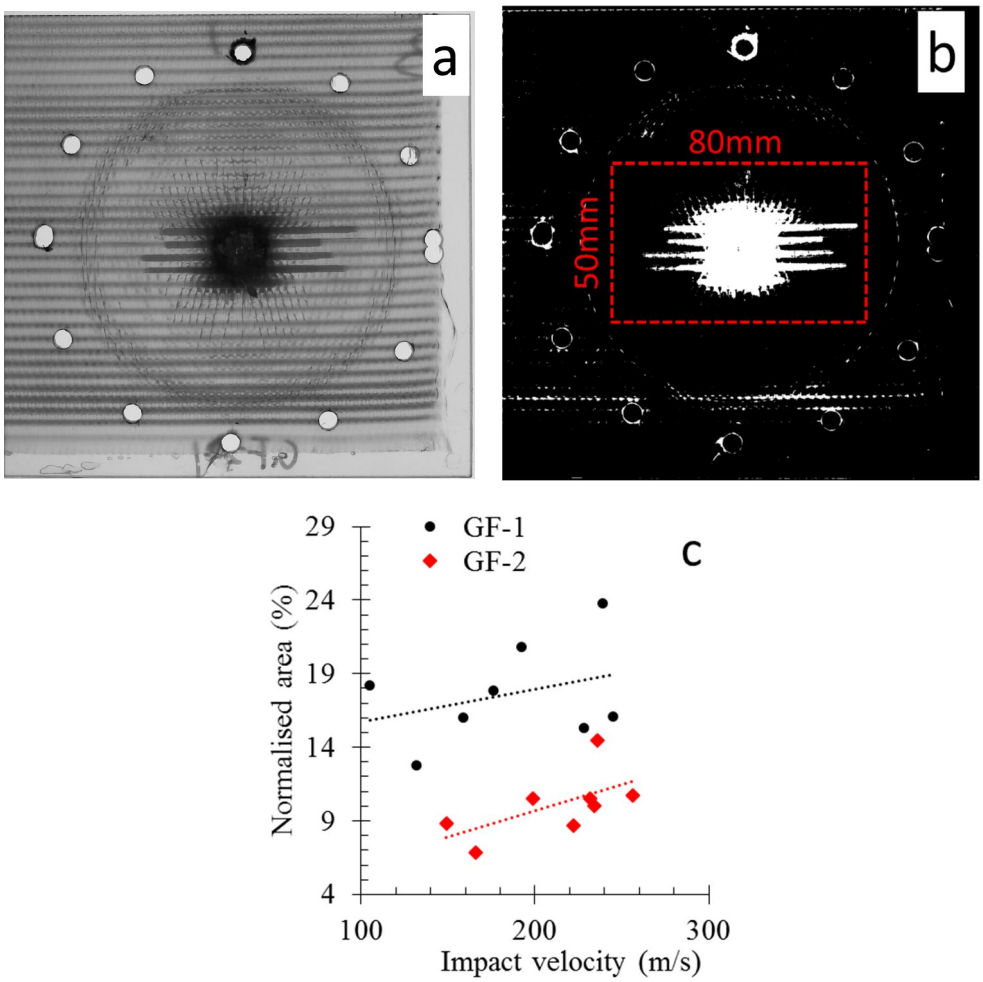


Figure 4-10 (a) The greyscale image and (b) the binary image of the GF-2 plate impacted at 199 m/s; (c) The normalised area of damage for GF-1 and GF-2 plates impacted at various velocities.

The binary image, obtained via the segmentation process, is shown in Figure 4-10 (b). As can be seen, the dissipated cracks, which are apparent in the photographs of the tested panel in Figure 4-9, are not reflected in the binary image. Those crack had similar intensity of grey colour as the reinforcing yarns, hence were filtered out. Based on the visual assessment of the tested panels, it was concluded that the dissipated damage on the surface of the panels was similar in all the cases, hence it was expected to provide a similar contribution

to the mechanical response and impact resistance of the plate in all the impact cases. On the other hand, the localised damage in the centre of the plate appeared to vary from case to case. Typical damage in the centre of the plate, as it appears in the binary image, is shown in Figure 4-10 (b). In all the test panels, the central damaged region, shown in white colour, was contained within the area marked by the red dashed rectangle with the dimension as shown in Figure 4-10 (a). The area of damaged region within the red rectangle was calculated for all the plates. The percentage of its area to the area of the 100-mm-diameter circular region was calculated and the results are shown in Figure 4-10 (c).

The data in Figure 4-10 (c) were fitted with the trend lines, which suggest that for both materials, the damage area tends to increase as the impact velocity increases. The largest damage regions were found in the plates impacted at velocities over 230 m/s. However, the data points are largely scattered. At the velocities around 230 m/s, some are even 30% less than their corresponding maximums. This may be attributed to the fact that only rough measurement can be made by using the images. In the images, different damage modes are superimposed and there is no information about the damage distribution in the thickness direction. Therefore, the results and the trends in Figure 4-10 (b) should be viewed with great care.

4.5.2 X-ray computed tomography (XCT)

The observation and measurements of the damage, as was conducted in Section 4.5.1 for glass-fibre reinforced composites, is not applicable to the opaque CF-IM7 plates. The failure and damage on the tested CF-IM7 plates were inspected by using a Nanotom 160NF X-ray computed tomography (XCT) system. GF-2 plates were also scanned for comparison purpose. The tested plates were cut through the centres of impacts into strips as shown by Figure 4-11 (a) along the weft direction because the damage modes along the weft are more extended. The resolution of the tomographs is 18 μm/voxel.

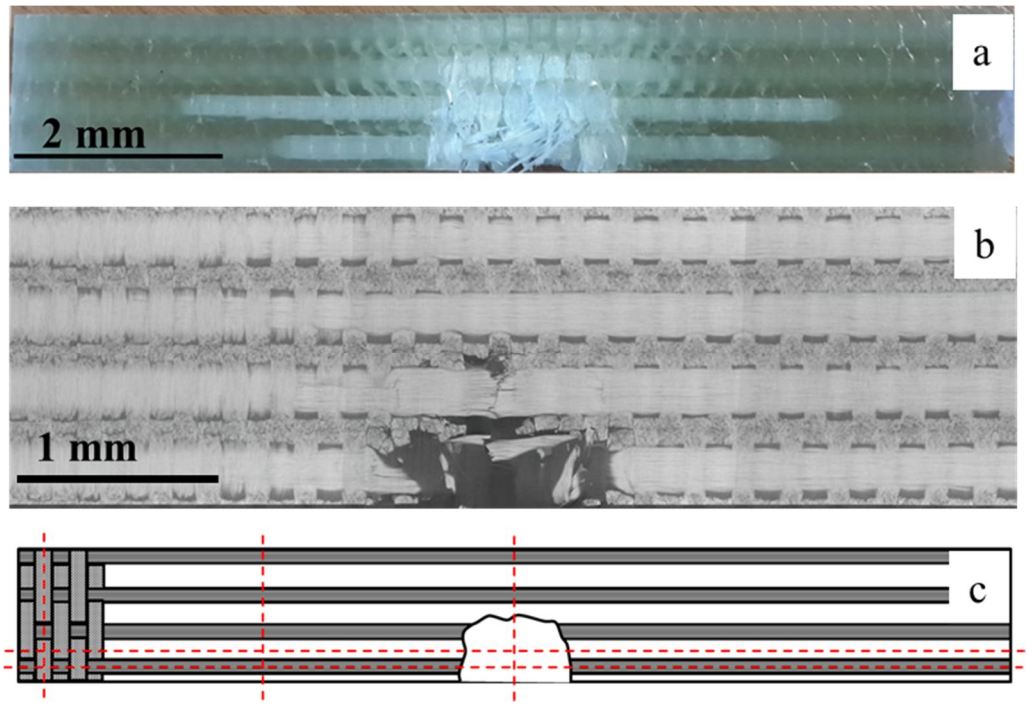


Figure 4-11 (a) A strip specimen of GF-2 for XCT, (b) An XCT image transverse to the thickness direction for GF-2, and (c) A schematic for the positions of images where analysis were made. All of them are viewed along the thickness direction.

The results of XCT are stacks of images along the three dimensions of the specimens. The stacks were observed one by one along the three directions. Similar to the direction of observation in Figure 4-8 and Figure 4-9, the stacks transverse to the thickness, e.g. Figure 4-11 (b), were firstly viewed. However, unlike the views in Figure 4-8, they hardly show any failure and damage except the ones around the hole.

Observations of failure and damage modes were carried out on stacks of the other two directions. Those, parallel to the warp and the specimen width, i.e. Figure 4-12 and Figure 4-14, show the crimped warp yarns and are called “warp views” in the following, while those parallel to the weft and the specimen length, i.e. Figure 4-13 and Figure 4-15, show the straight weft yarns and are called “weft views”. The locations of these stacks are illustrated by the dashed lines in Figure 4-11 (c). The warp views were taken at the impact centre, near the end of specimen and locations between them. Positions at the interfaces of neighbouring warp yarns were avoid. The weft yarns are sparsely arranged. The weft views were taken cutting the yarns or at gaps among the yarns.

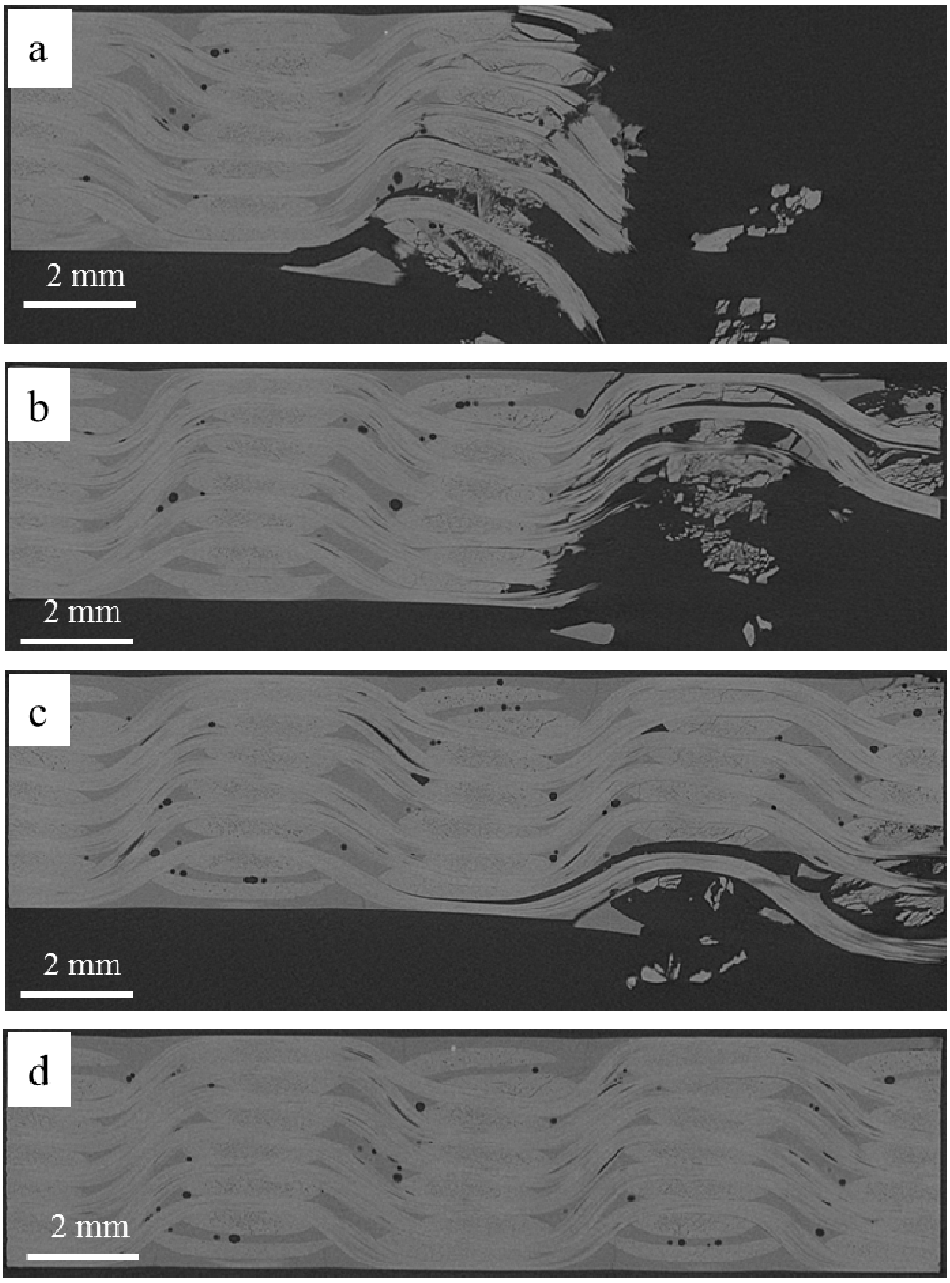


Figure 4-12 CF-IM7 XCT images of cross sections parallel the warp direction. From (a) to (d), the location is farther away from impact.

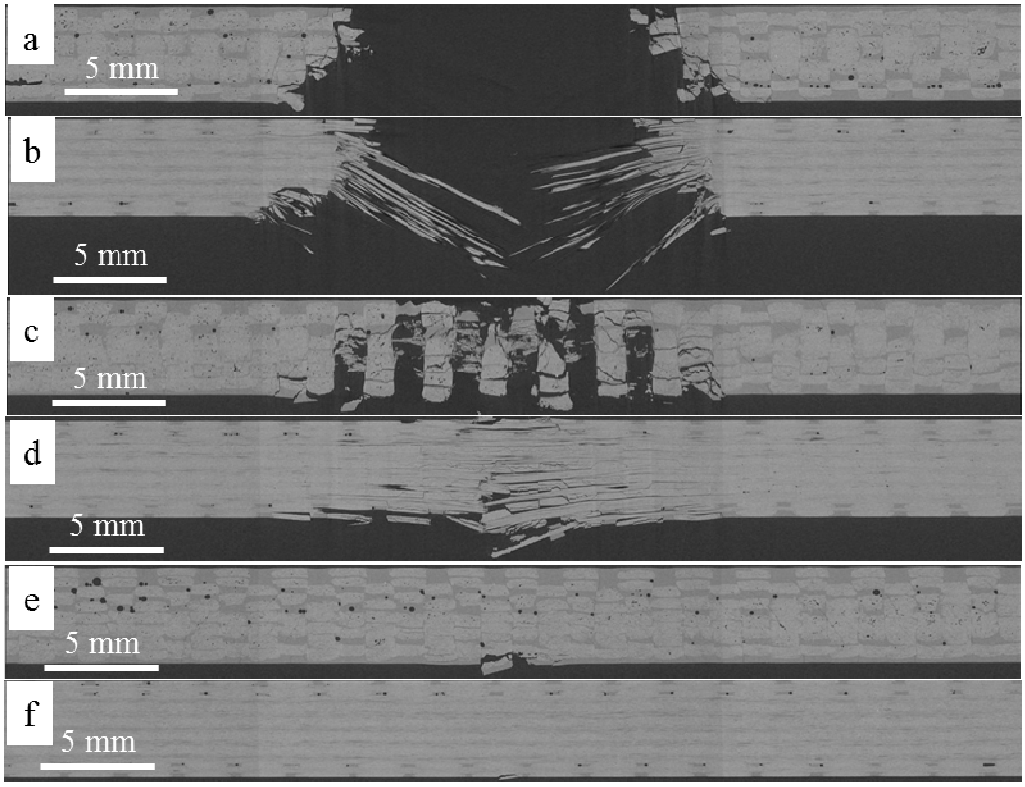


Figure 4-13 CF-IM7 XCT images of cross sections parallel the weft direction. From (a) to (f), the location is farther away from impact.

Figure 4-12 and Figure 4-13 are images for the CF-IM7 plate impacted at 163 m/s, which is the closest to the extrapolated ballistic limit (161 m/s) among the penetrated plates. Such a plate could have the damage and failure characteristics of both rebounding and penetration.

As shown by Figure 4-12 (a), a hole at the impact centre due to material loss is apparent. Warp and weft yarns in the vicinity of the hole are crushed and broken, especially near the bottom, i.e. the back face of impact. The area of failure and damage does not extend to the left-most weft yarns and their surrounding warp yarns. Figure 4-12 (b) is slightly away from the impact centre. On its top right corner, weft yarns are crushed but there is no breaking of warp yarns. In the bottom half, a large number of yarns and matrix are lost. Most of the left three sets of weft yarns and their surrounding are not damaged. Further away from the impact centre in Figure 4-12 (c), failure and damage are found near the bottom in the form of weft yarn crushing and also debonding along the lowest warp yarn. Figure 4-12 (d) is near the circular boundary, where no apparent failure and damage is found.

The weft views of the same plate are shown in Figure 4-13, where the top

face is the front face of impact. It is revealed in Figure 4-13 (a) and (b) that there is more damage and material loss near the back face and the hole is in the shape of a truncated cone. In the vicinity of this hole, weft yarns are bent and some warp yarns are crushed. No damage is found away from the impact region. On the gap next to the weft yarns in (b), Figure 4-13 (c) shows warp yarn loss in a staggered manner. The second sets of weft yarns away from the impact centre as shown in Figure 4-13 (d) were not in the path of the projectile but still bent, most likely due to interaction with the debonded warp yarns. In the next yarn gap (e) and the next set of weft yarns (f), only small damaged areas are visible at the back face.

To sum up these observations, there is more damage and material loss near the back face of impact. The sectional view of the hole looks like a truncated cone, similar to the damage geometry which was commonly found for laminated composites [192, 193]. In the warp direction, the damage modes of yarn breakage and crushing only extend to two or three weft yarns away from the impact centre. On the other hand, the damage modes along the weft yarns extend to locations far from the impact centre.

It can also be seen in these figures that defects due to imperfect RTM manufacturing distribute all over the specimens. Voids of different sizes are found at resin rich regions while few exist where yarns are closely packed, such as the weft yarns in Figure 4-13 (b), (d) and (f). At the same time, some warp yarns in Figure 4-12 are not completed impregnated. Neither of these defects is found for the glass composite GF-2 in Figure 4-14 and Figure 4-15. However, the presence of the defects is not the main reason why CF-IM7 did not outperform GF-1 and GF-2 in the ballistic impact test. As reported in some comparisons [194-196] for glass fibre laminates and carbon fibre laminates, glass fibre composites exhibited high ballistic limits due to (1) larger density as discussed in Section 4.4.3 and (2) more ductility (or larger strain to failure) as will be shown in the following XCT results.

The GF-2 plate in Figure 4-14 and Figure 4-15 was impacted at 183 m/s (V_{50}=180 m/s). The damage modes in Figure 4-8 are also presented in these figures. The debonding of weft yarns in Figure 4-8 (a) is found at the bottom right corner of Figure 4-14 (b) and in the middle of Figure 4-15 (d). The localised damage of warp yarns, Figure 4-8 (b), barely extends to the location represented

by Figure 4-15 (e). The matrix cracks normal to weft yarns in Figure 4-8 (c) are not obvious in the weft views and warp views, because they are located in the resin rich regions of the superficial layers (see Figure 4-15 (b), (d) and (f)), where the wavy pattern of debonding in Figure 4-8 (d) could also be located.

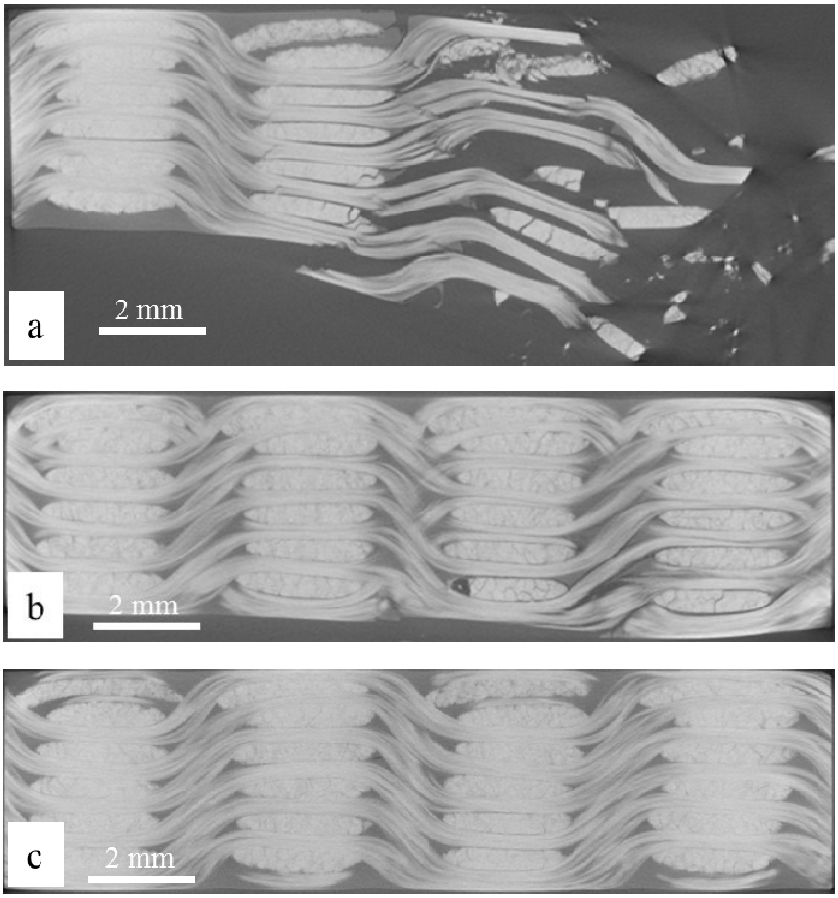


Figure 4-14 GF-2 XCT images of cross sections parallel the warp direction. From (a) to (c), the location is farther away from impact.

Similar to the CF-IM7 plate, the GF-2 plate is also more damaged near the back face. Crushing and breakage of both weft and warp yarns together with debonding are found in similar locations. This suggests that the two impacts may involve similar process.

Unlike the CF-IM7 plate, there is not a distinct penetration hole in the GF-2 plate. In Figure 4-14 (a) and Figure 4-15 (a), a number of warp yarns are still hanging at the impact centre. This is sensible as glass fibres are known for having larger strain to failure than carbon fibres. This difference may also be the reason why the area and extent of yarn damage are also smaller in GF-2. Figure 4-14 (b) is right at the middle between the impact centre and the boundary. Apart from the one weft yarn on the bottom right, which is crushed, no yarn damage

is found. The same position for CF-IM7, in Figure 4-12 (c), shows extensive yarn damage. In Figure 4-15 (d), the crushing and breaking of GF-2 yarns only exist in the bottom layer, while its counterpart of CF-IM7 in Figure 4-13 (d) shows severe damage in the weft yarns.

On the other hand, the debonding along the gaps among warp yarns is more extensive in the GF-2 plate. Around the third set of weft yarns from the impact centre, in Figure 4-15 (f), there is apparent debonding in the centre of the thickness, while there is no debonding at all at this position for the CF-IM7 plate as shown by Figure 4-13 (f).

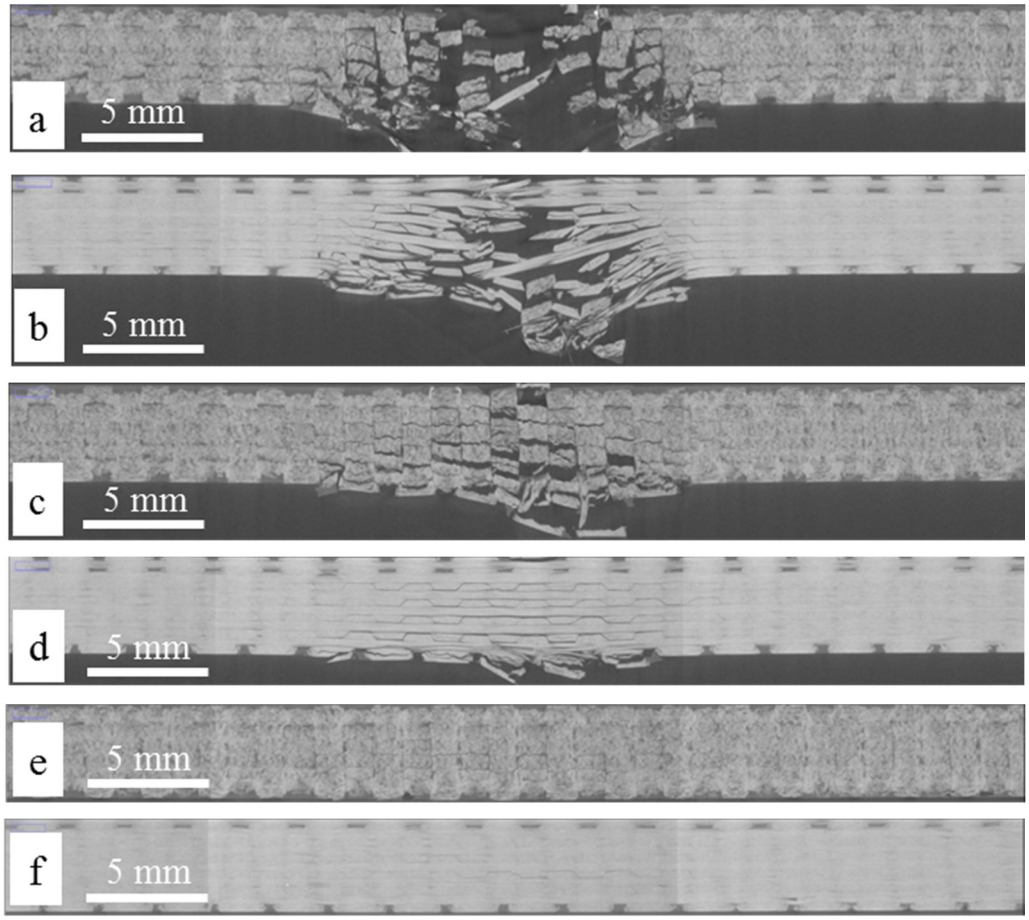


Figure 4-15 GF-2 XCT images of cross sections parallel the weft direction. From (a) to (f), the location is farther away from impact.

To summarise this section, the observations clearly show that, for both GF-2 and CF-IM7, more material loss and damage occurred at the back face of impact. Consequently, the penetration generates holes in the shape of a truncated cone in the plates. Similar failure and damage modes are found in the two composites, namely the breakage and crushing of fibre yarns along with debonding of yarns from the matrix. The failure modes along the weft direction

are extended, while those along the warp direction are only found in the impact vicinity. Meanwhile, due to the smaller strain to failure of carbon fibres, the yarn damage modes in CF-IM7 are more extended than those in GF-2, while it is the opposite for the debonding.

4.6 Conclusions

In this chapter, the experimental equipment, data acquisition and processing techniques of ballistic impact tests are described. The tests were carried out with three types of 3D woven composites and one type of laminated composite. The trajectory of the projectile was recorded by high speed camera and then analysed to obtain the impact and residual velocities. Then the velocity pairs were fit to the Jonas-Lambert equation by non-linear curve fitting in order to obtain the ballistic limit V_{50}. Statistical analysis of the experimental data showed that for GF-1 and GF-2 composites, there was high uncertainty in determining the limit velocity due to a large scatter of the experimental data. On the other hand, the fitting was reasonable for CF-IM7 and QI-IM7 composites. The analysis of the experimental data suggests that the GF-2 composite has the highest impact resistance, followed by GF-1, CF-IM7 and QI-IM7. However, if the difference in density is considered, the three types of 3D woven composites have similar efficiency in resisting penetration.

The damage modes in the impacted plates of GF-2 and CF-IM7 were observed by using XCT. For both composites, there is more damage and material loss near the back face of impact. The failure and damage modes are crushing and breakage of yarns in both weft and warp directions, accompanied by debonding between the yarns and the matrix. These failure modes along the warp direction are only found in the impact vicinity, while those along the weft direction are more extended. Meanwhile, the yarn damage modes are more extended in CF-IM7 than in GF-2 while the debonding is more extended in GF-2.

Chapter 5 Phenomenological macro scale modelling for impact behaviour of 3D woven composites

5.1 Introduction

Various approaches to modelling the constitutive behaviour of the textile composites have been outlined and discussed in Chapter 2. In general, the material model should contain three main components, namely, the elastic behaviour, the appropriate failure criteria, and the capability to define the evolution of damage. When modelling the response of the material under impact loadings, strain rate sensitivity should also be accounted for in the model formulation. This type of models usually do not come as standard provisions in commercial finite element codes, since at present there is no unique established methodology of modelling the textile composites. However, the readily available material model MAT162 in LS-DYNA, which is developed for modelling the response of composite materials based on plain weave reinforcements, incorporates all the desired characteristics of the material response as described above. To obtain the same characteristics by using other explicit FE packages, e.g. Abaqus/Explicit, user defined material subroutines need to be scripted. Therefore, LS-DYNA is selected as the simulation platform in present study.

In this chapter, a phenomenological macro scale modelling approach of using MAT162 of LS-DYNA to predict the impact behaviour of the 3D woven composites is presented. The input parameters required by MAT162 are introduced. The damage parameters and element deletion parameters were selected by simulating several uniaxial loading cases of a single element. Subsequently, the selected input data and MAT162 were employed to simulate the ballistic impact tests described in Chapter 4. The predictions are compared with experimental data and with models of a new macro scale material model developed in one of the parallel projects [8] via a multi scale modelling approach. It will be shown that by using MAT162 it is possible to have good predictions of the ballistic tests; however MAT162 does have limitations which should also be paid attention to.

5.2 The input data for MAT162

To define an orthotropic composite material in MAT162, more than 30 input parameters should be specified. The parameters are listed in Table 5-1, along with their LS-DYNA notations. In this study, character “A” is used to refer to the weft direction of the composite, “B” denotes the warp direction and “C” denotes the through-thickness direction.

Table 5-1 Definition of the inputs parameters for MAT162.

Input	Abbreviation (subscripts for symbols associate)
Mass density	RO
Young's modulus - longitudinal direction	EA
Young's modulus - transverse direction	EB
Young's modulus - through-thickness direction	EC
Poisson's ratio BA	PRBA
Poisson's ratio CA	PRCA
Poisson's ratio CB	PRCB
Shear modulus AB	GAB
Shear modulus BC	GBC
Shear modulus CA	GCA
Longitudinal tensile strength	SAT
Longitudinal compressive strength	SAC
Transverse tensile strength	SBT
Transverse compressive strength	SBC
Through-thickness tensile strength	SCT
Crush strength	SFC
Fibre mode shear strength	SFS
Matrix mode shear strength AB plane	SAB
Matrix mode shear strength BC plane	SBC
Matrix mode shear strength CA plane	SCA
Scale factor for residual compressive strength	SFFC
Element eroding axial strain	E_LIMT
Scale factor for delamination criterion	S_DELM
Limit compressive volume strain for element eroding	ECRSH
Limit tensile volume strain for element eroding	EEXPN
Parameter for fibre damage in A direction	AM1
Parameter for fibre damage in B direction	AM2
Damage parameter for crush failure	AM3
Damage parameter for matrix and delamination damage	AM4
Coefficient for strain rate dependent strength properties	CRATE1
Coefficient for strain rate dependent axial moduli	CRATE2
Coefficient for strain rate dependent shear moduli	CRATE3
Coefficient for strain rate dependent transverse moduli	CRATE4

5.2.1 Elastic and strength properties

Some of the input elastic and strength properties were determined in the experimental study as described in Chapter 3, where the composite samples were tested under quasi-static uniaxial tension and compression tests in the weft and warp directions, as well as under in-plane shear loading. The through-thickness elastic properties, i.e. EC, GBC, GCA, PRCA and PRCB were determined following the meso scale unit cell analysis as described in Appendix 1, where an overview of the involved multi-scale modelling in [8] is provided.

According to the LS-DYNA material model MAT162 formulation [111], the tension/shear combined failure criteria of fabric lamina are listed in Eq.(5-1) and (5-2).

$$f_6 = \left(\frac{\langle \sigma_{\mathrm{A}} \rangle}{S_{\mathrm{AT}}}\right)^2 + \frac{\tau_{\mathrm{AB}}^2 + \tau_{\mathrm{CA}}^2}{S_{\mathrm{AFS}}^2} - 1 = 0 \tag{5-1}$$

$$f_7 = \left(\frac{\langle \sigma_{\mathrm{B}} \rangle}{S_{\mathrm{BT}}}\right)^2 + \frac{\tau_{\mathrm{AB}}^2 + \tau_{\mathrm{BC}}^2}{S_{\mathrm{BFS}}^2} - 1 = 0 \tag{5-2}$$

$$S_{\mathrm{AFS}} = S_{\mathrm{FS}}\,, S_{\mathrm{BFS}} = S_{\mathrm{FS}} \times \frac{S_{\mathrm{BT}}}{S_{\mathrm{AT}}} \tag{5-3}$$

where σ is the normal stress acting in the material direction represented by its subscript, τ is the shear stress. $\langle\ \rangle$ are Macaulay brackets defined as follows:

$$\langle x \rangle = \begin{cases} 0, & x < 0 \\ x, & x \geq 0 \end{cases} \tag{5-4}$$

Quantities f_i in Eq. (5-1), Eq. (5-2) and Eq. (5-8) to Eq. (5-11) below are the failure indicators for each specific mode of damage. As soon as a failure indicator reaches the value of zero, the damage is initiated. Their subscript numbering starts from 6 in the user manual [111], as the subscripts from 1 to 5 are used for UD laminates.

It is worth mentioning that if the shear terms in Eq.(5-1) and (5-2) are

ignored, the criteria essentially become the maximum stress criteria. The two in-plane tensile strength properties S_{AT} and S_{BT} are obtained from QS tension tests in Chapter 3, while no information could be found in the open literature that specifies how to determine the fibre shear strength S_{FS}. As an initial trial, S_{FS}, is assigned a value of 1200 MPa to reduce contributions of the shear terms and hence to approximate the maximum stress criteria.

The compressive failure of fibres is based on the maximum stress failure criteria as follows:

$$f_8 = \left(\frac{\langle \sigma_A' \rangle}{S_{AC}}\right)^2 - 1 = 0, \quad \sigma_A' = -\sigma_A + \langle -\sigma_C \rangle \tag{5-5}$$

$$f_9 = \left(\frac{\langle \sigma_B' \rangle}{S_{BC}}\right)^2 - 1 = 0, \quad \sigma_B' = -\sigma_B + \langle -\sigma_C \rangle \tag{5-6}$$

where S_{AC} and S_{BC} are the compressive strength values obtained from QS compression tests.

Fibre crush failure is controlled by fibre crush strength S_{FC} as follows:

$$f_{10} = \left(\frac{\langle p \rangle}{S_{FC}}\right)^2 - 1 = 0, \quad p = -\frac{\sigma_A + \sigma_B + \sigma_C}{3} \tag{5-7}$$

In this study, S_{FC} is estimated to be twice the in-plane compression strength [197]. Conservative predictions or safety margins are preferable in the aero engine industry, hence, the smaller of the two compression strengths, which is the warp compression strength for both GF-1 and CF-IM7 composites, is used to make a conservative estimation.

The matrix shear strength, S_{AB}, is used in the in-plane matrix failure criterion Eq. (5-8). Its values for both GF-1 and CF-IM7 composites are determined in the following Section 5.2.2.

$$f_{11} = \left(\frac{\tau_{AB}}{S_{AB}}\right)^2 - 1 = 0 \tag{5-8}$$

In MAT162 model, through-thickness tensile and shear strength properties are associated with the interlaminar matrix failure, according to the criterion Eq. (5-9). However, unlike 2D laminated composites, the 3D woven composites that are employed in current study do not have explicit interlaminar interfaces. The XCT results for the impacted plates in Section 4.5.2 do not show any sign of delamination. This delamination criterion was inactivated by assigning a very small value to the scale factor *S* (parameter S_DELM). Energy dissipation can still happen via through-thickness straining but will not lead to delamination in MAT162 and associated degradation of properties. As an initial trial, a conservative value of 50 MPa was used for all three strengths, namely the through-thickness tensile strength S_{CT} and shear strengths S_{BC} and S_{CA}. This value was slightly higher than the matrix shear strength. The actual strength values should be higher due to the presence of through-thickness reinforcement.

$$f_{12} = S^2 \left\{ \left(\frac{\langle \sigma_C \rangle}{S_{CT}} \right)^2 + \left(\frac{\tau_{BC}}{S_{BC}} \right)^2 + \left(\frac{\tau_{CA}}{S_{CA}} \right)^2 \right\} - 1 = 0 \qquad (5\text{-}9)$$

5.2.2 Parameter calibration by single element modelling

In this section, parameters related to the damage definition and element deletion conditions, are calibrated by modelling the uniaxial loading of a single element. Unlike the calibration by Brown [114], Xiao et al. [100] and Gama and Gillespie [198], where coupon tests were simulated, this approach of modelling single element excludes the interaction among elements, thus ensure that the element is in a pure tensile or compressive, or shear stress state. Furthermore, running single element modelling reduces the computational costs, hence the simulation time. It becomes practically possible to apply a low strain rate in the simulations to represent the QS loading by using MAT162, which is only implemented for explicit FE analysis. Otherwise, either time scaling or mass time scaling is essential to reduce the simulation time to a feasible level when modelling a QS coupon test in explicit analysis. The calibration procedure as presented here was carried out for GF-1 composite. Then the input data for CF-IM7 was obtained following the same procedure.

5.2.2.1 Methodology

A single element model employed in the current study is shown in Figure 5-1. The single integration point solid element was used. The element dimensions are 2.5 mm in length, 2.5 mm in width and 0.5 mm in thickness. In the tension and compression models, the nodes on the left end are translationally constrained in x-direction. For the nodes on the right hand side, displacement in the x-direction is applied at a rate of 1 mm/min. In the shear models, x and y translational constraints are applied on the nodes on the left end. The displacement on the right end is along the y axis. In all the models, the material thickness direction is aligned with the z-axis. In-plane weft and warp directions are aligned with the x- and y-axes, respectively, depending on the loading cases.

Damage parameters AM1 and AM2 control the fibre damage evolution in the weft and warp directions respectively; AM3 is related to the fibre crush and punch shear damage, while AM4 defines the matrix and delamination damage. Based on the stress-strain curves obtained in the QS material tests, a trial and error approach was adopted to determine the appropriate values for AM1, AM2 and AM4. There is no stress-strain curve corresponding to the modes related to AM3. A conservative assumption is made here that the modes related to AM3 fail abruptly and no damage evolution is involved. This is achieved by assigning a large value, AM3=100, to this parameter.

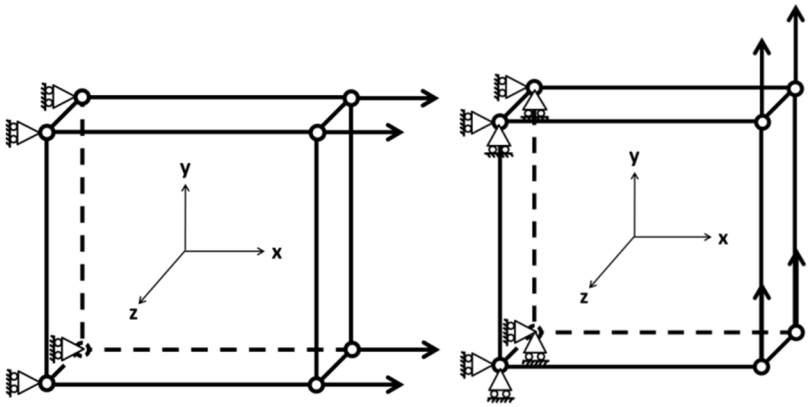


Figure 5-1 Single element model of MAT162 in LS-DYNA for uniaxial tension/compression (left) and shear (right).

5.2.2.2 QS tension

Modelling stiffness reduction after damage onset

Stress-strain curves under tension in the weft and the warp direction were

obtained experimentally as presented in Chapter 3. The stiffness degradation, which generally occurred after the on-set of damage, is taken into account. The initial moduli and the stress values at the onset of damage were used as the inputs of MAT162. After damage initiation, the stiffness reduction was controlled by negative values of the damage parameters, AM1 for the weft direction and AM2 for the warp direction. This approach of modelling the tensile stress-strain curves is referred to as Method 1.

Following this method, the stress-strain curves under tensile loading in the warp direction were calculated for two different values of AM2, as shown in Figure 5-2. It can be seen that the stress-strain curve beyond the damage initiation point are sensitive to the values of the damage parameters. The post-initiation stiffness becomes apparently lower when AM2 is changed from -1.5 to -1.3. Based on a trial and error approach, the parameter values AM1=-1.3 and AM2=-1.5 have shown to provide a good approximation to the experimental post-initiation stiffness values in the weft direction and in the warp direction, as shown in Figure 5-3 and Figure 5-4, respectively.

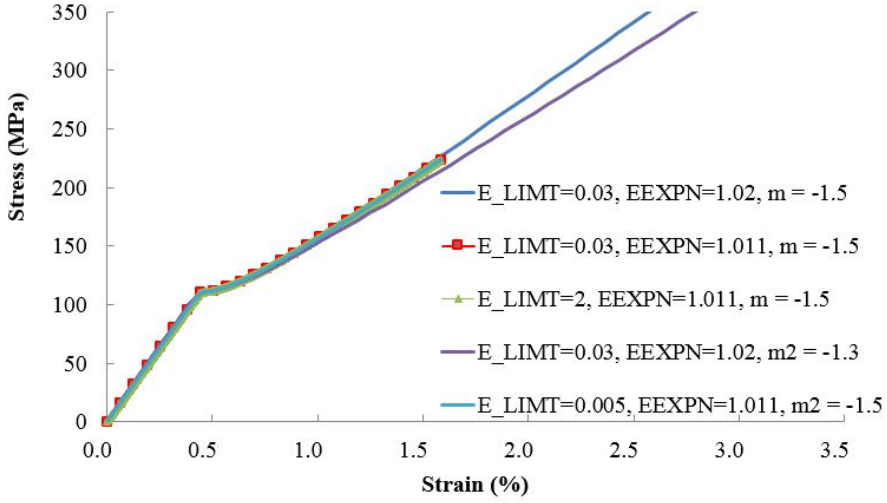


Figure 5-2 Calibration of parameters for damage and element deletion for single element model of GF-1 under QS warp tension.

The strength inputs of MAT162 were assigned with the value of damage on-set stresses hence no more inputs were available to explicitly define the ultimate strength. This was achieved by employing element deletion in this study.

According to MAT162 formulation, two parameters could be used for this purpose, namely, E_LIMT (element eroding axial strain) or EEXPN (limit tensile volume strain for element eroding). However, the criterion for axial strain,

E_LIMT, fails to delete the element properly. Stress-strain curves calculated with various values of EEXPN and E_LIMT are shown in Figure 5-2. As can be seen, at E_LIMT=0.005 the element was not deleted at 0.5% of axial strain as was expected. It was also found that E_LIMT did not interact with EEXPN. Comparing stress-strain curves in Figure 5-2 calculated for three values of E_LIMT=0.005, 0.03 and 2, while keeping EEXPN=1.011 fixed, little variation among the curves can be observed. Since the element deletion based on E_LIMT has proven to be unreliable, its effect was eliminated by prescribing a very large value to this parameter, E_LIMT=2, which corresponds to 200% of axial strain.

This left a single element deletion criterion, based on tensile volume strain EEXPN, to define the ultimate strength. An appropriate value of this parameter, EEXPN=1.011, was determined in the parametric study as presented in Figure 5-2 to ensure that the element was deleted once the axial stress reaches 223 MPa, which was the strength value determined experimentally. For the deleted elements, both the stress and the strain are reduced to zero. It is worth noting that this method is very sensitive to the choice of EEXPN value. When EEXPN is increased by 1% (from 1.011 to 1.02), while E_LIMT and AM2 are kept fixed, the ultimate stress increases beyond 350 MPa.

Modelling linear response until the final failure

Table 5-2 The inputs used in modelling the tension of GF-1, and the strain energy density after the final failure which is normalised to the experimental values.

	Method 1	Method 2	Method 3
E_A (GPa)	15.92	15.92	7.82
S_{AT} (MPa)	57.26	206.46	206.46
E_B (GPa)	24.77	24.77	16.78
S_{BT} (MPa)	110.08	223.49	223.49
AM1	-1.3	100	100
AM2	-1.5	100	100
Normalised weft tension strain energy density	105%	51%	100%
Normalised warp tension strain energy density	115%	66%	94%

For comparison, two simpler methods of parameter definition were also considered, where the material was assumed to be linearly elastic until the final failure. The difference between the two methods is in defining the elastic moduli.

Specifically, in one case, denoted as Method 2, the stiffness value prior to the damage onset was used. In the second case, Method 3, the stiffness was defined as a secant modulus calculated as a ratio of the ultimate tensile stress to the ultimate tensile strain. In both cases, once the stress reaches the ultimate tensile stress value, the stress drops rapidly to zero, which was modelled by assigning large positive values to the damage evolution parameters, AM1=AM2=100.

Comparison of the three methods

The inputs used in these three methods are summarised in Table 5-2. The stress-strain curves calculated with these three data sets are plotted simultaneously with the experimental data in Figure 5-3 and Figure 5-4. The experimental data are represented by bilinear stress-strain curves, constructed based on the values of the elastic moduli before and after the damage onset, damage initiation stresses and ultimate stresses determined experimentally.

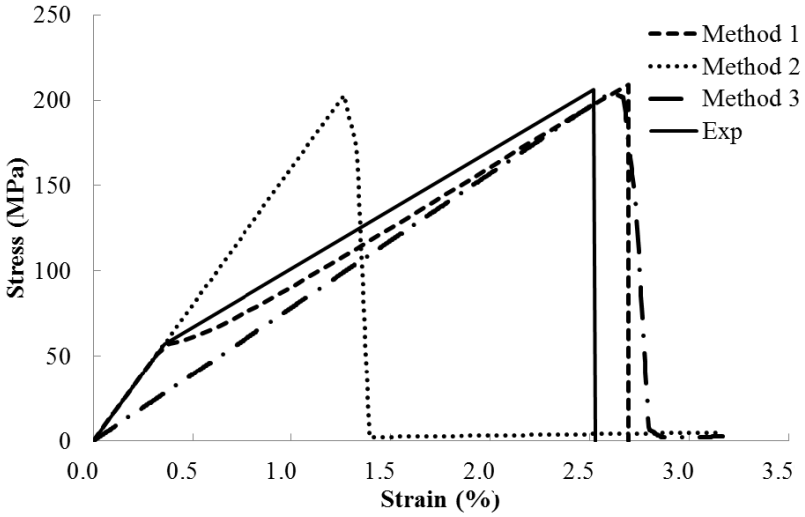


Figure 5-3 Approximation of the stress-strain curves obtained under QS tension in the weft direction.

As can be seen in both Figure 5-3 and Figure 5-4, Method 1 provides the closest representation of the experimental stress-strain curves. One of the indicators for energy dissipation capability is the strain energy density at the final material failure, which essentially is the area under the stress-strain curve. The strain energy densities calculated based on the dataset of Method 1 are given in Table 5-2, and these are larger than the corresponding experimental values by 5% and 15% for weft and warp tension, respectively.

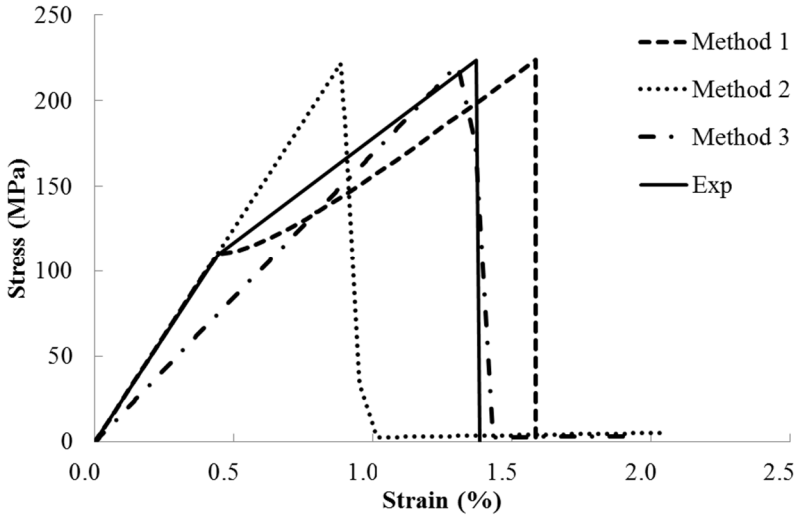


Figure 5-4 Approximation of the stress-strain curves obtained under QS tension in the warp direction.

As expected, for Method 2 and Method 3, the stresses rapidly reduced to zero after the failure stresses defined by S_{AT} and S_{BT} were reached. Since the stiffness value corresponding to dataset Method 2 is higher than that in Method 3, the ultimate stress was reached at a small strain, hence the strain energy densities at the final failure were 49% and 34% smaller than in the experiments. In an impact simulation, this would result in a significant underestimation of the impact resistance. Because of that, Method 2 was considered to be inapplicable for modelling the impact cases and therefore will not be further discussed. Stress-strain curves obtained with the dataset 'Method 3' appear to underestimate the elastic behaviour to some extent, however, the calculated strain energy density is very similar to the experimental one. Later in this section, both 'Method 1' and 'Method 3' were assessed by modelling the dynamic loadings of a single element.

5.2.2.3 QS compression

The experimental stress-strain curves under uniaxial compression are shown in Figure 5-5. The elastic behaviour under the compression is found to be different from that under tension. The compressive moduli should be used rather than the tensile ones. Meanwhile, for this type of loading, the stress-strain relation is linear until the maximum stress is reached. Beyond this point, a gradual softening was observed under the compression in the weft direction, while under the warp compression, the stress drops abruptly but residual strength

remains. To describe the effect of the material softening, positive values of damage parameters should be used in MAT162. The parameter values AM1=0.5 and AM2=100 were determined in a parametric study to define the softening behaviour in the weft and the warp directions, respectively. The limit for elastic modulus reduction (OMGMX) was set to 0.99 to enable nearly complete loss of stiffness.

The softening takes place until the residual strength defined by SFFC (scale factor for residual compressive strength) is reached. The residual strength is based on the observation on the tested specimens, all of which are still in one-piece and show some residual load carrying capability. It should be noted that the experimental curves in Figure 5-5 terminate at the point when the experiment was stopped, and this is not associated with the total loss of load-carrying capability.

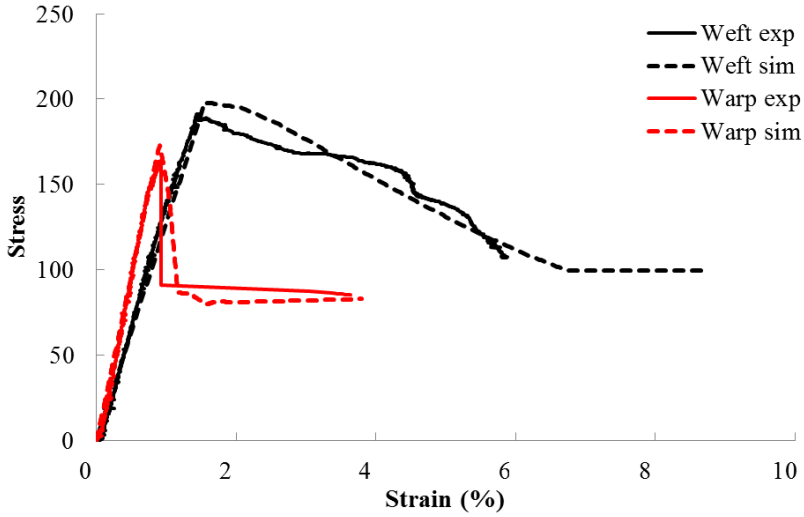


Figure 5-5 QS compression stress-strain curves of the single element model and their comparison to experiment.

For GF-1 composite, the only available SFFC in MAT162 is set to 0.5 such that the residual strength for weft and warp compression cannot be less than 50% of the original values. This corresponds to the residual stress values at the nearly flat plateaus of the stress-strain curves as shown in Figure 5-5. The failure is predicted once any one of the element deletion criteria is activated. The element deletion associated with compression is based on compressive volumetric strain, ECRSH. The experimental data shows that the tested specimens maintained some residual strength when strained to about 8%. As an initial trial, ECRSH is assumed to be 10%. This results in the element deletion at the ends of the

simulation curves in Figure 5-5.

5.2.2.4 QS Shear

The experimental shear stress strain curves are shown in Figure 5-6. It can be seen that the stress-strain curves for the four types of 3D woven composites are linear up to the damage initiation stress of approximately 40 MPa. Beyond this point, the stiffness gradually reduces to zero. Qualitatively, shear stress-strain curves are similar to those obtained under warp tension, hence they were constructed applying the same method as was used for modelling the material response under tension in the warp direction. The stress at which the curve became nonlinear is defined as the shear strength, S_{AB}, in MAT162. The stiffness reduction is controlled by the damage parameter AM4=-0.3. The approximation of the shear stress-strain curves is shown in Figure 5-6. The overall shape of the stress-strain curve is captured, however, the discrepancy in approximation of the nonlinear part is apparent. Due to the formulation of the stiffness degradation in MAT162, a rapid reduction in stiffness occurred after damage initiation. Beyond this point, the tangent stiffness did not change and the stress continued to increase until the element deletion was activated, which was defined by the shear strain criterion (EPSSH) in MAT_ADD_EROSION. The failure strain of the tested specimens varies in the range from 6.5% to 8%. A value of EPSSH=0.7, which correspond to 7% of shear strain, was used in this study.

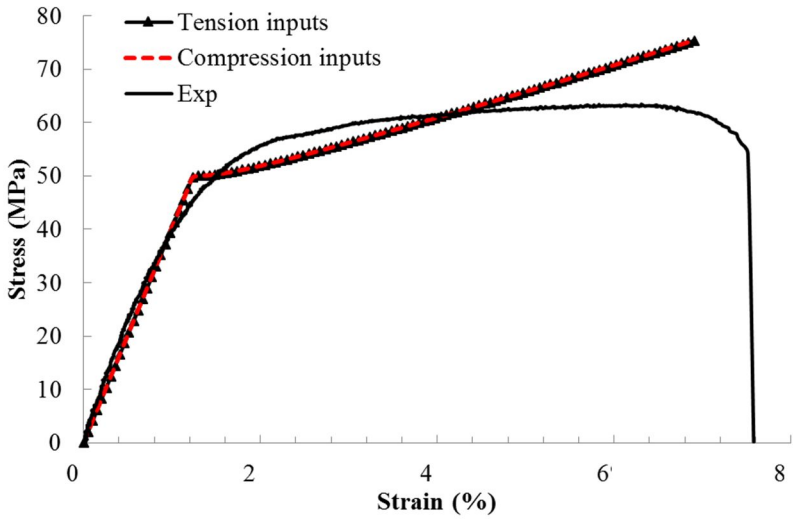


Figure 5-6 QS in-plane shear stress-strain curves of the single element model and their comparison to experiment.

Since the shear stress-strain curve in Figure 5-6 was calculated under pure

shear loading, it is not affected by the choice of the in-plain elastic moduli values from either the compression data or from Method 1 of tension. The shear behaviour was identical in both cases.

5.2.2.5 Summary for QS single element modelling

Based on the QS experimental data and single element model simulations, all the damage parameters and element deletion parameter have been calibrated. To match specific loading cases, the calibration results in five sets of input data. Two of these data sets, denoted 'T1M1' and 'T2M1', explicitly model the bilinearity of the tensile stress-strain relation. The input values of the parameters for these data sets are generally the same, except for the element deletion parameter EEXPN, which was employed to define the failure stress of the material. Method 2 in the tension model underestimates the dissipated energy for material failure and thus is not discussed in the following. The set of inputs for Method 3 is denoted as 'TM3' while the set for the compression model is 'C'. This results in four sets of the input parameters, which are summarised in Table 5-3.

Table 5-3 The inputs parameters for GF-1 used in the four methods.

Input	T1M1	T2M1	TM3	C
EA (GPa)	15.92	15.92	7.82	12.79
EB (GPa)	24.77	24.77	16.78	19.42
SAT (MPa)	57.26	57.26	206.46	206.46
SBT (MPa)	110.076	110.076	223.49	223.49
OMGMX	0.57	0.57	1	1
EEXPN	1.023	1.011	4	4
AM1	-1.3	-1.3	100	0.5
AM2	-1.5	-1.5	100	10

5.2.3 Strain rate scaling

5.2.3.1 Scaling factors

In Chapter 3, the QS and SHPB compression tests indicate apparent strain rate dependency for the compressive strength. By taking the QS strain rate (5.56×10^{-4}/s) as a reference, two scaling factors are determined for the

compressive strength of GF-1 composite, namely, C_{rate} =0.0686 for weft compression and C_{rate} =0.0527 for warp compression. However, according to MAT162 material model formulation, the rate-dependency of six strength values, namely, S_{AT}, S_{AC}, S_{BT}, S_{BC}, S_{FC} and S_{FS}, are all controlled by C_{rate1}, as follows:

$$\{S_{\text{RT}}\} = \{S_0\}\left(1 + C_{\text{rate1}} ln \frac{\{\dot{\bar{\varepsilon}}\}}{\dot{\varepsilon}_0}\right)$$

$$\{S_{\text{RT}}\} = \begin{Bmatrix} S_{\text{AT}} \\ S_{\text{AC}} \\ S_{\text{BT}} \\ S_{\text{BC}} \\ S_{\text{FC}} \\ S_{\text{FS}} \end{Bmatrix} \text{ and } \{\dot{\bar{e}}\} = \begin{Bmatrix} |\dot{\varepsilon}_{\text{A}}| \\ |\dot{\varepsilon}_{\text{A}}| \\ |\dot{\varepsilon}_{\text{B}}| \\ |\dot{\varepsilon}_{\text{B}}| \\ |\dot{\varepsilon}_{\text{C}}| \\ \left(\dot{\varepsilon}_{\text{BC}}{}^2 + \dot{\varepsilon}_{\text{CA}}{}^2\right)^{1/2} \end{Bmatrix} \tag{5-10}$$

Similarly, for the strain rate scaling of moduli according to Eq. (5-11), both the weft modulus E_{A} and the warp modulus E_{B} are controlled by C_{rate2}.

$$\{E_{\text{RT}}\} = \{E_0\}\left(1 + \{C_{rate}\} ln \frac{\{\dot{\bar{\varepsilon}}\}}{\dot{\varepsilon}_0}\right)$$

$$\{E_{\text{RT}}\} = \begin{Bmatrix} E_{\text{A}} \\ E_{\text{B}} \\ E_{\text{C}} \\ G_{\text{AB}} \\ G_{\text{BC}} \\ G_{\text{CA}} \end{Bmatrix}, \{\dot{\bar{e}}\} = \begin{Bmatrix} |\dot{\varepsilon}_{\text{A}}| \\ |\dot{\varepsilon}_{\text{B}}| \\ |\dot{\varepsilon}_{\text{C}}| \\ |\dot{\varepsilon}_{\text{AB}}| \\ |\dot{\varepsilon}_{\text{BC}}| \\ |\dot{\varepsilon}_{\text{CA}}| \end{Bmatrix} \text{ and } \{C_{rate}\} = \begin{Bmatrix} C_{\text{rate2}} \\ C_{\text{rate2}} \\ C_{\text{rate4}} \\ C_{\text{rate3}} \\ C_{\text{rate3}} \\ C_{\text{rate3}} \end{Bmatrix} \tag{5-11}$$

In this study, the rate scaling factors for the elastic moduli, i.e. C_{rate2}, C_{rate3} and C_{rate4}, are set to zero as baseline values. Since the difference between the scaling factors of the warp and weft compressive strengths is relatively low, e.g. 10% at 5000/s. C_{rate1} =0.0686 was used for an initial trial. If energy dissipation is over predicted in the simulation, C_{rate1} =0.0527 could be used for more conservative prediction.

Reference strain rate

The scaling factors are clearly dependent on the reference strain rate. In MAT162, the reference strain rate is mandatory at 1/s. However, this was overlooked in the published work of using MAT162 [114, 198]. Consider the weft compression of GF-1 composite as an example (S_{AC}=199 MPa). According

to Eq. (5-10), when C_{rate} = 0.0686, the correct scaling should use the QS strain rate as the reference strain rate. The correct values of dynamic strength at 1/s, 1000/s, 5000/s and 10000/s are calculated as Case I in Table 5-4. This cannot be achieved in MAT162 due to the mandatory reference strain rate of 1/s.

Table 5-4 The dynamic strength values calculated according to Eq. (5-10).

	$\dot{\varepsilon}_0$ (1/s)	S_0 (MPa)	C_{rate}	S_{RT} (MPa)			
				1/s	1000/s	5000/s	10000/s
Case I	5.56×10^{-4}	199	0.0686	301	396	418	427
Case II	1	199	0.0686	199	293	315	325
Case III	1	199	0.1298	199	377	418	437
Case IV	1	301	0.0453	301	396	418	427

Case II represents the method in [114, 198], where the QS properties and the determined strain rates are directly used as the inputs of MAT162. It can be seen that the strength values at each strain rate are much lower than the correct values. This is all caused by overlooking the mandatory reference strain rate of 1/s in MAT162.

In Case III, to achieve the correct strength at 5000/s, scaling factor was increased without adjusting the strength input. Although the right value of strength at 5000/s is obtained, this method implies a stronger strain rate dependency. The strength at 1000/s is underestimated while strength at 10000/s is overestimated. Meanwhile, the scaling factor determined by this method is not objective. To achieve the correct strength at 1000/s, the scaling factor should be increased to 0.1441, and consequently the strength values at rates above 1000/s will be overestimated. Similarly, the scaling factor has to be another value in order to achieve the correct predictions of the strength at 10000/s. However, in this case, the strength at rates below 10000/s will be underestimated.

In Case IV, both the strength input and the scaling factors are adjusted to the reference strain rate of 1/s, i.e. $\dot{\varepsilon}_0$ =1/s and S_0 =301 MPa. Then, they were used together with $\dot{\varepsilon} = 5.56\times10^{-4}$/s and S_{RT} =199 MPa in Eq. (5-10) to calculate the corresponding strain rate scaling factor. Then the right strength values at the higher strain rates can be obtained for MAT162 whose reference strain rate is mandatory at 1/s. This method is employed in this study. Those strength inputs

controlled by C_{rate1}, namely S_{AT}, S_{AC}, S_{BT}, S_{BC}, S_{FC} and S_{FS} are assigned with their values at 1/s, all of which, according to Eq. (5-10), are 1.513 times higher than the corresponding QS values. The strain rate scaling factors for GF-1 composite are summarised in Table 5-5.

Table 5-5 The strain rate scaling parameters for GF-1.

Strain rate scaling parameters	Value
C_{rate1}	0.0453
C_{rate2}	0
C_{rate3}	0
C_{rate4}	0
Adjustment Factor for S_{AT}, S_{AC}, S_{BT}, S_{BC}, S_{FC} and S_{FS}	1.513

5.2.4 Assessment of the input sets under high rate loadings

In Sections 5.2.2, four sets of input data were determined that provide good accuracy of predictions in their specific loading conditions. Before carrying out an impact modelling at plate or component scale, it is necessary to check whether they provide reasonable predictions under other types of loading, in particular, when the strain rate dependency, as defined in Section 5.2.3, is taken into account. In this section, the four sets of input data were adjusted according to Table 5-5 for high strain rate dynamic analysis. The single element model under four uniaxial loading cases at a strain rate of 5000/s were simulated, namely tension in the weft and the warp direction, and compression in the weft and the warp direction. Their stress-strain curves with the four input sets are shown in Figure 5-7.

5.2.4.1 'T1M1' and 'T2M1'

The properties in data sets 'T1M1' and 'T2M1' were determined to represent the bilinearity of the QS stress-strain curves under tensile loadings. The damage onset stress values, which were used as the tensile strength inputs, were scaled at dynamic strain rates. However, the scaling factors determined in QS and SHPB tests reflect the strain rate effects on the measured maximum stress. Therefore, they should only be applicable for scaling the maximum stress values. With the input sets 'T1M1' and 'T2M1', the maximum stress is

controlled by element deletion. Tensile stress-strain curves in Figure 5-7 (a) and (b) show that these two sets of input data fail to provide reasonable control of maximum stress. Therefore, the element deletion parameters, which were calibrated for QS tension, need recalibration to match the desired maximum stress levels, which are illustrated by the dashed lines in each figure.

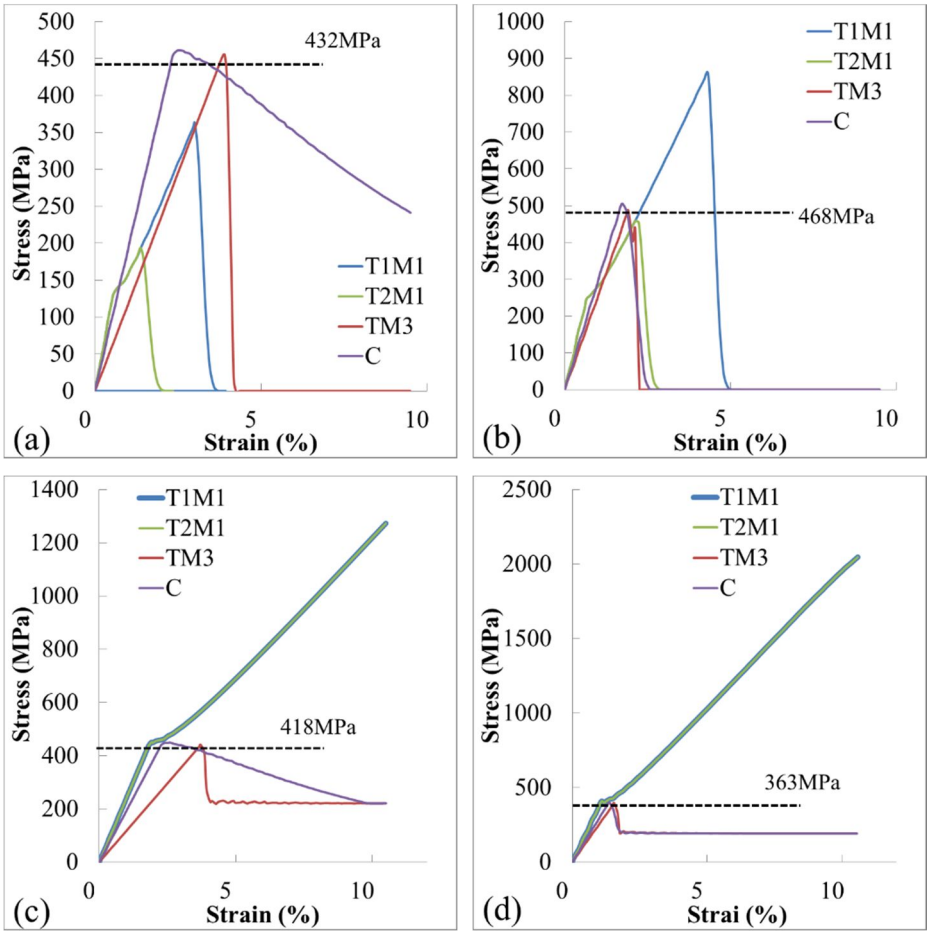


Figure 5-7 The stress-strain curves of the four sets of input data under dynamic uniaxial (a) weft tension, (b) warp tension, (c) weft compression and (d) warp compression.

The compressive behaviour predicted with these two data sets is even less accurate, as can be seen from stress-strain curves in Figure 5-7 (c) and (d). In particular, under the loading in the weft direction, the damage behaviour both under tension and under compression is controlled by the same damage evolution parameter AM1. As a consequence, the compressive stress-strain curves also become bilinear, which was not the case in the experiment. In addition, the element deletion, based on tensile strain that controls the maximum stress, is not triggered under the compressive loading. As can be seen in Figure 5-7 (c) and (d), under the dynamic compression, material failure is not predicted

even when the stresses calculated with ‘T1M1’ and ‘T2M1’ reach unrealistically large values.

5.2.4.2 ‘TM3’ and ‘C’

The properties in data sets ‘TM3’ and ‘C’ define material as linearly elastic until the maximum stress. The maximum stresses are the strength inputs, hence, the maximum stresses in all four dynamic loading cases are very close to the values calculated according to Eq. (5-10).

The differences between the tensile and the compressive moduli are apparent under loading in the weft direction, as can be seen in Figure 5-7 (a) and (c). However, in terms of strain energy density (area under the curves), the difference is substantially more significant after the maximum stress. In Figure 5-7 (a), the tensile stress calculated with ‘TM3’ drops to zero abruptly, once the maximum stress is reached, which is very similar to the failure mode observed experimentally. However, the tensile stress calculated with input set ‘C’ decreases gradually beyond the failure point, due to the small value of its damage parameter, which approximates the gradual stiffness degradation in the weft compression. This gradual degradation is not consistent with the tensile experiment. If used, the input set ‘C’ can put the simulation in the danger of significantly exaggerating strain energy and consequently ballistic impact resistance.

On the other hand, the abrupt drop of stress predicted with ‘TM3’ for the weft compression in Figure 5-7 (c) contradicts the experimental observation of residual compressive strength. However, potential underestimation of the strain energy due to this abrupt failure can be compensated by adjusting the residual strength, i.e. the stress values at the plateaus, or by delaying element deletion, i.e. elongating the plateaus.

5.2.4.3 Summary for the assessment

The assessment of four sets of input properties revealed that ‘T1M1’ and ‘T2M1’ inputs, which explicitly defined the bilinear-like material behaviour after the damage initiation, are unsuitable for defining the material response at high strain rates. With small damage parameters such as those of the input set ‘C’, unrealistic stress degradation beyond the maximum tensile stress was obtained. This can result in significant overprediction of the ballistic impact

resistance. The reasonable predictions of high strain rate material response were only achieved with 'TM3', which will be employed to carry out impact simulations. The full set of properties 'TM3' is given in Table 5-6.

5.2.5 Discussions

In the process of determining the input parameters for MAT162, the limitations of MAT162 were revealed. First of all, there is no good way of modelling the bilinear tensile elastic behaviour in MAT162. The only method of representing the bilinear behaviour that could be identified was to assign negative values to the appropriate damage parameters, which results in an increase in stress beyond the damage onset point. However, no option is available to explicitly define the ultimate stress. The element deletion criteria were used for this purpose in present study, which allowed to obtain a good agreement between the experiment and predictions for one specific loading case, while failed to deliver reasonable predictions under other types of loading. Because of that, a conservative modelling approach has been taken, where the tensile behaviour was considered to be linearly elastic until the maximum stress. To approximate the strain energy density better, the secant modulus at the maximum stress should be used instead of the real elastic modulus from experiment.

In addition, in the current version of MAT162, the in-plane tensile and compressive behaviour can only be described by a single damage evolution parameter. Hence it is not possible to define within the same model abrupt final failure under tension, and gradual stiffness degradation under compression, as observed in the experiments. As conservative predictions are preferable, both tension and compression can be modelled as brittle, by assigning a large positive value to the damage evolution parameter. If necessary, the underestimated strain energy under compression can be easily compensated by adjusting the residual compressive strength.

Finally, assigning the rate sensitivity to the material properties is not straightforward, due to the mandatory reference strain rate of 1/s. Furthermore, the strain rate dependency in MAT162 model is controlled by an insufficient number of scaling factors. Specifically, six strength parameters are all scaled by a single factor. Under such a simplification, the strain rate factors are more like

calibration parameters one can manipulate rather than descriptions of the real strain rate dependency.

Table 5-6 The MAT162 inputs for GF-1 and CF-IM7.

Input	GF-1	CF-IM7	Unit
RO	1.851×10^{-9}	1.458×10^{-9}	ton/m^3
EA	7.820	62.71	GPa
EB	16.78	18.32	GPa
EC	13	9.32	GPa
PRBA	0.1453	0.037	
PRCA	0.1919	0.015	
PRCB	0.2703	0.01	
GAB	4.032	3.85	GPa
GBC	4.002	5.83	GPa
GCA	6.695	3.05	GPa
SAT	312.61	1145.80^1 or1586.72^2	MPa
SAC	301.40	408.32^1 or 565.44^2	MPa
SBT	338.40	580.07^1 or 803.29^2	MPa
SBC	262.45	155.79^1 or 215.74^2	MPa
SCT	50	50	MPa
SFC	523.89	331^1 or 430^2	MPa
SFS	2000	4000^1 or 6000^2	MPa
SAB	47	47	MPa
SBC	50	50	MPa
SCA	50	50	MPa
SFFC	0.5	0.3	
E_LIMT	2	2	
S_DELM	1×10^{-9}	1×10^{-9}	
ECRSH	0.1	0.1	
EEXPN	4	4	
CRATE1	0.0453	0.0365^1 or 0.0635^2	
AM1	100	100	
AM2	100	100	
AM3	100	100	
AM4	-0.3	-0.3	
CRATE2	0	0	
CRATE3	0	0	
CRATE4	0	0	

1. Adjusted inputs for the strain rate scaling factor determined from weft compression;
2. Adjusted inputs for the strain rate scaling factor determined from warp compression.

5.2.6 Inputs for CF-IM7

The material property input for CF-IM7 composite was determined following the same calibration procedures as was adopted to obtain the input sets 'TM3' and 'C' for GF-1 composite. As can be seen from the stress-strain curves shown by Figure 5-8, good agreement was achieved between the experimental tensile stress-strain curves and those calculated for a single element model with 'TM3' in **Error! Reference source not found.**. Similarly, good approximation was achieved with 'C' for the compression test data as shown in Figure 5-9.

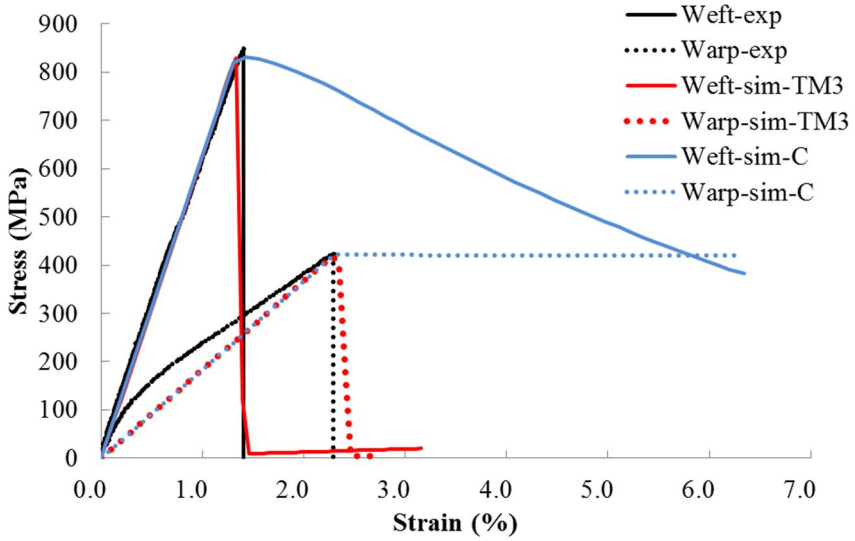


Figure 5-8 The stress-strain curves of single element tension model for CF-IM7 when the data set 'TM3' is used. In the curves with the suffix 'C', only the damage parameters are changed into the compressive ones.

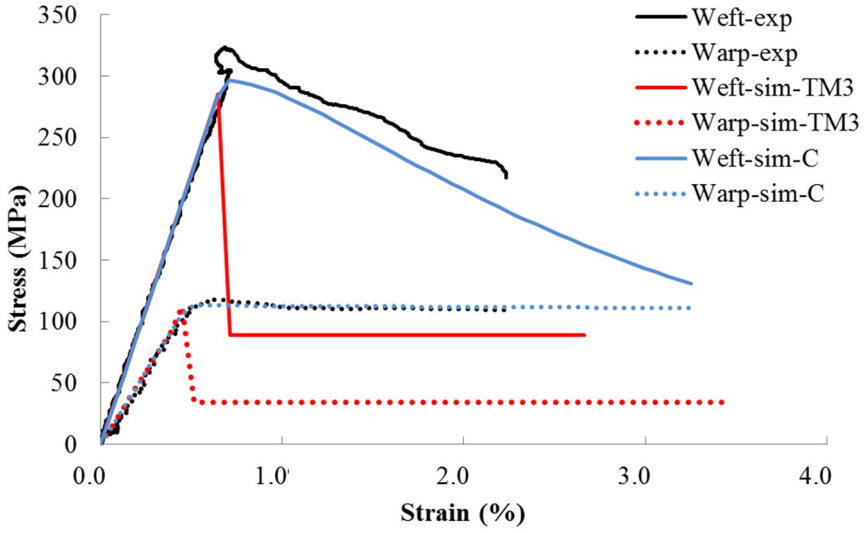


Figure 5-9 The stress-strain curves of single element compression model for CF-IM7 when the data set 'C' is used. In the curves with the suffix 'TM3', only the damage parameters are changed into the tensile ones.

However, predictions of compressive behaviour with the damage evolution parameters of 'TM3' (the curves denoted "sim-TM3" in Figure 5-9), and predictions of the tensile response with the damage evolution parameters of 'C' (the curves denoted "sim-C" in Figure 5-8), were rather inaccurate due to stiffness degradation both under tension and under compression being controlled by a single damage evolution parameter. Therefore, the set which provides conservative predictions, i.e. 'TM3', was chosen for the subsequent studies.

5.3 Simulation of the ballistic impact tests

Full sets of input data for MAT162 have been determined so far. In this section, they are used for simulating the ballistic impact tests of GF-1 and CF-IM7 plates in Chapter 4.

5.3.1 Methodology

The composites for the plates were regarded as monolithic materials whose behaviour is described by MAT162. Three impact tests, whose impact velocities were respectively lower, slightly higher and much higher than the extrapolated ballistic limit, were simulated for each of GF-1 and CF-IM7 materials. The impact and residual velocities of these tests are marked as underlined in Table 4-2. In the ballistic impact tests of plates, the area exposed to impact is a 100 mm diameter circle. Hence, for the impact simulations, a finite element model of a circular composite plate was generated as shown in Figure 5-10.

Although the material and the loading are symmetric, the model was not simplified to its half or quarter in order to avoid complication of element deletion due to symmetry. The boundary conditions were applied by fully constraining the nodes along the periphery of the circular plate. The plate was meshed with single integration point hexahedron solid elements. Hourglass energy monitoring was switched on and stiffness-based hourglass control (Type 2 of Flanagan-Belytschko) provided by LS-DYNA was employed. In the experiments, the projectile was a steel ball bearing of 6.35 mm in radius, which was modelled as a rigid body of the same dimensions in the FE model. It was assigned an initial velocity along the x-axis, which is through the thickness direction of the plate. The weft direction is aligned with the y axis and the warp direction is aligned with the z axis. The contact between the plate and the

projectile was modelled by using the single surface contact with element deletion. In the single surface contact algorithm of LS-DYNA, the slave surface is defined by a list of parts and no master surface needs to be defined. When using this contact algorithm, only one contact definition is required to define all the contacts of multiple parts. In addition, this algorithm also considers the self-contact of each part, which needs to be accounted for when modelling the FBO, since the generated fragments can interact with each other. The friction coefficient was set to zero for initial analysis as recommended in [199] for one global contact which includes several components.

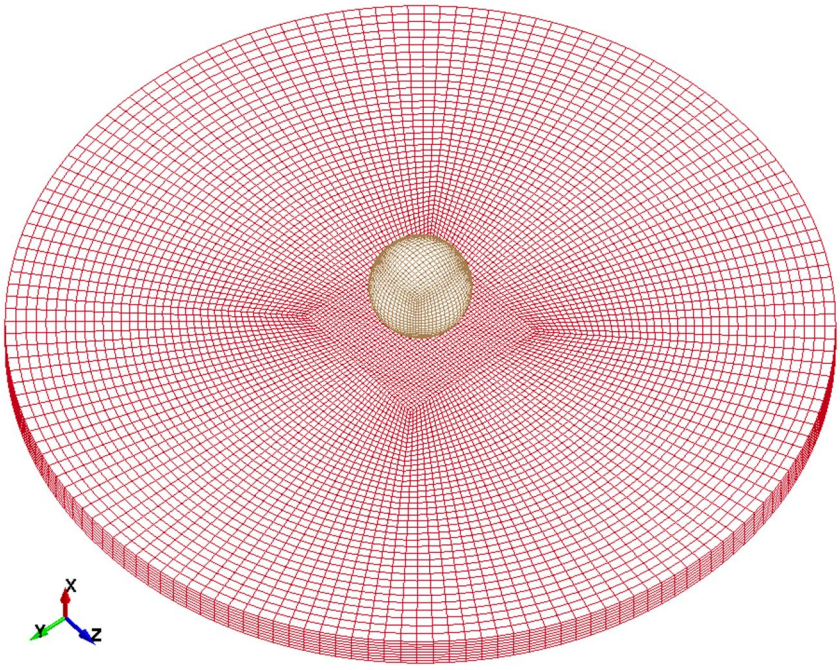


Figure 5-10 The LS-DYNA model for the ballistic impact tests.

A mesh sensitivity study was performed to determine an appropriate mesh density for this simulation. The number of elements in the plate was varied and the mesh of the projectile was altered accordingly to ensure a similar mesh size. The result of the sensitivity study is shown in Figure 5-11 with respect to the predicted projectile residual velocity vs. the number of element in the plate.

It can be seen that velocity predictions changed less than 2 m/s (4%) when the number of the elements exceeded 6.4×10^4 (the red marker). Therefore, the mesh which has 6.4×10^4 elements was used for the subsequent simulations. The corresponding mesh is shown in Figure 5-10. The central 20 mm × 20 mm square region was meshed with the uniform element size of 0.5 mm × 0.5 mm. The model had eight layers of elements in the thickness direction.

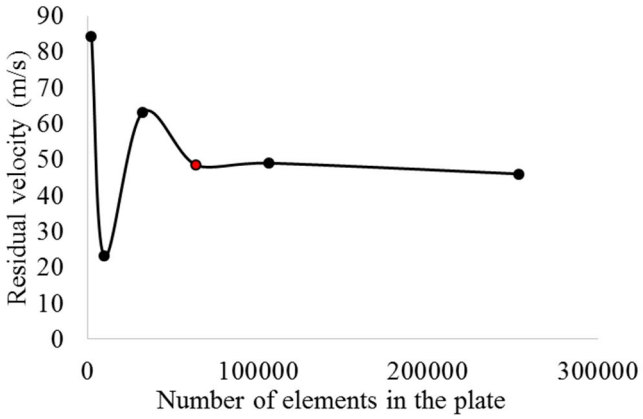


Figure 5-11 A mesh sensitivity study for modelling the plate impact test of CF-IM7.

An artificial neural network (ANN) model from multi-scale modelling

Following the dominating multi-scale approach for modelling 3D textile composites, the parallel PhD project [8] is targeted at developing reliable material models for macro scale simulation. This approach is concluded into a user-defined subroutine in LS-DYNA to deliver a macro scale material model (referred to as the ANN model in the following). As a comparison to MAT162, this ANN model is also employed for modelling the same impact tests. Except for the material model and its inputs, the plate impact models of ANN are the same as the MAT162 ones in every aspect. This study also serves to validate the whole multiscale modelling methodology incorporating ANN.

The development of this model starts from micro scale, where the unit cell composed of a single fibre and surrounding matrix is analysed to provide the properties of fibre yarns. Subsequently, the yarn properties are used in the analysis of a meso scale unit cell, which represents the smallest repeating unit of a textile composite. Then, this meso scale unit cell is employed in cooperating with an artificial neural network (ANN), which is essentially a sophisticated interpolation method, to establish the failure envelope for the macro scale model. The key procedures of these developments along with simple validations are provided in Appendix 1.

5.3.2 Velocity prediction

In the simulation results, the history of hourglass energy was commonly found to be less than 5% of the total energy, which indicates a valid dynamic analysis for reduced integration elements. The results in terms of residual velocities against the impact velocities are shown in Figure 5-12 together with

the ones from the experiment (Exp). The prediction bands of the ballistic impact tests on GF-1 and CF-IM7 are also included as the dashed lines and the dotted lines respectively.

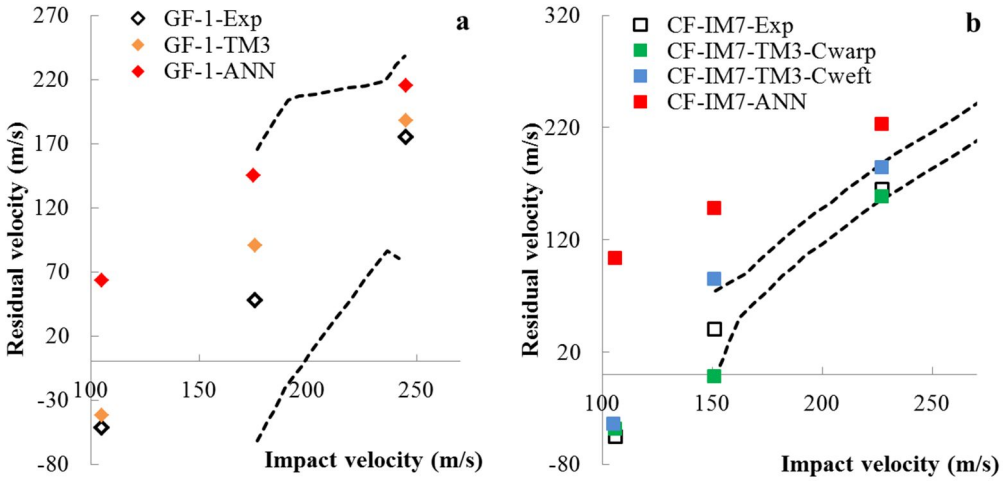


Figure 5-12 The residual velocities from the simulations with MAT162 and comparison with experimental results for (a) GF-1 and (b) CF-IM7. The prediction bands of the ballistic impact tests are shown as the dash lines.

It can be seen that, both ANN and MAT162 were able to capture the two trends of experimental results: (1) the impact resistance of CF-IM7 is less than GF-1; and (2) more energy is dissipated at higher velocity. However, all the residual velocities from the ANN simulation are substantially higher than the experimental results, indicating significantly conservative predictions of the impact resistance of the plates. Especially for CF-IM7, only a tiny impact resistance was predicted. The projectile still had 104 m/s of residual velocity V_r when impact velocity V_i was 106 m/s, V_r = 148 m/s for V_i = 151 m/s and V_r = 223 m/s for V_i = 228 m/s. The reasons for these discrepancies are beyond the scope of this thesis. Compared with the multiscale approach represented by this ANN model, the macro scale modelling approach in this thesis with MAT162 and the calibrated data show much better agreement with the experimental results with respect to the residual velocities.

For GF-1, the predicted residual velocity is 188 m/s at V_i = 245 m/s, 13 m/s higher than the experiment, indicating 41% of the initial energy is dissipated during the impact. This prediction is 8% lower than the experimental result. At V_i = 105 m/s, the simulation predicts projectile rebounding with 16% of the initial energy, compared to 24% in the experiment. The largest disagreement to the experiment in Figure 5-12 (a) is at V_i = 176 m/s. The experiment indicates

92.6% of the initial energy was dissipated during the impact, while the simulation predicted a dissipation of 73.4% with an underestimation of 19.2%. Given the scattered experimental results, especially close to the ballistic limit where the prediction band becomes wider indicating more uncertainty than the other ranges of velocities, the discrepancy is regarded as acceptable.

For CF-IM7, the prediction bands are narrower. At V_i = 151 m/s, the input set based on the strain rate dependency of weft direction (with the suffix 'Cweft') shows a significant discrepancy to the experiment. The weft direction behaves depending on the straight carbon fibres which are known as strain rate insensitive. By using it for impact simulation, the energy dissipation capability enhanced by strain rate sensitivity of the other loading directions was underestimated and consequently the impact resistance was underpredicted. On the other hand, the set with the strain rate dependency of warp direction (with the suffix 'Cwarp') gives much better results at all the three velocities. When using 'Cwarp', the largest discrepancy happens at V_i = 151 m/s. The predicted residual velocity is 2 m/s, which is 39 m/s less than the experiment. But in terms of energy dissipation, the discrepancy is only 7% of the initial energy. Clearly, 'TM3-Cwarp' is more appropriate for further modelling of impact on CF-IM7 structures.

Besides suggesting the choice of input sets, more importantly the figure indicates the accuracy achieved in predicting the residual velocity via this methodology. In spite of the simplifications and assumptions involved when modelling 3D woven composites with MAT162, by calibrating the single element model against the QS tests and considering the proper strain rate effects, conservative but acceptably accurate predictions can be made about the impact on these plates at various velocities. The method therefore brings the possibility of studying the application of 3D textile composites to fan containment casings using phenomenological macro scale FE analysis.

5.3.3 Prediction of damage and failure

The generalised Hashin failure criteria are implemented in MAT162 as Eq. (5-1) to (5-9). The values of *f* in these equations are informative about failure and damage. Failure takes place when *f* becomes 0. After that, the larger *f* is, the more severe the damage is. Taking advantage of this feature, the damage

prediction of MAT162 was examined via the fibre failure in both in-plane directions and matrix failure due to in-plane shear stress. The fibre crush failure is always localised within the impact vicinity and is therefore excluded.

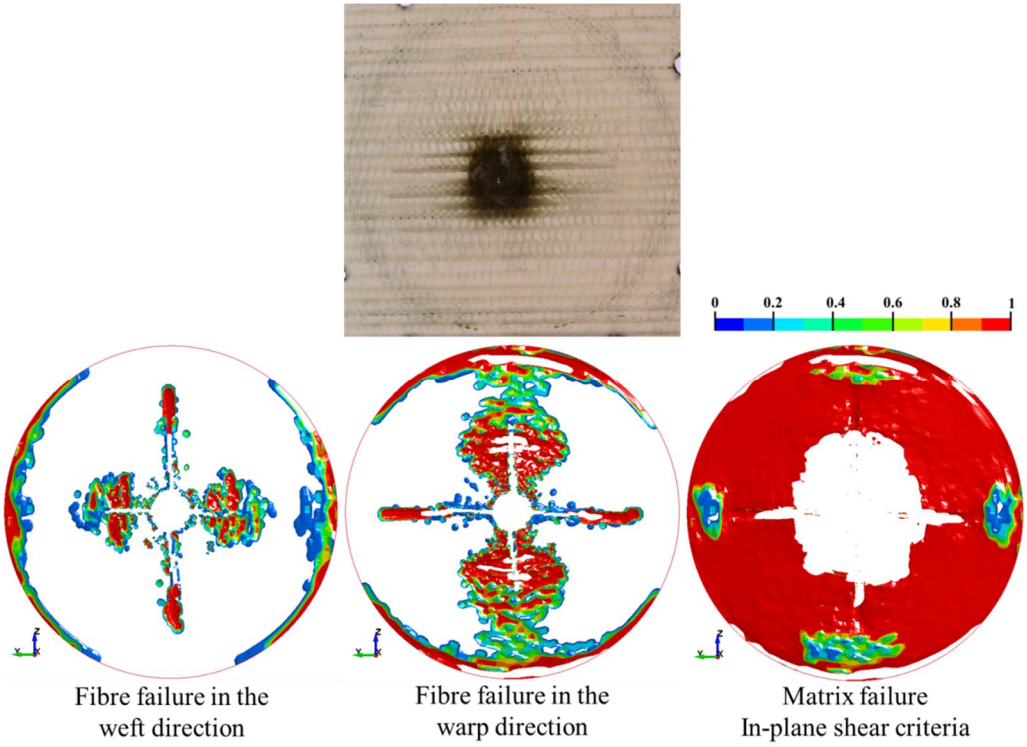


Figure 5-13 Comparison between simulation and experiment for the failure on the penetrated plate of GF-1 impacted at 176 m/s, viewed from the back fact of impact. Y (green) is the weft direction and Z (blue) is the warp direction.

The prediction about damage and failure on the penetrated GF-1 plate at V_i = 176 m/s is viewed from the back face of impact in Figure 5-13. The contour scale is from zero to unity, which corresponds to intact and failed/damage-initiated elements, respectively. The extent of the transparent regions in the contours is indicated by their boundaries. The weft direction is aligned with the Y axis and the warp direction with the Z axis.

Compared with the experiment, the first contour shows that the extended failure in the weft yarns is captured with slight exaggeration in ±90° directions. The fibre failure around the periphery indicates significant local stress, which could be one of the causes for the matrix cracks in the experiment. For the fibre failure in the warp direction as shown by the second contour, the failure area is over predicted. Clearly, the tensile stress based failure criterion is not accurate for the crimped fibres in the warp direction. Before transferring significant tensile loadings, the crimped fibres need to be straightened. The visual

inspection shows that matrix cracks spread widely in the tested plate. This is captured by MAT162 in the third contour, where the predicted matrix failure is all over the plate.

In a similar way, contours of a quarter of the CF-IM7 plate at V_i= 151 m/s are displayed in Figure 5-14, to study the prediction in the through-thickness direction and the process of failure during the impact. Each mode is displayed at four stages from the first contact in the first row to the full penetration in the last row. The development of the three modes shares a lot in common. Take the first column, the fibre failure in the weft direction, as an example, it starts right under the projectile when indention begins. As the projectile starts to penetrate, the failure first takes place along the weft direction on the back face of the impact, which is blue when viewed from the front face but is red from the back face. Then, in the next stage, failure appears and develops around the boundary and near the front face, until the last stage, where the plate has been fully penetrated.

Compared with the XCT results, again, the area for the warp fibre failure is exaggerated by the prediction. In addition, MAT162 does not have criteria to account for yarn/matrix debonding, which is a very important mode in the XCT observation. However, these contours show an important characteristic, which is also found in the XCT, that all the damage modes are more extended near the back face.

From both comparisons, it can be concluded that the prediction of MAT162 dose qualitatively show some important characteristics of failure and damage which happened during the impact on the 3D woven composites. However, the predictions tend to exaggerate the area of damage and should be viewed with care.

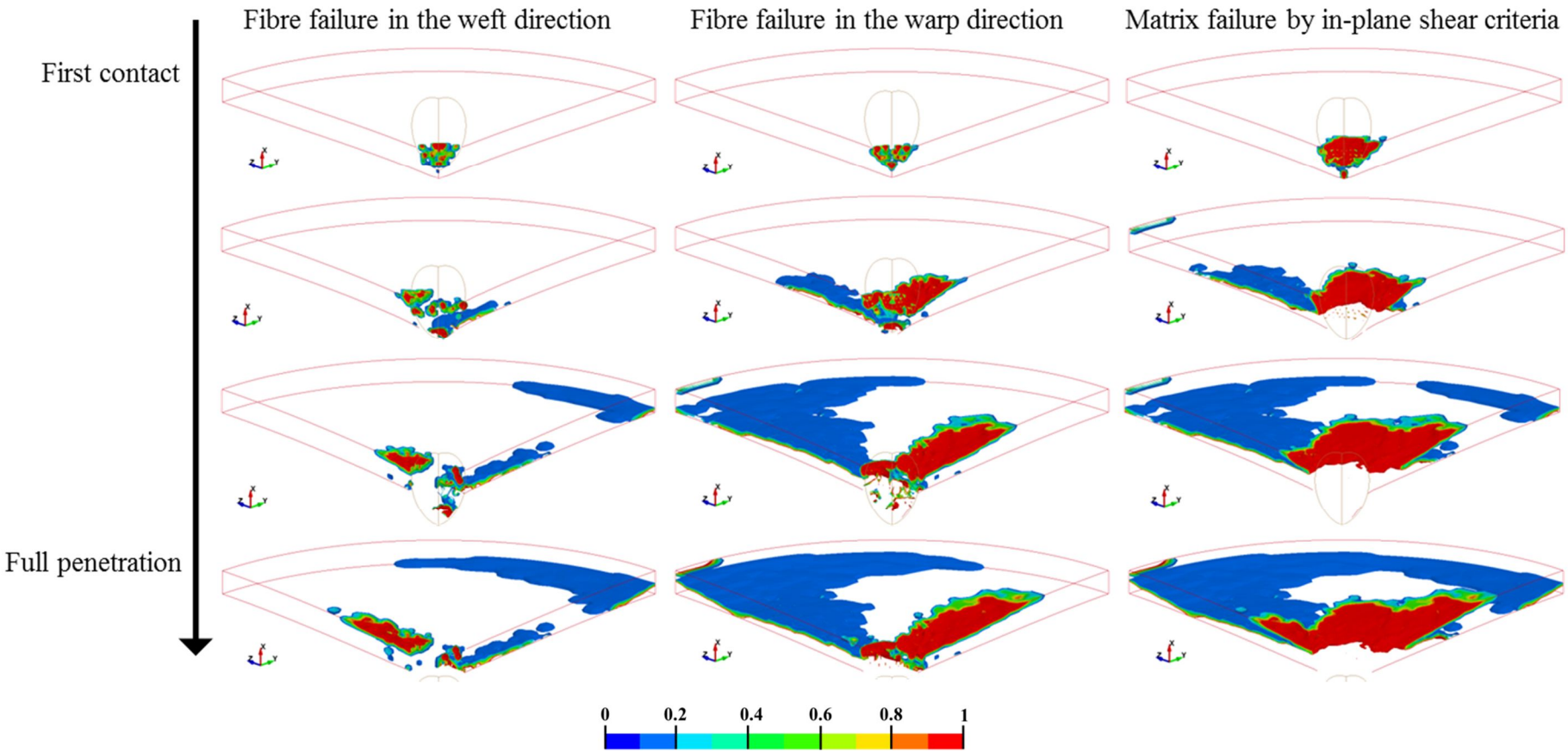


Figure 5-14 The three failure modes at their four stages on the CF-IM7 plate impacted at 163 m/s. A quarter of the plate is displayed. Y (green) is the weft direction and Z (blue) is the warp direction.

5.4 Conclusions

In this chapter, several limitations of MAT162 are revealed. The current version of MAT162 is not able to model the bilinearly or nonlinearly increasing stress-strain behaviour properly. To better represent the strain energy dissipated before the final failure, the secant moduli at the maximum stresses should be used. At the same time, MAT162 provides only one modulus input and one damage coefficient for one principle direction. Emphasis on the abrupt tensile failure may lead to underestimated compressive behaviour and consequently energy dissipation capability, while emphasis on the ductile compressive failure may lead to overestimation. And care should be taken when determining the strain rate coefficients, as the mandatory reference strain rate in MAT162 is 1/s. Using the QS properties and the associated scaling factors as the input parameters, like it was done in some previous studies, results in incorrect definition of dynamic properties and underestimation in the impact resistance.

After finding out the proper method and input data for MAT162, the ballistic impact tests of the GF-1 and CF-IM7 plates were simulated. Compared with the current ANN model developed via multi-scale modelling, this phenomenological modelling approach provides better prediction and accuracy. Although the failed area is exaggerated, some important characteristics of the failure and damage caused by impact loadings are captured by the simulation. The approach is therefore considered as viable and employed for studying the application of 3D textile composites to fan containment casings.

Chapter 6 Parametric study for plate impact tests

6.1 Introduction

In the ballistic impact tests described in Chapter 4, the spherical projectile impacted the flat plates normal to the surface. However, the fragmentation of the fan blade during FBO generates high velocity debris of various shapes. Even at the same velocity, these fragments can show different types of interaction with the casing. Specifically, sharp projectiles are likely to be more efficient in penetrating the casing, than the blunt ones. In addition, during the FBO, the released blade has a large circumferential momentum due to the rotation of the fan assembly. The impact on the casing could be at various oblique angles, rather than just normal to the surface. Also, quite different from flat plates, casing rings are curved structures.

It is evident that the entire complexity of the loading and failure modes taking place during the FBO event cannot be captured by testing and analysing the flat plate impacted at 90° by a sphere. Specifically, the failure related to the projectile shape, the obliquity and casing curvature may not be represented by such a simple case. In this study, the influence of projectile shape, impact obliquity and target curvature on damage and failure of textile composite plates was investigated by conducting appropriate parametric studies. A literature review is provided to present the severe deficiencies of research in this respect.

6.2 Literature review

6.2.1 Projectile Shape

A number of studies have been carried out to investigate the effects of projectile shape on the impact response of laminated composites during ballistic tests. Wen [200, 201] studied the high velocity penetration of several laminated composites by using flat-faced, hemispherical-tip, conical-tip and truncated-cone-nose projectiles. For predicting the ballistic limits, analytical expressions were proposed, which employed an empirical constant in combination with the energy balance. By using this analytical methods, good agreement with the experimental results was reported for laminated composites [202-204]. Ben-Dor et al. [205] generalised Wen's approach to determine the most efficient nose

shape for penetrating fibre reinforced plastics. It was concluded that the sharp cone and ogive nose shapes were actually less efficient in penetration than blunt tip projectiles. Later experimental studies [202, 203, 206] suggest that the effect of projectile shape is strongly dependent on the target material.

Ulven et al. [202] studied the effect of projectile shape through ballistic tests on VARTM manufactured satin weave carbon/epoxy laminate composite plates. Flat cylinder, fragment simulating projectile (FSP) and cylinders with hemispherical tip and conical tip were used. This study concluded that the conical projectile was the least efficient in penetration, followed by flat, hemispherical and FSP.

Jordan and Naito [203] carried out ballistic impact tests by using 2.85g FSPs with eight different nose shapes on plain weave E-glass/Phenolic laminate plates. The nose shapes were chisel, standard .30 calibre FSP, modified .30 calibre FSP, 120° cone, right circular cylinder, hemisphere, cube and parallelepiped. Plates of three thicknesses were tested. The plates were less resistant to the FSPs with the sharper nose, such as hemispherical and chisel, whilst those with a flat surface at the nose (cube and parallelepiped) were the least efficient in penetration. This conclusion about the shape effect is opposite to the one made in studies [202] and [205], where the projectiles with sharp nose shapes were found to be the least efficient in penetration. All these studies were carried out on 2D laminated composites. No account could be found in the open literature regarding the projectile shape effects for 3D composites.

A number of studies [192, 202, 203] suggested that the projectile shape effect is related to target thickness. Penetration of thin plates was found to have little relation with the projectile shape. During impact of thin plates the largest portion of energy is dissipated via the plate bending, regardless of the projectile shape. In thicker plates, the various projectiles can induce different failure mechanisms. In these studies, the thickness was varied, while the span was kept constant. However, in terms of bending, the ratio of span to thickness is of greater importance than the thickness alone. A plate of the same thickness could be prone to bending when the ratio is large, and be resistant to bending when the ratio is small. If the thickness and the ratio are changed simultaneously, it is not appropriate to conclude that the shape effect is related to the target thickness, rather than the ratio.

6.2.2 Obliquity

Most of the research into impact response of composites has been conducted considering the normal impact. Even for laminated composites, oblique impacts are rarely reported [207-212].

Lamontagne et al. [207, 208] conducted oblique tests on carbon/PEEK laminates at hypervelocity, which is beyond the range of velocities relevant to the aero engine applications.

López-Puente et al. [209] carried out ballistic impact experiments on AS-4 carbon fibre/8552 epoxy laminates, in which impact was applied at two angles, 0° (normal impact) and 45° at velocities ranging from 70 to 531 m/s. The ballistic limits and the extent of damage as determined experimentally were employed to validate the finite-element simulation, in which laminate constitutive behaviour was prescribed via a damage model. Once validated, the finite element model was employed to study the impact at different oblique angles. The study showed that the ballistic limit increased with impact obliquity. Meanwhile, the extent of damage due to oblique penetration was larger than that due to the normal penetration, while the opposite was true for the velocities below the ballistic limit. Similar conclusions were made by Pernas-Sánchez et al. [210], where impact tests on quasi-isotropic carbon/epoxy laminates were performed at 0° and 45° and then an analytical approach was proposed to investigate the other obliquities.

Hazell et al. [211, 212] also studied the oblique impact at 0° and 45° for carbon fibre reinforced plastics laminates. It was reported that more of the projectile kinetic energy was transferred to the target than in normal impact. The authors suggested that this were merely due to a geometrical effect, namely, the projectile needed to penetrate a greater thickness during oblique impact. After normalised to the plate thickness, the amount of energy absorbed were similar in the panels impacted at 0° and 45°.

6.2.3 Curvature of the target

There are many publications on the impact of curved composite structures, for example those reported in [213-217]. Most of them focused on 2D laminated composites, and considered only the low velocity impact cases. No account could be found regarding the effect of curvature for 3D composites at high

velocities.

Some interesting findings were reported for laminated composites. Kim et al. [216] developed a finite element technique utilising a modified Herzian contact law and applied it to investigate the effect of curvature on the impact response of composite laminates. The contact force during impact was found to be larger for plates with higher curvature. This was further interpreted as more kinetic energy being dissipated in the plates with larger curvature in the recent study [218]. However, it was pointed out in [219] that the effect of curvature is only significant when curvature is high. It is of interest to find out whether these findings still hold for 3D woven composites at high velocities.

6.2.4 Conclusions

Most of the research into the effect of projectile shape, impact obliquity and target curvature was focused on 2D laminated composites. It is unclear whether the conclusions in these researches are also applicable for 3D composites. Moreover, the available studies indicate that the effect of projectile shape is strongly dependent on the target material. A parametric study on these factors for the 3D woven composites should be carried out.

6.3 Methodology

The parametric study was conducted numerically in LS-DYNA for CF-IM7 composite targets by using MAT162, for which the values of input parameters were determined in Chapter 5. Finite element model was generated to represent the ballistic impact tests as described in Chapter 4. Specifically, the target was 4 mm-thick circular plates with 100 mm in diameter. In addition to that, models of circular plates with 50 mm and 200 mm in diameters were generated to study the effects of the span to thickness ratio. All plates were fully constrained along their peripheries. The contact algorithm and hourglass control were the same as those applied for the models in Chapter 5. Five types of rigid projectiles were considered. Their shapes and dimensions are shown by Figure 6-1. The spherical projectile is exactly the same as the one used in the experiment: 12.7 mm in diameter and made of steel. Its projection on the target is a 12.7 mm-diameter circle. There is no doubt that the volume of material right under the projectile would have influence on the test results. Given constant thickness, the projected

area was kept constant for different projectile shapes in this study, namely, the diameters of the conical, FSP and cylindrical projectiles were also 12.7 mm. The tip of a NATO .50 fragment simulator calibre was used for the FSP. In addition, all projectile masses were kept constant at 8.6 grams so that the kinetic energy was also constant when fired at the same velocity V_i.

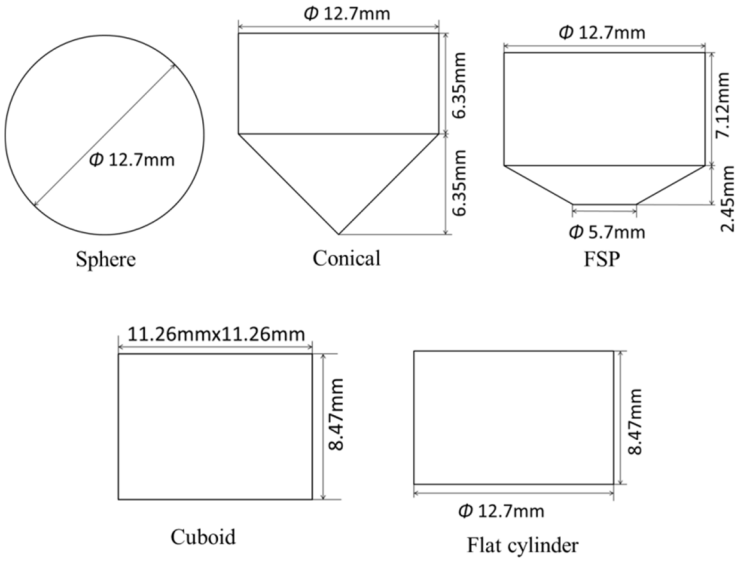


Figure 6-1 The dimensions of the projectiles.

Four values of initial velocities were assigned to the projectiles, namely 106 m/s, 151 m/s, 181 m/s and 227 m/s. These were the impact velocities measured by the high speed camera in the ballistic tests. The limit velocity was estimated to be 146 m/s and both the projectile rebounding and the penetration were simulated.

The effects of impact obliquity were investigated by using the 100-mm-diameter plates and the spherical projectile. The impact angle hereby is defined as the acute angle between the impact velocity vector and the normal direction of the plate. Five oblique impacts, namely at 15°, 30°, 45°, 60° and 75°, were simulated, along with normal impact (0°). The projectile was carefully placed so that the first contact took place right at the centre of the target plate. In this study, only the impact in the plane of material axes 1 and 3, as shown by Figure 6-2, is considered. The resultant impact velocity V is decomposed as the normal velocity V_N parallel with the material axis 3, and the tangential velocity V_T parallel with material axis 1. The material is orthotropic and unbalanced in the in-plane directions. The situation, where V_T is parallel to axis 2 or any other in-

plane direction between 1 and 2, is not considered.

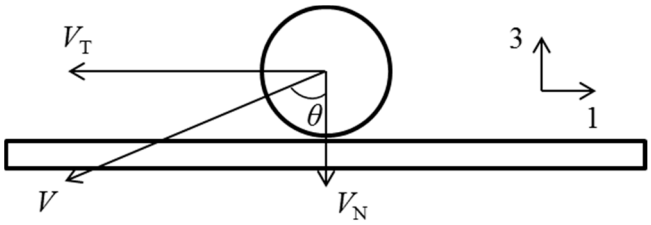


Figure 6-2 A schematic for the oblique impact model with indication of material axes.

It is apparent that the value of normal velocity V_N needs to be sufficiently high for the occurrence of penetration. Otherwise, penetration would not occur even at large V_T and V, in which case the projectile would essentially slide along the surface of the target. Therefore, V_N was kept constant and consequently V_T and V increase sharply at small impact angles. Two values of V_N, i.e. 106 m/s and 151 m/s, were used for each impact angle.

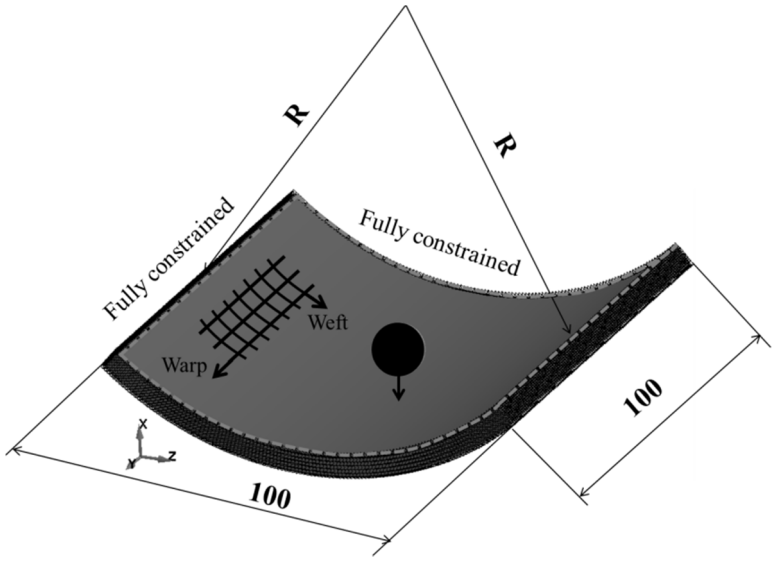


Figure 6-3 A schematic for the models with curved target plates.

The full scale fan casing in this study is represented by a ring of 2000 mm inner diameter, 20 mm thickness and 750 mm height. It is practically and financially difficult to test such a large component for research purposes. As a feasibility study for the larger project, 4:1 scaled ring prototypes of the casing have been manufactured [220]. Potential ballistic tests could be performed on these rings or parts of them, but it should be noticed that they are more curved than the full-scale casing. Their degree of curvature was used as a baseline for investigation of the effects of curvature to impact, the numerical tests were performed on curved plates representing the segment of a cylinder as shown by

Figure 6-3. Herein, the ratio of curvature radius, *R*, to span, *S*, is used as an indication of the degree of curvature. A smaller value of *R*/*S* means the plate is more curved. In addition to the ratio of 2.5 for the baseline model and 10 (*R* = 1000 mm) for the full scale fan casing, plates with ratios of 0.75 (*R* = 75 mm), 1.25 (*R* = 125 mm) and 3.75 (*R* = 375 mm) were also studied.

The plates were fully constrained along their four edges and impacted normally at the middle of the span and width by the above spherical projectile at 151 m/s. Material coordinates were carefully assigned so that the through-thickness direction of the material is pointing to the centre of the curvature for each element.

6.4 Results and discussion

6.4.1 Shape of projectile

6.4.1.1 Results summary

The residual velocities of the projectiles are plotted against the impact velocities in Figure 6-4 (a), (b) and (c), showing the effects of projectile shape for 50 mm, 100 mm and 200 mm plates, respectively. At the same impact velocity, the residual velocity is lower if the plate is more resistant to impact.

In all three cases, the curves for the flat cylinder are clearly above the others, indicating larger residual velocities for the same initial velocity. As shown in Figure 6-4 (b) and (c), at impact velocity of 106 m/s, this type of projectile rebounds from the 100 mm and 200 mm plates, and its rebounding velocity is apparently lower than those of the projectiles of other shapes. The rebounding of the projectile is due to the kinetic energy stored in the plate transferring back to the projectile. Rebounding velocity, i.e. negative residual velocity, could therefore be considered as an indication of this energy. In Figure 6-4 (b), for the flat cylinder, almost no energy was stored by the plate. At the other extreme, one third of the initial kinetic energy (48 J) was stored in the plate when impacted by the spherical projectile. These observations counter-intuitively suggest the cylinders with flat faces are more effective in penetration and damaging the target plate than the pointed projectiles, e.g. the conical projectile.

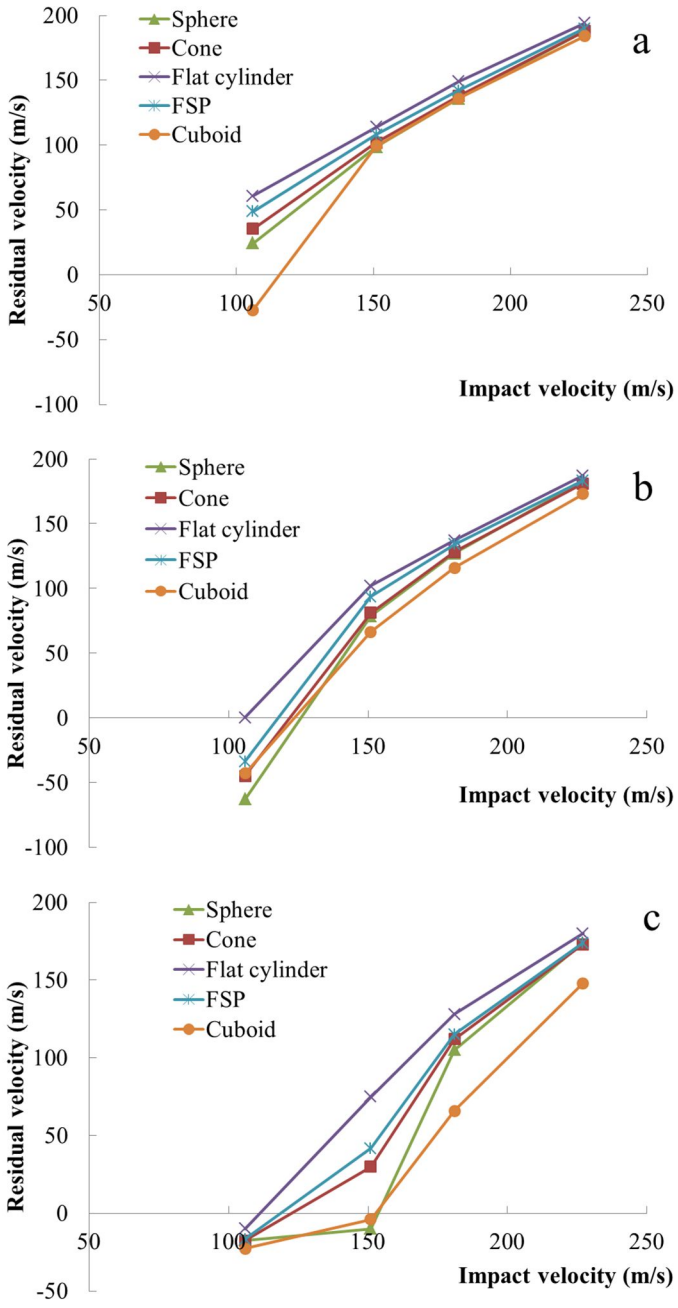


Figure 6-4 Impact velocities vs residual velocities for (a) 50 mm, (b) 100 mm and (c) 200 mm plates.

Based on the analysis as presented above, in terms of their penetration capability, the projectiles can be listed in an ascending order as cuboid, sphere, cone, FSP and flat cylinder. Interestingly, the cuboid projectile also has flat faces, but, unlike the flat cylinder, it is the least effective in penetration.

6.4.1.2 The process of impact

To identify the causes for different penetration capabilities of the projectiles as were presented in the previous section, the penetration process

needs to be understood. Depending on the shape of the projectile, there can be two types of first contact between the projectile and the target. The first one is a point contact for the conical and spherical projectiles, and the second type is the face contact for the FSP, the flat cylinder and the cuboid.

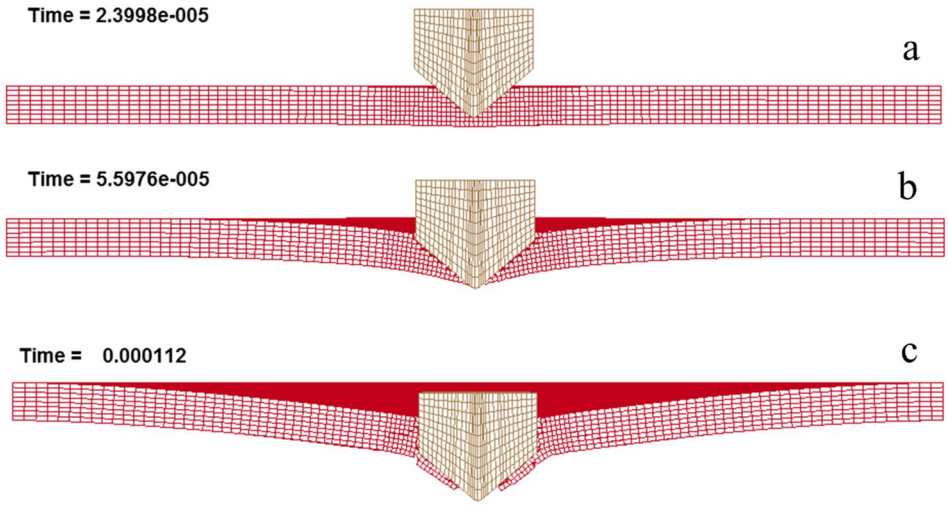


Figure 6-5 The penetration of the target with the conical projectile at 151 m/s.

A series of images showing interaction between the conical projectile and a flat plate are presented in Figure 6-5. In this case, the point contact initially indents and generates a “blind hole” in Figure 6-5 (a). As the projectile moves further down, the material around the hole is crushed and pushed away from the projectile path. The size and depth of the hole increases until the nose of the projective is fully buried in the plate, as shown in Figure 6-5 (b). This process will be referred to as hole enlargement. At its later stages, the projectile begins to push and bend the target plate. The kinetic energy is transferred from the projectile to the plate. Then the material around the projectile is cut by through-thickness shear stress as shown in Figure 6-5 (c). material around the projectile is cut by through-thickness shear stress. A plug is formed and propelled. Meanwhile, the bending of the plate becomes substantial.

The velocity history plots of this conical projectile are shown in Figure 6-6. It can be seen that the deceleration during the initial contact is minor, but it increases dramatically during the later stages of hole enlargement. After the target is penetrated and its resistance is lost at 0.000112 s (Figure 6-5 (c)), and the projectile travels at a constant residual velocity.

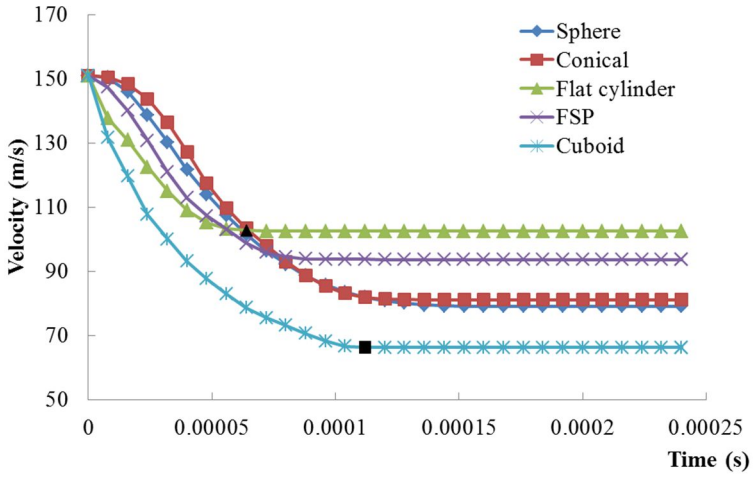


Figure 6-6 The velocity histories of different projectiles impacted onto the 100 mm plates at 151 m/s.

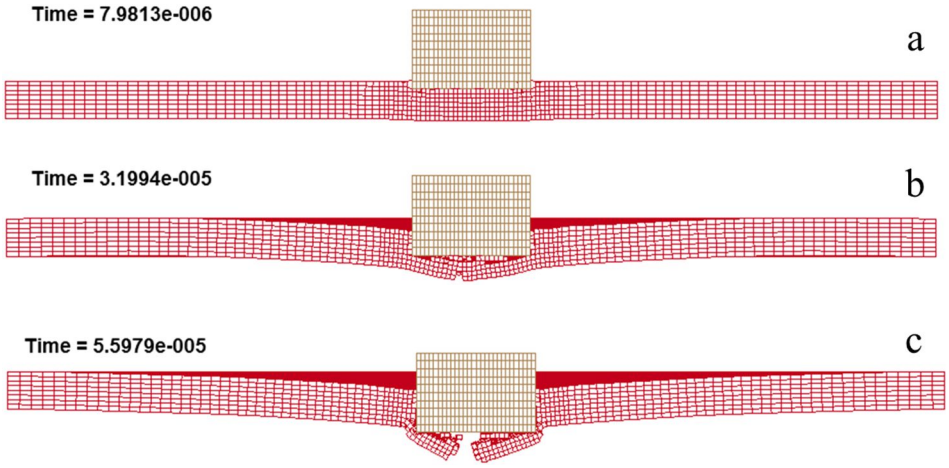


Figure 6-7 The penetration of the target with the flat cylinder projectile at 151 m/s.

Similarly, the impact process of the flat projectile is shown in Figure 6-7. By contrast, the face contact of the flat projectile leads to severe through-thickness shear and crush around the periphery of the projectile from the beginning of contact (Figure 6-7 (a)). As the projectile moves down through the plate (Figure 6-7 (b)), the shear and crush take place inside the plate. The plate is also pushed and bent by the projectile, which is accompanied by the tensile failure on the back surface. Greater deceleration is accompanied by a much earlier penetration (Figure 6-7 (c)) as compared to those observed for the conical projectile. The degree of bending and its associated kinetic energy transfer are also reduced. Same as in the case of the point contact, a plug is formed by the shear cutting and then propelled by the moving projectile. The volume of material under crush and shear plugging is related to the projected area of the projectile and also the thickness of the plate.

As can be seen in Figure 6-6, the velocity reduces very rapidly from the very beginning of this process, for both the flat cylinder and the cuboid. However, the deceleration of the cuboid is larger than the flat cylinder. Given they have the same cross-sectional area, the similar volume of material is under crushing and the similar weight of plug should be generated by them. The difference is then very likely to be attributed to the mechanism related to through-thickness shear.

6.4.1.3 The length of shear cutting

The shear failure of the target takes place around the edges of the projectile and is therefore related to the edge length. When the areas of the square and the circle are the same, the perimeter of a square is 13% larger than the circumference of the circle:

$$L_s = 4a = 4 \times \sqrt{\pi r^2} = 4 \times \sqrt{\pi} \frac{L_c}{2\pi} = \frac{2}{\sqrt{\pi}} L_c \approx 1.13 L_c \qquad (6\text{-}1)$$

where L_s is a perimeter of the square, a is the edge length of the square, r is the radius of the circle and L_c is the circumference of the circle.

To investigate the effect of shear cutting length, the cuboid was modified in a new model (denoted as “Modified Cuboid”) to have the same perimeter length as the flat cylinder, but this in turn decreases the projected area by 21.5%:

$$A_s = a^2 = (\frac{2\pi r}{4})^2 = \frac{\pi^2 r^2}{4} = \frac{\pi A_c}{4} \approx 0.785 A_c \qquad (6\text{-}2)$$

where A_s and A_c are the cross section areas of the cuboid and cylinder respectively.

Another model (denoted as “Modified Cylinder”) for this investigation was made by enlarging the cross section of the cylinder to have the same cutting length as the cuboid. This leads to a 27% increase of cross sectional area from the “Cuboid” and the “Cylinder” models. The projectile length of the “Modified Cylinder” is decreased correspondingly to keep the mass constant. The differences in shear cutting length and projected area are summarised in Table 6-1. The values are normalised to those of the cylinder. Projectile kinetic energy

during the impact, which is derived from the projectile velocity history, is shown in Figure 6-8.

Table 6-1 Projected areas and cutting lengths of the projectiles.

	Cuboid	Cylinder	Modified cuboid	Modified cylinder
Normalised projected area	1	1	0.785	1.27
Normalised cutting length	1.13	1	1	1.13

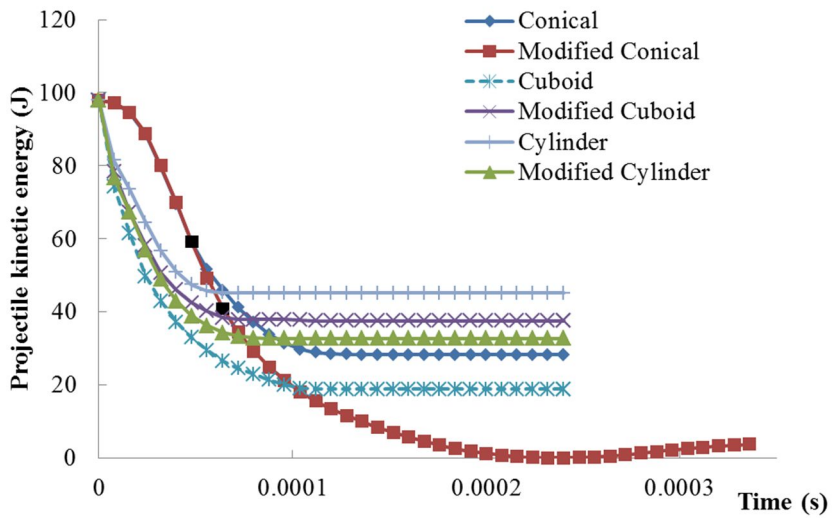


Figure 6-8 The kinetic energy histories of various projectiles when impacted at 151 m/s on the 100 mm plate.

It can be seen that the decrease of kinetic energy for the “Cuboid” is faster and greater than those for all other types of projectiles. Second largest reduction in kinetic energy was observed for the “Modified Cylinder”, followed by the “Modified Cuboid” and the “Cylinder”. In the “Modified Cuboid”, both the cutting length and the projected area of the projectile are smaller than those in “Cuboid”. Consequently, less energy is dissipated via the related mechanisms. The residual kinetic energy for the “Modified Cuboid” model increased to 37.5 J, from 18.9 J calculated with the “Cuboid”, much closer to 45.1 J of the “Cylinder”. Similar trend is found when comparing the “Modified Cylinder” with the “Cylinder”. Even though the analysis as presented here does not allow to specify whether it is the cutting length or the projected area that contributed most to the increase of the kinetic energy, effects of their contribution is evident.

On the other hand, the projectile in the “Modified Cylinder” has larger area and length as compared to the “Cuboid”. However, its residual kinetic energy is 32.7 J, which still higher than that calculated with the “Cuboid”. This suggests that there are some purely shape-related mechanisms affecting the impact performance of the plate.

6.4.1.4 Hole enlargement

Along with shear cutting, crushing and plug formation, hole enlargement with point contact projectiles also dissipates projectile kinetic energy. Its contribution and effects were investigated by modelling a larger conical projectile (denoted as “Modified Conical”). The taper height is increased by 20% while the taper angle is the same as the original cone. The height of its cylindrical part is also 6.35 mm. The density of the rigid projectile was changed accordingly to keep the projectile mass constant.

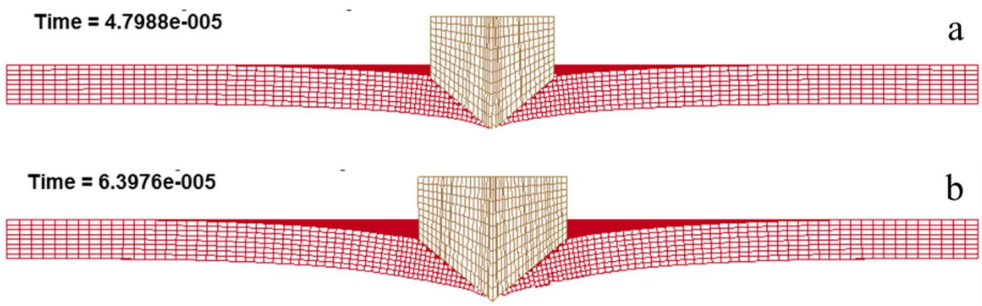


Figure 6-9 (a) the end of hole enlargement for the original conical and (b) the end of hole enlargement for the modified conical projectile.

Their kinetic energy histories and the end of hole enlargement for them are shown in Figure 6-8 and Figure 6-9, respectively. The two curves are identical before the hole enlargement for the original conical ends at 48μs (Figure 6-9 (a) and the left black square marker in Figure 6-8). Then the projectile in the “Conical” model starts to crush and shear off the target material, leading to the formation of shear plug, while the one in the “Modified Conical” continues hole enlargement until 64μs (Figure 6-9 (b) and the right black square marker in Figure 6-8). In the “Modified Conical”, the dissipation mechanisms related to hole enlargement contribute 59.5 J to the total dissipation of 94.1 J while it is 38.7 J to 69.7 J in the “Conical” model. This proves that the mechanisms related to hole enlargement play important roles in the energy dissipation for point contact impactors. The energy after hole enlargement is also increased which is

to be expected as the cross section of the projectile is larger in the “Modified Conical” model.

Clearly, this process is much related to how the hole is enlarged. In Figure 6-6, the hole enlargement of the spherical projectile leads to a faster deceleration than the conical one. During the hole enlargement, given the same depth, the hole made by the sphere has a larger area than the one by the conical. After the hole enlargement, less energy is dissipated by through-thickness shear cutting due to the smooth shape of sphere. Therefore, the final residual velocity ends up being close to the conical projectile. For conical projectiles, the degree of taper should greatly affects the hole enlargement. It is self-evident that the hole enlargement is less efficient when the degree of taper is larger, and consequently the projectile is more efficient in penetration.

The impact of the FSP is a combination of shear cutting due to face contact and hole enlargement due to its taper. Its initial shear cutting length is smaller than the “Cuboid” and the “Cylinder” models, so its deceleration in Figure 6-6 is in between the point contact group and the face contact group.

6.4.2 The span to thickness ratio

From Figure 6-4 (a) to (c), the span to thickness ratio is increased. Along with this increase, the residual velocity of each projectile decreases, no matter what the impact velocity is. Figure 6-10 (a) shows the histories of the kinetic energy, internal energy and their sum total energy in the plates of different sizes, when impacted by the spherical projectile at 151 m/s. The results for 50 mm, 100 mm and 200 mm plates are illustrated respectively by curves in black, blue and red.

In terms of peak and average values, it is evident that the greater the ratio, the greater all the three types of energy are. However, if the energies are normalised to their weights as in Figure 6-10 (b), the above trend is reversed, i.e. the 50 mm plate has the highest levels. This normalisation process essentially indicates the average energy densities in the target plates. The plate with a large span to thickness ratio actually behaves less efficient in dissipating the impact energy.

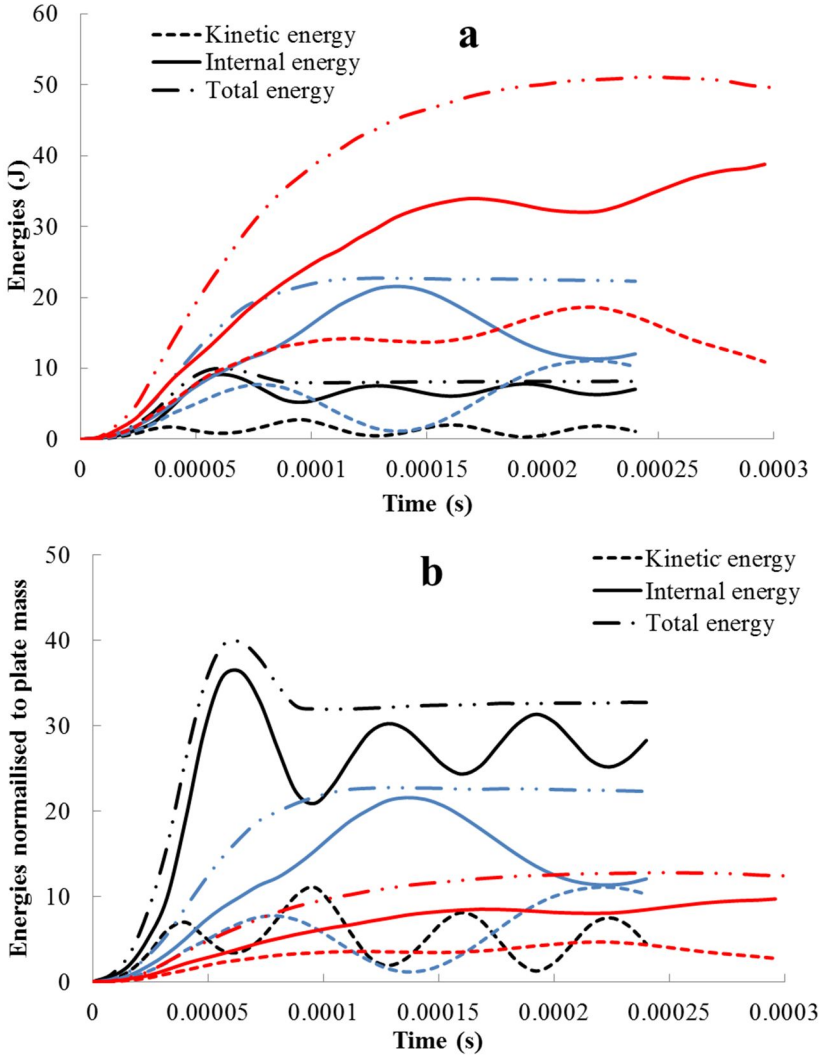


Figure 6-10 (a)When impacted at 151 m/s by the spherical projectile, the Kinetic, Internal and Total Energy histories of 50 mm plate in black, 100 mm plate in blue and 200 mm plate in red, and (b) these energies normalised to the mass ratios of the three target plates.

In Figure 6-10 (b), fluctuations of the kinetic and internal energy can be noticed especially in the 50 mm plate. This is the result of plate vibration and conversions between the kinetic energy and the internal energy. The vibration frequency is much higher in the 50 mm plates than the other two. At the end of Figure 6-10, several fluctuations are finished in the 50 mm plates, while the 200 mm plate is yet to reach its first peak of internal energy, indicating that the plate is still in contact with the projectile and being pushed by it. This trend reveals that the contact duration is longer in plate with large span to thickness ratio.

When impacted by the same projectile at a higher velocity (227 m/s), the above conclusions concerning the span to depth ratio are also applicable, as shown in Figure 6-11. Rather than significantly bending the plate, the high

velocity leads to localised crush during a much shorter contact. Therefore the internal energy related to bending and the kinetic energy related to vibration become much smaller in Figure 6-11.

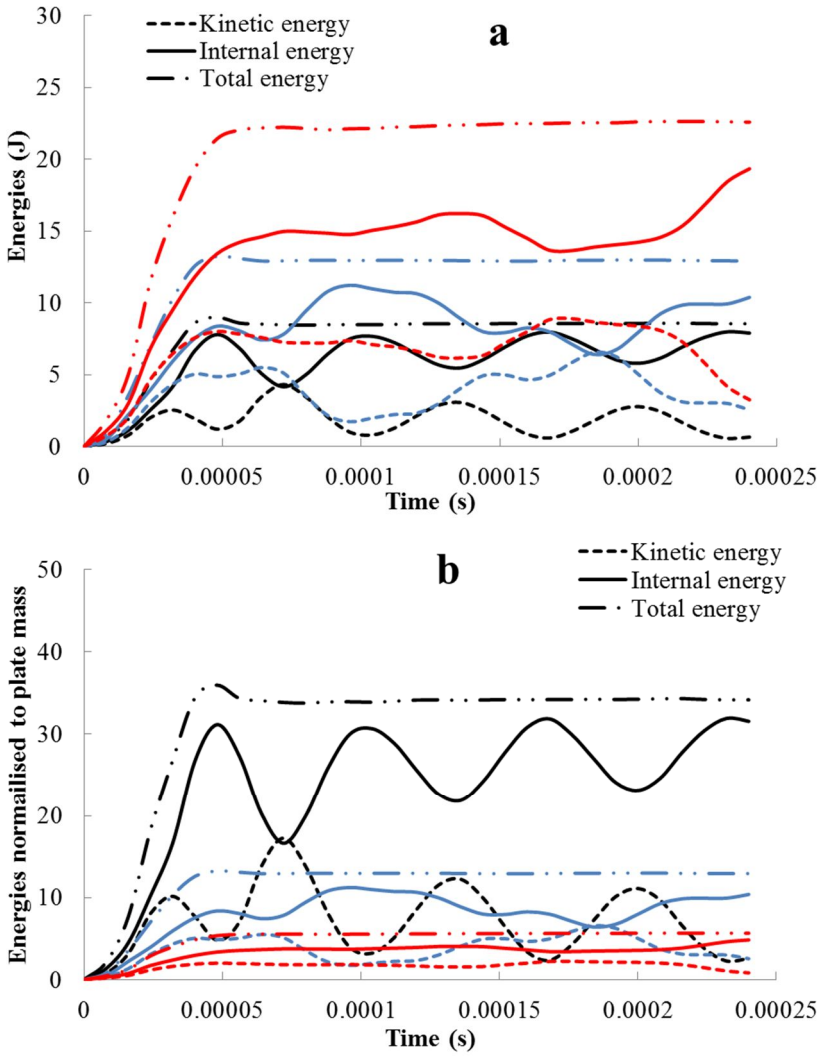


Figure 6-11 (a) When impacted at 227 m/s by the spherical projectile, the Kinetic, Internal and Total Energy histories of 50 mm plate in black, 100 mm plate in blue and 200 mm plate in red, and (b) these energies normalised to the mass ratios of the three target plates.

In contrast to the findings in [192, 202, 203], the projectile shape effect is more significant in a plate with a large span to thickness ratio. The reason behind this could be the duration of contact and its relation to bending. For instance, if the velocity histories of the cuboid and the flat cylinder, when fired at 151 m/s onto the 50 mm plate, are plotted, as shown in Figure 6-12. The time point when the velocity becomes constant is here regarded as the end of contact. They are illustrated by black markers in the figure. It is found that the duration of contact differs by about 1.6×10^{-5} s, while the duration difference in Figure 6-6 for the

100 mm plates is 4.8×10^{-5} s, three times larger. If the projectile is still in contact with the target plate, its residual kinetic energy makes it push the target farther away from the original position. The contact duration to some extent positively relates to the degree of bending. A larger difference in the contact duration leads to a larger difference in the degree of bending and consequently, energy dissipation. Therefore the shape effect is found to be more significant for plates with larger span to thickness ratios.

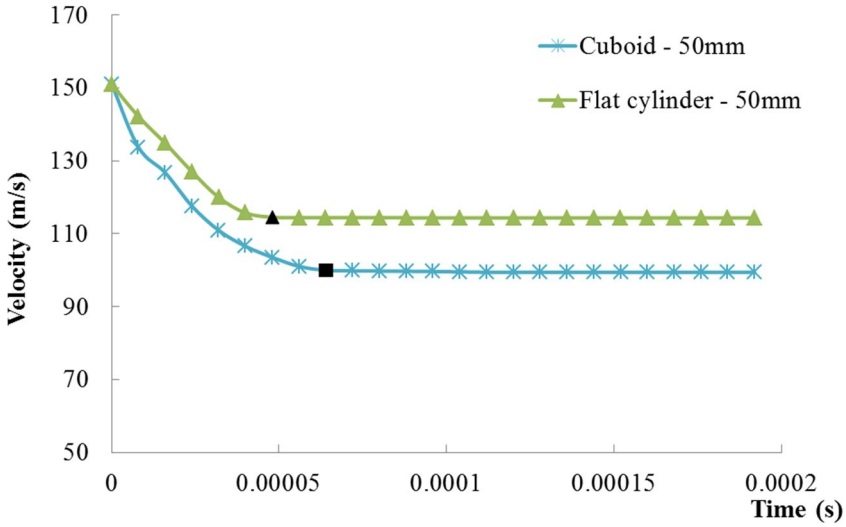


Figure 6-12 The velocity histories for the flat cylinder and the cuboid when fired at 151 m/s onto the 50 mm plates.

6.4.3 Oblique impact

The results of oblique impact simulations with constant normal velocities of 151 m/s and 106 m/s are shown in Figure 6-13 (a) and (b), respectively. The plots show the velocity vectors, normal (V_N) and tangential (V_T), before (solid lines) and after (dashed lines) the impacts.

In Figure 6-13 (a), the increase in residual V_N is barely noticeable from 0° to 15°, while it becomes more and more apparent when the impact angle is further increased. This means that penetration becomes easier at larger angles. A similar trend can also be seen in Figure 6-13 (b) (cf. 45R and 60R).

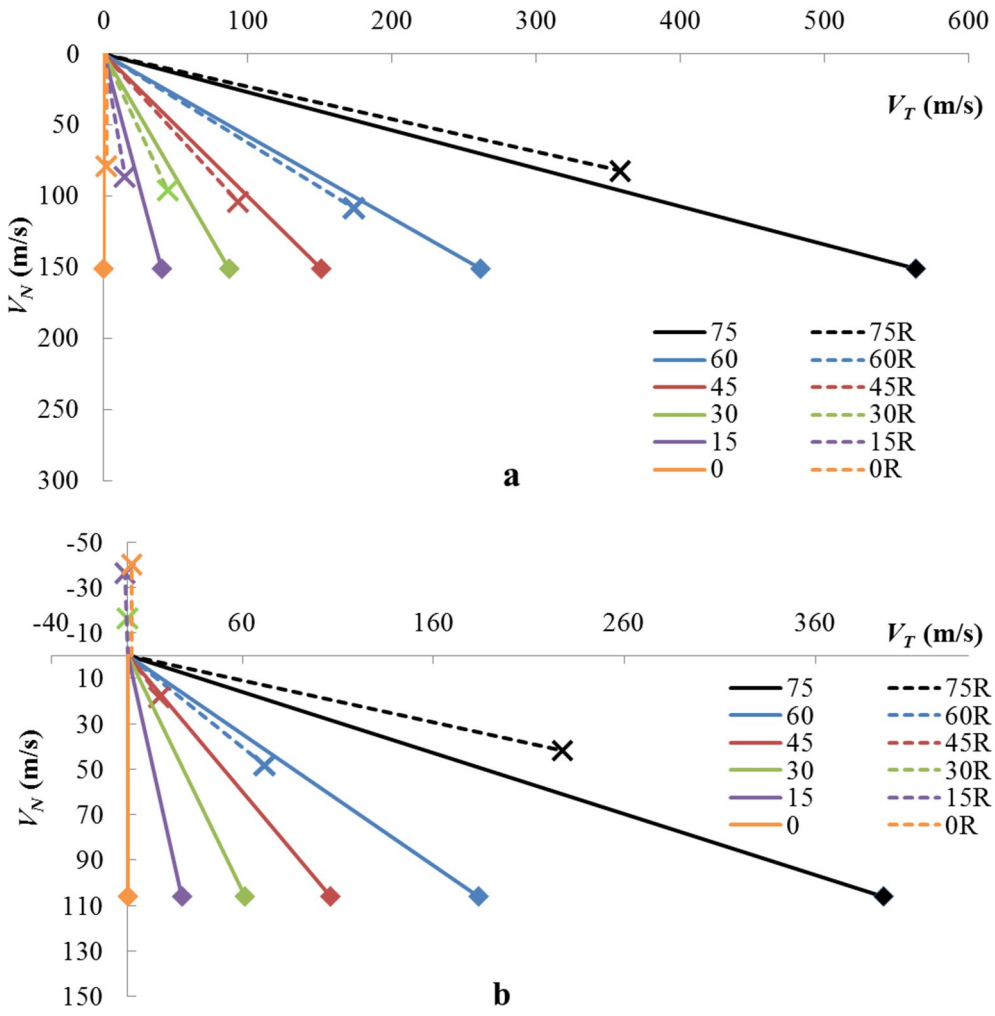


Figure 6-13 Velocity vectors, normal (V_N) and tangential (V_T), of oblique impacts at different angles with constant normal velocities (a) V_N = 151 m/s and (b) V_N = 106 m/s. Dashed lines denoted with "R" are residual velocities.

The exception to the increasing residual V_N as impact angle increases is the 75° impact. In Figure 6-13 (a), the V_N of 75R is much lower than that of 60R. When analysing the projectile trajectory, as shown in Figure 6-14 (a), it is found that due to the large tangential velocity of the 75° model, the projectile reaches the boundary before it can completely penetrate the plate. Afterwards, there is no resistance from the plate to V_N and V_T. This suggests that the resistance to the penetration of this impact is actually underestimated. At 60° (Figure 6-14 (b)), the projectile does not reach the boundary before penetration, as is the case for all the other angles. Therefore, the results at these angles are indicative of the real penetration resistance of the plates.

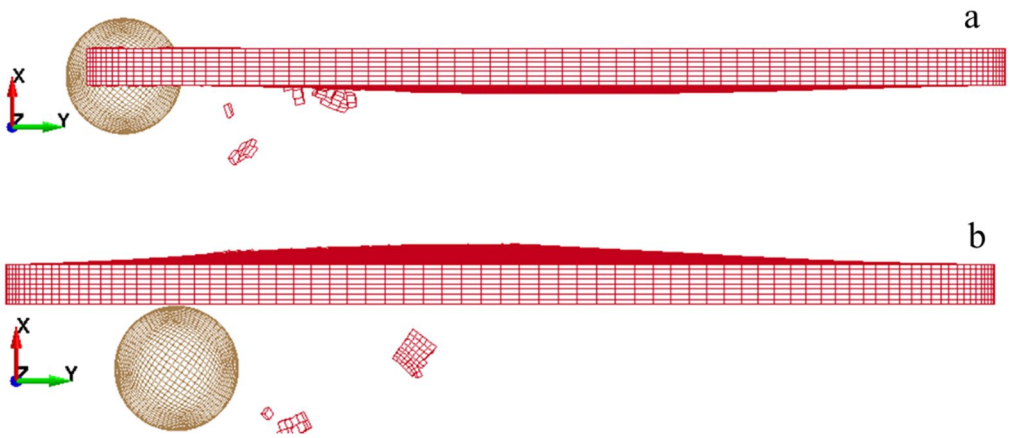


Figure 6-14 When V_N = 106 m/s, (a) at 75° the projectile reaches the edge of the plate before full penetration and (b) at 60° full penetration takes place before the projectile reaches the edge of the target.

Figure 6-15 (a) shows the changes of kinetic energy based on the normal velocities, before and after impact. Recall that rebounding takes place at 0°, 15° and 30° at 106 m/s. Energy is a scalar so the kinetic energy change does not take rebounding into consideration. Therefore for the rebounding cases, the less change in the kinetic energy actually stands for higher impact resistance and therefore more energy dissipation. Based on this, it is possible to find the common trend in Figure 6-15 (a) for both velocities, which is that the dissipated energy falls with increasing impact angle other than for the exception from 60° to 75°. This fall is attributed to an increase in hole opening resulting from the tangential velocity. A larger impact angle leads to a higher tangential velocity and a larger hole, and therefore less material of the plate is resisting the projectile moving vertically.

Figure 6-15 (b) is the kinetic energy changes based on the resultant velocities. The energy gradually increases with increasing impact angle, followed by a sharp rise from 60° to 75°. At 0°, the least amount of kinetic energy is dissipated. This indicates that the plate is most vulnerable to penetration at the normal impact. Thus, if impacts at various angles with constant resultant velocity were modelled, the normal velocities would obviously reduce with increasing impact angle and it would become more difficult to penetrate the target.

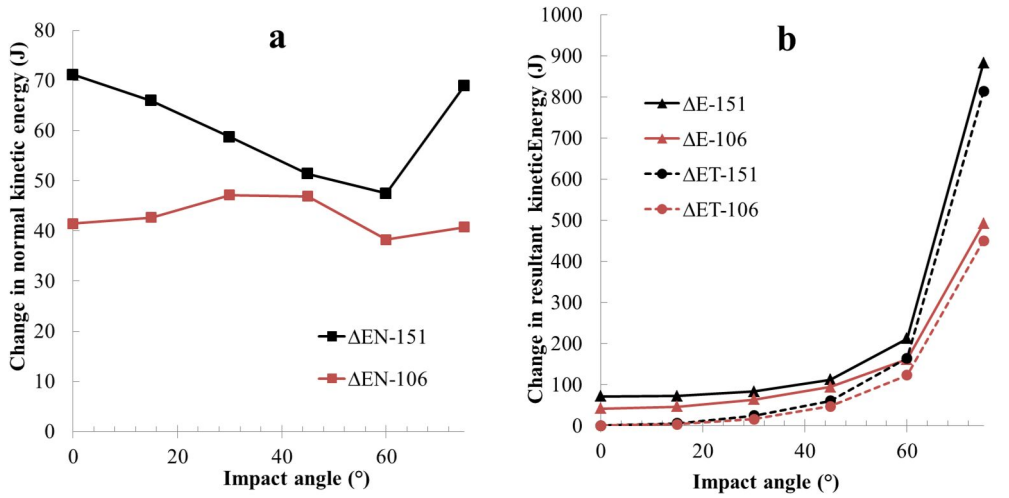


Figure 6-15 Resultant kinetic energy change of the projectile based on normal velocity E_N in (a); and the energy of tangential velocity E_T and resultant velocity E in (b).

The kinetic energy changes for tangential velocities are the subtraction of Figure 6-15 (a) from the resultant energy in (b). They are illustrated by the dashed lines in Figure 6-15 (b). It is worth noting that, at 75°, substantial amount of energy is dissipated through the reduction in tangential velocity. At 151 m/s, the tangential velocity change contributes 813 J to the total change of 882 J, while the normal velocity change accounts for only 69 J. The ratio is 164 J to 211 J to 47 J at 106 m/s. While the impact at 0° is along the through thickness direction, the impact at large angles is more like impact along the in-plane direction, where not only mechanical properties are superior but also the dimension is many times larger. When the impact angle becomes larger, the in-plane dimension increases and consequently the related energy dissipation mechanisms are also enhanced. One of the reasons behind the above exceptions at 75° is very likely to be that, from 60° to 75°, the in-plane behaviour becomes dominant.

6.4.4 Curvature of the target plate

The mass of the most curved plate (R/S=0.75) is 9% larger than the baseline plate, while the other plates are within 2% from the mass of the baseline plate. The mass difference is taken into account when analysing the results of impact simulations of plates with different degrees of curvature.

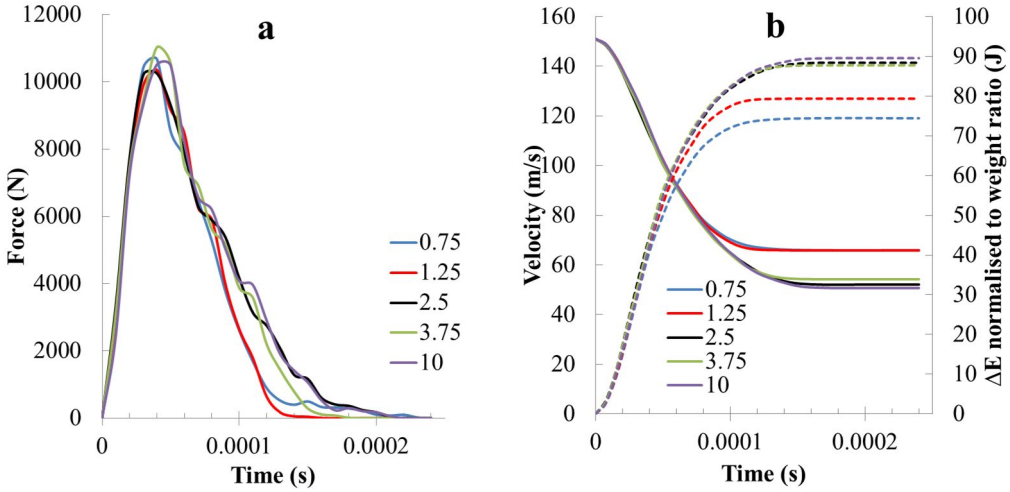


Figure 6-16 Histories of (a) contact force and of (b) velocity and change of kinetic energy for plates with different radius of curvature to span ratios.

Time histories of the contact force between the plate and the projectile are shown in Figure 6-16 (a) for plates with different radius-to-span ratios (*R/S*). Before the peak values, there are only slight differences among the curves, which are also reflected in the velocity history plots in Figure 6-16 (b) that show the deceleration of the projectile. The velocities are nearly identical before 50μs, when all the contact forces reach their peak values. After that, the contact forces begins to decrease, but after 80μs, for *R/S*=0.75 and *R/S*=1.25 it decreases at a much faster rate than in the other cases. These changes are also reflected in the velocity history plots in Figure 6-16 (b). Namely, the velocity reduction after 80μs is less substantial for the plates with *R/S*=0.75 and *R/S*=1.25, hence the residual velocities in these two case are higher than in all the others. When the same data is presented in terms of energy change normalised to the plate mass, and shown by the dashed lines in Figure 6-16 (b), it becomes clear that, in terms of impact resistance, the plate with *R/S*=0.75 is less efficient than the plate with *R/S*=1.25.

In addition, the figures show that the effects of target curvature only become noticeable when the value of *R/S* is relatively small, or in the other words, when the target plate is curved to a certain degree. This finding is in consistent with the conclusions made in [219]. In the present study, this transition happens somewhere between *R/S*=2.5 to *R/S*=1.25. In contrast to observations made in [218], the present study shows that the more curved the plate is, the less resistant it is to impact. Above *R/S*=2.5, the influence of

curvature is negligible. Therefore, it can be concluded that it is reasonable to assess the penetration resistance of the containment casing, which has a degree of curvature of *R/S*=10, based on the tests on flat panels (*R/S*= +∞) or on the scaled cylinder (*R/S*=2.5).

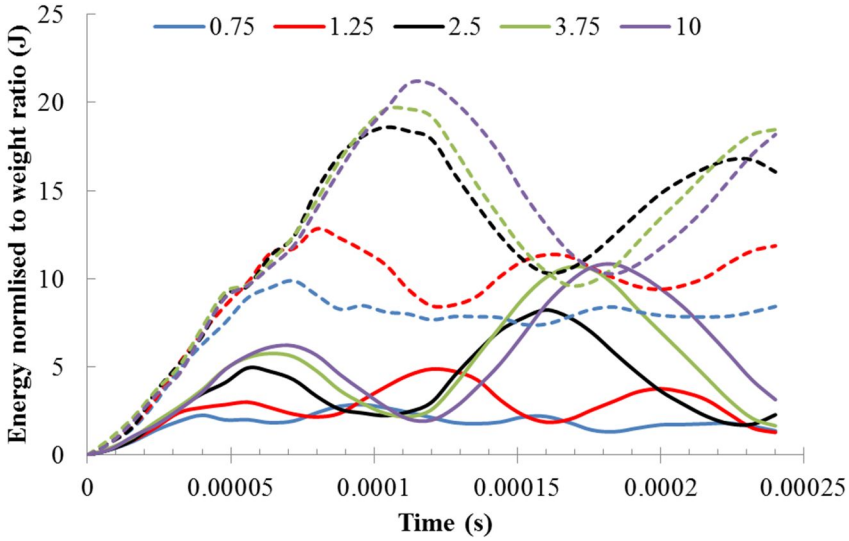


Figure 6-17 Histories of kinetic energy (solid line) and internal energy (dashed line) of the plates with different radius of curvature to span ratios.

The reasons behind these findings can be explained by analysing the histories of the kinetic energies (solid lines) and internal energies (dashed lines) of the plates in Figure 6-17. The residual velocities in Figure 6-16 (b) become constant after 1.3×10^{-4} s for *R/S*=0.75 and *R/S*=1.25, and after 1.6×10^{-4} s for the other three. The plates have been penetrated after these time points so the remaining parts of curves are merely energy conversion in the plates and therefore can be ignored.

It can be seen that the energy levels, especially the internal energies, of *R/S*=0.75 and *R/S*=1.25 are apparently lower than the other three. This indicates that the differences in Figure 6-16 (b) are related to the differences in the energies transferred to the plates. The analysis in Section 6.4.2 for flat plates indicates that bending has a significant contribution to the dissipated energy, and the more bending in the plate, the more resistant the plate is to penetration. But for curved plate, the larger curvature makes the plates more resistant to bending and therefore less kinetic energy can be converted to the energies in the plates, leaving higher levels of residual velocities in Figure 6-16 (b). The curvature is much less significantly changed from *R/S*=10 to 3.75 to 2.5, so the differences among them in these figures are trivial.

6.5 Conclusions

A parametric study has been performed to study the effects of the projectile shape, the target size, the impact obliquity and the target curvature on the impact performance of the CF-IM7 3D woven composite. It is found that, among the designated projectiles, the target plate is the least resistant to the penetration of the flat cylinder projectile, followed by the FSP, conical, spherical and cuboid projectiles. The difference between the flat cylinder and the cuboid indicates shape-related mechanisms can play significant roles in energy dissipation for the projectiles with flat end faces. In addition, shear cutting, crushing and plug formation, whose contributions are largely affected by the cutting length and projected area of the projectiles, are also significant mechanisms of energy dissipation. The penetration of the projectiles with a point contact, e.g. the conical projectile involves hole enlargement, whose contribution to energy dissipation can also be substantial.

The effects of the projectile shape become more apparent for plates with larger diameter-to-thickness ratios, as the larger ratios magnify the difference in the target bending. Meanwhile, the plate with a larger ratio dissipates more impact energy but with a lower efficiency.

The effect of impact obliquity is evident for both penetration and rebounding cases. The normal velocity required for penetration reduces with increasing impact angle. But in terms of resultant velocity, the trend is the opposite and the normal impact requires the least amount of energy for penetration.

It was revealed that plates with large curvature are less resistant to penetration as it is more difficult to bend them. However, the effects of the curvature only become apparent when the plate is curved to a certain degree. This transition happened when the ratio of target radius to target span, R/S, was decreased from 2.5 to 1.25 in this study. Therefore, it is reasonable to assess the impact behaviour of full scale casings by tests on flat plates whose $R/S=+\infty$ or scaled casings whose $R/S\geq 2.5$.

Chapter 7 Mixed element type analysis (META) and simulation of casings under impact loadings

7.1 Introduction

For modelling the FBO of metallic fan casings, it has been reported [221, 222] that very fine mesh should be used in the impact region to accurately predict the damage observed in experiments. For composite materials, mesh sensitivity of the impact analyses is particularly important [73, 223]. Fan casings are very large structures. For example, the fan of General Electric GEnx engine has a diameter more than 2800 mm [224]. The FE simulation of its FBO tests requires a very large number of elements and nodes, which can make the simulation costly.

During such event, the trajectory and impact of the blade is surprisingly repeatable, in spite of the fact that the event occurs randomly [225]. As a result, the impact performance of a fan casing can be assessed using the ballistic tests where a projectile is fired at high velocity onto a target at an oblique angle [225]. Unlike the FBO event at engine level, which usually involves several revolutions of the rotor, the circumferential motion of the projectile in ballistic tests can be controlled, making it a well-defined localized event. This also makes it possible to perform a numerical analysis with mixed element types, in which a critical local domain modelled with solid elements is embedded in a global domain modelled with elements of reduced dimensions, e.g. shell elements, and the different types of elements are coupled [226]. The concept has been practiced in the marine [227], automotive and aviation industries [228], and its use has been demonstrated in the multi-scale modelling of composites [229, 230].

In this study, the capability and limitations of a mixed element type analysis (META) in simulating the impact performance of composite structures were assessed. META then was used to simulate casing rings made from CF-IM7 3D woven composites under several simple impact loading cases, which more closely represent the conditions of an FBO event than the impact testing on plates.

7.2 META analysis for plate impact

7.2.1 General Methodology

In the present study, accuracy of META in predicting the damage and failure modes of composite materials was initially assessed by applying it for simulating the ballistic impact tests of the 2D composite laminates reported by Gama et al. [198]. In the tests, an air gun apparatus was applied to fire cylindrical projectiles of 13.8g mass, 12.7 mm in diameter and 14.02 mm in height onto plain-weave S-2 glass/SC15 composite plates. The impact velocity and the residual velocity of the projectile were measured and recorded in the experiments. Material model MAT162 in LS-DYNA is applicable for defining the constitutive behaviour of laminates based on plain weave reinforcements. Simulation was conducted in [198] for the ballistic impact tests by using MAT162 model, and a good agreement with the experiments was reported. The input properties which were specified for MAT162 in the simulation are listed in Table 7-1. The definitions of the parameters are listed in Table 5-1.

Table 7-1 MAT162 input parameters for the plain-weave S-2 glass SC15 composite from [198].

ρ [kg/m3]	EA [GPa]	EB [GPa]	EC [GPa]	PRBA	PRCA	PRCB
1850	27.5	27.5	11.8	0.11	0.18	0.18
GAB [GPa]	GBC [GPa]	GCA [GPa]	SAT [MPa]	SAC [MPa]	SBT [MPa]	SBC [MPa]
2.90	2.14	2.14	604	291	604	291
SCT [MPa]	SFC [MPa]	SFS [MPa]	SAB [MPa]	SBC [MPa]	SCA [MPa]	PHIC [°]
58	850	300	75	58	58	10
SFFC	E_LIMT	S_DELM	OMGMX	ECRSH	EEXPN	CRATE1
0.3	0.2	1.2	0.999	0.001	4.5	0.03
AM1	AM2	AM3	AM4	CRATE2	CRATE3	CRATE4
2	2	0.5	0.2	0	0.03	0.03

The target plates had nominal thickness of 13.2 mm, in-plane dimensions 178 mm × 178 mm and comprised 22 plies of lamina. The composite plates were placed between two square steel plates, both of which had central circular cut-

outs with a diameter of 101.6 mm. This assembly was bolted to the test rig. The size of the exposed area of the target is very similar that in the ballistic impact experiments as described in Chapter 4. To understand how META works for targets of different diameter-to-thickness ratios, both impact configurations were analysed by using META as shown in Figure 7-1.

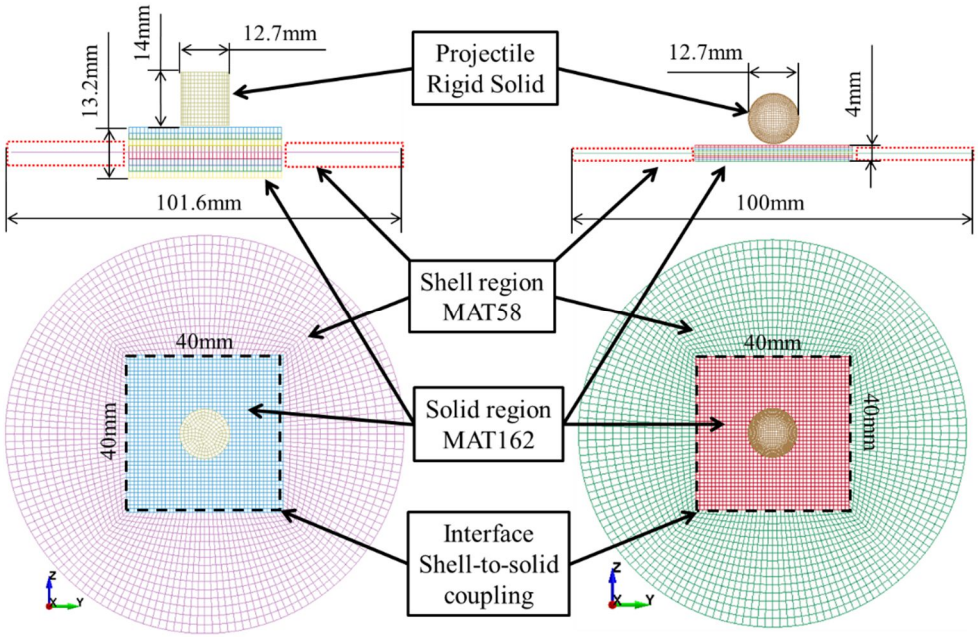


Figure 7-1 The META model for the two configurations of ballistic impact test.

In both cases, only the exposed area of the target was modelled explicitly. The displacement of the peripheral nodes are constrained in all directions In spite of symmetric in-plane material properties and loads, a whole circular plate model was built to avoid complexity arising from element deletion at the symmetry boundaries. A single surface contact algorithm was applied to all the material interfaces.

The META model for the plates as shown in Figure 7-1 employs two types of elements. Both the central impact region and the projectile were meshed with hexahedral solid elements with single integration point. Belytschko-Tsay shell formulation was used for the shell elements involved. Multiple integration points were set up in the thickness direction to represent the layup. Based on the result of the mesh sensitivity study in Section 5.3.1, the models for this study have a larger central region (40 mm × 40 mm) of uniform fine solid element (0.5 mm × 0.5 mm), which is referred to as the “solid region” in the following, and a surrounding region meshed with the shell elements (referred to as the “shell

region"). The mesh size for the impactor was chosen to be comparable to that at the centre of the plate. The mesh was carefully made so that all shell element nodes at the shell-solid interface were in alignment with the corresponding solid element nodes. Then the solid element nodes were constrained to the shell element nodes by using CONSTRAINED_ SHELL_TO_SOLID [112], as shown in Figure 7-2. In the current version of LS-DYNA (R7.1.2), the shell-to-solid constraint allows coupling of one shell node with a maximum of 9 solid nodes, i.e. 8 elements. All-solid models have also been constructed with exactly the same mesh sizes as the META models.

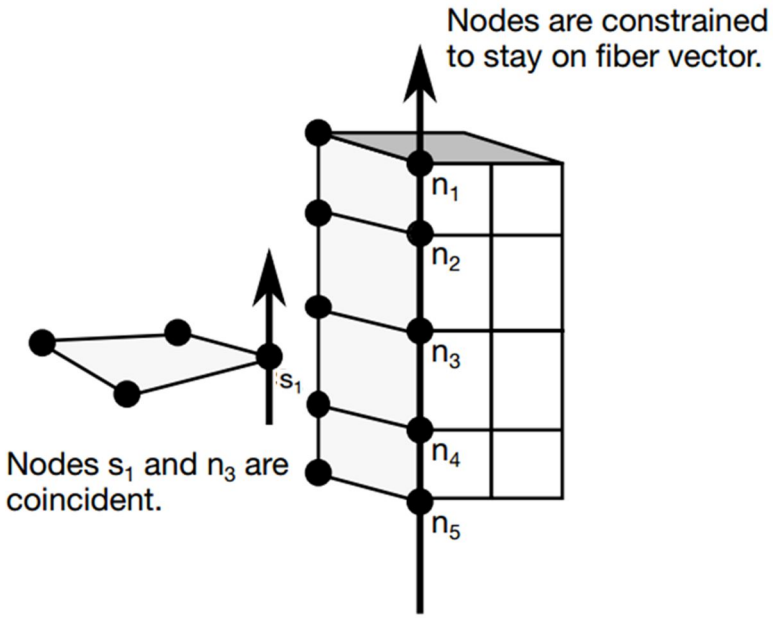


Figure 7-2 The shell-to-solid interface ties shell node s_1 to a line of nodes on the solid element n_1-n_5 [112].

Since the material model MAT162 is only available in solid element formulation, material model MAT58 of LS-DYNA [111] was used as the material model for the shell region. The differences between these two material models and their possible influences on META are discussed in Sections 7.2.2 and 7.2.3 below. The projectile was modelled as a rigid body with the properties of steel (ρ=7850 kg/m^3, E=210 GPa, υ=0.29). Energy time history was checked for each simulation to ensure the total energy of the system was constant and the hourglass energy was controlled to be less than 5% of the total energy.

7.2.2 Differences between MAT58 and MAT162

In contrast to MAT162, the strain rate dependency of composite materials is not accounted for in MAT58 model formulation. In addition, the

representation of the damaged material in the two models is different. MAT162 allows controlling gradual stiffness degradation due to damage via an appropriate definition of damage evolution parameters, while MAT58 only allows defining the residual strengths at tension (SLIMT1 and SLIMT2), compression (SLIMC1 and SLMC2) and shear (SLIMS) to represent damage in the composite.

These differences, if not treated carefully, can result in substantial discrepancies between the impact resistance predictions given by the two models. For a study on the feasibility of META as a methodology of modelling impact response, the differences in the two models should be reduced to a minimum. To “equalise” the impact energy dissipation capability of the two types of elements, simplifying assumptions were made and implemented as follows:

a) Strain rate effects were not considered in both MAT58 and MAT162. The strain rate scaling factors in MAT162 were set to zero;
b) The damage-related material constants, AM1 and AM2 in MAT162 model, were chosen in such a way to ensure that under the tensile in-plane loading the two models predict the same stress-strain response;
c) The progressive shear damage in MAT162 is neglected and the material is assumed to fail in an abrupt manner under shear loading. This was ensured by setting damage-related material parameter AM4 to a large value;
d) The residual strengths in both models are set to zero, i.e. SFFC= 0 in MAT162, SLIMT1=SLIMT2=SLIMC1= SLMC2= SLIMS= 0 in MAT58;
e) The element deletion criteria were deactivated in both material models by assigning very large trigger values. The solid and shell elements are given the same deletion criterion of 30% maximum effective strain (EFFEPS) provided by the keyword MAT_ADD_EROSION.

These changes resulted in another set of input data for MAT162, which is denoted as "Solid-2" in Table 7-2 and compared with the set employed in [198]. The corresponding inputs for MAT58 are given in Table 7-3 and this set of input data for the shell elements is denoted as "Shell-1". The definitions of the parameters are available in [111].

Table 7-2 Differences to the inputs of Table 7-1.

	m1=m2	m4	SFFC	CRATE1=CRATE3=CRATE4	E_LIMT	ECRSH	EEXPN	EFFEPS
Solid-1	2	0.2	0.3	0.03	0.2	0.001	4.5	None
Solid-2	6.5	1000	0	0	9999	1×10^{-9}	9999	0.3

Single element modelling, similar to that described in Chapter 5, was conducted to obtain the predictions of MAT162 model with the modified input properties (“Solid-2”) under in-plane tension, compression and shear. Similar analyses were carried out with shell element and MAT58 model. The calculated stress-strain curves are shown in Figure 7-3 .

Table 7-3 The set of input data for MAT58 ("Shell-1").

ρ [kg/m3]	EA [GPa]	EB [GPa]	EC [GPa]	PRBA	TAU1	GAMMA1
1850	27.5	27.5	11.8	0.11	0.18	0.18
GAB [GPa]	GBC [GPa]	GCA [GPa]	SLIMT1	SLIMC1	SLIMT2	SLIMC2
2.90	2.14	2.14	0	0	0	0
SLIMS	TSIZE	ERODS	SOFT	FS		
0	1×10^{-12}	9999	1	0		
E11C	E11T	E22C	E22T	GMS		
0.011406	0.022686	0.011406	0.022686	0.01308		
XC[MPa]	XT[MPa]	YC[MPa]	YT[MPa]	SC[MPa]		
291	604	291	604	75		

As can be seen, under each loading mode, the predictions of the initial elastic response obtained by using the three sets of inputs are very similar. Once the damage initiation is triggered, the stress-strain curves calculated with "Solid-1" suggest that the material maintains substantial load carrying capability, especially under the shear loading. This is similar to the actual material response as obtained in the shear tests in Chapter 3. As was explained above, it is challenging to model this kind of material response with MAT58. Therefore, there would be a substantial mismatch between the predictions of the two material models if the original inputs (“Solid-1”) were used. The modifications

to the input parameters bring the curves predicted by MAT162 ("Solid-2") and MAT58 ("Shell-1") much closer. There seems to be discrepancy for the shear curves, but in terms of strain energy density, which is defined as the area under the curves, it is rather insignificant, as listed in Table 7-4 for the three sets of input parameters. They are all normalised to the tensile one for the set “Shell-1”.

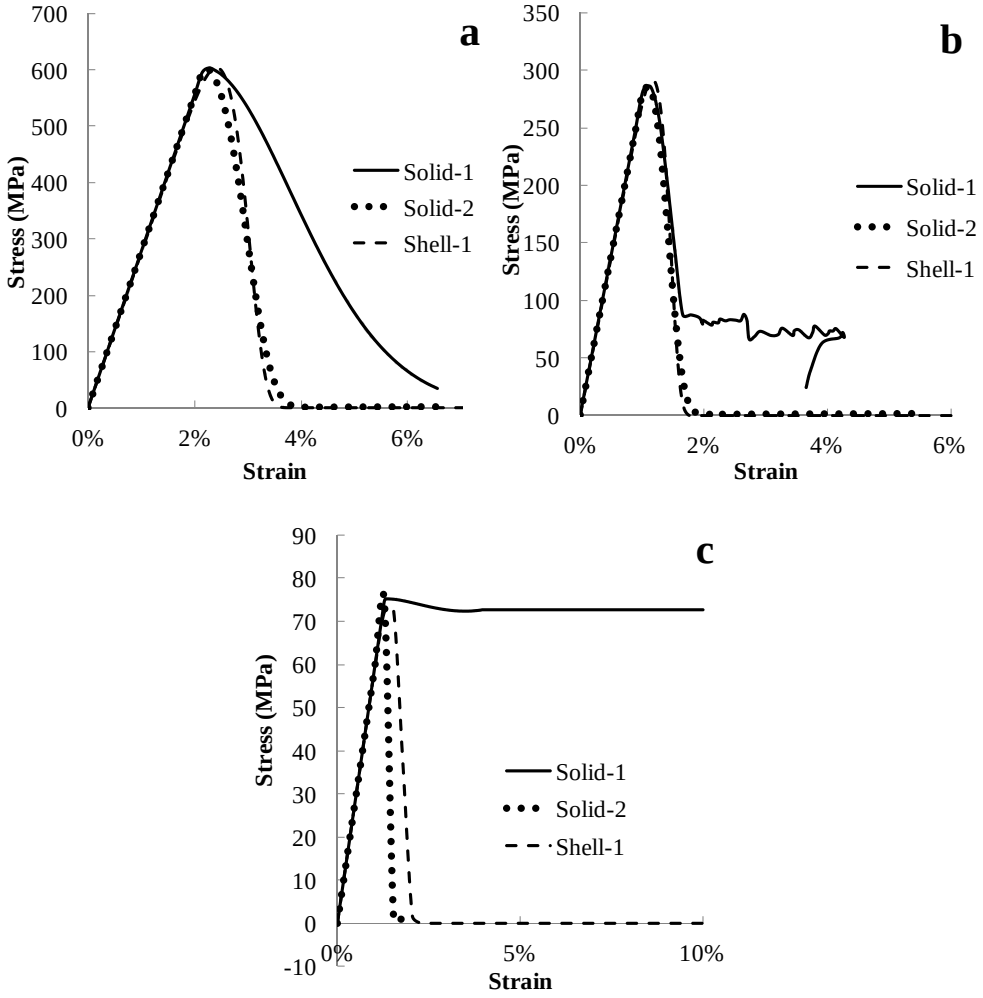


Figure 7-3 Stress-strain curves of the single element models of MAT162 and MAT58 under in-plane tension (a), compression (b) and shear (c).

Table 7-4 Normalised strain energy for the curves in Figure 7-3.

	Solid-1	Solid-2	Shell-1
Tension	170%	100%	100%
Compression	42%	23%	23%
Shear	59%	5%	7%

7.2.3 The relation between the prediction and the definition of the regions

This section presents the investigation whether the prediction is significantly affected by the material definition in the solid region and in the shell region. For this study, META models were generated for the plate impact tests described in Chapter 4, which is shown by the model on the right in Figure 7-1. Those are more representative for thin structures such as the fan containment casing. Along with the META models, solid-element-only (SEO) models, where the material behaviour was prescribed by MAT162, and shell-elements-only models, with MAT58 defining the constitutive response of the composite, were analysed for comparison purposes. Two impact cases were generated for each type of models, where the projectile was assigned an initial velocity of either 105 m/s or 227 m/s, which are respectively below and above the ballistic limit. The time histories of the kinetic energy of the projectiles are shown in Figure 7-4.

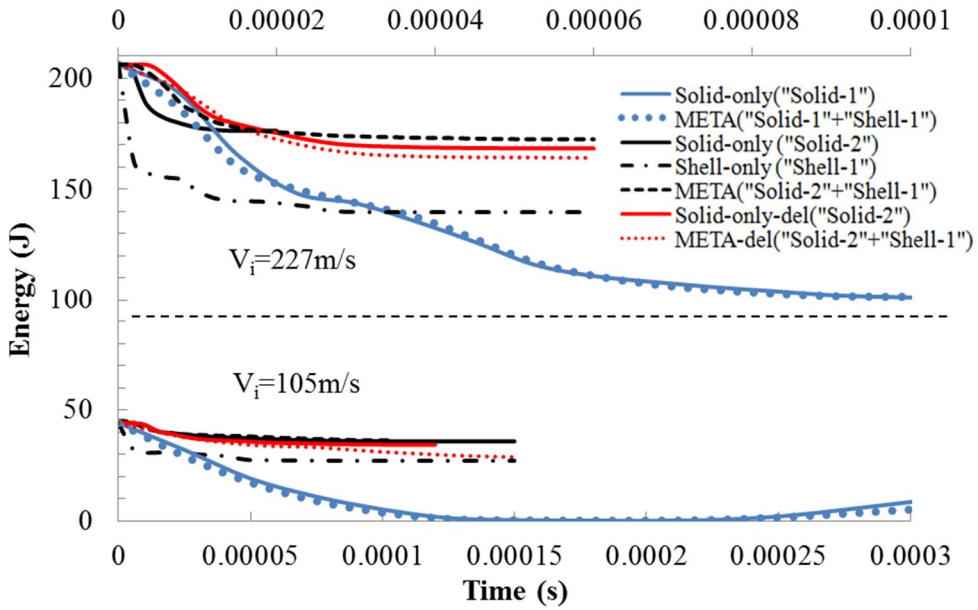


Figure 7-4 Significance of the solid region: projectile kinetic energies. The curves for 227 m/s are in the top; the ones for 105 m/s are in the bottom.

The energy curves calculated in the models with the modified input sets, i.e. "Solid-2" and "Shell-1", are shown in black. From these curves, it is easy to see that there is large discrepancy between the energy predictions of the solid-elements-only models and shell-elements-only models, though the two types of elements are defined to have nearly the same energy dissipation capability (see

Table 7-4 for the comparison). The likely cause for that is 2D stress state formulation in shell elements, which makes them not appropriate for modelling the material response in the impact region, where substantial through-thickness material compression and shear is caused by impact. This type of failure and deformation, however, can be reproduced if solid elements are used. The comparison of the calculated energy curves therefore indicates that simplifying the impact model by completely replacing the solid elements with the shell elements could lead to significant inaccuracy in predictions. On the other hand, also from the black curves, it can be seen that the energy predictions of the solid-only model and of the META model are very similar in both loading cases. The discrepancies in the final energy are 4 J at 227 m/s and less than 1 J at 105 m/s.

This similarity between the META and the solid-elements-only (SEO) models is not related to any premature element deletion. Simulations were repeated with another set of modified input properties for solid elements, where the deletion strain EFFEPS was doubled (denoted as "Solid-2-del"), while the input for the shell region remains "Shell-1". The appropriate energy curves are in red in Figure 7-4. The discrepancies in energy predictions were still found to be very small, 8 J at 227 m/s and 5 J at 105 m/s. The reason why the predictions of both the SEO model and the META model were lowered is related to the progressive crushing damage defined by a small value of AM3 in Table 7-1. When a larger strain is needed to trigger element deletion, the energy dissipated through this mechanism is increased.

Out of all the cases simulated, the highest energy dissipation was predicted by the SEO model with the input set "Solid-1", which are the blue curves in Figure 7-4. The projectile rebounded at the lower velocity and the contact was also prolonged. The predicted kinetic energy of this model is in good agreement with the one from its corresponding META model, where the input sets "Solid-1" and "Shell-1" are used for solid elements and shell elements respectively.

In all the META models analysed in this section, the material behaviour in the shell region was defined by the same set of input data, i.e. "Shell-1" in Table 7-3. Comparison of their energy curves revealed the impact response predictions can vary greatly depending on the material properties chosen for the solid region. With appropriate choice of the input properties, predictions obtained with META models are very similar to those obtained with their corresponding SEO

models. This indicates that the accurate definition of material behaviour in the solid region of the META model is crucial for accurate predictions of the impact response. This study also suggests that precise definition of the material behaviour in the shell region is of much smaller significance. This frees the concern about the differences between the material models that were raised in the Section 7.2.2. Therefore, the input set "Shell-1" and MAT58 are used for the shell regions in all the analyses involving META models below.

7.2.4 META for thick plates

The plates simulated in the previous section have a diameter to thickness ratio of 100:4, and can therefore be considered thin structures. Their deformation in the regions away from the impact site can be approximated by shell elements with good accuracy, therefore, META modelling was able to provide accurate predictions. Applicability of META for modelling the impact response of plates with large diameter to thickness ratio is investigated in the present study by simulating the impact of the thick plates as were used in the previous numerical and experimental study [198]. The FE model of the plate and of the projectile is shown in Figure 7-1. The plates had a diameter of 101.6 mm and thickness 13.2 mm, which results in a diameter to thickness ratio of 7.7. Two impact cases were simulated, where the projectile was assigned with the initial velocity of 360 m/s and of 800 m/s, at which the projectile rebounded and penetrated the target plate, respectively.

In addition to that, plates with different diameter to thickness ratios were studied by varying the diameter and keeping thickness constant at 4 mm (see the one on the right in Figure 7-1). For those plates, the initial projectile velocities were 105 m/s and 227 m/s.

Apparently, in this study, if the projectile size and shape are kept the same for all the loading cases, the projectile size increases relatively to the diameter of the plate, when the plate diameter is reduced. If the projectile is large enough to cause a widely extended 3D stress state, META is more likely to fail in delivering accurate prediction. On the contrary, META is expected to be more appropriate for small projectiles. To exclude the influence of projectile size in the study involving varying diameter-to-thickness ratio, the projectile size is varied, too, to keep the ratio of the projectile diameter to the plate diameter

constant. Similarly, the size of the solid region is varied accordingly so that the ratio of its area to the area of the entire plate is also constant.

The calculated time histories of the projectile kinetic energy are shown in Figure 7-5. The each of them is normalised to their initial kinetic energy values. Energy curves calculated with the SEO models are shown by solid lines, while dashed lines are used for the predictions of the META models.

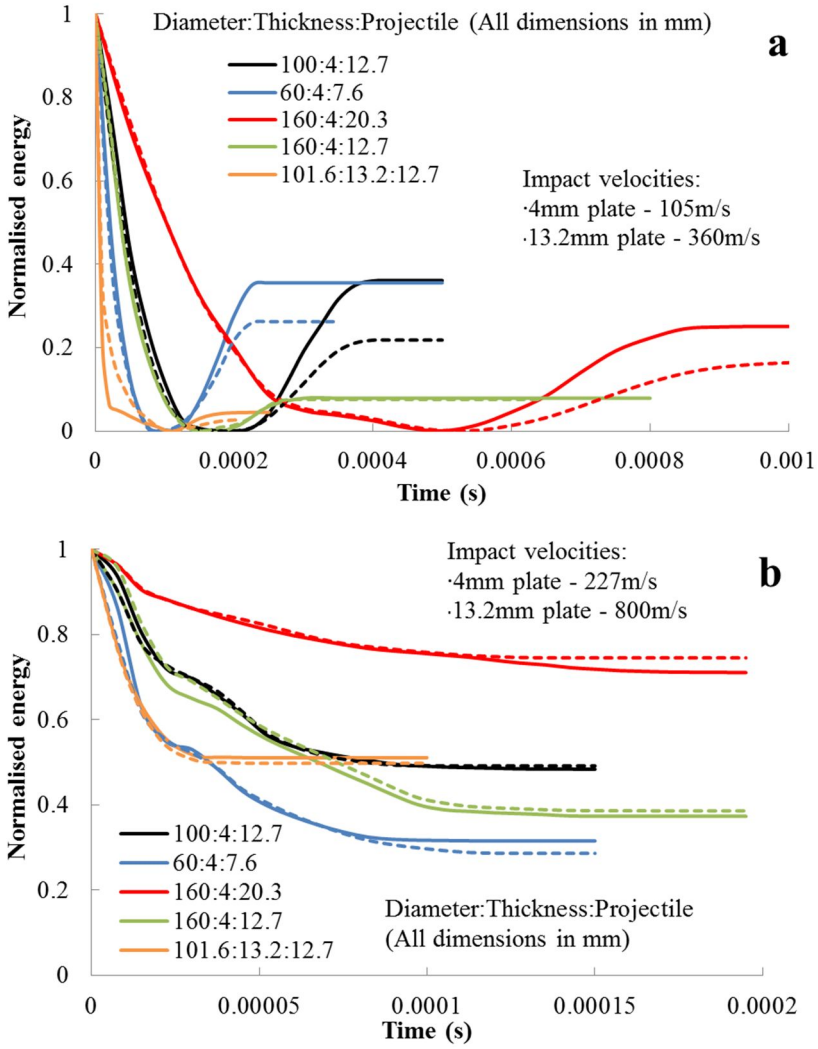


Figure 7-5 Projectile kinetic energy histories normalised to their initial values for the cases of rebounding (a) and penetration (b). The solid lines are for the SEO models and the dashed lines are for the META models.

Regarding the projectile size, as expected, for the 160 mm plate with "smaller" (12.7 mm diameter) projectile, the META prediction is very close to the corresponding solid model throughout the simulation. It confirms that META is applicable and more accurate for small projectiles.

The influence of the span-to-diameter ratio is studied by comparing the blue

(ratio=60:4), black (ratio=100:4) and red curves (ratio=160:4). The accuracy of META changes marginally with the diameter to thickness ratio. In the rebounding cases, as shown in Figure 7-5 (a), the discrepancies between the META models and their corresponding SEO models are 10%, 14% and 9%, respectively, from the plates with small diameter-to-thickness ratio to the plates with the large ratio. It is worth noting that, before rebounding, there are scarce discrepancies between the META models and their corresponding SEO models for all the three diameter-to-thickness ratios investigated. The lower final energies predicted by META models indicates the elastic energy stored in the plate was underestimated because of the shell region. The energy plots for the penetration scenarios are shown in Figure 7-5 (b). In these cases, the diameter-to-thickness ratio has even less noticeable effects on the results. The predictions of the META models are only 3%, 1% and 4%, respectively, different from those of the SEO models.

Even for the plates with the ratio of 7.7, META also provided very accurate predictions with respect to the final energy. Some discrepancy between the calculated energy curves in Figure 7-5 (a) was observed prior to the rebounding of the projectile. This could be an indication of a difference in the deformation of the target.

7.2.5 Deformation response of the plate

The deformation of the target, which is also an important aspect of modelling impact, was investigated for the 101.6-mm-diatmer 13.2-mm-thickness plate and the 100-mm-diameter 4-mm-thickness plate. They represent thick and thin targets, respectively, and will be referred to as “the thick plate” and “the thin plate” in the following. The deformation of the target plate under impact is studied by comparing the displacements at seven nodes in the X-direction, which is the through-thickness direction. All of these nodes are on the XY-plane, which is one of the two planes of material symmetry. The positions of those nodes in a META model of the target plate are shown in Figure 7-6. Nodes 1, 2 and 3 are on the central axis of the plate and are respectively located on the front face of impact, the middle plane of the plate and the back face. Nodes 4, 5 and 6 are located at the solid-shell interface. Node 7 is in the shell region. The same impact case was also simulated with the SEO model, and

displacements of the nodes at exactly the same positions were studied.

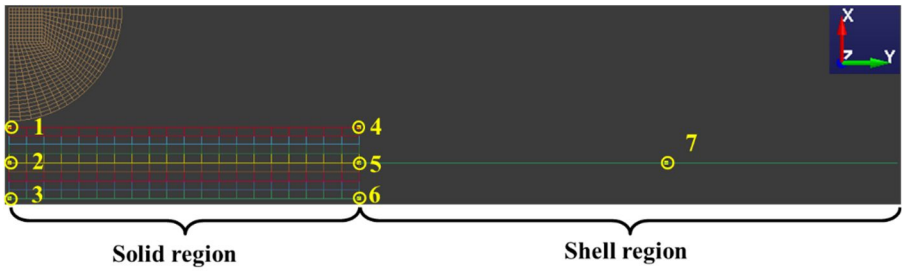


Figure 7-6 The nodes used to study the deformation of the target plate.

The comparison of the nodal displacements in the META and SEO models of the thin plate is presented in Figure 7-7.

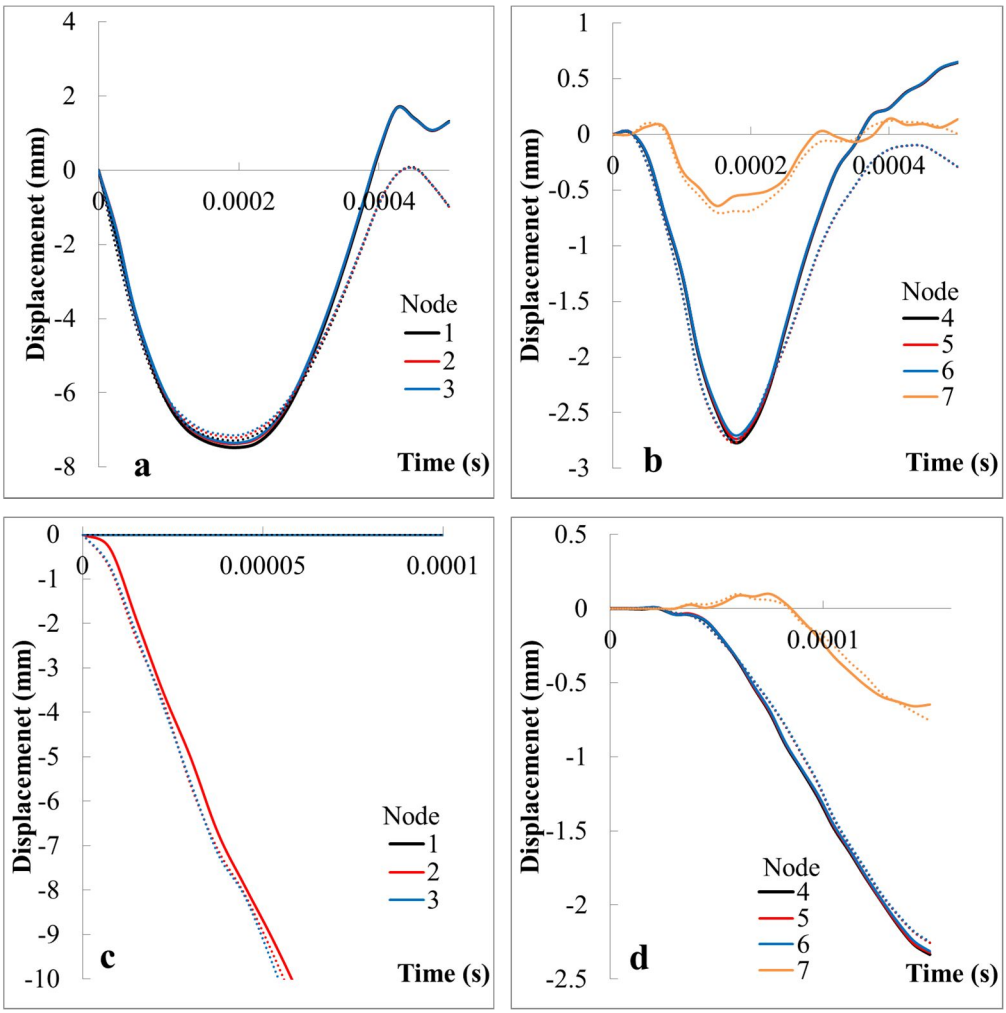


Figure 7-7 The displacements of the seven nodes for the 100:4:12.7 plates impacted at 105 m/s, i.e. rebounding (a and b), and 227 m/s,i.e. penetration (c and d). Solid lines are for the SEO models, dashed lines are for the META models.

Generally in the four figures, there is little difference in displacement at the nodes through the thickness, for instance at Nodes 1, 2 and 3 in Figure 7-7 (a). This indicates that the plate thickness was maintained during the impact. This

was captured by both the SEO and the META models. At the low velocity (Figure 7-7 (a) and (b)), the predictions by META are in good agreement with the SEO model before rebounding. After rebounding, the META predictions began to divert from those of the SEO model, leading to a discrepancy of approximately 1 to 2 mm for the nodes right under the projectile at the end of simulation. For the nodes at the interface, there is about 1 mm of discrepancy. The difference is minor for the nodes in the shell region. For the high velocity impact (Figure 7-7 (c) and (d)), the displacements predicted by the META model are very close to those of the SEO model throughout the simulation. The displacements for Nodes 1, 2 and 3 in Figure 7-7 (c), were zero throughout the simulation due to immediate element deletion after the contact began.

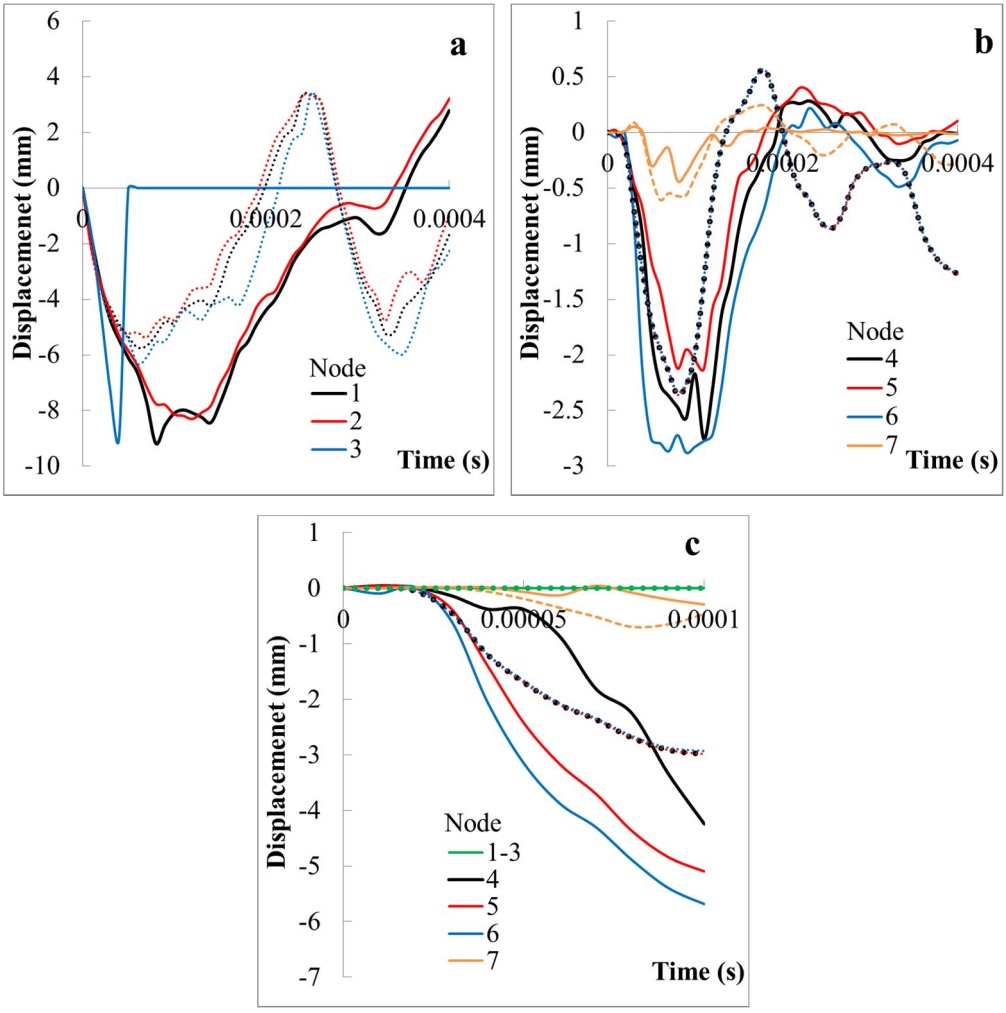


Figure 7-8 The displacements of the seven nodes in Figure 7-6 for the 101.6:13.2:12.7 plates impacted at 360 m/s, i.e. rebounding (a and b), and at 800 m/s i.e., penetration (c). Solid lines are for the SEO models, dashed lines are for the META models.

In the thick plate, the deflection predicted by the META model is less

accurate, as shown by Figure 7-8. For the case of projectile rebounding (Figure 7-8 (a)), the nodal displacements are obviously under predicted, and earlier rebounding of projectile was predicted for the META model. This indicates that the plate modelled with META has greater stiffness than the SEO model. Comparison of nodal displacements in Figure 7-8 (b) and (c), shows that in the SEO model, the node on the back face of the plate (Node 6) displaced more than the node on the front face (Node 4) and the node on the middle plane (Node 5). This may be attributed to bulge formation, which pushes the material near the front face sideways. This effect was not captured by META, as these displacements were predicted exactly the same. The minor differences for Node 7 displacements in both figures indicate that the shell element was able to accurately reflect the deformation at the middle plane of the plate.

7.2.6 Damage prediction

Prediction of material failure in the plate was also studied in a way similar to the analysis in Section 5.3.3. In the solid region where material model MAT162 was employed to define the material behaviour, the damage predictions of META at the end of the simulation were examined in terms of the fibre damage, the matrix damage and the delamination, all on the back face, where the most material damage occurs. The fibre crush failure is always localised within the impact vicinity and is thus excluded in the discussion. The contour plots of corresponding damage variables are shown in Figure 7-9. The contour scale varies from zero to one, which corresponds to intact and completely damaged/failed elements, respectively. The pattern of fibre damage is only indicative for the weft direction. Because of the material symmetry of the woven laminated composites [198] and the loading symmetry, the fibre damage in the warp direction is identical to that in the weft direction, and can therefore be visualised by rotating the contour plots showing weft fibre failure by 90°.

There are no variables specified in MAT58 that could be outputted for visualising failure or damage. Therefore, when the damage extends into the shell region of META model, this cannot be reflected in the contour plots as presented in Figure 7-9. Because of that, some forms of damage in the META models, such as the matrix damage of the thick plate impacted at 360 m/s, are shown as

a square pattern of the same size as the solid region.

By comparing the four SEO models, it can be seen that all three modes of damage tend to be more localised when penetration takes place (V_i=227 m/s and V_i=800 m/s). Except for some damage at the boundary of the thin plate, no damage extends beyond the central square region. For both the thick plate and the thin plate, accurate predictions of the shape and size of the damaged area for each mode were obtained with META. In lower velocity impact cases, when the projectile rebounded off the target, the localised damage modes, namely fibre damage and delamination of the thin plate, as well as the fibre damage in the thick plate, are also well captured in the META models.

Delamination is triggered by a criterion involving the direct stress and two shear stresses in the through-thickness direction. The small delamination failure in the thin plate suggests that in this case the values of those stress components were relatively small, which justifies the use of shell elements. At the same time, at the solid/ shell interface, those stress components become discontinuous, which results in false delamination predictions along the solid/shell interface in the META models.

The damage modes which extend beyond the solid element regions are the matrix damage in both plates in the case of rebounding, as well as the delamination in the thick plate. Matrix damage is determined by the in-plane shear stress and therefore could still be captured by the shell region. However, a large area of delamination indicates a major part of the thick plate was under high through thickness stress. Since the solid element area in the META model, was not sufficiently large to contain it, errors are introduced in the META predictions.

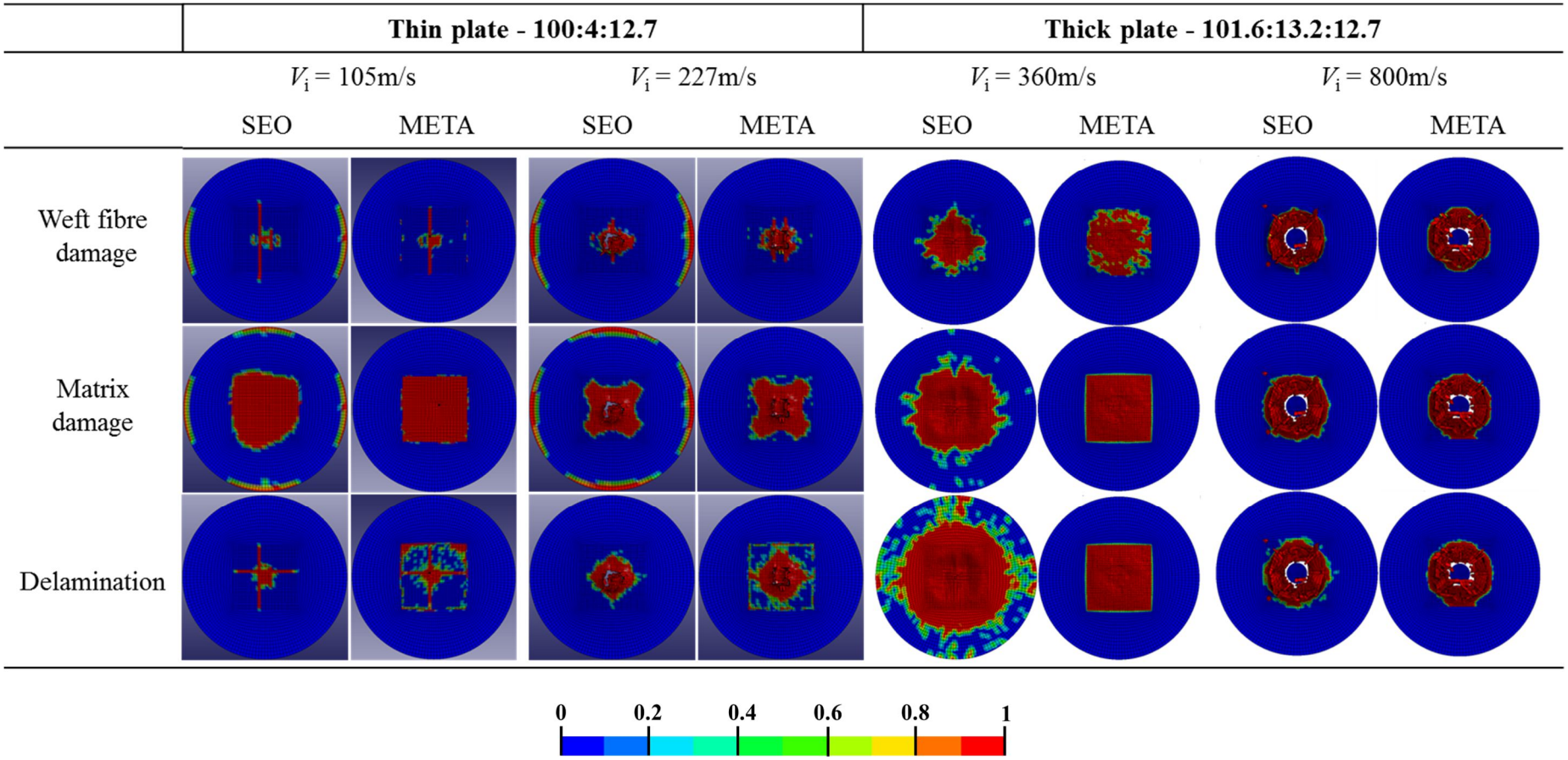


Figure 7-9 Damage predictions on the back face by MAT162 in the SEO and META models.

7.2.7 Using the ANN model with META

The analyses in the previous sections have shown that META can be an effective method of simplifying the computationally costly solid element models. When the ANN model in its present form was used for the solid region in META to model the ballistic impact tests of CF-IM7, the results, in terms of the final projectile kinetic energy, are in very good agreement with the all-solid-element ANN models as shown in Table 7-5. However, in all the cases considered, the predicted failure was very localised because of the premature element deletion. Because of the localised early failure, the plate deflections are relatively small, hence the contribution of the shell region into the impact response of the entire plate is insignificant. An improvement in the ANN model would be useful to fully assess the use of META with the ANN model.

Table 7-5 also shows the results when MAT162 was used, together with the calibrated inputs of CF-IM7 for the solid region of META. Again, META as a simplification method, makes prediction with very good accuracy compared to the equivalent SEO models. This is the case at all the velocities analysed.

Table 7-5 Final projecitle kinetic energies normalised to their initial values when the ANN was used in META to model the impacts on CF-IM7 plates.

V_i (m/s)	Exp	ANN-SEO	ANN-META	MAT162-SEO	MAT162-META
105	27%*	96%	96%	35%*	28%*
151	7%	96%	96%	27%	28%
227	52%	96%	95%	64%	64%

*The projectile rebounded.

7.3 META analysis for casing impact

It has been shown that META is able to deliver accurate predictions for the plate impact. In this section, the accuracy and efficiency of employing META for modelling large scale components are assessed. META and SEO models of a cylinder representing a fan containment casing have been constructed and analysed.

7.3.1 Methodology

The setup of the models follows an experiment described in [4] for testing composite fan casing components, as shown schematically in Figure 7-10. Geometric simplification was made by modelling the full scale fan casing as a ring of 2000 mm in inner diameter, 750 mm in length and 20 mm in thickness. Furthermore, the curved fan-blade-like projectile was simplified as a long thin plate. The bottom of the ring was fixed on a 30° slope. The projectile was fired along the horizontal direction to the ring, resulting in oblique impact on the inner surface of the ring.

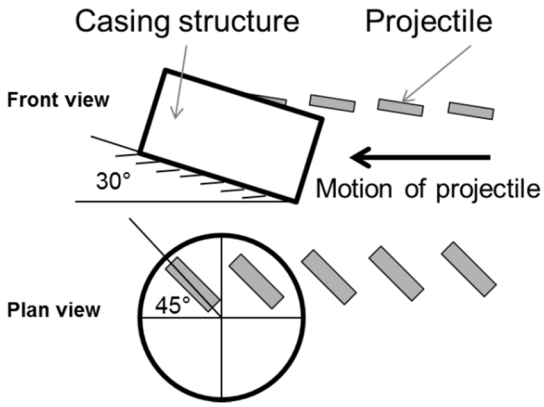
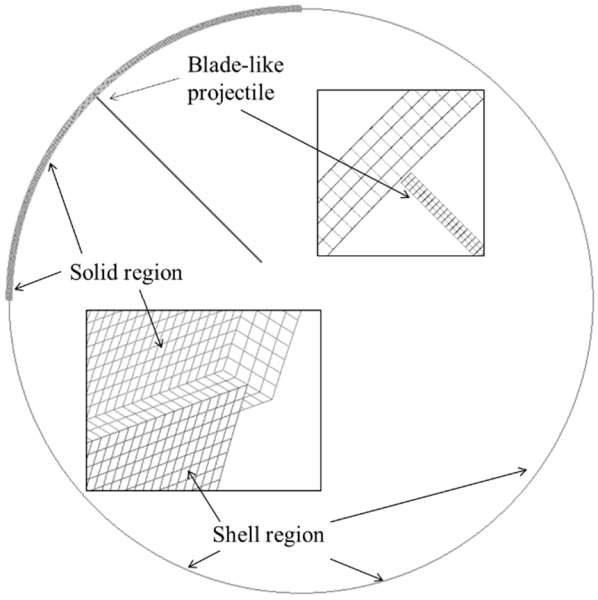


Figure 7-10 Test configuration for composite fan casing impact testing in [4].



Dimensions	Value in mm
Casing inner diameter	1990
Casing thickness	20
Casing length	750
Projectile length	800
Projectile width	250
Projectile thickness	5

Figure 7-11. The META model with quarter of the casing ring modelled with thin shell elements.

META models, as shown in Figure 7-11, and SEO models were built to simulate the test. The approach of META for plates described in Section 7.2.1

was adopted for the casing models, including the shell-solid region coupling, the material models for the composite and the single surface contact algorithm. The properties of the plain-weave S-2 glass/SC15 composite from [198] were used. The two yarn directions were set along the circumference and the length of the casing. In the META model, a quarter of the casing was modelled with 5 mm cubes of solid elements while the remainder was modelled with square shell elements with edge length of 5 mm. The mesh density and topology of the quarter of the casing in the SEO model were exactly the same as the META model. The projectile was modelled as rigid steel with mass of 7.875 kg and assigned an initial velocity of 120 m/s, giving an energy level of 57 kJ, which is close to the value employed in [225]. It was meshed with 3 layers of solid elements. The fan casing impact models were run on the high performance computing (HPC) system, at the University of Nottingham. 16 cores and 64G RAM were used.

7.3.2 Accuracy

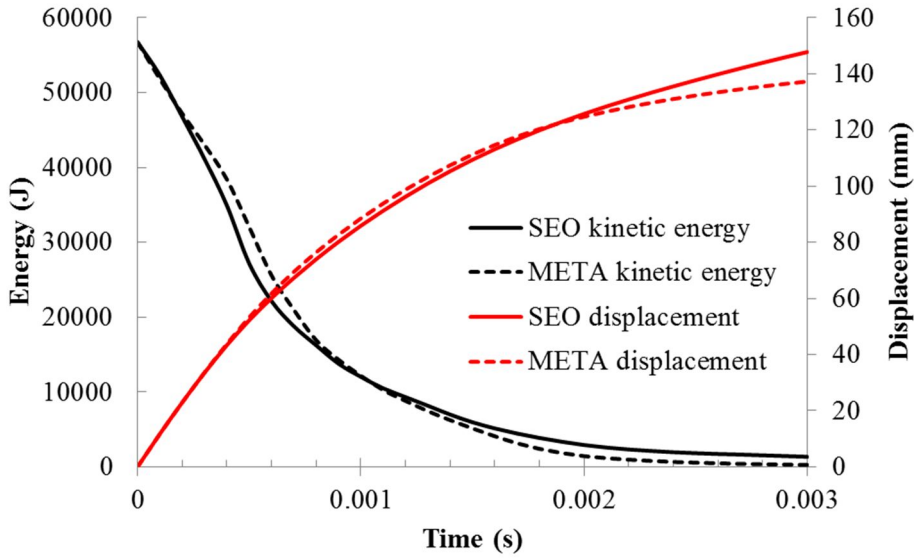


Figure 7-12. The projectile displacement and kinetic energy history in the casing impact model.

The time histories of projectile kinetic energy and displacement are shown in Figure 7-12. The kinetic energy reached a constant value close to 0 J at 3 ms, at which point the simulation was terminated. It can be seen that very good agreement between the META model and the SEO model is achieved for both projectile kinetic energy and displacement throughout the simulation. The

biggest discrepancy of 5% happened for the projectile displacement at the end of the simulation.

The deformations in the casing at 3 ms are compared in Figure 7-13. In general, the indentation and the deformation of the casing predicted by the META model are very close to the SEO model. In Figure 7-13 (b), in the region adjacent to the area of impact undergoes a rotation. This is captured by the META model in Figure 7-13 (a), where the top left quarter of the casing is modelled as a solid-element region. The rotation is observed near the interface between the two element regions. In particular, at the left interface, larger rotation is predicted by the META model than the SEO model. Far away from the impact region, neither deformation nor rotation is observed.

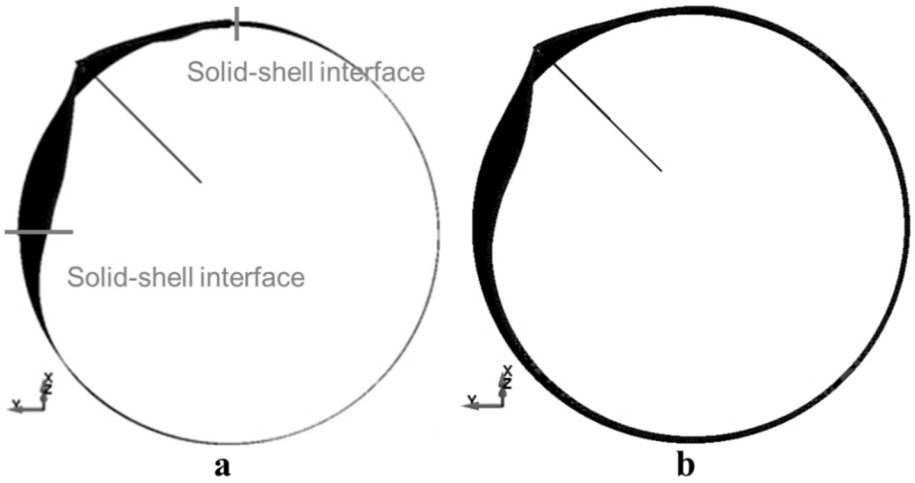


Figure 7-13. The deformation of the casing at 3 ms in (a) the META model; (b) the SEO model.

The contour plots in Figure 7-14 show the fibre damage along the circumference of the casing predicted by MAT162, viewing from the front face and back face of impact. In this case, fibre damage appears to be more of a global mechanism, as predicted by the SEO model in (a) and (c), and this damage mode extends far beyond the impact region. Again, due to the lack of implementation of a damage contour in MAT58 for the shell region, fibre damage cannot be illustrated here. Nevertheless, the damage patterns within the solid region are very similar for both the SEO and the META models. Such similarity is also observed for fibre damage along the height of the casing.

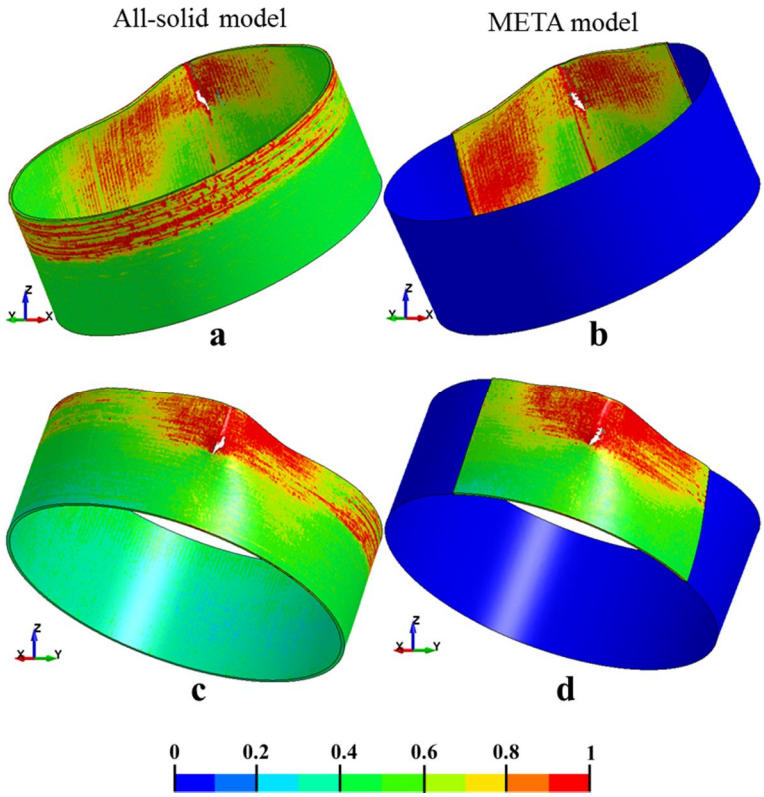


Figure 7-14 Results of the SEO model and the META model. Fibre damage contours viewing from the front face (a) and (b), and back face (c) and (d) of impact.

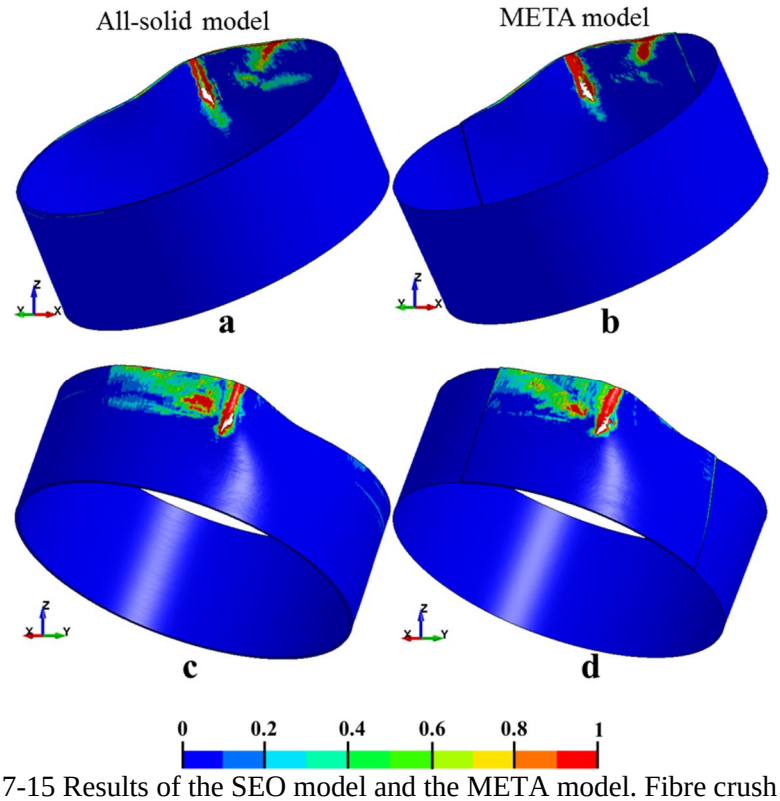


Figure 7-15 Results of the SEO model and the META model. Fibre crush failure contours viewing from the front face (a) and (b) and back face (c) and (d) of impact.

Fibre crush, as shown in Figure 7-15, is a localised failure mode, mostly concentrated in the impact region and its vicinity. The prediction for this mode

by the META model is in very good agreement with the solid model.

7.3.3 Saving

The computational savings of the above META model have been calculated by comparison with the SEO model, as shown by the first two columns in Table 7-6. The results are all normalised to the ones of the SEO model of using MAT162. By modelling one quarter of the casing with shell elements, the number of nodes is halved and the number of elements is reduced by 65%. The computational run time for the same event duration is saved by 40%. The saving in memory usage (34%) is less due to the solid-shell coupling.

Table 7-6 The simulation costs of the casing impact models when using MAT162 and ANN. All the results are normlised to the ones of the all-solid model of MAT162.

	SEO-MAT162	META-MAT162	SEO-ANN	META-ANN
Number of elements in the casing	100%	35%	100%	35%
Number of nodes in the casing	100%	50%	100%	50%
Memory required	100%	66%	76%	50%
Computational run time	100%	60%	25920%	6966%

A similar assessment was made for the ANN material model, which replaces MAT162 in the solid regions of the above two casing impact models. The models with ANN are found to be much more time-consuming than the ones with MAT162. In the SEO model with MAT162, it took about 6 hours of computational run time on the HPC to finish an event of 1 ms, which is merely the beginning of the impact. When ANN is used, it has been estimated that more than two months of real time is needed to finish the first 1 ms. In this case of using the ANN model, META is able to reduce the simulation time to a quarter of its corresponding SEO model, as shown in Table 7-6. The accuracy is not discussed here due to the aforementioned premature element deletion by the current ANN model.

7.4 Casing impact study

To investigate the performance of the 3D woven composites in an FBO scenario, in this section, META was used to model a casing made from CF-IM7

under four simple impact conditions. Instead of simplifying the blades as long thin plates, the twisted shape which is commonly found in fan blades was brought into consideration. In addition, rather than considering as rigid, the blades were modelled as deformable with conventional choice of titanium alloy and the popular new choice of composite materials.

7.4.1 Methodology

The casings in the META models, were generated in the same way as in Section 7.3.1 including the same dimensions, and the same boundary conditions. In this study, however, half of the casing is modelled with solid elements and the impactor is replaced by the twisted wide chord fan blade of a high bypass ratio turbofan aero engine, as shown in Figure 7-16. MAT162 with the inputs for CF-IM7 was used for the solid region and MAT58 was used for the shell region.

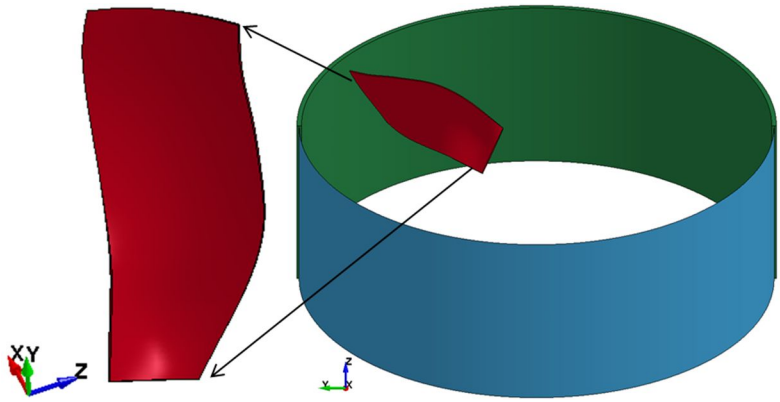


Figure 7-16 The META model of casing under ballistic impact by a single blade.

Simplifications were made to the geometry of the blade, such as excluding the sharp leading edge and trailing edge and assuming uniform thickness. The blade was modelled with single integration point solid elements. Three types of projectiles were considered. The deformable titanium blade was modelled with MAT_STRAIN_RATE_DEPENDENT_PLASTICITY and the inputs are given in Appendix 2. In addition, a rigid titanium blade was also considered, so was a blade made with CF-IM7, which was also the material for the casing. Its weft direction which has greater stiffness and strength was aligned with the radial direction of the blade. This would normally be the case to resist the centrifugal force during rotation. In addition, a rotational impact of the deformable titanium blade is also considered.

Table 7-7 A summary about the four models.

Notation	Impact	Projectile	Initial kinetic energy
BR	Ballistic	Rigid titanium	102kJ
BD	Ballistic	Deformable titanium	102kJ
BC	Ballistic	CF-IM7	33kJ
RD	Rotational	Deformable titanium	102kJ

The weight of fan blades and the energy during FBO are usually treated as confidential information by engine manufactures. The initial kinetic energy of this model was estimated in the rotational impact model by rotating the blade about the centre axis of the casing at 3000 revolutions per minute (RPM), which is normally the range of fan operating speed of a high bypass ratio turbo fan engines. The estimation was 127 kJ, based on a solid titanium blade. However, the real fan blades are actually lighter than the solid one modelled in this study, for instance, the widely-known hollow titanium fan blades developed by Rolls-Royce will be significantly lighter. Therefore, the initial energy for this study was scaled down to 102 kJ by a conservative assumption that the weight saving is 20%. An initial linear velocity was assigned to the solid titanium blade in the META ballistic impact model to match this energy level. In the META model with the CF-IM7 blade, the same initial velocity was assigned, but this resulted in an initial kinetic energy of only 33 kJ. The four models are summarised in Table 7-7.

7.4.2 Results

7.4.2.1 Blade movement during impact

At the simulated energy levels, the casings in all four models managed to contain the blade. The simulation was terminated after the blade became clearly incapable of penetrating the casing, which was identified from the analysis of the three momentum components of the blade, as shown by Figure 7-17. Deformations of the casings at specific time points in these models are shown in Figure 7-18.

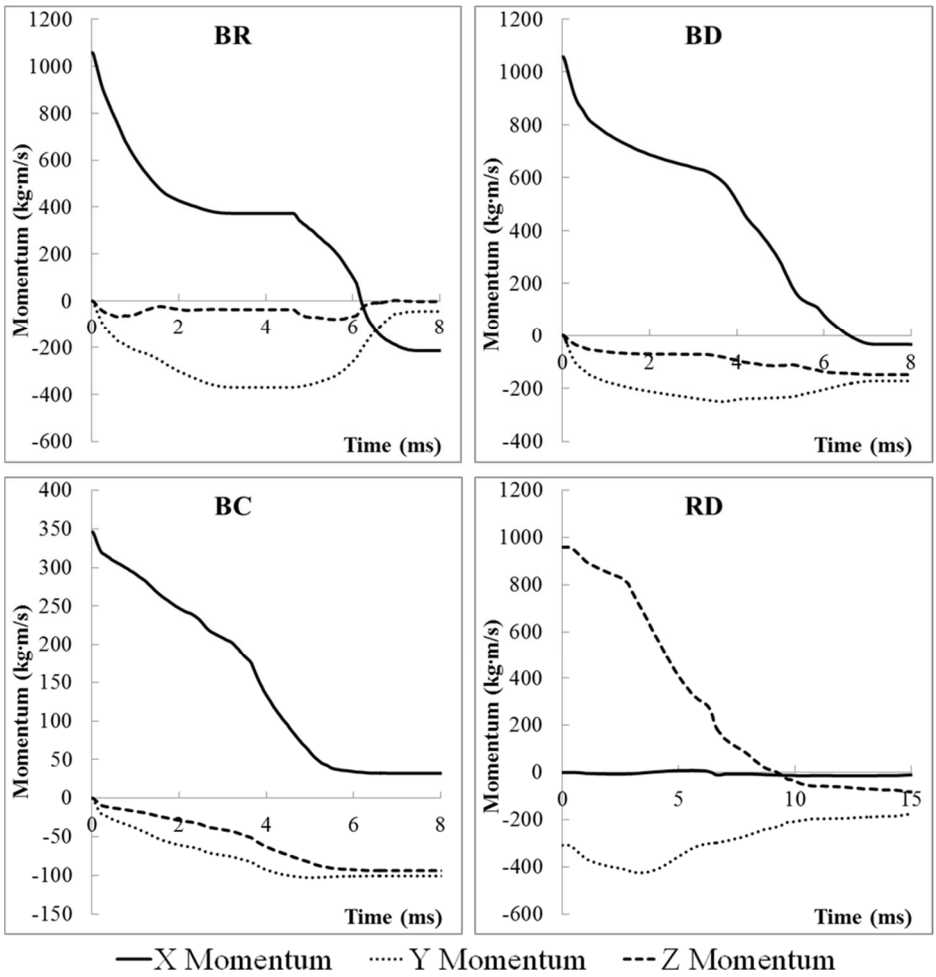


Figure 7-17 Momentum components of the blade during the impact. The coordinate systems are shown in Figure 7-18.

Given the coordinate system (see the dashed box in Figure 7-18), penetration would be indicated by the residual X-momentum in the BR, BD and RD models, and by the residual Z-momentum in the RD model. These momentums in the BR, BD and RD models become negative at about 6 ms, 6 ms and 9 ms respectively, indicating the "rebounding" of the blades. For BC, the X-momentum maintains a small positive value after 5 ms, but penetration also does not happen as shown in Figure 7-18. This positive residual is the result of the projectile sliding along the inner wall of the casing.

In the BR model with the rigid blade, first contact occurs before 3 ms, during which the projectile begins to tumble. At 3 ms, the tip of the blade already separates from the casing. This is reflected in Figure 7-17 as the X- momentum plateaus at about 400 kg·m/s. Even so, the casing continues to deform during this process due to the stress wave. At the same time, the blade hub gets closer to the casing and eventually from 5 ms, the second impact of the blade on the

casing occurs and lasts until 7 ms. Then the blade rebounds and separates from the casing. Similarly, the impact process of the other three models with deformable blades also involves a second impact, though the duration of the first contact differs. All these projectiles deformed and kept in contact with the casing after the first impact. It should be noted that in the rotational model the blade hub impacted onto the blade itself at the second impact, which is different from the ballistic cases. Separation is not observed in these three models after the second impact.

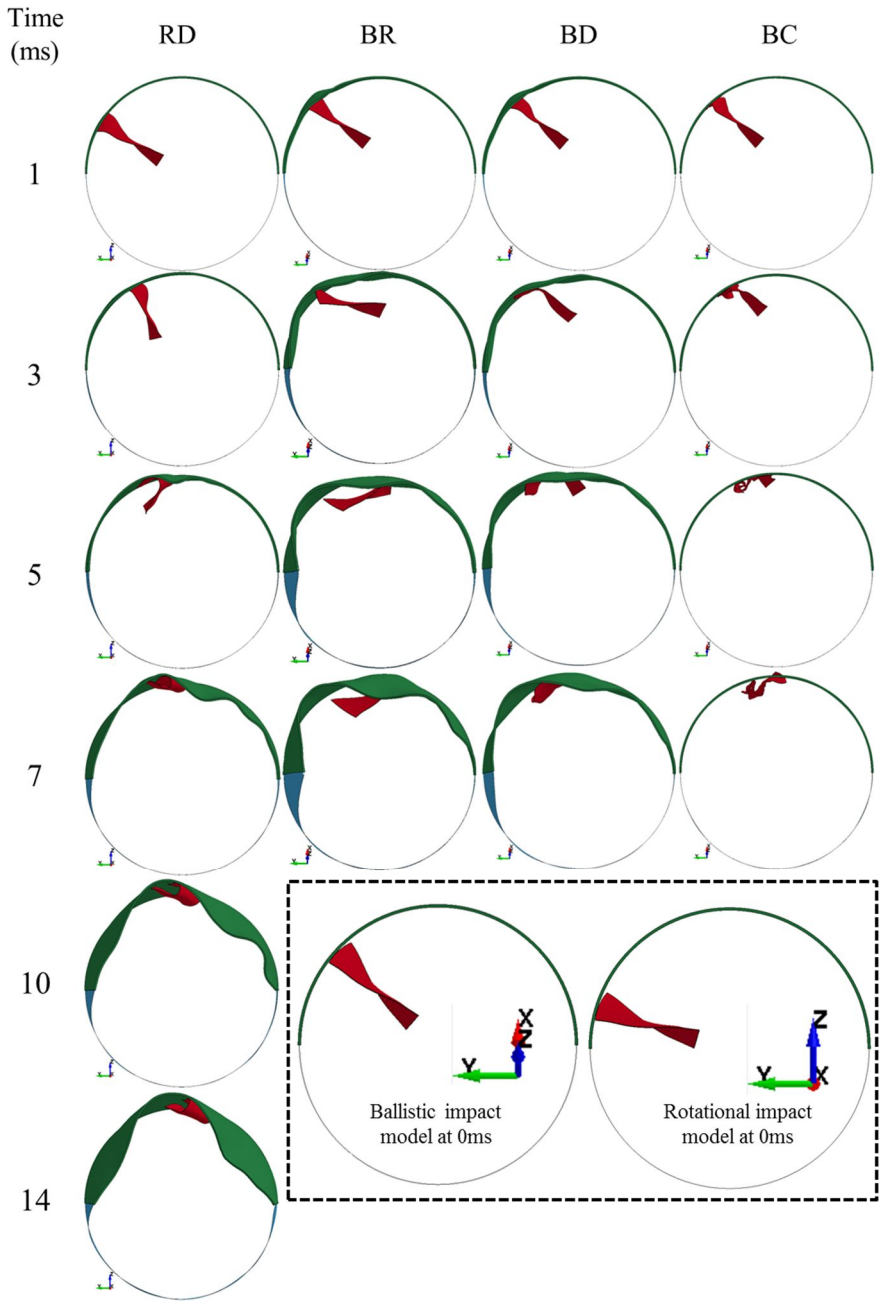


Figure 7-18 The impact process of the four models. The coordinate systems are also given: red for X, green for Y and blue for Z.

7.4.2.2 Casing deformation

While the casings impacted by the titanium blades deform substantially, the composite blade causes no obvious casing deformation. To better understand this difference, the casing deformation in terms of resultant displacements, is contour-plotted in Figure 7-19. It can be seen that in the BC model the maximum displacement was less than 10 mm throughout the simulated period. This is most likely due to the much lower level of impact energy.

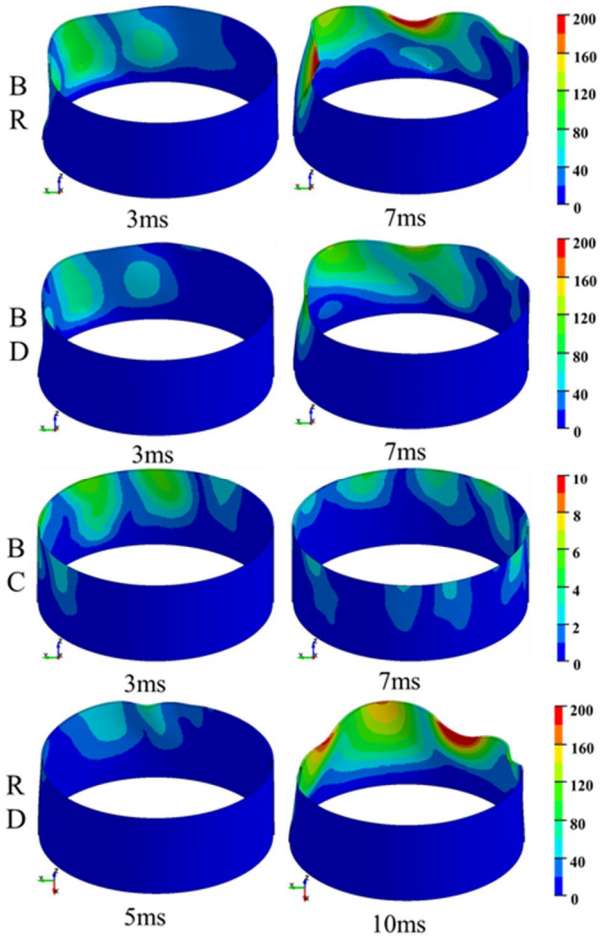


Figure 7-19 Deformation of the casing as resultant displacement (in mm) during the impact in the four impact models.

The energy of the models with the titanium blades is more than three times larger. At the ends of the first impacts (3 ms for BR, 3 ms for BD and 5 ms for RD), there are large regions of substantial displacement (above 80 mm for BR and BD, and above 40 mm for RD). By the ends of the second impacts, as shown in the second column in Figure 7-19, the free edges of the casings in BR and RD seemed to be wrapping towards their centres. There are regions where the displacement is as large as 200 mm. The corresponding displacements in BD are

about 100 mm, much less than the above two. By modelling the blade as deformable, a large part of the impact energy is dissipated through the blade deformation. It is self-evident that appropriate modelling of the blade is vital to the accuracy of the whole simulation. At the same time, the difference between the ballistic impact and rotational impact is revealed. With the same kinetic energy, the rotational impact leads to larger deformation to the casing than the ballistic impact, and therefore presents a larger threat. On the other hand, in all the four models, the deformations are minor along the fixed edges and in regions far away from the impact.

7.4.2.3 Failure and damage

The failure modes predicted by MAT162 are examined and presented as failure contours in Figure 7-20 in a way similar to the ones for panel impact in Section 5.3.3. While there is no failure at all in BC, the large deformations in the other models are reflected as the globally extended fibre failure, matrix failure and delamination. Shortly after the initial impact at 1 ms, BR and BD casings fail globally except for the fibre crush mode and fibre failure mode along the height of the casing. At the same step, the fibre failure in RD is very much more localised. By 7 ms, it can be seen that, except for the fibre crush failure, all the failure modes exist all over the solid region in these three models. It is very likely these failure modes also took place in the shell region, although MAT58 cannot display this information.

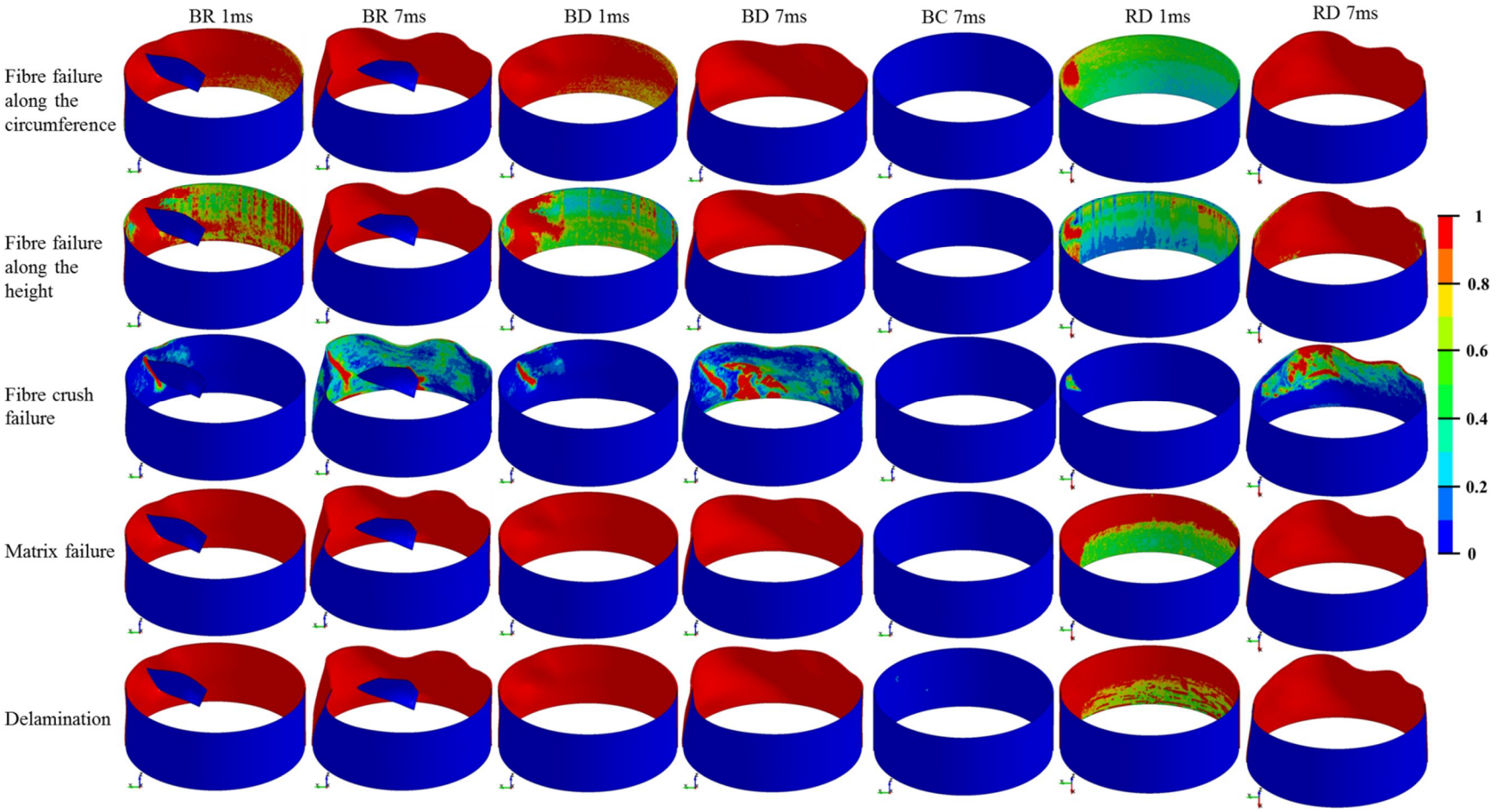


Figure 7-20 Pridiction of failure modes by MAT162 at 1 ms and 7 ms for the four models.

7.5 Conclusions

The impact loading of composite plates and full scale containment casing rings, were analysed by using mixed element type analysis (META). The capabilities and limitations of META were examined by comparing the predictions of the META models with those of their corresponding solid-element-only (SEO) models.

The modelling of plate impact started with an effort to minimise possible influences due to the differences between the material models for the solid elements (MAT162) and the shell elements (MAT58). It was found that the shell region has minor influence on the prediction of the projectile final kinetic energy. As long as the solid region is defined the same way as the corresponding SEO model, the projectile kinetic energy by the META model is very close to that predicted by the SEO. This is applicable to the plates whose diameter-to-thickness is within the range from 7.7 to 40. META also provides very accurate prediction about the localised damage modes in the plate. However, META has less accurate prediction of deformation and damage for the (thick) plates with small diameter-to-thickness ratio. This is because the impact of the thick plates involves a larger region of 3D stress, which extended into the shell region.

The savings obtained by employing META was assessed in the simulation of a full scale composite casing ring, where MAT162 and solid elements were used for a quarter of the ring and the rest three quarters of the ring were meshed with shell elements and modelled with MAT58. It gives predictions similar to the corresponding SEO model with respect to projectile trajectory, casing deformation and material failure. This was achieved with a 40% reduction in computational run time. The savings of META when the ANN model is used were also investigated. It was found that the SEO model which employs ANN requires a significant longer computational run time for simulating the same event duration than the SEO model which employs MAT162. In this case, by using META, the computational run time is 75% less than the corresponding SEO model.

The response of full scale fan casings made from CF-IM7 when impacted by blade-like projectiles, was investigated by using META. The setup of the above ballistic impact tests was employed but the projectile was modelled as a

rigid body of titanium (Ti), deformable Ti and deformable CF-IM7 in three models respectively. The rotational impact of the deformable Ti blade was also simulated. The impact energy level was estimated by rotating the Ti blades at 3000 RPM. The same rotational speed leads to significantly lower impact energy in the model with the CF-IM7 blade, where the impact caused no failure and trivial deformation to the casing. In all the models with the Ti blades, the casings managed to resist penetration during the first impact as well as the second impact caused by rigid blade tumbling or blade deformation. However, significant deformation (>100 mm) was found in the casings after the second impact. The prediction by MAT162 also indicates that, after the second impact, global failure of all the modes in the composites casings occurred except for the fibre crush mode.

Chapter 8 Conclusions and Recommendations

In this chapter, the main contributions and conclusions from this doctoral project are presented. Then, recommendations for future work are outlined.

8.1 Conclusions

Characterisation of 3D woven composites

- This study involves several characterisation tests for 3D woven composites, which provide important information for the macro scale simulation and the validation of multi-scale modelling approaches. The investigation is focused on a special form of 3D woven textile which is often referred to as 2.5D woven textile. Four types of 2.5D woven textile composites were tested under quasi-static in-plane tensile, compressive and shear loadings.
- The tension in both the weft and the warp directions shows that the tensile moduli and strengths are directly related to the mechanical properties and volume fraction of fibres. Out of the four types of composite tested, the one with IM7 carbon fibres (CF-IM7) possesses the largest strain energy density at final failure, which is also an indication of higher capability of dissipating impact energy. Via microscopic observation on specimens loaded to different levels of strain, the commonly-observed reduction of tensile stiffness is found to be caused by the debonding of yarns from the matrix.
- Under compression, the mechanical properties appear unrelated to the fibre contents, except the weft compressive strength. The stress-strain curves are generally linear until the maximum stress, where specimens failed under through thickness shear via fibre kinking for the weft compression or connection of debondings for the warp compression. The failed specimens are still in one piece and significant load carrying capability remains.
- In-plane shear was performed by two methods, i.e. 45° off-axis tensile shear and two-rail shear. Between these tests, only minor difference is found with respect to the shear moduli and the 0.2% offset strength, both of which also show little difference among the four composites as a result of matrix dominant behaviour. Non-linearity is commonly observed after the initial linear part. Fracture happened in the glass composites transverse to the

weaker yarns, while yarn rotation took place in the other composites and made the tests little representative of pure shear state at later stages of the testing.

- SHPB compression was carried out to obtain the compressive properties at high strain rates and then to establish the strain rate dependency for impact simulation. Unreliable measurements of compressive moduli were obtained due to non-constant strain rates in the early stages of the testing. However, the dynamic compressive strength results are more reliable and clearly rise with increasing strain rate for all the materials. The failure modes of the SHPB specimens resemble those under QS compressive loadings, namely fibre kinking in the weft specimens, and debonding and further crimping in the warp specimens.

Ballistic impact tests on composite plates

- Ballistic impact tests, which are even less reported for 3D woven composites than their characterisation tests, were performed in this study for the above 3D woven composites and a quasi-isotropic IM7 carbon fibre laminate. An air gun apparatus was used to fire rigid steel spherical projectiles onto clamped flat composite plates at various velocities. The ballistic limits are determined by non-linear curve fitting of the measured velocity pairs to the Jonas-Lambert equation, as an indicator of the resistance to penetration.
- The analysis shows that more tests are needed for the glass composites, but the conclusion can be drawn that GF-2 has the largest penetration resistance with the limit velocity being 180 m/s, followed by GF-1 (173 m/s), CF-IM7 (161 m/s) and QI-IM7 (134 m/s). However, the penetration resistances of the three types of 3D woven composites differ less than 10%, if normalised to their densities.
- Visual inspection and XCT were employed to observe the damage modes in the impacted plates. It is found that there is more damage and material loss near the back face of impact. Crushing and breakage of both weft and warp yarns together with the debonding are the failure modes observed in similar locations in both glass and carbon composites. The failure modes in the warp direction are only found in the impact vicinity, while those in the weft direction are more extended. In addition, the yarn damage modes are more

extended in CF-IM7, while debonding is more extended in GF-2.

Simulation of the ballistic impact tests

- As an achievement of a parallel PhD project, the ANN material model, developed via a multi-scale modelling approach, have been used in this work for the macro scale simulation of 3D textile composites. They are employed in LS-DYNA to simulate the ballistic impact tests on the plates. The simulation shows the correct trend, however at present underestimates the penetration resistance.
- The main simulations in this work employ a commercially available material model, MAT162 of LS-DYNA, as it includes three important features of modelling, i.e. mode-dependent failure criteria, damage mechanics and strain rate dependency. Following calibration and selection of input data, acceptably accurate prediction can be made by using MAT162 about the projectile velocities during plate impact. Important failure characteristics caused by the impact, such as fibre failure in the weft direction, are also captured. This provides a viable approach for FE analysis of 3D textile composites under impact loading alternative to multi-scale modelling approaches.
- The drawback of using MAT162 or similar phenomenological macro scale material models is also exposed. Even for each variation of the same textile architecture, this approach requires an extensive experimental testing programme to provide the material input data. The limitations and recommended developments regarding MAT162 are presented in the next section.

Parametric studies of plate impact tests

- Parametric studies were performed by FE simulation to understand the factors which may differentiate the commonly used plate impact tests from the rarely reported FBO tests, and how the impact performance of the IM7 carbon fibre 3D woven composites are affected by these factors.
- Projectile shape was found to affect the penetration resistance. Among the five designated projectiles, the flat cylinder projectile is the most efficient in penetration, followed by the FSP, conical, spherical and cuboid projectiles.

For projectiles with flat end faces, energy dissipation is related to shape-related mechanisms as well as size-related mechanisms such as shear cutting, crushing and plug formation. The penetration of projectiles with a point contact, e.g. the conical projectile, involves hole enlargement, whose contribution to energy dissipation can also be significant.

- The effects of the projectile shape are more apparent for a target with a larger span-to-thickness ratio, as the larger ratios magnify the difference in target bending caused by the projectiles. However, the dissipated energy, when normalised to the target mass, is actually lower for the plates with the larger ratios.
- The effect of impact obliquity is evident for both penetration and rebounding cases. The normal velocity required for penetration reduces with increasing impact angle, while the corresponding resultant rises significantly. Normal impact (0°) results in the most dangerous scenario as it requires the least amount of energy for penetration.
- It is also revealed that more curved are less resistant to penetration as it is more difficult to bend them. However, the effects of target curvature only become apparent when the plate is curved to a certain degree, which in this study happened when *R/S* was decreased from 2.5 to 1.25. Therefore, the impact tests on the flat plates are representative for the targeted casing structures whose $R/S \geq 2.5$.

Simulation of impact on composite casing structures

- Mixed element type analyses (META) has been employed to ease the computational requirements for simulating the localised impact of large composite casings. This method was assessed by modelling plate impact tests. It is found that, for plates whose diameter-to-thickness ratio are within the rage of 7.7 to 40, META provides accurate predictions of the projectile kinetic energy and the localised damage modes in the targets. However, when impact response and damage are widely extended, META is less accurate in predicting the target deformation and damage. The saving of META was assessed by modelling a ballistic impact for casings. The computational run time was reduced by 40% when a quarter of the casing was meshed as solid elements while the rest of the casing was meshed as

shell elements. The newly developed multi-scale ANN model takes a significantly longer run time to simulate the same event duration. In this case, the saving of run time by using META is 75%.

- The response of fan casings, made from CF-IM7, when impacted by blade-like projectiles was investigated in four META models, where blades were modelled as rigid titanium or deformable titanium or CF-IM7, the same material as the casing. At the considered energy levels, all the casings manage to contain the blades after the first impact as well as the second impact caused by rigid blade tumbling or blade deformation. Compared with the composite blade, the titanium blades are much heavier and possess larger kinetic energy, leading to severe deformation and damage of the casings.

8.2 Recommendations for future work

Characterisation tests for textile composites

- The through thickness (TT) reinforcements make 3D textile composites stronger than laminated composites in the through-thickness direction. However, the small thickness of the studied materials imposes challenges to the testing of through thickness properties, with issues such as the clamping in TT tension tests and strain measurements. It is recommended to develop appropriate testing techniques and investigate the TT properties of 3D textile composites. This topic is scarcely discussed in the open literature.
- The dynamic testing in this thesis has been limited to compressive loading. Efforts were made in developing appropriate methods for other loading conditions, but the testing was not conducted due to the time constraint in this project. In this study, it is found that the strain rate effects on the weft compressive strength are very different from those on the warp compressive strength. It is recommended to continue the development and carry out an investigation to understand how other mechanical properties, e.g. tensile strengths and shear strengths, are affected by strain rates.

Development of apparatus for impact tests

- The current gas gun apparatus can only fire 12.7 mm ball bearings normally onto a circular plate of 100 mm diameter. By simulation, a parametric study reveals that some factors do differentiate the plate impact tests from the FBO

impact. It is recommended to further develop the gas gun and the target fixture such that the parametric studies can be verified experimentally, so that the above factors can be investigated in more depth.

- The impact of casing structures has been studied by simulation only. It reveals that the rotational impact is not identical to the ballistic impact at the same kinetic energy. In order to get a better understanding about the performance of 3D textile composites during FBO, apparatus for rotational impact tests is recommended for future development.

Macro scale material model for textile composite

- Phenomenological macro scale material model similar to MAT162 is able to achieve acceptable accuracy in the impact simulation of 3D textile composites. If such models are developed based on MAT162, improvements are needed by addressing the exposed limitations of MAT162. These include the competency of modelling bilinear and non-linear stress-strain relation, the distinction of compressive behaviour from tensile behaviour and the difference in the strain rate effects on various mechanical properties.
- Appropriate material models for shell element formulation are also recommended to save the computational run time for simulations which involve little through thickness stress. It can also be used in the shell region in a META analysis.

References

1. Turner, M.G., A. Norris and J. Veres, *High fidelity 3D simulation of the GE90.* AIAA Paper, 2003. **3996**: p. 2003.

2. Griffiths, B., *2011 International Paris Air Show*. Composites World, 9th January 2011. 5th December 2012. Available from: http://www.compositesworld.com/articles/2011-international-paris-air-show.

3. King, J., *Composites for Aeroengines.* Materials World, 1997. **5**(6): p. 324-327.

4. Roberts, G.D., J.M. Pereira, M.S. Braley, W.A. Arnold, J.D. Dorer and W.R. Watson, *Design and testing of braided composite fan case materials and components*. 2009, National Aeronautics and Space Administration John H. Glenn Research Center at Lewis Field Cleveland.

5. GE Aviation, *New GEnx Engine Advancing Unprecedented Use of Composites in Jet Engines*. GE Aviation, 14th December 2014. 11th May. Available from: http://www.geaviation.com/press/genx/genx_20041214.html.

6. Albany International Corp., *LEAP Fan Casing*. 17th July 2015. Available from:http://www.albint.com/business/aec/en-us/aerospace/Pages/LEAP-Fan-Casing.aspx.

7. Roberts, G.D., D.M. Revilock, W.K. Binienda, W.Z. Nie, S.B. Mackenzie and K.B. Todd, *Impact testing and analysis of composites for aircraft engine fan cases.* Journal of Aerospace Engineering, 2002. **15**(3): p. 104-110.

8. Pan, Q., *Multi-scale modelling and material characterisation of textile composites for aerospace applications*, PhD thesis, University of Nottingham, 2016.

9. Yu, T., *Continuum Damage Models and Their Applications to Composite Components of Aero-Engines* PhD thesis, University of Nottingham, 2016.

10. Zhao, X., *Defects generation in the manufacturing of composite materials*, PhD thesis, University of Nottingham, 2016.

11. Hull, D. and T. Clyne, *An introduction to composite materials*. 1996: Cambridge university press.

12. Dixit, A. and H. Mali, *Modeling techniques for predicting the mechanical properties of woven-fabric textile composites: a Review*. Mechanics of Composite Materials, 2013. **49**(1): p. 1-20.

13. Kelkar, A.D., J.S. Tate and R. Bolick, *Structural integrity of aerospace textile composites under fatigue loading.* Materials Science and Engineering: B,

2006. **132**(1–2): p. 79-84.

14. Abrate, S., *Impact on Laminated Composite Materials.* Applied Mechanics Reviews, 1991. **44**(4): p. 155-190.

15. Mouritz, A.P., M.K. Bannister, P.J. Falzon and K.H. Leong, *Review of applications for advanced three-dimensional fibre textile composites.* Composites Part A: Applied Science and Manufacturing, 1999. **30**(12): p. 1445-1461.

16. Warrior, N.A., C.D. Rudd and S.P. Gardner, *Experimental studies of embroidery for the local reinforcement of composites structures: 1. Stress concentrations.* Composites Science and Technology, 1999. **59**(14): p. 2125-2137.

17. Mouritz, A.P., *Review of z-pinned composite laminates.* Composites Part A: Applied Science and Manufacturing, 2007. **38**(12): p. 2383-2397.

18. Miravete, A., *3-D textile reinforcements in composite materials*. 1999: Woodhead Publishing.

19. Tong, L., A.P. Mouritz and M. Bannister, *3D fibre reinforced polymer composites*. 2002: Elsevier.

20. Tyler, T., *Fibre Innovations braiding machine*. 8 July 2015. Available from: http://hexdome.com/weaving/triaxial/manufacturing/.

21. Chou, S., H.-C. Chen and C.-C. Wu, *BMI resin composites reinforced with 3D carbon-fibre fabrics.* Composites Science and Technology, 1992. **43**(2): p. 117-128.

22. Farley, G.L., B.T. Smith and J. Maiden, *Compression Response of Thick Layer Composite Laminates with Through-the-Thickness Reinforcement.* Journal of Reinforced Plastics and Composites, 1992. **11**(7): p. 787-810.

23. Khokar, N., *3D-Weaving: Theory and Practice.* The Journal of The Textile Institute, 2001. **92**(2): p. 193-207.

24. Soden, J.A. and B.J. Hill, *Conventional weaving of shaped preforms for engineering composites.* Composites Part A: Applied Science and Manufacturing, 1998. **29**(7): p. 757-762.

25. Xiaogang Chen, L.W. Taylor and L.-J. Tsai, *An overview on fabrication of three-dimensional woven textile preforms for composites.* Textile Research Journal, 2011. **81**(9): p. 932-944.

26. Ansar, M., W. Xinwei and Z. Chouwei, *Modeling strategies of 3D woven composites: A review.* Composite Structures, 2011. **93**(8): p. 1947-1963.

27. Dalmaz, A., P. Reynaud, D. Rouby, G. Fantozzi and F. Abbe, *Mechanical behavior and damage development during cyclic fatigue at high-temperature of a 2 · 5D carbonSiC composite.* Composites Science and

Technology, 1998. **58**(5): p. 693-699.

28. Dalmaz, A., D. Ducret, R. El Guerjouma, P. Reynaud, P. Franciosi, D. Rouby, G. Fantozzi and J.C. Baboux, *Elastic moduli of a 2.5D Cf/SiC composite: experimental and theoretical estimates.* Composites Science and Technology, 2000. **60**(6): p. 913-925.

29. Boitier, G., J. Vicens and J.L. Chermant, *Understanding the creep behavior of a 2.5D Cf–SiC composite-I. Morphology and microstructure of the as-received material.* Materials Science and Engineering: A, 2000. **279**(1–2): p. 73-80.

30. Ma, J., Y. Xu, L. Zhang, L. Cheng, J. Nie and N. Dong, *Microstructure characterization and tensile behavior of 2.5D C/SiC composites fabricated by chemical vapor infiltration.* Scripta Materialia, 2006. **54**(11): p. 1967-1971.

31. Ma, J., Y. Xu, L. Zhang, L. Cheng, J. Nie and H. Li, *Preparation and mechanical properties of C/SiC composites with carbon fiber woven preform.* Materials Letters, 2007. **61**(2): p. 312-315.

32. Zhu, Y., Z. Huang, S. Dong, M. Yuan and D. Jiang, *Fabricating 2.5D SiCf/SiC Composite Using Polycarbosilane/SiC/Al Mixture for Matrix Derivation.* Journal of the American Ceramic Society, 2007. **90**(3): p. 969-972.

33. Jekabsons, N. and J. Varna, *Micromechanics of Damage Accumulation in a 2.5D Woven C-Fiber/SiC Ceramic Composite.* Mechanics of Composite Materials, 2001. **37**(4): p. 289-298.

34. Nehme, S., A. Hallal, F. Fardoun, R. Younes, B. Hagege, Z. Aboura, M. Benzeggagh and F.H. Chehade, *Numerical/analytical methods to evaluate the mechanical behavior of interlock composites.* Journal of Composite Materials, 2011. **45**(16): p. 1699-1716.

35. Lu, Z., Y. Zhou, Z. Yang and Q. Liu, *Multi-scale finite element analysis of 2.5D woven fabric composites under on-axis and off-axis tension.* Computational Materials Science, 2013. **79**: p. 485-494.

36. Hallal, A., R. Younes, F. Fardoun and S. Nehme, *Improved analytical model to predict the effective elastic properties of 2.5D interlock woven fabrics composite.* Composite Structures, 2012. **94**(10): p. 3009-3028.

37. Llorca, J., C. González, J.M. Molina-Aldareguía, J. Segurado, R. Seltzer, F. Sket, M. Rodríguez, S. Sádaba, R. Muñoz and L.P. Canal, *Multiscale Modeling of Composite Materials: a Roadmap Towards Virtual Testing.* Advanced Materials, 2011. **23**(44): p. 5130-5147.

38. Bogdanovich, A.E., *Multi-scale modeling, stress and failure analyses of 3-D woven composites.* Journal of Materials Science, 2006. **41**(20): p. 6547-6590.

39. Kanouté, P., D.P. Boso, J.L. Chaboche and B.A. Schrefler, *Multiscale Methods for Composites: A Review.* Archives of Computational Methods in

Engineering, 2009. **16**(1): p. 31-75.

40. Ernst, G., M. Vogler, C. Hühne and R. Rolfes, *Multiscale progressive failure analysis of textile composites.* Composites Science and Technology, 2010. **70**(1): p. 61-72.

41. Ji, C., B. Sun, Y. Qiu and B. Gu, *Impact Damage of 3D Orthogonal Woven Composite Circular Plates.* Applied Composite Materials, 2007. **14**(5-6): p. 343-362.

42. Bahei-El-Din, Y.A. and M.A. Zikry, *Impact-induced deformation fields in 2D and 3D woven composites.* Composites Science and Technology, 2003. **63**(7): p. 923-942.

43. Ji, K.H. and S.J. Kim, *Dynamic Direct Numerical Simulation of Woven Composites For Low-velocity Impact.* Journal of Composite Materials, 2007. **41**(2): p. 175-200.

44. Lv, L. and Bohong Gu, *Transverse Impact Damage and Energy Absorption of Three-Dimensional Orthogonal Hybrid Woven Composite: Experimental and FEM Simulation.* Journal of Composite Materials, 2008. **42**(17): p. 1763-1786.

45. Hao, A., B. Sun, Y. Qiu and B. Gu, *Dynamic properties of 3-D orthogonal woven composite T-beam under transverse impact.* Composites Part A: Applied Science and Manufacturing, 2008. **39**(7): p. 1073-1082.

46. Hu, H., B. Sun, H. Sun and Bo. Gu, *A Comparative Study of the Impact Response of 3D Textile Composites and Aluminum Plates.* Journal of Composite Materials, 2010. **44**(5): p. 593-619.

47. Sun, B., Y. Liu and B. Gu, *A unit cell approach of finite element calculation of ballistic impact damage of 3-D orthogonal woven composite.* Composites Part B: Engineering, 2009. **40**(6): p. 552-560.

48. Li, Z., B. Sun and B. Gu, *FEM simulation of 3D angle-interlock woven composite under ballistic impact from unit cell approach.* Computational Materials Science, 2010. **49**(1): p. 171-183.

49. Hae-Kyu, H., P. Jungsun and K. Rakesh, *Ballistic Resistance of 3-D Orthogonal Woven Textile Composites with Helically Twisted Z-Strands*, in *50th AIAA/ASME/ASCE/AHS/ASC Structures, Structural Dynamics, and Materials Conference*. 2009, American Institute of Aeronautics and Astronautics.

50. Ghosh, R. and S. De, *Z-fiber influence on high speed penetration of 3D orthogonal woven fiber composites.* Mechanics of Materials, 2014. **68**: p. 147-163.

51. Schwer, L.E., *Impact of a 3D Woven Textile Composite Thin Panel: Damage and Failure Modeling.* Mechanics of Composite Materials and Structures, 1999. **6**(1): p. 9-30.

52. Pankow, M., A.M. Waas, C.-F. Yen and S. Ghiorse, *Shock loading of 3D woven composites: A validated finite element investigation.* Composite Structures, 2011. **93**(5): p. 1347-1362.

53. Naik, N.K. and S. Meduri, *Polymer-matrix composites subjected to low-velocity impact: effect of laminate configuration.* Composites Science and Technology, 2001. **61**(10): p. 1429-1436.

54. Udatha, P., C.V. Sesha Kumar, N.S. Nair and N.K. Naik, *High velocity impact performance of three-dimensional woven composites.* The Journal of Strain Analysis for Engineering Design, 2012. **47**(7): p. 419-431.

55. Tsai, S.W. and E.M. Wu, *A General Theory of Strength for Anisotropic Materials.* Journal of Composite Materials, 1971. **5**(1): p. 58-80.

56. Orifici, A.C., I. Herszberg and R.S. Thomson, *Review of methodologies for composite material modelling incorporating failure.* Composite Structures, 2008. **86**(1–3): p. 194-210.

57. Garnich, M.R. and V.M.K. Akula, *Review of Degradation Models for Progressive Failure Analysis of Fiber Reinforced Polymer Composites.* Applied Mechanics Reviews, 2009. **62**(1): p. 010801.

58. Hashin, Z. and A. Rotem, *A Fatigue Failure Criterion for Fiber Reinforced Materials.* Journal of Composite Materials, 1973. **7**(4): p. 448-464.

59. Hill, R. *A theory of the yielding and plastic flow of anisotropic metals*. in *Proceedings of the Royal Society of London A: Mathematical, Physical and Engineering Sciences*. 1948. The Royal Society.

60. Hashin, Z., *Failure Criteria for Unidirectional Fiber Composites.* Journal of Applied Mechanics, 1980. **47**(2): p. 329-334.

61. Tsai, S.W., *Strength Characteristics of Composite Materials*. 1965, DTIC Document.

62. Lee, J.D., *Three dimensional finite element analysis of damage accumulation in composite laminate.* Computers & Structures, 1982. **15**(3): p. 335-350.

63. Hoffman, O., *The Brittle Strength of Orthotropic Materials.* Journal of Composite Materials, 1967. **1**(2): p. 200-206.

64. Christensen, R.M., *Stress based yield/failure criteria for fiber composites.* International Journal of Solids and Structures, 1997. **34**(5): p. 529-543.

65. Chamis, C.C., *Failure Criteria for Filamentary Composites*. 1969, DTIC Document.

66. Chang, F.-K. and K.-Y. Chang, *A Progressive Damage Model for Laminated Composites Containing Stress Concentrations.* Journal of Composite

Materials, 1987. **21**(9): p. 834-855.

67. Tay, T.E., S.H.N. Tan, V.B.C. Tan and J.H. Gosse, *Damage progression by the element-failure method (EFM) and strain invariant failure theory (SIFT).* Composites Science and Technology, 2005. **65**(6): p. 935-944.

68. Mayes, J.S. and A.C. Hansen, *Composite laminate failure analysis using multicontinuum theory.* Composites Science and Technology, 2004. **64**(3–4): p. 379-394.

69. Ha, S.K., K.K. Jin and Y. Huang, *Micro-Mechanics of Failure (MMF) for Continuous Fiber Reinforced Composites.* Journal of Composite Materials, 2008. **42**(18): p. 1873-1895.

70. Liu, P.F. and J.Y. Zheng, *Recent developments on damage modeling and finite element analysis for composite laminates: A review.* Materials & Design, 2010. **31**(8): p. 3825-3834.

71. Hinton, M.J., A.S. Kaddour and P.D. Soden, *A comparison of the predictive capabilities of current failure theories for composite laminates, judged against experimental evidence.* Composites Science and Technology, 2002. **62**(12–13): p. 1725-1797.

72. Hinton, M. and A. Kaddour, *The background to the Second World-Wide Failure Exercise.* Journal of Composite Materials, 2012. **46**(19-20): p. 2283-2294.

73. Williams, K.V. and R. Vaziri, *Application of a damage mechanics model for predicting the impact response of composite materials.* Computers & Structures, 2001. **79**(10): p. 997-1011.

74. Talreja, R., *A Continuum Mechanics Characterization of Damage in Composite Materials.* Proceedings of the Royal Society of London. A. Mathematical and Physical Sciences, 1985. **399**(1817): p. 195-216.

75. Talreja, R., *Transverse Cracking and Stiffness Reduction in Composite Laminates.* Journal of Composite Materials, 1985. **19**(4): p. 355-375.

76. Ladeveze, P., O. Allix and L. Daudeville, *Mesomodeling of damage for laminate composites: Application to delamination.* Inelastic deformation of composite materials, 1990: p. 607-622.

77. Pickett, A.K., E. Haug and J. Rückert, *A fracture damaging law suitable for anisotropic short fibre/matrix materials in an explicit finite element code.* Composites, 1990. **21**(4): p. 297-304.

78. Frantziskonis, G. and S. Joshi, *Damage evolution and constitutive behavior of advanced composites.* Composite Structures, 1990. **16**(4): p. 341-357.

79. Randles, P. and J. Nemes, *A continuum damage model for thick composite materials subjected to high-rate dynamic loading.* Mechanics of

Materials, 1992. **13**(1): p. 1-13.

80. Yang, Q. and J.J. Engblom, *Finite element based sub-laminate damage model for intraply cracking.* Journal of Reinforced Plastics and Composites, 1995. **14**(3): p. 233-254.

81. Yazdchi, M., S. Valliappan and W. Zhang, *A continuum model for dynamic damage evolution of anisotropic brittle materials.* International journal for numerical methods in engineering, 1996. **39**(9): p. 1555-1583.

82. Matzenmiller, A., J. Lubliner and R.L. Taylor, *A constitutive model for anisotropic damage in fiber-composites.* Mechanics of Materials, 1995. **20**(2): p. 125-152.

83. Zhou, Y., Y. Wang, Y. Xia and S. Jeelani, *Tensile behavior of carbon fiber bundles at different strain rates.* Materials Letters, 2010. **64**(3): p. 246-248.

84. Zhou, Y., D. Jiang and Y. Xia, *Tensile mechanical behavior of T300 and M40J fiber bundles at different strain rate.* Journal of Materials Science, 2001. **36**(4): p. 919-922.

85. Yazici, M., *Loading Rate Sensitivity of High Strength Fibers and Fiber/Matrix Interfaces.* Journal of Reinforced Plastics and Composites, 2009. **28**(15): p. 1869-1880.

86. Wang, Y. and Y. Xia, *The effects of strain rate on the mechanical behaviour of kevlar fibre bundles: an experimental and theoretical study.* Composites Part A: Applied Science and Manufacturing, 1998. **29**(11): p. 1411-1415.

87. Fishpool, D., A. Rezai, D. Baker, S. Ogin and P. Smith, *Preferential energy absorbing interfaces for ballistic and structural applications,* in 18th International Conference on Composite Materials. 2011: Jeju Island.

88. Tanoglu, M., S.H. McKnight, G.R. Palmese and J.W. Gillespie Jr, *The effects of glass-fiber sizings on the strength and energy absorption of the fiber/matrix interphase under high loading rates.* Composites Science and Technology, 2001. **61**(2): p. 205-220.

89. Jacob, G.C., J.M. Starbuck, J.F. Fellers, S. Simunovic and R.G. Boeman, *Strain rate effects on the mechanical properties of polymer composite materials.* Journal of Applied Polymer Science, 2004. **94**(1): p. 296-301.

90. Sierakowski, R., *Strain rate effects in composites.* Applied Mechanics Reviews, 1997. **50**: p. 741.

91. Okoli, O.I. and G.F. Smith, *Failure modes of fibre reinforced composites: The effects of strain rate and fibre content.* Journal of Materials Science, 1998. **33**(22): p. 5415-5422.

92. Sun, C.T. and J.L. Chen, *A Simple Flow Rule for Characterizing Nonlinear Behavior of Fiber Composites.* Journal of Composite Materials, 1989.

23(10): p. 1009-1020.

93. Weeks, C.A. and C.T. Sun, *Modeling non-linear rate-dependent behavior in fiber-reinforced composites.* Composites Science and Technology, 1998. **58**(3–4): p. 603-611.

94. Thiruppukuzhi, S.V. and C.T. Sun, *Models for the strain-rate-dependent behavior of polymer composites.* Composites Science and Technology, 2001. **61**(1): p. 1-12.

95. Naik, N.K., P.J. Shankar, V.R. Kavala, G. Ravikumar, J.R. Pothnis and H. Arya, *High strain rate mechanical behavior of epoxy under compressive loading: Experimental and modeling studies.* Materials Science and Engineering: A, 2011. **528**(3): p. 846-854.

96. Ryou, H., K. Chung and W.-R. Yu, *Constitutive modeling of woven composites considering asymmetric/anisotropic, rate dependent, and nonlinear behavior.* Composites Part A: Applied Science and Manufacturing, 2007. **38**(12): p. 2500-2510.

97. Xing, L. and K.L. Reifsnider, *Progressive failure modeling for dynamic loading of woven composites.* Applied Composite Materials, 2008. **15**(1): p. 1-11.

98. Donadon, M.V., S.F.M. De Almeida, M.A. Arbelo and A.R. de Faria, *A three-dimensional ply failure model for composite structures.* International Journal of Aerospace Engineering, 2009. **2009**.

99. Maio, L., E. Monaco, F. Ricci and L. Lecce, *Simulation of low velocity impact on composite laminates with progressive failure analysis.* Composite Structures, 2013. **103**: p. 75-85.

100. Xiao, J.R., B.A. Gama and J.W. Gillespie Jr, *Progressive damage and delamination in plain weave S-2 glass/SC-15 composites under quasi-static punch-shear loading.* Composite Structures, 2007. **78**(2): p. 182-196.

101. Brown, K.A., R. Brooks and N.A. Warrior, *The static and high strain rate behaviour of a commingled E-glass/polypropylene woven fabric composite.* Composites Science and Technology, 2010. **70**(2): p. 272-283.

102. Raimondo, L., L. Iannucci, P. Robinson and P.T. Curtis, *Modelling of strain rate effects on matrix dominated elastic and failure properties of unidirectional fibre-reinforced polymer–matrix composites.* Composites Science and Technology, 2012. **72**(7): p. 819-827.

103. Daniel, I.M., B.T. Werner and J.S. Fenner, *Strain-rate-dependent failure criteria for composites.* Composites Science and Technology, 2011. **71**(3): p. 357-364.

104. Yen, C.-F. and A.A. Caiazzo, *Innovative processing of multifunctional composite armor for ground vehicles*. 2001: Army Research Laboratory.

105. Cowper, G.R. and P.S. Symonds, *Strain-hardening and strain-rate effects in the impact loading of cantilever beams*. 1957: Division of Applied Mathematics, Brown University.

106. Johnson, G.R. and W.H. Cook. *A constitutive model and data for metals subjected to large strains, high strain rates and high temperatures*. in *Proceedings of the 7th International Symposium on Ballistics*. 1983. The Hague, The Netherlands.

107. Sun, C.T., *1.20 - Strength Analysis of Unidirectional Composites and Laminates*, in *Comprehensive Composite Materials*, A.K. Zweben, Editor. 2000, Pergamon: Oxford. p. 641-666.

108. Daniel, I., *Failure of composite materials.* Strain, 2007. **43**(1): p. 4-12.

109. Koerber, H. and P. Camanho, *High strain rate characterisation of unidirectional carbon–epoxy IM7-8552 in longitudinal compression.* Composites Part A: Applied Science and Manufacturing, 2011. **42**(5): p. 462-470.

110. Koerber, H., J. Xavier and P. Camanho, *High strain rate characterisation of unidirectional carbon-epoxy IM7-8552 in transverse compression and in-plane shear using digital image correlation.* Mechanics of Materials, 2010. **42**(11): p. 1004-1019.

111. LSTC, *LS-DYNA Keyword User's Manual Version R7.1*. Vol. II, May, 2014.

112. LSTC, *LS-DYNA Keyword User's Manual Version R7.1*. Vol. I, May, 2014.

113. Williams, K. and R. Vaziri. *Fnite element analysis of the impact response of CFRP composite plates*. in *Tenth International Conference on Composite Materials. V. Structures*. 1995.

114. Brown, K.A., *Finite element modelling of the static and dynamic impact behaviour of thermoplastic composite sandwich structures*, PhD thesis, University of Nottingham, 2007.

115. Hamouda, A.M.S. and M.S.J. Hashmi, *Testing of composite materials at high rates of strain: advances and challenges.* Journal of Materials Processing Technology, 1998. **77**(1–3): p. 327-336.

116. Field, J.E., S.M. Walley, W.G. Proud, H.T. Goldrein and C.R. Siviour, *Review of experimental techniques for high rate deformation and shock studies.* International Journal of Impact Engineering, 2004. **30**(7): p. 725-775.

117. ASTM International, *ASTM D3039 / D3039M-08, Standard Test Method for Tensile Properties of Polymer Matrix Composite Materials*. 2008: West Conshohocken, PA.

118. ASTM International, *ASTM D6641 / D6641M-14, Standard Test*

Method for Compressive Properties of Polymer Matrix Composite Materials Using a Combined Loading Compression (CLC) Test Fixture. 2014: West Conshohocken, PA.

119. Lindholm, U.S., *Some experiments with the split hopkinson pressure bar*. Journal of the Mechanics and Physics of Solids, 1964. **12**(5): p. 317-335.

120. Hauser, F., *Techniques for measuring stress-strain relations at high strain rates.* Experimental Mechanics, 1966. **6**(8): p. 395-402.

121. Cox, B.N., M.S. Dadkhah, W.L. Morris and J.G. Flintoff, *Failure mechanisms of 3D woven composites in tension, compression, and bending.* Acta Metallurgica et Materialia, 1994. **42**(12): p. 3967-3984.

122. Cox, B. and M. Dadkhah, *The macroscopic elasticity of 3D woven composites.* Journal of Composite Materials, 1995. **29**(6): p. 785-819.

123. Cox, B.N., M.S. Dadkhah and W.L. Morris, *On the tensile failure of 3D woven composites.* Composites Part A: Applied Science and Manufacturing, 1996. **27**(6): p. 447-458.

124. Brandt, J., K. Drechsler and F.J. Arendts, *Mechanical performance of composites based on various three-dimensional woven-fibre preforms.* Composites Science and Technology, 1996. **56**(3): p. 381-386.

125. Callus, P.J., A.P. Mouritz, M.K. Bannister and K.H. Leong, *Tensile properties and failure mechanisms of 3D woven GRP composites.* Composites Part A: Applied Science and Manufacturing, 1999. **30**(11): p. 1277-1287.

126. Tan, P., L. Tong, G.P. Steven and T. Ishikawa, *Behavior of 3D orthogonal woven CFRP composites. Part I. Experimental investigation.* Composites Part A: Applied Science and Manufacturing, 2000. **31**(3): p. 259-271.

127. Leong, K.H., B. Lee, I. Herszberg and M.K. Bannister, *The effect of binder path on the tensile properties and failure of multilayer woven CFRP composites.* Composites Science and Technology, 2000. **60**(1): p. 149-156.

128. Bogdanovich, A.E., M. Karahan, S.V. Lomov and I. Verpoest, *Quasi-static tensile behavior and damage of carbon/epoxy composite reinforced with 3D non-crimp orthogonal woven fabric.* Mechanics of Materials, 2013. **62**: p. 14-31.

129. Lomov, S., M. Karahan, A. Bogdanovich and I. Verpoest, *Monitoring of acoustic emission damage during tensile loading of 3D woven carbon/epoxy composites.* Textile Research Journal, 2014. **84**(13): p. 1373-1384.

130. Kuo, W.-S. and T.-H. Ko, *Compressive damage in 3-axis orthogonal fabric composites.* Composites Part A: Applied Science and Manufacturing, 2000. **31**(10): p. 1091-1105.

131. Kuo, W.-S., T.-H. Ko and C.-P. Chen, *Effect of weaving processes on*

compressive behavior of 3D woven composites. Composites Part A: Applied Science and Manufacturing, 2007. **38**(2): p. 555-565.

132. Warren, K.C., R.A. Lopez-Anido and J. Goering, *Experimental investigation of three-dimensional woven composites.* Composites Part A: Applied Science and Manufacturing, 2015. **73**: p. 242-259.

133. ASTM International, *ASTM D7078 / D7078M-12, Standard Test Method for Shear Properties of Composite Materials by V-Notched Rail Shear Method*. 2012: West Conshohocken, PA.

134. Dai, S., P.R. Cunningham, S. Marshall and C. Silva, *Influence of fibre architecture on the tensile, compressive and flexural behaviour of 3D woven composites.* Composites Part A: Applied Science and Manufacturing, 2015. **69**: p. 195-207.

135. ASTM International, *ASTM D695 standard test method for compressive properties of rigid plastics*. 2010: West Conshohocken, PA.

136. ASTM International, *ASTM D790 standard test methods for flexural properties of unreinforced and reinforced plastics and electrical insulating materials*. 2010: West Conshohocken, PA.

137. Gerlach, R., C.R. Siviour, J. Wiegand and N. Petrinic, *The strain rate dependent material behavior of S-GFRP extracted from GLARE.* Mechanics of advanced materials and structures, 2013. **20**(7): p. 505-514.

138. Shokrieh, M.M. and M.J. Omidi, *Investigating the transverse behavior of Glass–Epoxy composites under intermediate strain rates.* Composite Structures, 2011. **93**(2): p. 690-696.

139. Schaefer, J., B. Werner and I. Daniel, *Strain-rate-dependent failure of a Toughened matrix composite.* Experimental Mechanics, 2014. **54**(6): p. 1111-1120.

140. Chen, X., Y. Li, Z. Zhi, Y. Guo and N. Ouyang, *The compressive and tensile behavior of a 0/90 C fiber woven composite at high strain rates.* Carbon, 2013. **61**: p. 97-104.

141. Ravikumar, G., J.R. Pothnis, M. Joshi, K. Akella, S. Kumar and N.K. Naik, *Analytical and experimental studies on mechanical behavior of composites under high strain rate compressive loading.* Materials & Design, 2013. **44**: p. 246-255.

142. Sun, B., B. Gu and X. Ding, *Compressive behavior of 3-D angle-interlock woven fabric composites at various strain rates.* Polymer Testing, 2005. **24**(4): p. 447-454.

143. Pan, L., K. Liu, F. Zhang, B. Gu and B. Sun, *Finite element modeling of compressive properties of three-dimensional woven composites under various strain rates.* Journal of Composite Materials, 2014: p. 0021998314549819.

144. Sun, B. and B. Gu, *High strain rate behavior of 4-step 3D braided composites under compressive failure.* Journal of Materials Science, 2007. **42**(7): p. 2463-2470.

145. Sun, B., F. Liu and B. Gu, *Influence of the strain rate on the uniaxial tensile behavior of 4-step 3D braided composites.* Composites Part A: Applied Science and Manufacturing, 2005. **36**(11): p. 1477-1485.

146. Sun, B. and B. Gu, *Shear Behavior of 3D Orthogonal Woven Fabric Composites under High Strain Rates.* Journal of Reinforced Plastics and Composites, 2006. **25**(17): p. 1833-1845.

147. Pankow, M., A. Salvi, A.M. Waas, C.F. Yen and S. Ghiorse, *Split Hopkinson pressure bar testing of 3D woven composites.* Composites Science and Technology, 2011. **71**(9): p. 1196-1208.

148. Gerlach, R., C.R. Siviour, J. Wiegand and N. Petrinic, *In-plane and through-thickness properties, failure modes, damage and delamination in 3D woven carbon fibre composites subjected to impact loading.* Composites Science and Technology, 2012. **72**(3): p. 397-411.

149. Hufenbach, W., M. Gude, C. Ebert, M. Zscheyge and A. Hornig, *Strain rate dependent low velocity impact response of layerwise 3D-reinforced composite structures.* International Journal of Impact Engineering, 2011. **38**(5): p. 358-368.

150. Hufenbach, W., R. Böhm, M. Thieme, A. Winkler, E. Mäder, J. Rausch and M. Schade, *Polypropylene/glass fibre 3D-textile reinforced composites for automotive applications.* Materials & Design, 2011. **32**(3): p. 1468-1476.

151. Hufenbach, W., A. Hornig, B. Zhou, A. Langkamp and M. Gude, *Determination of strain rate dependent through-thickness tensile properties of textile reinforced thermoplastic composites using L-shaped beam specimens.* Composites Science and Technology, 2011. **71**(8): p. 1110-1116.

152. Sarkar, S. and S.N. Atluri, *Effects of multiple blade interaction on the containment of blade fragments during a rotor failure.* Finite Elements in Analysis and Design, 1996. **23**(2–4): p. 211-223.

153. Yuri, S., G. Dmitriy, R. Alexander, K. Sergey and R. Vadim, *Numerical Analysis of Aircraft Engine Fan Blade-Out*, in *42nd AIAA/ASME/SAE/ASEE Joint Propulsion Conference & Exhibit*. 2006, American Institute of Aeronautics and Astronautics.

154. Heidari, M., D.L. Carlson, S. Sinha, R. Sadeghi, C. Heydari, H. Bayoumi and J. Son, *An efficient multi-disciplinary simulation of engine fan-blade out event using MD Nastran.* American Institute of Aeronautics and Astronautics, New York, 2008.

155. Sinha, S.K. and S. Dorbala, *Dynamic loads in the fan containment structure of a turbofan engine.* Journal of Aerospace Engineering, 2009. **22**(3): p. 260-269.

156. Xuan, H.-j. and R.-r. Wu, *Aeroengine turbine blade containment tests using high-speed rotor spin testing facility.* Aerospace Science and Technology, 2006. **10**(6): p. 501-508.

157. He, Q., H. Xuan, L. Liu, W. Hong and R. Wu, *Perforation of aero-engine fan casing by a single rotating blade.* Aerospace Science and Technology, 2013. **25**(1): p. 234-241.

158. Carney, K.S., J.M. Pereira, D.M. Revilock and P. Matheny, *Jet engine fan blade containment using an alternate geometry.* International Journal of Impact Engineering, 2009. **36**(5): p. 720-728.

159. Kasano, H., *Recent Advances in High-Velocity Impact Perforation of Fiber Composite Laminates.* JSME International Journal Series A Solid Mechanics and Material Engineering, 1999. **42**(2): p. 147-157.

160. Hazell, P.J. and G.J. Appleby-Thomas, *The impact of structural composite materials. Part 1: ballistic impact.* The Journal of Strain Analysis for Engineering Design, 2012. **47**(7): p. 396-405.

161. Richardson, M.O.W. and M.J. Wisheart, *Review of low-velocity impact properties of composite materials.* Composites Part A: Applied Science and Manufacturing, 1996. **27**(12): p. 1123-1131.

162. Abrate, S., *Impact on laminated composite materials.* Appl Mech Rev, 1991. **44**(4): p. 155-90.

163. Baucom, J.N. and M.A. Zikry, *Low-velocity impact damage progression in woven E-glass composite systems.* Composites Part A: Applied Science and Manufacturing, 2005. **36**(5): p. 658-664.

164. Walter, T.R., G. Subhash, B.V. Sankar and C.F. Yen, *Damage modes in 3D glass fiber epoxy woven composites under high rate of impact loading.* Composites Part B: Engineering, 2009. **40**(6): p. 584-589.

165. Larsson, F., *Damage tolerance of a stitched carbon/epoxy laminate.* Composites Part A: Applied Science and Manufacturing, 1997. **28**(11): p. 923-934.

166. Hosur, M., U. Vaidya, C. Ulven and S. Jeelani, *Performance of stitched/unstitched woven carbon/epoxy composites under high velocity impact loading.* Composite Structures, 2004. **64**(3): p. 455-466.

167. Caprino, G., V. Lopresto and D. Santoro, *Ballistic impact behaviour of stitched graphite/epoxy laminates.* Composites Science and Technology, 2007. **67**(3): p. 325-335.

168. Jia, X., B. Sun and B. Gu, *Ballistic penetration of conically cylindrical steel projectile into 3D orthogonal woven composite: a finite element study at microstructure level.* Journal of Composite Materials, 2010: p. 0021998310381150.

169. Cui, F., B. Sun and B. Gu, *Fiber inclination model for finite element analysis of three-dimensional angle interlock woven composite under ballistic penetration.* Journal of Composite Materials, 2011. **45**(14): p. 1499-1509.

170. Hosur, M.V., A. Abraham, S. Jeelani and U. Vaidya, *Studies on the Influence of Through-the-Thickness Reinforcement on Low-Velocity and High Strain Rate Response of Woven S2-Glass/Vinyl Ester Composite.* Journal of Composite Materials, 2001. **35**(12): p. 1111-1133.

171. Chiu, C., M. Lai and C. Wu, *Compression failure mechanisms of 3-D angle interlock woven composites subjected to low-energy impact.* Polymers and Polymer Composites, 2004. **12**(4): p. 309-320.

172. Pearson, J., M. Zikry, M. Prabhugoud and K. Peters, *Global-local assessment of low-velocity impact damage in woven composites.* Journal of Composite Materials, 2007. **41**(23): p. 2759-2783.

173. Seltzer, R., C. González, R. Muñoz, J. LLorca and T. Blanco-Varela, *X-ray microtomography analysis of the damage micromechanisms in 3D woven composites under low-velocity impact.* Composites Part A: Applied Science and Manufacturing, 2013. **45**: p. 49-60.

174. Lv, L., B. Sun, Y. Qiu and B. Gu, *Energy absorptions and failure modes of 3D orthogonal hybrid woven composite struck by flat-ended rod.* Polymer Composites, 2006. **27**(4): p. 410-416.

175. Muñoz, R., F. Martínez-Hergueta, F. Gálvez, C. González and J. LLorca, *Ballistic performance of hybrid 3D woven composites: Experiments and simulations.* Composite Structures, 2015. **127**: p. 141-151.

176. SINOMA, *SINOMA homepage*. 20th September 2014. Available from: http://www.sinoma.com.cn/.

177. Gurit, *PRIME™ 20LV Epoxy Infusion System*. 20th August 2014. Available from: www.gurit.com/files/documents/prime-20lvv12pdf.pdf.

178. Nanjing Fiberglass Research and Development Institute, *Properties of high-strength glass fibres*. 14th March 2014. Available from: http://www.fiberglasschina.com/browse.php?id=91&pid=18.

179. Soden, P.D., M.J. Hinton and A.S. Kaddour, *Lamina properties, lay-up configurations and loading conditions for a range of fibre-reinforced composite laminates.* Composites Science and Technology, 1998. **58**(7): p. 1011-1022.

180. Hexcel, *HexTow® IM7 Carbon Fiber*. 4th January 2016. Available from: http://www.hexcel.com/resources/datasheets/carbon-fiber-data-sheets/im7.pdf.

181. iMetrum, *iMetrum homepage* 20th September 2015. Available from: http://www.imetrum.com/.

182. Fernie, R. and U.o. Nottingham, *Loading Rate Effects on the Energy Absorption of Lightweight Tubular Crash Structures*. 2002: University of

Nottingham.

183. ASTM International, *ASTM D3518 / D3518M-08, Standard Test Method for In-Plane Shear Response of Polymer Matrix Composite Materials by Tensile Test of a ±45° Laminate*. 2008: West Conshohocken, PA.

184. Lamontage, C.G., G.N. Manuelpillai, E.A. Taylor and R.C. Tennyson, *Normal and oblique hypervelocity impacts on carbon fibre/peek composites.* International Journal of Impact Engineering, 1999. **23**(1): p. 519-532.

185. Chen, W.W. and B. Song, *Split Hopkinson (Kolsky) bar: design, testing and applications*. 2010: Springer Science & Business Media.

186. Morrison, F.A., *Data correlation for drag coefficient for sphere.* Michigan Technology University, Houghton, MI, 2010.

187. Montgomery, R., *Viscosity and thermal conductivity of air and diffusivity of water vapor in air.* Journal of Meteorology, 1947. **4**(6): p. 193-196.

188. Hexcel, *Hexcel homepage*. 7th August 2014. Available from: http://www.hexcel.com/.

189. Tracker, *Tracker homepage*. 23th October 2014. Available from: http://physlets.org/tracker/.

190. Lambert, J. and G. Jonas, *Towards standardization in terminal ballistics testing: velocity representation*. 1976, DTIC Document.

191. ImageJ, *ImageJ - RSB Home Page*. 20th July 2016. Available from: https://imagej.nih.gov/ij/.

192. Gellert, E.P., S.J. Cimpoeru and R.L. Woodward, *A study of the effect of target thickness on the ballistic perforation of glass-fibre-reinforced plastic composites.* International Journal of Impact Engineering, 2000. **24**(5): p. 445-456.

193. Mouritz, A.P., *Ballistic impact and explosive blast resistance of stitched composites.* Composites Part B: Engineering, 2001. **32**(5): p. 431-439.

194. Wonderly, C., J. Grenestedt, G. Fernlund and E. Cěpus, *Comparison of mechanical properties of glass fiber/vinyl ester and carbon fiber/vinyl ester composites.* Composites Part B: Engineering, 2005. **36**(5): p. 417-426.

195. Naik, N.K. and P. Shrirao, *Composite structures under ballistic impact.* Composite Structures, 2004. **66**(1–4): p. 579-590.

196. Zhou, F., C. Zhang, X. Chen, C. Zhu and P. Hogg, *An experimental comparison of different carbon and glass laminates for ballistic protection,* in 18th International Conference on Composite Materials. 2011: Jeju Island.

197. Collings, T.A., *Transverse compressive behaviour of unidirectional carbon fibre reinforced plastics.* Composites, 1974. **5**(3): p. 108-116.

198. Gama, B.A. and J.W. Gillespie Jr, *Finite element modeling of impact, damage evolution and penetration of thick-section composites.* International Journal of Impact Engineering, 2011. **38**(4): p. 181-197.

199. LS-DYNA Support, *Contact modelling in LS-DYNA*. 20th July 2016. Available from: http://www.dynasupport.com/tutorial/ls-dyna-users-guide/contact-modeling-in-ls-dyna.

200. Wen, H.M., *Predicting the penetration and perforation of FRP laminates struck normally by projectiles with different nose shapes.* Composite Structures, 2000. **49**(3): p. 321-329.

201. Wen, H.M., *Penetration and perforation of thick FRP laminates.* Composites Science and Technology, 2001. **61**(8): p. 1163-1172.

202. Ulven, C., U.K. Vaidya and M.V. Hosur, *Effect of projectile shape during ballistic perforation of VARTM carbon/epoxy composite panels.* Composite Structures, 2003. **61**(1–2): p. 143-150.

203. Jordan, J.B. and C.J. Naito, *An experimental investigation of the effect of nose shape on fragments penetrating GFRP*. International Journal of Impact Engineering, 2014. **63**(0): p. 63-71.

204. Sabet, A., N. Fagih and M.H. Beheshty, *Effect of reinforcement type on high velocity impact response of GRP plates using a sharp tip projectile.* International Journal of Impact Engineering, 2011. **38**(8–9): p. 715-722.

205. Ben-Dor, G., A. Dubinsky and T. Elperin, *Optimal nose geometry of the impactor against FRP laminates.* Composite Structures, 2002. **55**(1): p. 73-80.

206. Tan, V.B.C., C.T. Lim and C.H. Cheong, *Perforation of high-strength fabric by projectiles of different geometry*. International Journal of Impact Engineering, 2003. **28**(2): p. 207-222.

207. Lamontage, C.G., G.N. Manuelpillai, E.A. Taylor and R.C. Tennyson, *Normal and oblique hypervelocity impacts on carbon fibre/peek composites.* International Journal of Impact Engineering, 1999. **23**(1, Part 2): p. 519-532.

208. Lamontagne, C.G., G.N. Manuelpillai, J.H. Kerr, E.A. Taylor, R.C. Tennyson and M.J. Burchell, *Projectile density, impact angle and energy effects on hypervelocity impact damage to carbon fibre/peek composites.* International Journal of Impact Engineering, 2001. **26**(1): p. 381-398.

209. López-Puente, J., R. Zaera and C. Navarro, *Experimental and numerical analysis of normal and oblique ballistic impacts on thin carbon/epoxy woven laminates.* Composites Part A: Applied Science and Manufacturing, 2008. **39**(2): p. 374-387.

210. Pernas-Sánchez, J., J.A. Artero-Guerrero, D. Varas and J. López-Puente, *Experimental analysis of normal and oblique high velocity impacts on carbon/epoxy tape laminates.* Composites Part A: Applied Science and Manufacturing, 2014. **60**: p. 24-31.

211. Hazell, P.J., G. Kister, C. Stennett, P. Bourque and G. Cooper, *Normal and oblique penetration of woven CFRP laminates by a high velocity steel sphere.* Composites Part A: Applied Science and Manufacturing, 2008. **39**(5): p. 866-874.

212. Hazell, P.J., G.J. Appleby-Thomas and G. Kister, *Impact, penetration, and perforation of a bonded carbon-fibre-reinforced plastic composite panel by a high-velocity steel sphere: An experimental study.* The Journal of Strain Analysis for Engineering Design, 2010. **45**(6): p. 439-450.

213. Ramkumar, R.L. and Y.R. Thakar, *Dynamic Response of Curved Laminated Plates Subjected to Low Velocity Impact.* Journal of Engineering Materials and Technology, 1987. **109**(1): p. 67-71.

214. Christoforou, A.P. and S.R. Swanson, *Analysis of Simply-Supported Orthotropic Cylindrical Shells Subject to Lateral Impact Loads.* Journal of Applied Mechanics, 1990. **57**(2): p. 376-382.

215. Palazotto, A., R. Perry and R. Sandhu, *Impact response of graphite/epoxy cylindrical panels.* AIAA Journal, 1992. **30**(7): p. 1827-1832.

216. Kim, S.J., N.S. Goo and T.W. Kim, *The effect of curvature on the dynamic response and impact-induced damage in composite laminates.* Composites Science and Technology, 1997. **57**(7): p. 763-773.

217. Kistler, L.S. and A.M. Waas, *Experiment and analysison the response of curved laminated composite panels subjected to low velocity impact.* International Journal of Impact Engineering, 1998. **21**(9): p. 711-736.

218. Yokoyama, N.O., M.V. Donadon and S.F.M. de Almeida, *A numerical study on the impact resistance of composite shells using an energy based failure model.* Composite Structures, 2010. **93**(1): p. 142-152.

219. Krishnamurthy, K.S., P. Mahajan and R.K. Mittal, *Impact response and damage in laminated composite cylindrical shells.* Composite Structures, 2003. **59**(1): p. 15-36.

220. Sitnikova, E. and S. Li, *Manufacturing the subscale prototype for the containment casing*, in *Report for project "Simulation Methodology for Impact Damage in Composite Components of Aero-Engines"*. 2015, University of Nottingham.

221. Knight Jr, N.F., N. Jaunky, R.E. Lawson and D.R. Ambur, *Penetration simulation for uncontained engine debris impact on fuselage-like panels using LS-DYNA.* Finite Elements in Analysis and Design, 2000. **36**(2): p. 99-133.

222. Ambur, D.R., N. Jaunky, R.E. Lawson and N.F. Knight Jr, *Numerical simulations for high-energy impact of thin plates.* International Journal of Impact Engineering, 2001. **25**(7): p. 683-702.

223. Johnson, H.E., L.A. Louca, S. Mouring and A.S. Fallah, *Modelling impact damage in marine composite panels.* International Journal of Impact

Engineering, 2009. **36**(1): p. 25-39.

224. Marsh, G., *Composites get in deep with new-generation engine.* Reinforced Plastics, 2006. **50**(11): p. 26-29.

225. Carney, K., J.M. Pereira, D. Revilock and P. Matheny, *Jet engine fan blade containment using an alternate geometry.* International Journal of Impact Engineering, 2009. **36**(5): p. 720-728.

226. Alesi, H., R. Jones and N. Mileshkin, *A technique for coupling plate and solid elements*, in *Computational Mechanics' 95*. 1995, Springer. p. 702-707.

227. Osawa, N., K. Hashimoto, J. Sawamura, T. Nakai and S. Suzuki, *Study on shell–solid coupling FE analysis for fatigue assessment of ship structure.* Marine Structures, 2007. **20**(3): p. 143-163.

228. Shim, K.W., D.J. Monaghan and C.G. Armstrong, *Mixed Dimensional Coupling in Finite Element Stress Analysis.* Engineering with Computers, 2002. **18**(3): p. 241-252.

229. Nilakantan, G., M. Keefe, T.A. Bogetti and J.W. Gillespie Jr, *Multiscale modeling of the impact of textile fabrics based on hybrid element analysis.* International Journal of Impact Engineering, 2010. **37**(10): p. 1056-1071.

230. Nilakantan, G., M. Keefe, T.A. Bogetti, R. Adkinson and J.W. Gillespie Jr, *On the finite element analysis of woven fabric impact using multiscale modeling techniques.* International Journal of Solids and Structures, 2010. **47**(17): p. 2300-2315.

231. Li, S. and Z. Zou, *The use of central reflection in the formulation of unit cells for micromechanical FEA.* Mechanics of Materials, 2011. **43**(12): p. 824-834.

232. Hill, R., *The mathematical theory of plasticity*. Vol. 11. 1998: Oxford university press.

233. Pan, Q., E. Sitnikova and S. Li, *Strength prediction for textile composites using artificial neural network, principle component analysis and unit cells*, in *20th International Conference on Composite materials*. 2015: Copenhagen.

234. ACAE, *Mechanical properties of TC4*. 2012.

Appendix 1. Macro scale artificial neural network (ANN) material model from multi-scale modelling

This ANN material model, which was used in the studies in Chapter 5 and Chapter 7, is developed in a parallel PhD project [8] by using a multiscale modelling approach. It has been implemented as User Define Material Subroutine in LS-DYNA for the macro scale simulation of 3D textile composites. A flow chart of this multiscale simulation methodology is illustrated by Figure A1-1. In this appendix, the key procedures of its development are introduced.

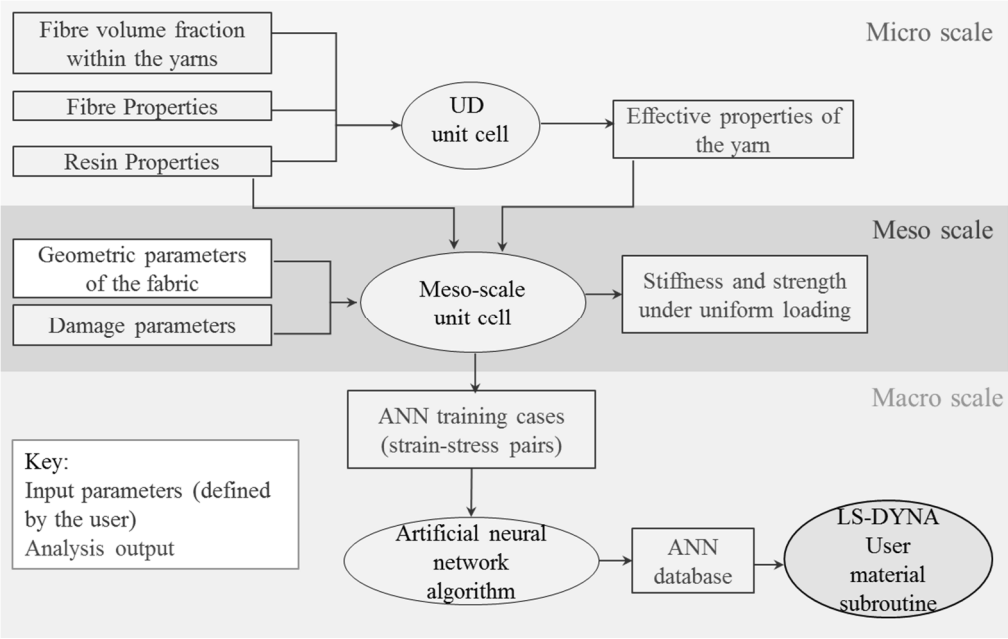


Figure A1-1 A flow chart for the multiscale simulation [8].

Micro scale

The multiscale modelling starts from micro scale level, where a yarn within fibre-reinforced textile composites can be considered as unidirectional (UD) composites, to obtain the mechanical behaviour of the yarns. The packing pattern of fibres within a yarn was assumed as regular and represented by hexagonal unit cells as shown by Figure A1-2. The dark region represents a fibre. Its volume fraction was estimated to be 78.6% in Chapter 3.

Mesh was generated for the whole hexagonal unit cell but only half of it was analysed to save computational effort. Central reflection symmetry boundary condition based on [231] was imposed on the unit cell.

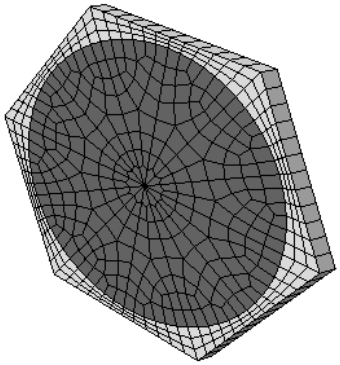


Figure A1-2 Hexagonal unit cell for micro scale simulation [8].

Rate sensitivity of the fibre and the matrix were taken into consideration by scaling their uniaxial moduli and strengths via user-defined subroutine UMAT according to Eq. 3-19 in Chapter 3. To obtain the scaling factors for the PRIME 20LV resin, disk specimens were tested at various dynamic strain rates by using the SHPB apparatus in Chapter 3, together with cylindrical specimens tested under quasi-static compression according to ASTM D695-10 Standard Test Method for Compressive Properties of Rigid Plastics. Despite it has been shown in Chapter 3 that the strain rate during the initial elastic deformation was not constant, its chord moduli was also taken into consideration in this scaling. Taking the QS as the reference strain rate, the scaling factors for strength and modulus are 0.0193 and 0.1175 respectively.

For the glass fibres used in GF-1 and GF-2, the dependency of their moduli and strength was assumed to be the same as the matrix. Carbon fibres were regarded as strain rate insensitive. Maximum principle stress criteria were applied to predict the failure initiation for both fibre and matrix.

The micro-scale had gone through sanity check before it was used in further analysis. The fibre in the unit cell model was assigned the same material properties as the matrix. In such case, a sane model should predict that the effective properties are the same as those of the matrix. This check was also applied to meso-scale unit cell. The majority of issues related to implementation could be found by such checks, however, passing them does not mean the model nor is the methodology validated. For micro-scale level, the modelling was validated against numerous extensive researches on the testing and prediction of various UD composites, for example as in Table A1-1. It was generally found that the prediction is accurate especially for longitudinal properties.

Table A1-1 The predicted effective properties in [8] compared with [179].

	E_1 (GPa)	E_2 (GPa)	υ_{12}	υ_{23}	G_{12} (GPa)	G_{23} (GPa)
Experimental	45.6	16.2	0.278	0.4	5.83	5.786
Unit cell prediction	45.7	11.8	0.252	0.401	4.33	4.215

Then the unit cell was analysed at various strain rates from QS to 10^3/s to find out corresponding dynamic effective properties of the yarns namely six moduli (E_x, E_y, E_z, G_{xy}, G_{yz} and G_{zx},) and nine strength properties (S_{xt}, S_{xc}, S_{yt}, S_{yc}, S_{zt}, S_{zc}, S_{xy}, S_{yz} and S_{zx}). Again, based on Eq. 3-19 in Chapter 3, the strain sensitivity of the yarns with respect to these fifteen properties was also defined.

Meso scale

At meso scale, the unit cells of the 3D woven composites were created according to the micro CT results in Chapter 3. It was assumed that the outmost two layers have minor effects on the mechanical properties of the whole plate so that the unit cell could be largely simplified into as shown by Figure A1-3.

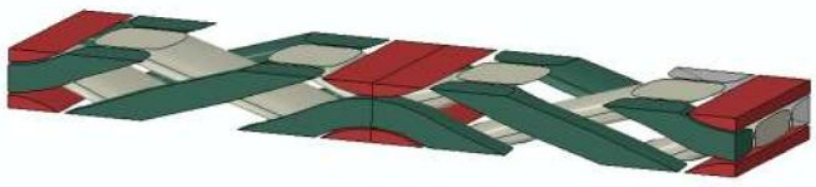


Figure A1-3 Simplified unit cell for meso scale modelling.

The geometry of the unit cell was generated in TexGen based on the measured geometrical parameters in Chapter 3 and then Hypermesh was employed to generate high-quality mesh. Periodic boundary conditions were imposed to the unit cell in Abaqus. The strain-rate dependent material properties of matrix and yarns, which were found in micro-scaling modelling, were used.

The yarns within the unit cell were regarded as UD composites, whose damage initiation was predicted by the failure criteria posed by Hashin [60]. After damage initiation, the stiffness begins to degrade until the final failure and this process was predicted by the damage evolution law by Matzenmiller et al. [82]. The matrix was treated as isotropic material, whose final failure was predicted by von Mises criterion [232].

Table A1-2 The predicted effective properties [8] compared with the experimental values.

		GF-1	GF-2	CF-T300	CF-IM7
Weft tension modulus	Sim.	18.81	22.94	56.99	62.9
	Exp.	15.92±0.55	25.67±1.45	55.16	62.71±0.43
	error	18%	-11%	3%	1%
Warp tension modulus	Sim.	24.61	20.61	51.66	55.83
	Exp.	24.77±3.12	21.83±0.76	48.68	35.79±3.43
	error	-1%	-6%	6%	56%
In-plane shear modulus	Sim.	4.95	4.73	4.19	3.6
	Exp.	4.03±0.14	4.06±0.50	3.41±0.54	3.85±0.42
	error	23%	17%	23%	-6%
Weft tension strength	Sim.	223.16	443.3	512.21	1308.45
	Exp.	206.46±13.57	336.79±31.44	485.29	832.11±40.69
	error	8%	32%	6%	57%
Warp tension strength	Sim.	185.16	210.48	327.27	352.06
	Exp.	223.49±3.35	213.21±6.81	335.53	421.36±25.14
	error	-17%	-1%	-2%	-16%
Weft compression strength	Sim.	185.08	329.67	422.45	1038.01
	Exp.	199.07±5.08	323.18±9.36	386.22±32.81	296.52±17.6
	error	-7%	2%	9%	250%
Warp compression strength	Sim.	184.85	242.39	296.87	309.37
	Exp.	173.33±6.92	167.5±15.37	189.45±31.05	113.13±7.06
	error	7%	45%	57%	173%

After sanity checks, validation for meso-scale unit cell model was carried out against the experimental results of the four 3D woven composites in Chapter 3. The effective properties predicted by the meso-scale unit cell modelling are compared with experimental results in Table A1-2 with errors normalised to corresponding experimental values.

It seems that, though some of the properties were accurately predicted, the discrepancy of the others is significant. The ones with more than 20% are underlined in the table. If the deviation of experimental results in Chapter 3 is taken into consideration, those still significantly larger than 20% are marked in bold. It can be seen that the prediction is least accurate for CF-IM7, whose compressive strengths were overestimated by more than 1.5 times. While the predictions for the other three composites are generally in acceptable

accuracy. Relatively accurate prediction is made on the weft tension modulus, in-plane shear modulus and warp tension modulus for all the four composites. The least accurate prediction is the warp compressive strength, which seems to be significantly over predicted for GF-2, CF-T300 and CF-IM7. This is possibly more related to the experiment as the warp specimens under compression may buckle early and become unstable due to yarn crimping, while the unit cell model excluded the possibility of instability and predicted failure only when the criteria were satisfied. As a whole, the prediction of the meso-scale unit cell modelling is considered as acceptable. It was then used with ANN to predict the effective properties of the 3D woven composites for any loading conditions.

ANN

ANN is essentially a sophisticated interpolation method, where a complicated structure consists of numerous neural elements in several layers. Only the key procedures of using ANN method are introduced here. Detailed procedures and an overview about ANN could be found in [233].

A full ANN can comprise numerous neural elements in several layers. Several types of ANN have been developed by varying the connections among the elements. The ANN used in this study is a feed-forward (FF) ANN, which provides accurate prediction in a simple network. Each element within the network has multiple inputs (x_1,x_2,…x_n) and one output y. The relationship $f(x)$ between the inputs and output is defined with weight coefficients ω_i and threshold θ as Eq. (A1-1). A process called training, during which the weight coefficients and threshold are determined through complicated iterations for each element, is required before any prediction can be made by ANN.

$$y = f\left(\sum_{i=1}^{n} \omega_i x_i - \theta\right) \tag{A1-1}$$

The inputs of ANN in this study are the six strain components and the strain rate while the outputs are the six stress components. For instance, for a specific strain rate, if the direct strains ε_{11}, ε_{22}, ε_{33}, were assigned values from the set [0, 0.3, -0.3] and the shear strains γ_{11}, γ_{22}, γ_{33} were assigned values from the set [0, 0.3], there would be 215 loading conditions as the all-zero condition needs to be

excluded. Furthermore, if 30 increments were defined for each loading condition, there would be 6450 strain combinations. The stress for each strain combination was then calculated by the meso-scale unit cell model. This process was repeated for the other strain rate. Eventually, a large number of stress-strain pairs were generated. Half of them were used to train the ANN and then the quality of training was tested against the other half. The error was found to be commonly less than 1% in [233].

Then the parameters and structure of the trained ANN were coded into a database file, which can be accessed by LS-DYNA solver via the user-defined subroutines to predict the material response at macro-scale level. The final failure of the material and its corresponding element deletion was designated to happen when the tangential stiffness matrix (DDSDDE) becomes singular.

Appendix 2. The properties of titanium

Table A2-1 The properties of Titanium used to model deformable blade-shape impactor provided by ACAE [234].

Material	Density (kg/m^3)	Young's modulus (GPa)	Poisson's ratio
Titanium	4453.2	110.3	0.310

Table A2-2 The strain rate dependency of the Titanium provided by ACAE [234].

Strain rate (1/s)	Yielding strength (MPa)	Strain at yielding
0	896.3	0.18
4.4×10^{-4}	965.2	0.18
4.4	1158.3	0.18
520	1254.8	0.18
10000	1392.7	0.18
1.0×10^{5}	1461.7	0.18